UNIVERSITY OF OKLAHOMA

GRADUATE COLLEGE

INITIATION MECHANISMS OF NOCTURNAL CONVECTION WITHOUT NEARBY SURFACE BOUNDARIES OVER THE GREAT PLAINS

A DISSERTATION

SUBMITTED TO THE GRADUATE FACULTY

in partial fulfillment of the requirements for the

Degree of

DOCTOR OF PHILOSOPHY

By

Dylan Walter Reif
Norman, Oklahoma
2020

INITIATION MECHANISMS OF NOCTURNAL CONVECTION WITHOUT NEARBY SURFACE BOUNDARIES OVER THE GREAT PLAINS

A DISSERTATION APPROVED FOR THE
SCHOOL OF METEOROLOGY

BY THE COMMITTEE CONSISTING OF

Dr. Howard Bluestein, Chair

Dr. Caleb Fulton

Dr. Steven Cavallo

Dr. David Parsons

Dr. Alan Shapiro

Acknowledgments

May 3, 1999. I'll never forget that day. Going to the public storm shelter at Whittier Middle School with my family and then seeing the damage done by the F5 tornado in Moore, OK, a few days later are things that I'll never forget. That day didn't spark my love for meteorology, but it solidified it. Ever since I was a child, I wanted to become a meteorologist. I remember attending the open house for the National Severe Storms Lab when it was at North Base. I was probably 5 or 6 years old. I thought weather was the coolest thing, and I wanted to become a meteorologist so I could "do something with the radar in the big golf ball."

Fast-forward almost 25 years, and I can say I've accomplished that goal. I got my B.S. in Meteorology in 2013, my Master's in 2015, and now my Ph.D. in 2020. Throughout my graduate career, I was privileged to operate the RaXPol Doppler radar. I'll never forget my first chase with it. I was so nervous about messing up. Fortunately, I did not and was part of some of the most memorable data-collection events. The Sulphur, OK, and Dodge City, KS events (both in 2016) come to mind. Chasing with RaXPol is something that I treasure and will forever.

I would not have had all of these experiences without the many people in my life who have supported me and motivated me to keep going. First, I need to thank my parents for always being there for me, even when times get tough. They've supported me in every decision I've made, and I have always relied on their advice and guidance through the most difficult times. I would not be the person I am today without them. I simply cannot thank them enough.

Next, I thank my sister. We're always there for each other. She supported me when times were tough and is willing to share my celebration when things are good. I couldn't ask for a better sister, and I'm extremely proud to be her brother.

Zach Wienhoff, Chris Riedel, and Kyle Thiem. We started graduate school at the same time, and I knew each of you before then. We had some good times together, from the long nights studying for Fundamentals and Dynamics, to playing catch on the front lawn of the NWC, to playing Pokémon go together during the summer of 2016 (and still today, but we won't talk about how I've played a mobile game for nearly five years). Graduate school has been challenging, but you made it a little easier every day. Thank you.

Next to my committee members Alan Shapiro, Dave Parsons, and Steven Cavallo. I had the privilege of having each of you as an instructor, whether it be for undergraduate or graduate courses. I can honestly say that your classes were some of the most challenging, but they were also some of the most rewarding classes that I took. Fundamentals was a challenge, to say the least, but it served as a good reminder of the expectations in graduate school. That was probably the most valuable thing I learned in that class, and I applied that lesson to all of my other courses and had similar success in all of my classes. Dynamics I and II were easily some of the most important classes for me. I got to challenge myself with the material and Dynamics I was a good introduction to the level of math that would be expected throughout graduate school.

I had the pleasure of meeting Tammy Weckwerth at the pre-PECAN science meeting in March of 2015 and got to work with her during PECAN that summer. During 2018, I got to study under her as an NCAR ASP graduate student visitor and that summer was one of the best experiences that I had. It was nice to gain a different perspective by working in a different environment and having a different advisor guide me through a research project. Tammy has been one of my most-valuable contacts and she has been an important contributor to my success.

Finally, I need to thank my advisor, Howie "Cb" Bluestein. It has been an honor and a privilege to be your graduate student, and I cannot thank you enough for the opportunities you have given me throughout my time here at OU. I've made so many connections, taught undergraduate courses, filled in for you in your graduate-level courses when you were away, served on different field projects, and presented at so many conferences, and I have you to thank for all of these opportunities. When I took your (3) classes here, I worked extra hard because I thought it would be embarrassing not to do well in my advisor's class. When you told me that I would become RaXPol's operator back in 2016, I can't tell you how excited and nervous I was. I hadn't chased storms like that before, and my only field experience was in PECAN, but you gave me a chance. I've had an absolute blast operating that radar, and I've learned so much too.

Table of Contents

Acknowledgments **iv**

List of Tables **x**

List of Figures **xii**

Abstract **xxvii**

1 Introduction **1**
- 1.1 Nocturnal Convection Initiation 2
  - 1.1.1 20-Year Climatology (1996-2015) 3
  - 1.1.2 NB CI Mode Initiation Mechanisms 4
- 1.2 Atmospheric Gravity Waves 6
  - 1.2.1 Atmospheric Bores 7
    - 1.2.1.1 Hydraulic Theory 8
    - 1.2.1.2 Conditions for Wave Trapping 8
  - 1.2.2 Atmospheric Bore Characteristics 11
  - 1.2.3 Ascent Associated with Atmospheric Bores 12
- 1.3 Nocturnal Low-Level Jet 14
  - 1.3.1 LLJ Formation 16
  - 1.3.2 Ascent associated with the LLJ 17
- 1.4 Potential Vorticity Anomalies 22
  - 1.4.1 Characteristics of PV anomalies 23
  - 1.4.2 Ascent associated with PV anomalies 26

2 Methods **47**
- 2.1 Idealized Nocturnal Atmospheric Profile 47
- 2.2 Idealized Numerical Simulations: Cloud Model 1 49
  - 2.2.1 Atmospheric Gravity Waves 50
  - 2.2.2 Nocturnal Low-Level Jet 52
- 2.3 PV Inversion 58
  - 2.3.1 Inversion Technique 58
  - 2.3.2 Anomaly Creation 61

3 Sounding Analysis **72**
- 3.1 Modifications to the Composite Sounding 73
- 3.2 Real Soundings 75

4 Atmospheric Gravity Waves 80
4.1 Gravity Wave Characteristics 80
4.1.1 Average Nocturnal Environment (ATAW Simulation) 80
4.1.2 Parameter Space of Nocturnal Environments 81
4.2 Atmospheric Bores Moving in Directions Less Conducive for Wave Trapping 86
4.3 Impact of Westerly Wind Shear 89
4.3.1 Hypothesis 89
4.3.2 Atmospheric Bore Characteristics in the Presence of Linear Westerly Vertical Wind Shear 90
4.3.2.1 Comparison of 45° bore to -45° bore 91
4.4 Vertical Velocity and Net Displacement 93
4.4.1 Vertical Velocity 93
4.4.2 Net Vertical Displacement 97
4.4.2.1 Inclusion of Westerly Wind Shear 99
4.5 Summary 101

5 Nocturnal Low-Level Jet 149
5.1 LLJ characteristics 150
5.1.1 Average Nocturnal Simulation and Average Heating (ATAW) 150
5.2 LLJ Typical Nocturnal Environments 154
5.2.1 Different Baroclinic Zone Strengths 157
5.3 Influence of the initial zonal wind 159
5.4 Vertical Velocity 160
5.4.1 Relationship between vertical velocity and the LLJ 163
5.5 Net Displacement 164
5.5.1 Passive Tracers 166
5.6 Analysis using the Sawyer-Eliassen Equation 167
5.7 Summary 169

6 PV Anomalies 213
6.1 Introduction 213
6.2 Base-State Environment/Anomaly Creation 214
6.3 Error Analysis Associated with PV Inversion 215
6.4 Characteristics of PV Anomalies 216
6.5 Ascent associated with PV anomalies 219
6.5.1 Presence of Vertical Wind Shear 220
6.5.2 Analysis using quasi-geostrophic theory 225
6.5.3 Net Displacement 227
6.6 Summary 228

7 Summary 242

Reference List 249

Appendix A

Finite Differencing Scheme for 3-D Poisson Operators 264

List of Tables

1.1 Vertical velocity (m s^{-1}) and mean and maximum net displacement associated with observed bores from past studies. *Loveless et al. (2019) included 8 separate atmospheric bores in their study. 14
1.2 PV anomaly strengths (PVU) from previous studies 28

2.1 Low- and mid-level lapse rates (K km^{-1}) and the depth of the low-level lapse rate (km AGL) for the low lapse rate (WT; weak temperature), average lapse rate (AT; average temperature), and high (strong) lapse rate (ST; strong temperature) environments, and the maximum wind speed (m s^{-1}) and its depth for the weak winds (WW), average wind (AW), and strong wind (SW) environments. 48
2.2 CM1 model specifications for the gravity wave simulations 53
2.3 "Cropland/Grassland Mosaic" used in the CM1 simulations. Note that the soil moisture availability is set to zero. The original value is in parenthesis. 54
2.4 CM1 model specifications for the low-level jet simulations 56

3.1 CAPE (J kg^{-1}), CIN (J kg^{-1}), displacement to LFC (m) and starting parcel pressure (hPa) for real NB CI mode soundings 77

4.1 Maximum and Average Vertical Velocity for simulations with atmospheric bores. The bore speed is also noted. 96

5.1 Average vertical velocity (cm s^{-1}) computed using the integral of the average vertical velocity during the night (0000 UTC - 1200 UTC). 163
5.2 Net displacements (meters) computed using the integral of the average vertical velocity during the night (0000 UTC - 1200 UTC). 165

5.3 Net Displacement (m) computed using passive tracer position at 0800 UTC - 0000 UTC. The passive tracer starting at 700 m is the one used. 167

6.1 Vertical velocity and net displacement of parcels associated with PV anomalies in environments with westerly wind shear of 1 m s^{-1} km $^{-1}$ 223

6.2 Isentrope slopes ($\times$ 10^{-3}) for the environment modified by westerly wind shear (the mean slope) and the environment modified by the PV anomaly and the westerly wind shear (the maximum slope). 224

6.3 Typical Scales used in the Scale Analysis 226

List of Figures

1.1 CS CI mode events from Reif and Bluestein (2017). (a) Events per hour (%), (b) Pertencage of events of each LLJ classification from Bonner (1968), (c) orientation of the linear systems, and (d) CI location relative to the surface boundary. 29

1.2 As in Fig. 1.1, but for AB CI mode events and (d) percentage of events associated with each severe type. 30

1.3 As in Fig. 1.1, but for NB CI mode events and (d) percentage of storm types (areal, linear, or single cell). 31

1.4 Flow regime for the two-layer atmosphere. Figure from Rottman and Simpson (1989). F_0 is the Froude number, D_0 is the non-dimensional height (ratio of the height of the obstacle d_0 to the inversion height h_0, and $g^{'} = g(\rho_1 - \rho_2)/\rho_1)$ where $\rho_1 > \rho_2$. 32

1.5 Illustration of the partially blocked flow regime (flow follows both the solid red and solid dashed line) and the completely blocked flow regime (flow follows the solid red line). 33

1.6 (a) Wind speed (m s^{-1}) as a function of height where $U = z - 2$ and (b), 1/U^2 as a function of height. The system-relative wind speed increasing as a function of height is seen in (a) (assuming that $c = 0$) and there is a critical layer at $z = 2$km AGL. The red dashed line denotes this critical layer. There is a rapid decrease with height of 1/U^2 above this critical layer and this effect contributes to the rapid decrease with height in the Scorer parameter. 34

1.7 (a) AERI temperature (°C) and (b) AERI water vapor mixing ratio (g kg^{-1}) on 15 July 2015 at Greensburg Kansas. (c) Temperature (black line) and dewpoint (green line) and (d) pressure (hPa) at Greensburg, KS. The vertical black dashed line denotes the time of bore passage. Figure from Grasmick et al. (2018). 35

1.8 (a),(c) Radar reflectively factor (dBZ) and (b),(d), radial velocity (m s^{-1}) for KLNX (North Platte, Nebraska). In (b) and (d), red colors indicate velocity away from the radar and green colors indicate velocity towards the radar. The black arrows point to the parallel fine lines indicating the bore. . 36

1.9 (a) Vertical velocity (m s^{-1}) and (b) mixing ratio (g kg^{-1}). (c) Signal-to-noise ratio (dB) and (d) vertical velocity (m s^{-1}). The sustained net displacement is denoted in panels (b) and (c). (a) and (b) from Koch et al. (2008a). (c) and (d) from Haghi et al. (2017). 37

1.10 Specific humidity (g kg^{-1}; color-filled), potential temperature (black contours), and wind speed (colored barbs) on 1 June 2015 at (a) 0000 UTC, (b) 0400 UTC, (c) 0800 UTC, and (d) 1200 UTC. The horizontal convergence is contoured in blue. 38

1.11 Wind speed (m s^{-1}) observed during PECAN on 3 June 2015 (IOP02), 20 June 2015 (IOP12), and 22 June 2015 (IOP13). The black ovals indicate the diagonal striations. Figure from Smith et al. (2019). 39

1.12 (a) - (c). Schematic of the development of the diagonal striation. A full barb is 10 m s^{-1} and the enhanced convergence is outlined in the dark-orange ovals. (d) A point profile observed from a Doppler lidar. Note the collocation of the diagonal striation and the enhanced vertical velocity. Figure from Smith et al. (2019). 40

1.13 Top row: illustration of the tilting of planetary vorticity onto the horizontal. Bottom row: illustration of the tilting of relative vertical vorticity onto the horizontal. Curved arrows indicate the sense of the circulation, and the colors in the bottom row indicate the wind speed (darker colors indicate stronger wind speeds). 41

1.14 (a) 2 June 2015, WV-DIAL backscatter (b) 15 June 2015 celiometer baskscatter at S-Pol, and (c) 5 July 2015 WV-DIAL backscatter. The dashed line indicates the implied vertical motion. Figures from Shapiro et al. (2018). . . 42

1.15 HRRR Surface Temperature (°F) at 0000 UTC for (a) 2 June 2015, (b) 15 June 2015, and (c) 5 July 2015. The black arrows indicate the temperature gradient (points to warmer temperatures). Figures from Shapiro et al. (2018). 43

1.16 Wind speed (contoured; m s^{-1}) and potential temperature (quasi-horizontal contours (K)) for (a) a cyclonic PV anomaly and (b) and anticyclonic PV anomaly. The bold line indicates the dynamic tropopause. From Thorpe (1986) and appeared in Hoskins et al. (1985). 44

1.17 West-east cross section of the composite (a) temperature anomaly (K), (b) wind speed anomaly (m s^{-1}), (c) PV anomaly, and (d) relative humidity anomaly (%). Figure from Cavallo and Hakim (2010). 45

1.18 (a) West-east cross section of a cyclonic PV anomaly (oval), and isentropic surface near the PV anomaly (below the oval) and the westerly vertical wind shear (the arrows on the right of the panel). (b) A south-north cross section of the same PV anomaly in (a). The dashed lines denote the isentropes. Ascent is downshear (east) of the cyclonic anomaly. Figure from Raymond and Jiang (1990). 46

2.1 (a) (b) and (c) are examples of “bad” soundings not included in the composite. (d), (e), and (f) are examples of “good” soundings included in the composite. 62

2.2 The NB CI mode composite sounding. The hodograph is in m s^{-1}. 63

2.3 The nine nocturnal environments created. The strength of the winds increase from left to right and the environmental stratification increases from top to bottom. 64

2.4 The +1 σ (red curves), average (black curves), and -1 σ (blue curves) for (a) temperature, (b) $\frac{\partial \theta}{\partial z}$, (c) u-wind component, and (d) v-wind component from the composite sounding in Fig. 2.2. 65

2.5 (a) Potential temperature computed from the ± 1 σ temperature, and (b) potential temperature computed from the ± 1 σ lapse rates. Lines are as in Fig. 2.2. 66

2.6 Heating rate (K day^{-1}) for the average-heating LLJ simulations. Time increases from top to bottom starting at 1200 UTC and the horizontal distance is on the x-axis. 67

2.7 Initial meridional wind profiles for (a) WW, (b) AW, and (c) SW gravity wave simulations. 68

2.8 Terms used to calculate the Scorer parameter in the ATAW simulation. (a) N^2, (b) $\frac{\partial^2 U}{\partial z^2}$, (c) Term 1 of Equation 1.1, and (d) Term 2 of Equation 1.1. . . 69

2.9 Scorer Parameter for (a) WTWW, (b) WTAW, (c) WTSW, (d) ATWW, (e) ATAW, (f) ATSW, (g) STWW, (h) STAW, and (i) STSW gravity wave simulations. The blue dashed line indicates the rapid decrease in the Scorer parameter. 70

2.10 Percent difference between the current iteration and the previous iteration as the iteration number increases. Φ is the red curve and Ψ is the black curve. The dashed curves represent an exponential fit. 71

3.1 (a) The NB composite sounding. (b) as in (a), but a 50% reduction in the dewpoint depression at 900 hPa, (c) as in (a), but a 50% reduction in the dewpoint depression at 800 hPa, and (d) as in (a), but a 50% reduction in the dewpoint depression at 700 hPa 78

3.2 a) 1200 UTC KOUN sounding on 9 June 2001, b) 1200 UTC KLBF sounding on 17 July 2009, and c) 1200 UTC KLBF soundings on 16 July 2010. . 79

4.1 (a) Potential temperature (contoured every 2 K) and vertical velocity (color-filled) for the ATAW bore at 240 min. (b) Near-surface temperature for the ATAW bore at 240 min. The leading edge of the bore is denoted by the vertical black line. (c) The flow regime for the ATAW bore. Note that $g^{'} = (\theta_{inv} - \theta_{sfc})/\theta_{sfc}$. The red dot is in the partially-blocked flow regime. . 103

4.2 As in Fig. 4.1a, but for the (a) WTWW, (b) WTAW, (c) WTSW, (d) ATWW, (e) ATAW, (f) ATSW, (g) STWW, (h) STAW, and (i) STSW simulations. The WT simulations are shown at 60 min, the AT simulations are shown at 220 min, and the ST simulations are shown at 100 min. 104

4.3 A zoomed-in image to one wave associated with the bore like feature in the ATAW simulation at (a) 140 min and (b) 260 min. The dashed line indicates the crest of the isentropes associated with this wave. 105

4.4 Vertical velocity (color-filled) and potential temperature (K; contoured every 2K) for (a) the ATAW bore and (b) the ATSW bore at 260 min and (c) the STAW bore and (d) the STSW bore at 100 min. The vertical dashed lines denote the crests of the bore and the average wavelength is denoted in the upper left of each panel. 106

4.5 Wind speed minus bore speed for the ATAW simulation at 220 min. Red colors indicate positive difference and blue indicate negative. Isentropes contoured every 2K 107

4.6 As in fig 4.2, but for the near-surface temperature at 120 min. The leading edge of the bore is dented by the vertical dashed line (In the WT simulations, this line denoted the density current). 108

4.7 Flow regime for the nine simulations. $g' = (\theta_{inv} - \theta_{sfc})/\theta_{sfc}$. The red dots denote the WT simulations, the green dots denote the AT simulations, and the blue dots denote the ST simulations. The shade of the dots represent the strength of the wind speed. The flow regime for the red dots are at the origin because there is no stable layer, so it's technically undefined. 109

4.8 As in Fig. 4.1a, but for the a) ATWW, b) ATAW, c) ATSW, d) STWW, e) STAW, and f) STSW simulations at 240 min initialized by a stronger cold pool. 110

4.9 As in fig 4.8, but for the near-surface temperature at 120 min. 110

4.10 Horizontal cross-sections of potential temperature (color-filled) for the a) WTWW, b) WTAW, c) WTSW, d) ATWW, e) ATAW, f) ATSW, g) STWW, h) STAW, and i) STSW simulations. In e), dashed lines denote the density current (white line) and the bore (black line). 111

4.11 Illustration of the angles of the 45°, 0°, and -45° bores. 112

4.12 Potential temperature (black lines every 2K) and vertical velocity (color-filled) for the 45° bore for the a) WW, b) AW, and c) SW simulations at 120 min in WT environments. d), e), f) are the surface temperature corresponding to the panels on the left. 113

4.13 As in Fig. 4.13, but for AT environments at 220 min. 114

4.14 As in Fig. 4.13, but for ST environments at 120 min. 115

4.15 Comparison of the 0° bores in the AT simulations for a) - c), without vertical shear and d)- f), with vertical shear. Potential temperature is contoured every 2K and vertical velocity is color filled. 116

4.16 As in Fig. 4.15, but for the ST simulations 117

4.17 As in Fig. 4.15, but for the 45° bores. 118
4.18 As in Fig. 4.17, but for the ST simulations. 119
4.19 Two-dimensional illustrations the 45° (top) and -45° (bottom) density currents. Height is on the y-axis and the horizontal distance in the density-current-relative reference frame (X' on the figure) is on the x-axis. The arrow on the circles indicates the sense of the circulation. The circle at the density current head represents the baroclinically-generated horizontal vorticity. The circle outside o the density current represents the horizontal vorticity that is generated by the vertical wind shear. The arrow in the density current indicates its propagation direction. The westerly environmental wind speed is indicated by the lines and arrows on the left of the panels. . . 120
4.20 Comparison of the (a) - (c) 45° density currents, (d) - (f) -45° density currents. 121
4.21 Comparison of the a) - c) 45° bores, d) - f) 0° bores, and g) - i) -45° bores in the AT simulations with vertical shear at 160 min. 122
4.22 As in Fig. 4.21, but for the ST simulations at 120 min. 123
4.23 As in Fig. 4.21, but for the surface temperature (°C) in the AT simulations at 120 min. 124
4.24 As in Fig. 4.23, but for the ST simulations with vertical wind shear. 125
4.25 Potential temperature (contoured every 2K) and vertical velocity (color-filled) for the AT simulations with vertical wind shear at 260 min. The vertical black dashed line denotes the crests of the bores. 126
4.26 Illustration of the superposition of waves. The left if a schematic of the process and the right is the possible process in the ATAW simulation at 240 min. The different orientation of the waves is denoted by the lines in the circle. The inset is the same region just zoomed for clarity. 127

4.27 a) - c) Potential temperature (contoured every 2K) and vertical velocity (color-filled) for the 0 ° bores in the AT simulations at 240 min. The corresponding vertical velocity at 500 m AGL is shown on the right. 128
4.28 As in Fig. 4.27, but for the ST simulations at 120 min. 129
4.29 Comparison of the length of the bore in the a) ATAW simulation and b) STAW simulation without vertical shear. The vertical velocity associated with the bores is given in c) and d). 130
4.30 As in Fig. 4.27, but for the vertical velocity at the 306 K surface rather than at 500 m. 131
4.31 As in Fig. 4.30, but for the ST simulations at 120 min. The vertical velocity is shown on the 320 K isentropic surface. 132
4.32 As in Fig. 4.27, but for the 45° bore without vertical wind shear. 133
4.33 As in Fig. 4.32, but for the bores in the ST simulations. 134
4.34 Vertical velocity (cm s^{-1}) for the 45° bores in the ST simulations for (a) - (c) AT simulations without vertical wind shear and (d) - (f) with vertical wind shear. 135
4.35 As in Fig. 4.34, but for the ST simulations. 136
4.36 As in Fig. 4.21, but for the vertical velocity 500 m AGL at 240 min. 137
4.37 As in Fig. 4.36, but for the ST simulations at 120 min. 138
4.38 As in Fig. 4.27, but for simulations with stronger density currents. 139
4.39 As in Fig. 4.38, but for the ST simulations. 140
4.40 Illustration of how the net vertical displacement by the bore is computed. . 141
4.41 Net displacement for parcels associated with the 0^{-1} bore (solid lines) and the 45° bore (dashed line). The red lines are the maximum displacement and the black lines are the mean displacement. a) - c) is the AT simulation at 160 min and d) - f) is the ST simulation at 120 min. 142

4.42 Passive tracers initialized at 125 m (blue curve), 700 m (red curve) and 1500 m (large black curve) and potential temperature contoured every 2 K (thin black lines) for the a) - c) AT simulations at 200 min and d) - f) ST simulations at 160 min. 143

4.43 As in Fig. 4.41, but for the simulation with a strong cold pool. 144

4.44 As in Fig. 4.41, but for (a),(b),(c), AT simulations without westerly wind shear at 200 min, and (d),(e),(f), AT simulations with westerly wind shear at 200 min. 145

4.45 As in Fig. 4.41, but for (a),(b),(c), AT simulations with vertical wind shear at 160 min, and (d),(e),(f), ST simulations with vertical wind shear at 150 min. 146

4.46 As in Fig. 4.41, but for (a),(b),(c) 45° bore in the AT simulations with westerly wind shear and (d),(e),(f), -45° bore in the AT simulations with vertical wind shear at 160 min. 147

4.47 As in Fig. 4.46, but for the ST simulations with vertical shear at 120 min. . 148

5.1 a) Incoming shortwave radiation (W m^{-2}) and b) Net radiation at the surface (incoming - outgoing) (W m^{-2}). 171

5.2 Skin temperature (°C) for the ATAW simulation at a) 1800 UTC, b) 2200 UTC, c) 0200 UTC, and d) 0600 UTC. 172

5.3 Potential temperature as a function of height at 2100 UTC (red curve) and 0600 UTC (blue curve). 173

5.4 As in 5.2, but for potential temperature. Height is on the y-axis and the horizontal distance is on the x-axis. 174

5.5 (a),(b) potential temperature at 2100 UTC (red curve) and 0800 UTC blue curve. (c),(d) meridional wind component (m s^{-1}). (a) and (c) have no moisture in the simulation. (b) and (d) have no moisture in the atmosphere, but include soil moisture. 175

5.6 As in Fig. 5.4, but for the zonal wind component. 176

5.7 As in Fig. 5.4, but for the meridional wind component. 177

5.8 Wind barbs (full barb is 10 m s^{-1}) at 500 m AGL for (a) 1800 UTC, (b) 2200 UTC, (c) 0200 UTC, and (d) 0600 UTC. 178

5.9 As in Fig. 5.4, but for the vertical velocity (color filled) and potential temperature (contoured every 2K). 179

5.10 Skin temperature (°C) for the (a) WTWW, (b) WTAW, (c) WTSW, (d) ATWW, (e) ATAW, (f) ATSW, (g) STWW, (h) STAW, and (i) STSW simulations. 180

5.11 As in Fig. 5.10, but for potential temperature. Height is on the y-axis and the horizontal distance is on the x-axis. 181

5.12 (a) Vertical velocity (color-filled; cm s^{-1}) and (b) skin temperature (°C). The “pillars” of vertical velocity correspond to the noisy skin temperature. . 182

5.13 As in Fig. 5.11, but for the zonal wind component. 183

5.14 As in Fig. 5.11, but for the meridional wind component. 184

5.15 As in Fig. 5.11, but for the hodographs. The zonal wind is on the x-axis and the meridional wind is on the y-axis. The color of the dot gets lighter as time increase. 185

5.16 Skin temperature for the AW simulations for (a),(b),(c) weak heating (10 K hr^{-1} max), (d),(e),(f), average heating (20 K hr^{-1} max), and (g),(h),(i), strong heating (30 K hr^{-1} max). The mid-level stability in these simulations increases from top to bottom. 186

5.17 Potential temperature at 0800 UTC for the AW simulations for (a),(b),(c) weak heating (10 K hr^{-1} max), (d),(e),(f), average heating (20 K hr^{-1} max), and (g),(h),(i), strong heating (30 K hr^{-1} max). The mid-level stability in these simulations increases from top to bottom. Height is on the y-axis and horizontal distance is on the x-axis. 187

5.18 The zonal wind component at 0800 UTC for the AW simulations for (a),(b),(c) weak heating (10 K hr^{-1} max), (d),(e),(f), average heating (20 K hr^{-1} max), and (g),(h),(i), strong heating (30 K hr^{-1} max). The mid-level stability in these simulations increases from top to bottom. Reds represent westerly winds and blues represent easterly winds. 188

5.19 As in Fig. 5.18, but for the meridional wind component. 189

5.20 Hodographs for the AW simulations for (a),(b),(c) weak heating (10 K hr^{-1} max), (d),(e),(f), average heating (20 K hr^{-1} max), and (g),(h),(i), strong heating (30 K hr^{-1} max). The mid-level stability in these simulations increases from top to bottom. The zonal wind is on the x-axis and the meridional wind is on the y-axis. The color of the dot gets lighter as time increase. 190

5.21 Skin Temperature (°C) at 0000 UTC for the WW simulations for (a),(b),(c), NoUWIND simulations and (d),(e),(f), UWIND2 simulations. Static stability increases from top to bottom. 191

5.22 As in Fig. 5.21, but for the ATSW simulation. 192

5.23 Potential temperature (K; contoured every 2 K) at 0800 UTC for the AW simulations for (a),(b),(c), NoUWIND simulations and (d),(e),(f), UWIND2 simulations. Static stability increases from top to bottom. Height is on the y-axis and horizontal distance is on the x-axis. 193

5.24 The zonal wind component at 0800 UTC for the AW simulations for (a),(b),(c), NoUWIND simulations and (d),(e),(f), UWIND2 simulations. Static stability increases from top to bottom. Height is on the y-axis and horizontal distance is on the x-axis. 194

5.25 The meridional wind component at 0800 UTC for the AW simulations for (a),(b),(c), NoUWIND simulations and (d),(e),(f), UWIND2 simulations. Static stability increases from top to bottom. Height is on the y-axis and horizontal distance is on the x-axis. 195

5.26 Hodographs for the AW simulations for (a),(b),(c), NoUWIND simulations and (d),(e),(f), UWIND2 simulations. Static stability increases from top to bottom. Height is on the y-axis and horizontal distance is on the x-axis. The zonal wind is on the x-axis and the meridional wind is on the y-axis. The color of the dot gets lighter as time increase. 196

5.27 Vertical velocity (color-filled; cm s^{-1}) and potential temperature (contoured every 2 K) for the (a) WTWW, (b) WTAW, (c) WTSW, (d) ATWW, (e) ATAW, (f) ATSW, (g) STWW, (h) STAW, and (i) STSW simulations under the average heating. 197

5.28 Maximum vertical velocity (cm s^{-1}) for the (a) WTWW, (b) WTAW, (c) WTSW, (d) ATWW, (e) ATAW, (f) ATSW, (g) STWW, (h) STAW, and (i) STSW simulations under the average heating. 198

5.29 Vertical velocity (color-filled; cm s^{-1}) and potential temperature (contoured every 2 K) for (a),(b),(c) weak heating (10 K hr^{-1} max), (d),(e),(f), average heating (20 K hr^{-1} max), and (g),(h),(i), strong heating (30 K hr^{-1} max). The mid-level stability in these simulations increases from top to bottom. . 199

5.30 Maximum vertical velocity (cm s^{-1}) for (a),(b),(c) weak heating (10 K hr^{-1} max), (d),(e),(f), average heating (20 K hr^{-1} max), and (g),(h),(i), strong heating (30 K hr^{-1} max). The mid-level stability in these simulations increases from top to bottom. 200

5.31 Vertical velocity (color-filled; cm s^{-1}) and potential temperature (contoured every 2 K) for the (a),(b),(c) NoUWIND, and (d),(e),(f) UWIND2 WW simulations. The mid-level stability in these simulations increases from top to bottom. 201

5.32 Maximum vertical velocity (cm s^{-1}) for the (a),(b),(c) NoUWIND, and (d),(e),(f) UWIND2 WW simulations. The mid-level stability in these simulations increases from top to bottom. 202

5.33 Average vertical velocity (cm s^{-1}) for the (a),(b),(c) NoUWIND, and (d),(e),(f) UWIND2 WW simulations. The mid-level stability in these simulations increases from top to bottom. The dashed black curve is a fourth-order polynomial fit. The solid red line is the average vertical velocity over the time period and the dashed red line is the average vertical velocity over the same time computed from the fitted curve. 203

5.34 As in Fig. 5.33, but for the (a) WTWW, (b) WTAW, (c) WTSW, (d) ATWW, (e) ATAW, (f) ATSW, (g) STWW, (h) STAW, and (i) STSW average-heating simulations. 204

5.35 As in Fig. 5.34, but for the weak-heating simulations. 205

5.36 As in Fig. 5.34, but for the strong-heating simulations. 206

5.37 Illustration of an X-Z cross section of the vertical velocity location relative to the jet maximum and the surface heating. The red contours represent vertical velocity (deeper reds indicate stronger vertical velocities), and the blue shading represents the southerly component of the wind associated with the LLJ (darker blues indicate stronger wind speeds). The westward offset of w compared to the LLJ maximum is due to the advection of it by the inertial oscillation. 207

5.38 Passive tracers initialized at three levels for the (a) WTWW, (b) WTAW, (c) WTSW, (d) ATWW, (e) ATAW, (f) ATSW, (g) STWW, (h) STAW, and (i) STSW average-heating simulationsat 0800 UTC. The blue curve (pt1) represents tracers initialized at 125 m AGL, the red curve (pt2) represents tracers initialized at 700 m AGL, and the black curve (pt3) represents tracers initialized at 1500 m AGL. The displacements in the upper right are the difference in the 0800 UTC maximum position and the 0000 UTC maximum position. 208

5.39 As in Fig. 5.38, but for the weak-heating simulations. 209

5.40 As in Fig. 5.38, but for the strong-heating simulations. 210

5.41 As in Fig. 5.38 but for the (a),(b),(c) NoUWIND and (d),(e),(f) UWIND2 WW simulations at 0800 UTC. Static stability increases from top to bottom. 211

5.42 ω (kPa s^{-1}) computed from the Sawyer-Eliassen equation. This result uses the total wind rather than the geostrophic wind, and the model data were smoothed to prevent numerical instability. 212

6.1 Base-state potential temperature for a) WL environments (1.5 K km^{-1}), b) SL environments (3.5 K km^{-1}), and c) SL environments (6.5 K km^{-1}). d) 1 PVU anomaly, e) 2 PVU anomaly, and f) 3 PVU anomaly (prior to smoothing) embedded in the environment in a), b), and c), respectively. . . 230

6.2 PV difference between iteration and initial PV field for a) WL1, b) AL1, c), SL1, d), AL2, and e) SL3 anomalies. Positive differences indicates the inverted field is stronger. 230

6.3 Potential temperature (black lines; contoured every 2 K) and meridional wind speed (contoured every 1 m s^{-1}; the red curve is positive, blue curve is negative) for the WL1 anomaly. 231

6.4 As in Fig. 6.3, but for the AL1 anomaly 232

6.5 As in Fig. 6.3, but for the SL1 anomaly 233

6.6 As in Fig. 6.3, but for the AL2 anomaly 234

6.7 As in Fig. 6.3, but for the SL3 anomaly 235

6.8 Schematic of possible trajectories around a stationary PV anomaly embedded in background flow. The red line in the right panel represents the displacement of a parcel moving from south to north. The blue line in the bottom panel represents the displacement of a parcel moving from east to west. 236

6.9 a) Westerly wind shear (m s^{-1} km^{-1}) and b) southerly wind shear (m s^{-1} km^{-1}) from the composite sounding. 237

6.10 North-south cross section of the potential temperature field modified by the PV anomaly and the 1 m s^{-1} km^{-1} westerly vertical wind shear for the a) Wl1, b) AL1, c) SL1, d) AL2, and e) SL3 anomalies. f) Schematic of the cyclonic circulation. The red box indicates the location of the more stronger potential temperature modification and the green box represents where the vertical velocity would be strongest (based on the slope of the isentropes). 238
6.11 Vertical vorticity ($\times 10^{-5}$ s^{-1}) and vertical velocity computed from the Sutcliffe-Trenberth form of the QG omega equation (contoured every 0.1 cm s^{-1}) for the a) WL1, b) AL1, c) SL1, d) AL2, and e) SL3 PV anomalies. 239
6.12 The total distance traveled during the night for an air parcel (black curved arrow) at the radius of maximum winds (dashed circle) and the meridional distance traveled (the red arrow) for the same air parcel. The net displacement that air parcels experience depends on the meridional distance traveled (the red arrow), not the total distance traveled (the black arrow). 240
6.13 An X-Z cross section of the net displacement associated with the PV anomaly in an environment without vertical shear (top panel) and one with vertical shear (bottom panel). The isentropes associated with the environment are black and those associated with the PV anomaly are blue. The parcel in an environment with vertical shear realized a higher net displacement in a shorter horizontal distance than a parcel in an environment without vertical wind shear. However, the parcel's total displacement through the anomaly in an environment with vertical shear (red line) is not the sum of the displacement of the environmental isentrope and the PV-modified isentrope (dashed red line). 241

Abstract

Nocturnal convection initiation accounts for nearly half of all CI events (daytime and nighttime) over the Great Plains over the warm season. There are three main types of CI events: those that occur on surface boundaries, those that occur on the cold side of surface boundaries, and those that occur with no nearby surface boundaries (NB [no boundary] CI mode). This study focuses on the poorly-understood NB nocturnal CI mode events. These storms typically occur in environments with weak forcing or occur far away from preexisting convection and away from surface boundaries. There are preferred characteristics to these events, however. For example, these events form later at night (around 0900 UTC), occur on the eastern side of the low-level jet (LLJ), and the linear systems tend to be oriented north/south. Three initiation mechanisms are explored here in detail: ascent due to atmospheric bores, ascent due to the nocturnal LLJ, and ascent associated with cyclonic potential vorticity (PV) anomalies. The gravity wave and LLJ mechanisms are explored using three-dimensional idealized numerical simulations, and PV inversion is used to explore the PV anomaly mechanism. A composite sounding was created based on 108 proximity soundings for NB CI mode events. Nine environments representing a range in winds and temperature are used to test each mechanism's effect on a range of nocturnal environments. In these simulations, the vertical velocity associated with atmospheric bores is between 0.5 and 1 m s^{-1}, and the net displacement is 200 – 500 m. The vertical velocity associated with the LLJ is 1 cm s^{-1}, but due to the sustained ascent throughout the night, the net displacements can be as much as 1 km. Finally, the ascent associated with PV anomalies is between 0.1 and 1 cm s^{-1}, and the net displacement is typically between 50 and 100 m. Based on these displacements, gravity waves and the LLJ are likely CI mechanisms, while PV anomalies are not likely to cause CI.

Chapter 1

Introduction

During the warm season, precipitation over the Great Plains region of the United States is most common at night (e.g., Kincer 1916; Wallace 1975; Riley et al. 1987). This nocturnal maximum has been examined utilizing rainfall data (Riley et al. 1987; Surcel et al. 2010), severe storm reports (Horgan et al. 2007), and even thunder reports (Easterling and Robinson 1985). Local nocturnal maxima in precipitation have been discovered in other parts of the world too. A secondary, but smaller, maximum in precipitation occurs at night over the Amazonia region of South America (Rickenbach 2004) as well as portions of China (Yuan et al. 2012; Yang et al. 2015).

Much of this nocturnal precipitation over the U.S. (around 70%) is attributed to eastward-propagating convective systems (Fritsch et al. 1986; Carbone et al. 2002; Carbone and Tuttle 2008). These mesoscale convective systems (MCS) typically initiate during the late afternoon in the lee of the Rocky Mountains, grow upscale into a larger convective system and move eastward across the Plains (Tripoli and Cotton 1989a,b; Carbone et al. 2002; Carbone and Tuttle 2008; Weckwerth and Romatschke 2019; Cheeks et al. 2020).

The phase speed of regions of precipitation associated with MCSs is eastward at around 15 m s^{-1} (Carbone et al. 2002; Carbone and Tuttle 2008; Cheeks et al. 2020), and the average lifetime for MCSs that propagate across the Plains region is 12 hr (Cheeks et al. 2020). These systems are most common between June and August (Fritsch et al. 1986; Carbone and Tuttle 2008) and occur in environments with high convective available potential energy (CAPE), a nearby baroclinic zone, and vertical wind shear (Maddox 1983; Coniglio et al. 2010). Due to their prevalence and contribution to extreme rainfall, these systems have been the subject of extensive research (Maddox 1983; Carbone et al. 1990; Augustine and Caracena 1994; Carbone et al. 2002; Carbone and Tuttle 2008).

1.1 Nocturnal Convection Initiation

The remaining precipitation over the Great Plains (30%) comes from systems that initiate at night (Weckwerth and Romatschke 2019). Over the Plains, convection initiation (CI) at night accounts for around half of the total CI events (Wilson and Roberts 2006). Despite the prevalence of nocturnal CI, its forecast skill CI is lower than that of daytime CI (Davis et al. 2003; Surcel et al. 2010; Stelten and Gallus Jr 2017), because in part features responsible for nocturnal CI may be harder to observe via the conventional observing network as these features are above the surface (e.g., Weckwerth et al. (2019)). The Plains Elevated Convection at Night (PECAN; Geerts et al. (2017)) field project was a six-week field project from 1 June 2015 to 15 July 2015 that aimed to improve our understanding of this nocturnal precipitation over the Plains, and one of its focus areas was on improving our understanding of nocturnal CI.

Weckwerth et al. (2019) and Weckwerth and Romatschke (2019) examined daytime and nocturnal CI that occurred during PECAN. They classified five main types of CI events: frontal overrunning (14% of events), low-level jet (LLJ)-only events (10%), events near an MCS (35%), bore and density current events (25%), and pristine (CI not influenced by preexisting convection or surface boundaries) CI events (16%). Of these, the LLJ-only events had a 23% probability of detection (POD), the lowest of all nocturnal CI events. Frontal overrunning events and events near MCSs had the highest POD during PECAN (65% and 71%, respectively). The average POD for pristine CI events was 50% during PECAN. Stelten and Gallus Jr (2017) tested the predictability of CI events using numerical simulations and showed that events associated without any obvious mesoscale mechanisms and away from the LLJ had the lowest forecast skill and events associated with the LLJ were better predicted in terms of CI location than other types of nocturnal CI.

1.1.1 20-Year Climatology (1996-2015)

Stelten and Gallus Jr (2017) and Weckwerth and Romatschke (2019) only examined CI events between May and August of 2015 (including PECAN events). Reif and Bluestein (2017) formulated a 20-year (1996-2015) climatology of nocturnal CI events over the Great Plains. In this climatology, 35% of nocturnal CI events form on the cold side of surface boundaries (CS CI mode), 23% of systems initiate on surface boundaries (AB (at-boundary) CI mode), and 24% of systems form without nearby surface boundaries (NB (no boundary) CI mode).

The CS CI mode has been the subject of many past studies (e.g., Colman (1990); Horgan et al. (2007)) and is the CI mode most often thought of as elevated convection, or convection that occurs above a stable layer. A common initiation mechanism of these storms is air moving up and over a stationary front, and CI occurs on the cold side (Colman 1990; Trier et al. 2020). This type of mechanism has been referred to as “frontal overrunning” (Moore et al. 2003) or “isentropic upglide” (Trier et al. 2020). *Altocumulus castellanus* is a cloud type commonly associated with elevated convection and is commonly associated with areas of isentropic ascent (Corfidi et al. 2008). Reif and Bluestein (2017) showed that CS CI mode storms form early at night (Fig. 1.1a) and around 250 km on the cold side of the surface boundary (Fig. 1.1d).

Storms in this CI mode have the potential for back building in a process known as rearward off boundary development (ROD; Peters and Schumacher (2015); Hitchcock and Schumacher (2020)). This process occurs when air is lifted over an outflow boundary from an MCS. The air reaches saturation on the cold side of this outflow boundary, and convection can form. The bow-and-arrow Type of initiation is another mechanism for storms to form behind the parent MCS Keene and Schumacher (2013). The orientation of this convection relative to that of the parent MCS distinguishes it from ROD. The bow-and-arrow storms are oriented perpendicular to the MCS, while ROD convection is oriented similarly to that of the outflow boundary. While these types of convection are related to a preexisting system, they illustrate that CS CI mode events are important to understand because of their association with flash-flooding.

The AB CI mode events are more-or-less well understood. These storms form due to strong surface convergence associated with surface boundaries, typically drylines and cold fronts. They have an early initiation time during the night (Fig. 1.2a), have a peak initiation month of May, and are associated with SW/NE oriented surface boundaries (Fig. 1.2c). Events in this mode also tend to be more severe than those in the other two CI modes. Over 40% of all events in this mode are associated with a severe hail report (Fig. 1.2d).

The NB CI mode events are poorly understood in comparison to the other two CI modes. There is no strong surface forcing (or any noticeable surface features of any kind), so how does CI occur? To start to answer this question, the characteristics of events in this mode will be examined. Reif and Bluestein (2017) speculated that if these storms had no common initiation mechanisms, then there should not be any preferred characteristics. These events initiate later during the night (Fig. 1.3a) and later during the warm season. This later initiation time was also found by Stelten and Gallus Jr (2017) and Weckwerth and Romatschke (2019). Nearly 75% of these systems are associated with a low-level jet (LLJ) (Fig. 1.3b), and the linear systems tend to be oriented N/S (Fig. 1.3c). Nearly half of the events in this mode are linear systems (Fig. 1.3d). The preferred characteristics suggest that there is at least some mechanism responsible for the initiation of these events.

1.1.2 NB CI Mode Initiation Mechanisms

Due to the lack of any notable surface or upper-level forcing, how does CI occur? Based on the later initiation time at night and the prevalence of the LLJ with NB CI mode events, it is speculated that the LLJ is one initiation mechanism. However, it is hypothesized that the LLJ is not the only mechanism responsible for NB CI mode events. Other mechanisms include initiation via atmospheric gravity waves, the low-level jet, and cyclonic PV anomalies. This study will focus on improving our understanding of these proposed NB CI mode events initiation mechanisms through idealized numerical simulations.

MCSs are common over the Plains, and these systems commonly generate gravity waves (e.g., Crook 1986, 1988; Koch et al. 1991; Knupp 2006; Koch et al. 2008b,a; Adams-Selin and Johnson 2013; Haghi et al. 2017; Mueller et al. 2017; Grasmick et al. 2018; Parsons et al. 2019; Haghi et al. 2019; Adams-Selin 2020; Haghi and Durran 2020). If these gravity waves propagate far ahead of the parent system or if that parent system dissipates, these gravity waves may not appear as surface boundaries in typical observing networks and may be hard to detect via the operational radar network (e.g., Wilson et al. 2018). Ascent associated with the gravity waves or atmospheric bores can cause CI (e.g., Wilson and Roberts 2006; Knupp 2006; Parker 2008; French and Parker 2010; Wilson et al. 2018; Parsons et al. 2019).

Ascent associated with PV anomalies in environments with vertical shear, while weak, could be persistent enough to lift a parcel to its level of free convection (LFC) (Trier et al. 2000; Jirak and Cotton 2007; Li and Smith 2010). It has been speculated that PV anomalies are commonly associated with the nocturnal precipitation maximum (Carbone et al. 2002). This relationship is due to the similar phase speed and timing of the eastward-propagating PV anomalies and the eastward-propagating precipitation. However, the relationship between PV anomalies and nocturnal CI is not yet established.

Case studies and a review of the initiation mechanisms were discussed in Reif and Bluestein (2018). An in-depth review of these three initiation mechanisms will be described in more detail. The characteristics of each will be discussed. How these features are generated over the Plains and the ascent associated with each of these features will be described.

1.2 Atmospheric Gravity Waves

Gravity waves, including lower tropospheric gravity waves, mountain waves, and deep-tropospheric gravity waves, are common in the atmosphere. Mountain waves typically form in the lee of mountains and can extend the depth of the troposphere. These waves are associated with severe hazards such as downslope winds, rotors, and clear-air turbulence (Durran 1986a,b, 1990). The mountain waves' eastward extent may not reach the Plains (because the Colorado/Kansas border is 250 km from the Rocky Mountains).

Rising and sinking motion resulting from the latent heating of the parent storm triggers a gravity wave response (Knight et al. 2004; Fovell et al. 2006). These gravity waves can result in CI ahead of the parent storm, causing the storm to appear to jump forward. This jump is referred to as a discrete propagation. Low-frequency deep-tropospheric gravity waves can be generated by a latent-heat responsive from convective systems, have a phase speed of over 30 m s^{-1} and is associated with vertical velocities of around 0.5 m s^{-1} (Adams-Selin and Johnson 2013).

These gravity waves can modify CAPE due to vertical motions in the mid-troposphere (Lane and Reeder 2001; Adams-Selin and Johnson 2013; Adams-Selin 2020). Different heating profiles are associated with different wave modes. The $n = 1$ wave mode corresponds to an increase in heating over the troposphere (maximized at mid levels) and is similar to that produced by the convective region of an MCS. This mode is typically associated with a reduction of CAPE (Adams-Selin and Johnson 2013; Adams-Selin 2020). The $n = 2$ and $n = 3$ heating profiles are similar to those produced by the stratiform precipitation of an MCS and are typically associated with rising motion over the lower troposphere. The $n = 1$ mode is typically associated with a reduction of CAPE, the $n = 2$ mode is associated with an increase of both CAPE and CIN, and the $n = 3$ mode is associated with a reduction of CIN (Lane and Reeder 2001). While CI associated with the deep-tropospheric waves generated by MCSs is close to the parent storm and is not pristine CI, the modification of the atmosphere by these waves can prime the environment, making it more conducive for another mechanism to initiate convection. Because these waves are typically generated by preexisting convection, they are not examined in this study.

Lower-tropospheric gravity waves are common over the Plains at night and have been associated with pristine CI (e.g., Wilson et al. 2018). These gravity waves include low-level gravity waves caused by the disturbance of low-level stable layers, atmospheric bores, (e.g., Koch et al. 1991), and solitons (e.g., Koch et al. 2008a). For this study, we will focus on atmospheric bores because of their high frequency of occurrence over the Plains and their association with nocturnal CI.

1.2.1 Atmospheric Bores

Bores were first identified in water, but atmospheric bores were not observed until the mid 20th century (Tepper 1950). One of the most well-documented types of bores is the Morning Glory off the northeastern coast of Australia (Clarke 1972). An atmospheric bore is a type of gravity wave produced when stable air is forced upward (Crook 1986, 1988; Knupp 2006; Koch et al. 2008b; Haghi et al. 2017, 2019). Over the Great Plains, the interaction of a density current (typically produced by an MCS) or a cold front with the nocturnal stable layer is a common way in which bores form.

Bores have been recognized to be important in the maintenance of their parent MCSs (Wilson and Roberts 2006; Parker 2008) and potentially in the initiation of new convection (Knupp 2006; Marsham et al. 2011; Grasmick et al. 2018; Parsons et al. 2019). Atmospheric bores have started to receive much attention in the literature because of their importance to convective systems and precipitation maximum over the Plains. These studies include observation-based studies that observe bores via ground-based radar, surface observing stations, vertically-pointing lidars, and microwave radiometers (Koch et al. 2008b; Bluestein and Snyder 2015), and airborne radars (Mueller et al. 2017; Grasmick et al. 2018). There have also been numerical simulations of real bore events (e.g., Blake et al.

2017; Chipilski et al. 2018), and idealized simulations (e.g., Crook 1988; Martin and Johnson 2008; Haghi and Durran 2020). These studies will be discussed more in the following sections.

1.2.1.1 Hydraulic Theory

Consider the atmosphere as two-layers: the lower layer has high density, and the upper layer has a lower density. Laboratory experiments conducted in this simplified framework involved moving an obstacle through two fluids (e.g., Rottman and Simpson (1989)) and shed more light on conditions favorable for bore formation.

Baines and Davies (1980) illustrated a flow regime for different combinations of obstacle speed, obstacle depth, and the bore depth in this two-layer atmosphere. Bore generation is favored in two regimes: the partially-blocked flow regime and the completely-blocked flow regime (Fig. 1.4) (Rottman and Simpson 1989). The other two flow regimes (the supercritical and subcritical flow regimes) do not favor bore generation.

In a partially- or completely-blocked flow regime, some or all of the low-level fluid (i.e., the more stable air) cannot make it over the obstacle (it is blocked). The fluid is deflected up and back upstream (e.g., in the same direction as the density current is moving; Fig. 1.5), creating a hydraulic jump. A bore can be generated, which will propagate ahead of the obstacle. In the atmosphere, the obstacle is typically a density current from an MCS. Haghi et al. (2017) showed that in typical nocturnal environments, a partially-blocked flow regime is common.

1.2.1.2 Conditions for Wave Trapping

A density current moving through a stable layer is not enough for bore formation. There must be some way to trap the wave energy from leaking upward. Otherwise, the bore (or other gravity waves) would dissipate (Lindzen and Tung 1976; Crook 1988). How can this wave energy be trapped in the lower atmosphere?

Lindzen and Tung (1976) showed that the trapping mechanisms for mesoscale gravity waves (wavelength of 100-400 km) include a layer with strong static stability, a layer above that with much weaker static stability, some critical level (c–$u = 0$) above the duct where u is the system-relative wind speed and c is the density current speed, and strong vertical shear above the duct. For atmospheric bores, this critical layer may or may not be relevant to bore generation. Crook (1988) showed that a rapid decrease in the Scorer parameter (Scorer 1949) with height could trap the wave energy beneath that layer. He also showed that a temperature inversion above the layer where l^2 decreases rapidly could help reflect the wave energy to the surface for atmospheric bores. He did not mention the critical layer in this study, but was still able to generate a bore. In many cases, the wind speed's direction opposes the bore's direction, so there is no critical layer at all. However, in his simulations, far above the bore (where the bore speed is presumably zero), then there would be a critical layer because the wind speed is zero.

The Scorer parameter is

$$l^2 = \frac{N^2}{(U-c)^2} - \frac{\dfrac{\partial^2 U}{\partial z^2}}{(U-c)} \tag{1.1}$$

where $N^2 \equiv \frac{g}{\theta}\frac{\partial \theta}{\partial z}$ is the Brunt-Väisälä frequency, U is the environmental wind speed normal to the propagation direction of the density current, and c is the speed of the speed of the density current. In the case of laboratory experiments with fluids that are not air, the Brunt-Väisälä frequency is defined in terms of density rather than potential temperature.

A rapid decrease with height of the Scorer parameter can occur in three ways: a decrease in N^2 with height, a decrease in the second term (including the minus sign), or an increase with height of $U - c$. The rapid decrease in N^2 occurs at the transition from a stable lower atmosphere to a less stable atmosphere above that (indicated by the $\frac{\partial \theta}{\partial z}$ term). A rapid decrease in the second term is satisfied by the curvature of the environmental wind profile. The LLJ (discussed in the next section) is a common way to satisfy this second criterion in the atmosphere. Finally, an increase in $U - c$ will occur as the system-relative wind speed increases with height. If $U - c = 0$, then the Scorer parameter is undefined and there is a critical layer if that occurs above the wave duct (Lindzen and Tung 1976). If $U - c$ increases with height, then $\frac{1}{U-c}$ decreases with height, and this decrease is most rapid near the critical layer (Fig. 1.6)

The system-relative wind speed depends on the direction that the density current propagates with respect to the LLJ. Conditions favorable for bore formation might be along one orientation, but if the density current propagates in a different direction, then a bore might not form. This direction also means that certain portions of the density current might be more favorable to bore formation than others. Blake et al. (2017) examined how these conditions are impacted by looking at cross-sections at different angles through a density current/bore. They showed that in a SE/NW oriented cross-section, the conditions were less favorable for wave trapping than the conditions through a S/N oriented cross-section. This difference in wave trapping is likely because of the angle between the propagation direction of the density current and the environmental wind speed. If that angle increases from 0° to 90°, then U decreases to 0. If U = 0, the second term in Equation 1.1 is zero, and the conditions for wave trapping are less favorable.

Over the Great Plains, the common southerly LLJ is largely responsible for the rapid decrease in the Scorer parameter with height (e.g., Haghi et al. 2017). However, the atmosphere typically has a westerly component of the shear vector that can extend above the height of the LLJ (Parsons et al. 2019). While the shear associated with the total wind will likely favor bore production in a direction aligned with the highest vertical wind shear (for the most optimal wave trapping), this added westerly wind shear may affect the stability above the bore. Warm and moist air can be advected eastward by this westerly wind, destabilizing the environment above the bore. However, while the effects of the westerly wind on the destabilization of the environment are largely understood (e.g., Reif and Bluestein (2017, 2018), the effects of the vertical wind shear on the bore's structure are not (Parsons et al. 2019).

The necessary conditions for atmosphere bore generation are common over the nocturnal Great Plains. These conditions include a low-level stable layer, a rapid decrease in the Scorer parameter with height (usually achieved by the nocturnal LLJ), and a partially- or completely blocked flow regime.

A recent paper by Haghi and Durran (2020) suggested that shallow-water theory is not quantitatively applicable to bores that move in a direction opposite to the LLJ wind direction. For example, they showed that the wave direction solved from linear theory is opposite to the propagation direction of atmospheric bores. Based on this, they suggest that the observed bores are not the result of linear trapped wave dynamics. Furthermore, they suggest that a low-level stable layer topped by a less stable layer is not essential for bore development, but can help modify the bore structure and support waves downstream. Finally, in their simulations, the most important environmental feature necessary for an atmospheric bore was a strong LLJ opposing the bore motion. While this new research brings into question the applicability of linear theory to atmospheric bores, the simulations they conducted with an LLJ and a low-level stable layer were still able to produce atmospheric bores, but they were not well-described by the linear theory.

1.2.2 Atmospheric Bore Characteristics

The passage of an atmospheric bore has been observed many times (Koch et al. 1991, 2008b; Toms et al. 2017; Mueller et al. 2017; Grasmick et al. 2018; Loveless et al. 2019). Common characteristics include a surface temperature that remains the same or increases when the bore passes (Fig. 1.7) (Smith 1988; Koch et al. 2008b; Chipilski et al. 2018). This temperature increase is the result of the turbulent mixing of warmer air down to the surface. Other characteristics include a sustained increase in the surface pressure (Koch et al. 2008b) and a shift in the wind direction (Koch et al. 2008b).

Bores appear on radar as parallel bands of enhanced radar reflectivity factor (Fig. 1.8) (Coleman et al. 2010; Bluestein and Snyder 2015; Mueller et al. 2017; Grasmick et al.

2018) and can appear on satellite as parallel bands of clouds (Haghi et al. 2019). Density currents also appear as a finelines on radar reflected factor, but there will usually only be one “fineline” in the case of a density current (e.g., Grasmick et al. 2018). The temperature change associated with the passage of the feature can distinguish between the two. While the bore is associated with little temperature change, a density current is associated with a rapid temperature drop (Koch et al. 1991; Coleman et al. 2010; Mueller et al. 2017).

Atmospheric bores are vertically-trapped gravity waves. Untrapped gravity waves will tilt upstream with height (evidenced by the potential temperature) (Durran et al. 2015; Haghi et al. 2019). The vertically-aligned isentropes is one way to distinguish an atmospheric bore from a vertically-propagating gravity wave.

Various methods to identify and track atmospheric bores have been developed and these methods largely rely on surface-based observations. Chipilski et al. (2018) developed an algorithm to track atmospheric bores and distinguish bores from density currents using numerical simulations. This algorithm worked by detecting the surface pressure increase and the vertical velocity at 1 km AGL to identify the feature and using the surface temperature change over 15 minutes to distinguish between bores (where there is little-to-no surface temperature change) and density currents (where the surface temperature decreases). Haghi et al. (2017) identified bores by tracking the parallel bands of radar reflectivity factor. They further distinguished undular bores from non-undular waves by examining the pressure difference associated with the feature’s passage (non-undular waves have no sustained pressure increase).

1.2.3 Ascent Associated with Atmospheric Bores

One of the most critical features of bore passage is its potential to initiate convection. A semi-permanent displacement in the depth of the stable layer associated with the passage of atmosphere bores has been frequently observed through vertically-pointing lidar data as an increase in the scattering layer (Knupp 2006; Mueller et al. 2017; Grasmick et al.

2018; Haghi et al. 2017; Parsons et al. 2019; Loveless et al. 2019). This semi-permanent increase can lift parcels into the vertical, potentially lifting it to the LFC and creating new convection (Knupp 2006; Loveless et al. 2019).

Observations of this semi-permanent displacement have relied on vertically pointing lidars and other similar instruments (Fig. 1.9). Common variables used to determine this displacement are changes in the signal-to-noise ratio (Knupp 2006; Haghi et al. 2017), changes in the refractive index (Parsons et al. 2019), changes in the Brunt-Väisälä frequency (Parsons et al. 2019), changes in the turbulent energy dissipation rate (Parsons et al. 2019), changes in the moisture (Knupp 2006; Mueller et al. 2017; Grasmick et al. 2018), or the changes in the isentropes (Knupp 2006; Chipilski et al. 2018). These methods can give slightly different results depending on the environmental conditions. For example, in unsaturated environments, the isentropes' displacement might give a good result, but it would not in saturated environments as the potential temperature is not conserved.

Analyzing the magnitude of the vertical velocity poses problems when assessing the potential for CI. Observations of vertical velocity using lidars depend on the presence of scatterers for the lidar to retrieve any signal. These scatterers have mass, thus weighing the atmosphere down, resulting in a weaker observed vertical velocity than what would otherwise occur (Parsons et al. 2019). However, numerical simulations of bores do not have this limitation, so it is possible to assess that potential in a model framework more accurately than in observations.

This displacement can be as much as 2 km (Parsons et al. 2019) and is commonly 500 – 1000 m. Table 1.1 shows a list of net displacements of vertical velocities from selected observed bores. The average vertical velocity near the leading edge of bores is between 1-2 m s^{-1}. The mean net displacement of parcels is between 400 m and 1000 m. This ascent can be enough to cause CI in optimal environments with high low-level moisture and low lapse rates above that layer of enhanced moisture.

Table 1.1: Vertical velocity (m s^{-1}) and mean and maximum net displacement associated with observed bores from past studies. *Loveless et al. (2019) included 8 separate atmospheric bores in their study.

Study	Vertical Velocity (m s^{-1})	Mean Net Displacement (m)	Max Net Displacement (m)
Crook (1988)	2.4	–	–
Karyampudi et al. (1995)	–	–	950
Knupp (2006)	–	600 - 900	2000
Koch et al. (2008b)	1	600	–
Koch et al. (2008a)	1.5	400-700	–
Mueller et al. (2017)	–	1000	–
Grasmick et al. (2018)	–	–	1000
Parsons et al. (2019)	–	658 - 892	892
Loveless et al. (2019)*	1.5	400-1000	1000

1.3 Nocturnal Low-Level Jet

The Great Plains nocturnal LLJ is a low-level wind maximum frequently below 1 km above ground level (AGL). The wind direction is predominantly southerly, but northerly LLJs can occur (Song et al. 2005; Gebauer et al. 2017). They can be hundreds of km in width and span a length of 1000 km.

Bonner (1968) presented one of the earliest climatologies of the LLJ. He used the 0000 UTC and 1200 UTC soundings over a 2-yr period. In this climatology, the speed maximum occurred at 800 m above the surface, and the maximum frequency of occurrence was near NW Oklahoma. While there was no quantitative estimate for the jet's length and width, he showed that the length of the jet was roughly 6-12° latitude (500-1000 km), and the width was 2-5° longitude (200-550 km). The jet was frequent throughout the year, occurring on 65% of the days in Fort Worth, TX, and was more prominent in the summer than in the winter.

One limitation of the Bonner (1968) climatology is the temporal resolution of the radiosondes. The sounding data are only available at 1200 UTC and 0000 UTC. Mitchell et al. (1995) and Arritt et al. (1997) used the NOAA wind profiler network to fill in the gaps. In their 1-yr study, the peak LLJ occurrence was between 7 and 10 UTC. The average duration of any low-level wind maximum was 4 hours (Mitchell et al. 1995). The frequency of LLJs was most common in the summer months, in agreement with the Bonner (1968) climatology.

While the height of the LLJ wind maximum was near 800 m AGL in Bonner (1968), Whiteman et al. (1997) used soundings over a 2-yr period from April 1994 to March 1996 to show that half of the LLJ wind maxima were below 500 m AGL. The studies by Mitchell et al. (1995) and Arritt et al. (1997) use wind profiler data, which do not have data below 500 m AGL. Those studies may have underestimated the LLJs strength or did not capture the LLJ correctly.

Bonner (1968) grouped the strength of the LLJ according to three criteria: a criterion 1 LLJ has winds that exceed 12 m s^{-1}, a criterion 2 LLJ has winds that exceed 16 m s^{-1}, and a criterion 3 LLJ has winds that exceed 20 m s^{-1}. To be considered an LLJ, the wind speed must decrease to half of the listed value at the next higher minimum or to 3 km, whichever level is lower in altitude. The average speed of the LLJ averaged over the year in his study was 13 m s^{-1} at Fort Worth and 14 m s^{-1} at Topeka, KS. These winds associated with the LLJ are strong and can reach speeds double that of the daytime wind speed (Shapiro and Fedorovich 2010).

Smith et al. (2019) examined observed LLJs from the PECAN field campaign and compared those observations to numerical simulations using the Weather Research and Forecasting (WRF; Skamarock et al. (2008)) model. The maximum wind speed's typical height was near 500 m AGL, but there was considerable variation throughout the night. In some events, the height could be near 900 m, but a couple of hours later could be below 500 m. They referred to this feature as a diagonal striation (Fig. 1.11). This diagonal striation results from the veering of the winds with height and time and the downslope advection of the jet. It is generally collocated with an area of rising motion (Fig. 1.12). This feature illustrates the jet's heterogeneity with space and time, and this heterogeneity can be important for rising motion (Gebauer et al. 2018). This heterogeneity of the LLJ will be discussed in a later section.

1.3.1 LLJ Formation

Blackadar (1957) proposed one of the earliest ideas for the formation of this LLJ. At sunset, the friction force decreases as the turbulence from daytime mixing decreases. This decrease in the friction force allows for an inertial oscillation of the ageostrophic wind. The maximum wind speed occurs with this ageostrophic component (which rotates clockwise throughout the night) aligns with the geostrophic wind. The inertial oscillation of the wind has been frequently observed (Bonner 1968; Arritt et al. 1997; Parish 2016; Bluestein et al. 2018) and modelled (Shapiro and Fedorovich 2009, 2010; Fedorovich et al. 2017; Rotunno et al. 2018). The Blackadar (1957) theory does not explain why the LLJ is preferred over the Great Plains region, and it does not describe why some LLJs can be much stronger (more than 100% stronger) than the geostrophic wind (Shapiro and Fedorovich 2009, 2010; Shapiro et al. 2016).

Holton (1967) suggested that the diurnal temperature oscillation could explain the diurnal wind oscillation in the boundary layer over sloped terrain. He suggested that this oscillation is likely a significant component of the wind oscillation's amplitude. However, he noted that the solutions lagged the observed phase by a few hours and the actual LLJ winds are stronger than his solution. Bonner and Paegle (1970) used the effects of the sloping terrain (periodicity of the geostrophic wind) but did not explicitly take the terrain into account. Their approach was simple. While it did reproduce the LLJ reasonably well, the solutions were highly sensitive to the choice of the mean geostrophic wind, viscosity, and the phase difference between the two. However, the effects of the slope (whether directly or indirectly) could contribute to the LLJ.

Shapiro et al. (2016) presented a unified theory that combines the Blackadar (1957) and Holton (1967) theories. The Blackadar (1957) mechanism is represented by the diurnal variations in the turbulent diffusivity. The Holton (1967) mechanism is represented by the diurnal variations in the surface buoyancy due to the heating and cooling of the sloped surface. In their analytical solution, the LLJ was strongest for slope angles representative of the Great Plains. The combined mechanisms produced jets that represented the timing, strength, and vertical structure of observed jets.

1.3.2 Ascent associated with the LLJ

The nocturnal LLJ has long been attributed to the nocturnal precipitation maximum. Pitchford and London (1962) showed that nocturnal thunderstorms and the LLJ occurred at the same time on nearly 2/3 of the summer nights with an LLJ between 1955 and 1957. Bonner (1966) showed that strong upward vertical motion exists downstream of the jet max and exists in the LLJs right exit region (a similar location to the CI location of NB CI mode events associated with the LLJ in Reif and Bluestein (2017)). More recently, Walters and Winkler (2001) showed a strong connection between the LLJ and the spatial distribution of cloud-to-ground lightning. While it could be a coincidence that the thunderstorms occurred in conjunction with the LLJ as both are common over the Plains, there are mechanisms associated with the LLJ that further indicate its relationship to this precipitation maximum. These mechanisms include “frontal overrunning,” speed convergence at the terminus of the LLJ, or ascent that occurs on the anticyclonic-shear side of the jet.

“Frontal overrunning” is a process that occurs when warm, moist air gets advected northwards up and over an east-west oriented quasi-stationary front (e.g., Trier and Parsons (1993)). This process is common with elevated convection on the cold side of these stationary fronts (Colman 1990; Reif and Bluestein 2017). While vertical displacements can be well-described by these mechanisms, other features likely need to be present before CI can occur (Trier et al. 2020).

Another common process is the idea of convergence at the terminus of the LLJ. After a parcel moves poleward through the LLJ and reaches the maximum speed, the parcel will slow down and converge into the slower moving parcels ahead. It has been speculated that this process can be responsible for elevated CI (Squitieri and Gallus Jr 2016; Degelia et al. 2018; Trier et al. 2020). This process is difficult to observe as a large domain of relatively tightly-spaced vertical profiling systems would be needed with an adequate vertical resolution near the surface. Modern reanalysis models such as the fifth version of the European Centre for Medium-Range Weather Forecasts (ECMWF) reanalysis model ERA5 (Hersbach 2016) could provide adequate vertical resolution near the surface (ERA5 has about 20 vertical levels in the lowest 1 km). However, direct observations of this convergence is challenging. Despite this challenge, Bonner (1968) suggested that the downstream decrease in the mean speed would produce a divergence of -1.3×10^{-5} s^{-1}. If one assumes zero vertical velocity at the ground and integrates the continuity equation to 500 m AGL, there is rising motion of 0.65 cm s^{-1}.

The westerly component of the LLJ is responsible for moisture advection eastward (e.g., Gebauer et al. 2018). Low-level warm advection associated with this westerly component and the north-south baroclinic zone resulting from differential diabatic heating across the sloping terrain can make the environment more conducive for CI (Parish 2016). These processes are responsible for increasing CAPE and reducing CIN throughout the LLJ region, illustrating the importance of the LLJ in modifying the environment (Parsons et al. 2019). Even weak rising motion can result in CI in these primed environments (e.g., Reif and Bluestein 2017, 2018; Gebauer et al. 2018; Parish et al. 2020).

Recent attention has been paid to the ascent that occurs along the eastern, or anticyclonic-shear, side of the jet. Walters and Winkler (2001) noted that there is more convection on the eastern side of the jet. Reif and Bluestein (2017) showed that the majority of NB CI mode events occur on the eastern side of the LLJ, and linear systems that initiate tend to be oriented N/S.

Pu and Dickinson (2014) used the time tendency of the vertical vorticity to illustrate how rising motion can exist.

$$\frac{\partial w}{\partial z} = \frac{1}{f}\left(\frac{\partial \zeta}{\partial t} + \beta v + \varepsilon \zeta\right) \tag{1.2}$$

where w is the vertical velocity, f is the Coriolis parameter, $\beta = \frac{\partial f}{\partial y}$, ζ is the vertical vorticity, and $\varepsilon = C_d \times |\boldsymbol{V}|/H$ is the bulk aerodynamic formula which simulated friction due to surface viscosity. They used data from the North American Regional Reanalysis (NARR; Mesinger et al. 2006) and three simulations to show, using the linearized form of the vertical vorticity equation, the diurnal cycle of the vertical velocity and the meridional wind at 500 m AGL. They explained the vertical velocity pattern through the vorticity tendency, the meridional transport of planetary vorticity, and drag (Equation 1.2). They showed that the convergence was consistent with the vorticity tendency term, not the meridional transport or drag terms. As the jet slows down after reaching its maximum strength, the anticyclonic (cyclonic) vorticity weakens (increases) as a function of time. According to Equation 1.2, if $\frac{\partial \zeta}{\partial t} > 0$, then $\frac{\partial w}{\partial z} > 0$. This condition of $\frac{\partial w}{\partial z} > 0$ implies convergence through mass continuity. For the time and spatial scales that they are examining, this relationship is reasonable.

Consider, however, the full non-linear vorticity equation

$$\frac{\partial \zeta}{\partial t} = -\vec{v} \cdot \nabla \zeta - \beta v - \delta\left(\zeta + f\right) + F \tag{1.3}$$

where F is the friction term and δ is the divergence. Vorticity is generated (or destroyed) through horizontal advection of vorticity, meridional advection of planetary vorticity, the stretching of vorticity, and frictional effects. In their analysis, they neglected the non-linear terms (the horizontal advection term and the stretching of relative vorticity), which can be justified by assuming that u=0 and that there is no variation along y of ζ (i.e., $\partial \zeta / \partial\ y = 0$). Furthermore, ζ was smaller than f in their reanalysis and simulation data and could be neglected. However, in LLJs where the meridional wind speed can be much stronger than the geostrophic wind, neglecting ζ may not be valid.

They state that vertical motions develop “to balance the anomalous vorticity tendency.” If $w = 0$ at the surface, then $w > 0$ above the jet. However, based on their analysis using Equation 1.2, the anomalous vorticity can be explained by the stretching of planetary vorticity. While their argument is satisfied by Equation 1.2, it is incomplete. They do not explain how vertical velocity develops, only that the vertical velocity is consistent with the observed vorticity tendency.

To propose another possible mechanism for generating rising motion, consider the horizontal vorticity equation (along the y-direction) (Bluestein 1992, equation 4.5.133).

$$\frac{D\zeta_y}{Dt} = -\delta_y\zeta_y + \left[(\zeta + f)\frac{\partial v}{\partial z} + \zeta_x\frac{\partial v}{\partial x}\right] + \frac{\partial}{\partial z}\left(-\alpha\frac{\partial p}{\partial x}\right) + \frac{\partial F_x}{\partial z} \tag{1.4}$$

where $-\delta_y\zeta_y$ is the stretching of an air parcel along the y-axis, $(\zeta + f\,)\frac{\partial v}{\partial z}$ is the tilting of absolute vorticity onto the horizontal, $\zeta_x\frac{\partial v}{\partial x}$ is the tilting of the horizontal relative vorticity oriented along the x-axis onto the y axis, $\frac{\partial}{\partial z}\left(-\alpha\frac{\partial p}{\partial x}\right)$ is the solenoidal term, and $\frac{\partial F_x}{\partial z}$ is the frictional term. The first term on the RHS on only valid in the entrance region of the jet, so we can ignore it here. ζ is smaller than f on the synoptic scale, so we can neglect relative vorticity as well. Finally, we can neglect the friction term. This equation presents another way to generate a vertical circulation.

The solenoid term (which may explain, in part, the mechanism for ascent illustrated in Shapiro et al. 2018) is responsible for generating a vertical circulation. The expanded solenoidal term is $-\frac{\partial \alpha}{\partial z}\frac{\partial p}{\partial x} - \alpha\frac{\partial}{\partial z}\left(\frac{\partial p}{\partial x}\right)$. If we linearize this equation in terms of its base state and perturbation, assume the Boussinesq and hydrostatic approximations, then the solenoid term can be written as

$$\frac{\partial}{\partial z}\left(-\alpha\frac{\partial p}{\partial x}\right) \approx -\frac{\partial B}{\partial x} \tag{1.5}$$

where $B \equiv -g\frac{\rho'}{\bar{\rho}}$, and $\bar{\rho}$ is the average density subject to the Boussinesq approximation (i.e., $\bar{\rho}$ is constant). The horizontal vorticity generated by the solenoid term can be expressed through the horizontal gradient of buoyancy.

Now consider how a vertical circulation can be generated through the tilting term of the horizontal vorticity equation (Equation 1.4). Above the jet, a circulation is generated with rising motion east of the LLJ maximum (Fig. 1.13); consistent with the CI location of nocturnal storms). The tilting of relative vertical vorticity onto the horizontal generates a circulation of the same sense on the western side of the jet, but is in the opposite direction on the eastern side of the jet (Fig. 1.13). For strong LLJs, neglecting the tilting of relative vertical vorticity may not be valid, and in this case, the strongest rising motion above the jet may be near the jet core and just to its west. This analysis suggests that the tilting of vertical vorticity onto the horizontal can generate rising motion and may be another mechanism for LLJ-induced CI.

The boundary layer deepens westward across the plains and generally mirrors the sloping terrain (e.g., Sun and Wu 1992; Jones and Bannon 2002) (Fig. 1.10). This deeper PBL results from a drier western portion and the differential heating across the plains (stronger heating as one approaches the mountain from the east) (e.g., Sun and Wu 1992; Markowski and Richardson 2011). Gebauer et al. (2018) provided another explanation for the enhanced convection on the jet's eastern flank. If the PBL (and thus the LLJ) is deeper on the western side, that deeper layer experiences a deeper inertial oscillation. As the night progresses, the inertial oscillation results in increasing convergence along a N/S oriented line. The westerly winds from above the jet could bring additional moisture eastward from prior convection over the lee of the Rockies, and once that moisture interacts with the enhanced convergence, CI can occur. This mechanism may partly explain the later initiation time of these events noted in Reif and Bluestein (2017).

Shapiro et al. (2018) presents a different explanation for ascent above the jet. They showed that ascent between 3 and 10 cm s^{-1} exists above the jet (Fig. 1.14) centered along the maximum in a horizontally varying buoyancy gradient. This weak, but persistent, ascent results from an inertia-gravity response due to the release of the frictional constraint at sunset. The maximum magnitude of that ascent occurred 3.5 hr after sunset. This horizontal buoyancy gradient can arise from differential heating due to the sloping terrain (e.g., Holton 1967, differential heating of the terrain itself (e.g., Gebauer et al. 2018; Gebauer and Shapiro 2019), or the northward advection of warmer temperatures (see Fig. 1.15 for examples of this gradient).

It is possible to have a sea-breeze-like circulation in the presence of a baroclinic zone, which could produce weak convergence near the surface and weak rising motion aloft. As the baroclinic zone's width increases, the solenoidal term decreases. This decrease in the solenoidal term weakens the solenoidal circulation and the vertical motion. The Sawyer-Eliassen equation (Bluestein 1993; reproduced below) can explain the vertical circulation associated with baroclinic zones when the length scales are large and Coriolis effects need to be included. It is typically applied to synoptic-scale features, so its application in the mesoscale or smaller is questionable, but a qualitative assessment of the circulation may still be obtained.

$$\begin{aligned}\frac{\partial^2\psi}{\partial y^2}\left[-\frac{R}{f_0 p}\left(\frac{p}{p_0}\right)^{\kappa}\frac{\partial\theta}{\partial p}\right]+\frac{\partial^2\psi}{\partial y\partial p}\left(2\frac{\partial u_g}{\partial p}\right)+\frac{\partial^2\psi}{\partial p^2}\left(f_0-\frac{\partial u_g}{\partial y}\right)\\ =2\left[\frac{R}{f_0 p}\left(\frac{p}{p_0}\right)^{\kappa}\left(\frac{\partial\theta}{\partial y}\frac{\partial v_g}{\partial y}+\frac{\partial\theta}{\partial x}\frac{\partial u_g}{\partial y}\right)\right]-\frac{R}{f_0 p}\frac{1}{c_p}\frac{\partial}{\partial y}\left(\frac{dQ}{dt}\right)\end{aligned}\tag{1.6}$$

where Ψ is the streamfunction, p is pressure, θ is the potential temperature, u_g is the zonal geostrophic wind, and dQ/dt is diabatic heating. $2\frac{R}{f_0 p}\left(\frac{p}{p_0}\right)^{\kappa}\left(\frac{\partial v_g}{\partial y}\frac{\partial\theta}{\partial y}\right)$ represents changes in the across-front temperature gradient due to geostrophic stretching and deformation along the front. $2\frac{R}{f_0 p}\left(\frac{p}{p_0}\right)^{\kappa}\left(\frac{\partial u_g}{\partial y}\frac{\partial\theta}{\partial x}\right)$ represents in changes in the across-front temperature gradient due to the tilting of the along-front temperature gradient into the cross-front direction by the geostrophic shearing deformation. The last term on the RHS of Equation 1.6 is the differential diabatic heating term.

1.4 Potential Vorticity Anomalies

Potential vorticity (PV) is a concept introduced in the 1940s (Rossby 1939; Ertel 1942) and popularized in the 1980s by Hoskins et al. (1985). PV represents the vorticity that an air column would have if it were brought isentropically to some standard latitude and stretched or shrunk to some standard depth. Ertel's PV is given by

$$PV = \Pi = \frac{1}{\rho}\zeta_a \cdot \nabla\theta \tag{1.7}$$

where ρ is the density, ζ_a is the absolute vorticity, and θ is the potential temperature. PV is commonly expressed in terms of potential vorticity units (PVU) where 1 PVU = 10^{-6} m^2 s^{-1} K kg^{-1}.

1.4.1 Characteristics of PV anomalies

PV anomalies are either cyclonic (positive in the northern hemisphere) or anticyclonic (negative in the northern hemisphere). Consider Equation 1.7 and assume that there is a cyclonic PV anomaly. A cyclonic PV anomaly can occur with any combination of these three features: strong static stability (more positive $\nabla\theta$), cyclonic vorticity, or lower density. Magnitudes of cyclonic PV anomalies from selected studies are given in Table 1.2.

The typical characteristics of a cyclonic PV anomaly (Fig. 1.16a) are a cyclonic wind perturbation around the PV anomaly, and the isentropes are effectively "pulled" in towards the center of the anomaly (Thorpe 1986). The cyclonic wind perturbation increases the vorticity, and the more tightly-spaced isentropes increases $\frac{\partial\theta}{\partial z}$. Both of those effects increase the PV. The opposite is true for anticyclonic PV anomalies (Fig. 1.16b).

Cavallo and Hakim (2010) composited 568 tropopause polar vortices (TPVs) over a two-year period (Fig. 1.17). These TPVs are cyclonic PV anomalies located at or near the tropopause. The structure of this composite cyclonic PV anomaly is similar to that shown by Thorpe (1986), which is characterized by a 3-4 PVU cyclonic anomaly, a maximum wind speed of 14-15 m s^{-1} around the anomaly, anomalously high relative humidity below the PV anomaly, and rising motion downshear. The peak vortex radius was between 400 and 600 km, and the lifetime of the TPV was around one month.

PV is conserved for adiabatic and frictionless flows, and this conservation principle is useful in many applications. One application is that PV can be used as a forecast error growth tracker (Davies and Didone 2013), and the error pattern based on the analysis minus forecast metric can help identify insight about the nature of the error and how it evolves (Dirren et al. 2003; Davies and Didone 2013). Another application of the conservation principle is that features can be tracked, sometimes for days or weeks (Cavallo and Hakim 2010).

Another useful feature is the definition of the dynamic tropopause (Reed 1955; Danielsen 1968; Shapiro 1980). Rather than using the static stability to define the tropopause, PV is used. It has been shown that PV between 1 and 3 PVU roughly defines the tropopause. This idea also led to the identification of tropopause folds (Reed 1955; Shapiro et al. 1987). These features are characterized by higher PV, strong static stability, can extend down into the lower troposphere, and can exchange stratospheric air with the troposphere (Reed 1955; Shapiro et al. 1987; Koch et al. 2005). Tropopause folds have been associated with turbulence and inertia-gravity waves (Koch et al. 2005).

Dynamic tropopause maps allow the tracking of features such as TPVs or cyclonic PV anomalies (Morgan and Nielsen-Gammon 1998; Cavallo and Hakim 2010). An advantage to these tropopause maps is that features on the tropopause can be identified regardless of the pressure at the tropopause. The potential temperature on the dynamic tropopause can be used to identify PV features near the tropopause. For example, cold areas are cyclonic PV anomalies, and a sharp gradient in potential temperature corresponds to upper-level jet streams (Morgan and Nielsen-Gammon 1998).

However, the nonconservation of PV can illuminate processes that might be important. Examples of PV generation by friction could be related to orographic effects (Li and Smith 2010), while PV generation by diabatic processes is commonly seen in thunderstorms such as MCSs (Raymond and Jiang 1990; Jiang and Raymond 1995; Trier et al. 2000). Diabatic processes in the MCS (such as latent heating) can generate a lower-tropospheric cyclonic PV anomaly (e.g., Davis and Trier 2002). This cyclonic PV anomaly is associated with a cyclonic vorticity perturbation, which could create an MCV (Moore and Montgomery 2005; Conzemius et al. 2007).

Lackmann (2002) and Brennan et al. (2008) showed how latent heat release can alter the PV field. For example, latent heating associated with a frontal rainband generates cyclonic PV at low levels. East of that PV anomaly, if an LLJ is present, then the wind field induced by the generated PV anomaly can modify the LLJ, increasing the southerly flow. This modification can alter the moisture transport by the LLJ and alter the characteristics of the precipitation. Weijenborg et al. (2017) examined the structure and evolution of PV anomalies at the convective scale ($<$ 10 km) and showed that PV anomalies are coherent phenomena at these small scales. At the synoptic scale, geostrophic balance is a good assumption (Hoskins et al. 1985), but at the convective scale, there is a question of the type of balance and how much of the flow is unbalanced. These small-scale PV anomalies have a longer life than the parent convection. They speculate that these small-scale anomalies could still influence the flow or initiate new convection even after the parent storm dissipates.

The conservation of PV is not the only thing that makes PV a useful tool. PV is also invertible. Given some balance condition and base state, one can diagnose the potential temperature and wind field associated with a given PV field (Hoskins et al. 1985; Davis and Emanuel 1991; Winters and Martin 2017). This principle is useful for diagnosing a PV anomaly's effects on the flow and temperature structure nearby or how the flow and temperature structure would be without the anomaly present. This procedure is called PV surgery (Browning et al. 2000; Roebber et al. 2002; Nielsen-Gammon and Gold 2008a; Torn and Romine 2015).

PV surgery has been used in a wide variety of application including severe weather events (Nielsen-Gammon and Gold 2008a,b; Torn and Romine 2015), hurricanes (Wu and Emanuel 1995), and extratropical cyclones (Davis and Emanuel 1991; Hakim et al. 1996; Hardy et al. 2017), and forecast error analysis (Browning et al. 2000). The alteration of the PV anomalies affected the CAPE and vertical wind shear, modifying or even potentially changing the convective mode for an event (Torn and Romine 2015). This alteration highlights the importance of understanding the effect that PV anomalies may have on the environment.

PV thinking can also be applied to surface cyclogenesis. The Rossby penetration depth is given as

$$H = \frac{fL_R}{N} \tag{1.8}$$

Consider an upper-tropospheric PV anomaly moving over a baroclinic zone. The effects of the upper-level PV anomaly can extend to the surface determined by Equation 1.8. These effects result in a cyclonic PV anomaly created at or near the surface and can result in surface cyclogenesis (Bluestein 1993; Martin 2013).

1.4.2 Ascent associated with PV anomalies

By themselves, a PV anomaly cannot induce rising motion. However, the interaction of that PV anomaly and an environment with vertical wind shear can be associated with rising motion (Fig. 1.18) (Raymond and Jiang 1990). Hoskins et al. (1985) suggested that three components are related to ascent associated with PV anomalies: ascent due to PV advection, ascent due to boundary temperature advection, and ascent due to isentropic upglide. They also compared the ascent to an eastward-moving anomaly to that of a "vacuum cleaner." Air goes up on the eastern side and down on the western side (Hoskins et al. 1985). If the deformation of the PV anomaly by the vertical wind shear is weak, then ascent can be analyzed by isentropic upglide (Raymond and Jiang 1990).

Li and Smith (2010) suggested that PV anomalies generated from diabatic effects can be associated with rising motion. The sun heats the Rocky Mountains, which then heats the air. This diabatic heating results in the generation of PV anomalies, which are advected eastward and could play a role in nocturnal convection (Raymond and Jiang 1990; Carbone et al. 2002; Li and Smith 2010). The phase speed of these drifting PV anomalies and phase speed of the eastward propagating precipitation are similar (15 m s^{-1}). One must use caution when connecting the effects of PV anomalies to precipitation because of PV nonconservation. Precipitation is a diabatic process, which generates PV, and could explain this similarity between the PV phase and the precipitation phase. However, Parker and Ahijevych (2007) speculate that ascent associated with a PV anomaly advected over the middle troposphere could aid in the redevelopment of a convective system under the right conditions.

The magnitude of the ascent associated with these mid-tropospheric PV anomalies is commonly between 1 and 5 cm s^{-1} (Jiang and Raymond 1995; Trier et al. 2000). Like the ascent related to the LLJ, this ascent appears to be weak and unlikely to cause new convection. However, it has been suggested that the net displacement associated with the PV anomalies can be up to 500 m (Trier et al. 2000). Air parcels revolve around a PV anomaly, and in the presence of vertical wind shear, there are areas where parcels experience rising motion (e.g., Raymond and Jiang 1990). However, the duration they experience rising motion depends on the size and strength of the PV anomaly. In the case of the LLJ, the parcels can remain in the zone of ascent for longer periods of time. The connection between CI and ascent related to PV anomalies is unclear.

Table 1.2: PV anomaly strengths (PVU) from previous studies

Study	Anomaly Strength	Date	Notes
Davis (1992)	6.22 PVU	1200 UTC 15 Dec 1987	
	2.69 PVU	1200 UTC 5 Feb 1988	
Stoelinga (1996)	2.1 PVU		950 - 700 hPa
	2.69 PVU		400 hPa
Hertenstein and Schubert (1991)	1.6 PVU		
	1.4 PVU		Total field; Not anomaly
Huo et al. (1999)	3.5 PVU		400 hPa
	2.5 - 3 PVU		900 hPa
Moore and Montgomery (2005)	0.2 - 0.4 PVU		10 K day^{-1} heating rate
Clark et al. (2010)	2.5-3 PVU	1 Jun 2007	600 - 500 hPa
Lackmann (2011)	1.5 PVU	25 Jan 2000	900 - 700 hPa
Campa and Wernli (2012)	2 - 3 PVU	0600 UTC 26 Dec 1999	
	3 - 5 PVU	0000 UTC 14 Mar 1994	
	2 - 3 PVU	0000 UTC 28 Feb 2010	

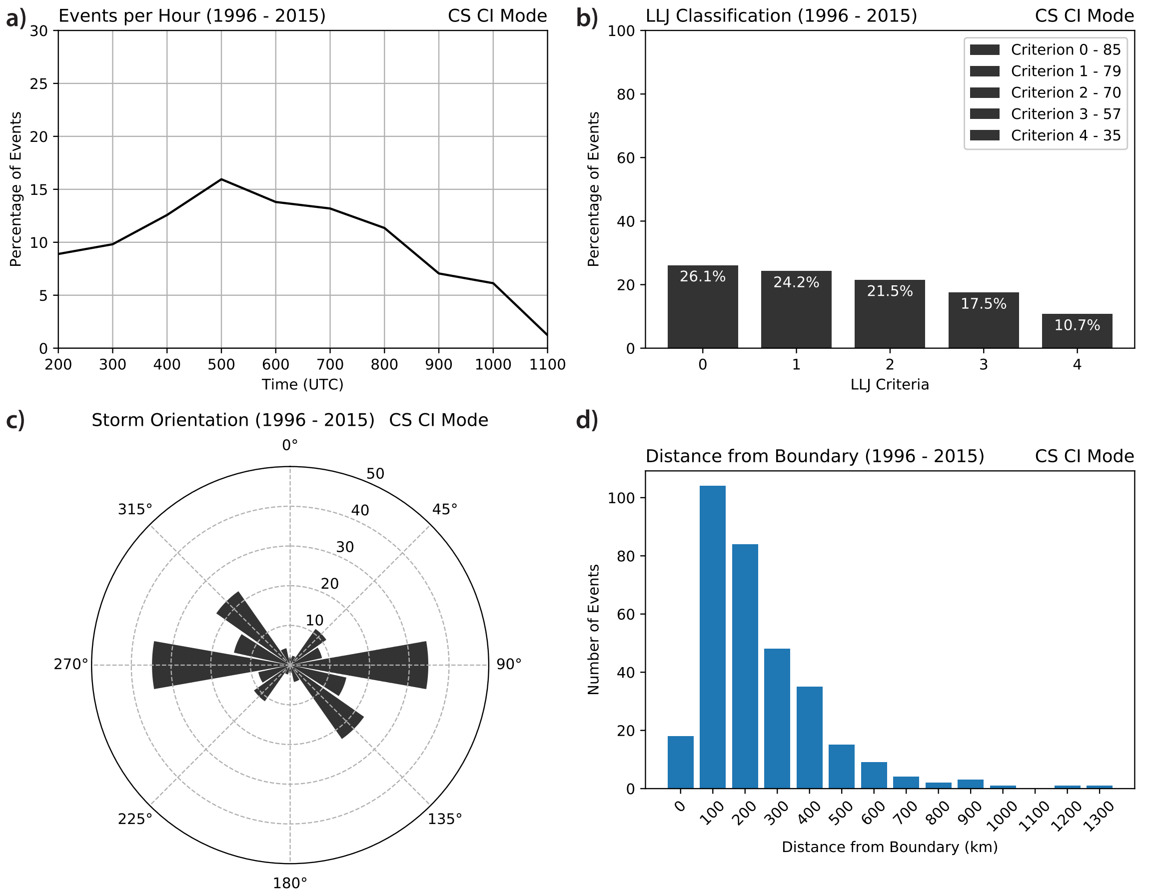

Figure 1.1: CS CI mode events from Reif and Bluestein (2017). (a) Events per hour (%), (b) Pertencage of events of each LLJ classification from Bonner (1968), (c) orientation of the linear systems, and (d) CI location relative to the surface boundary.

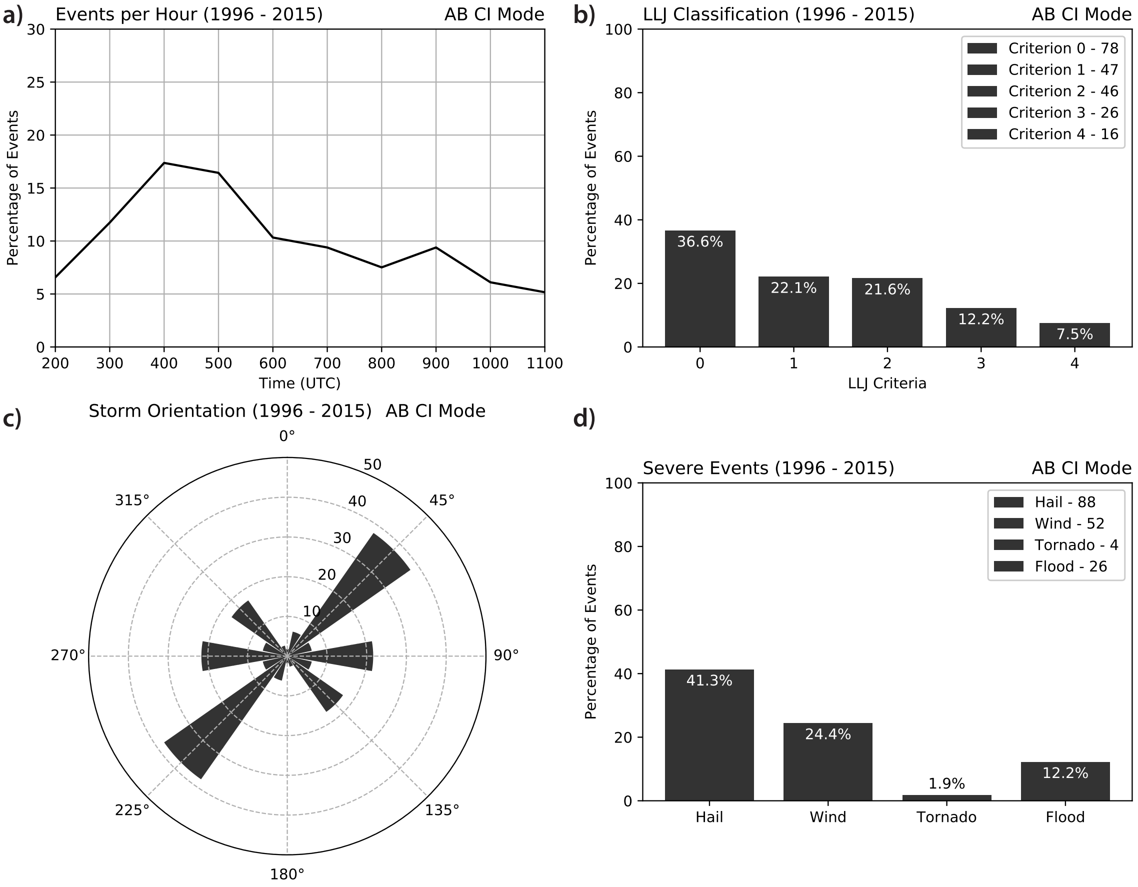

Figure 1.2: As in Fig. 1.1, but for AB CI mode events and (d) percentage of events associated with each severe type.

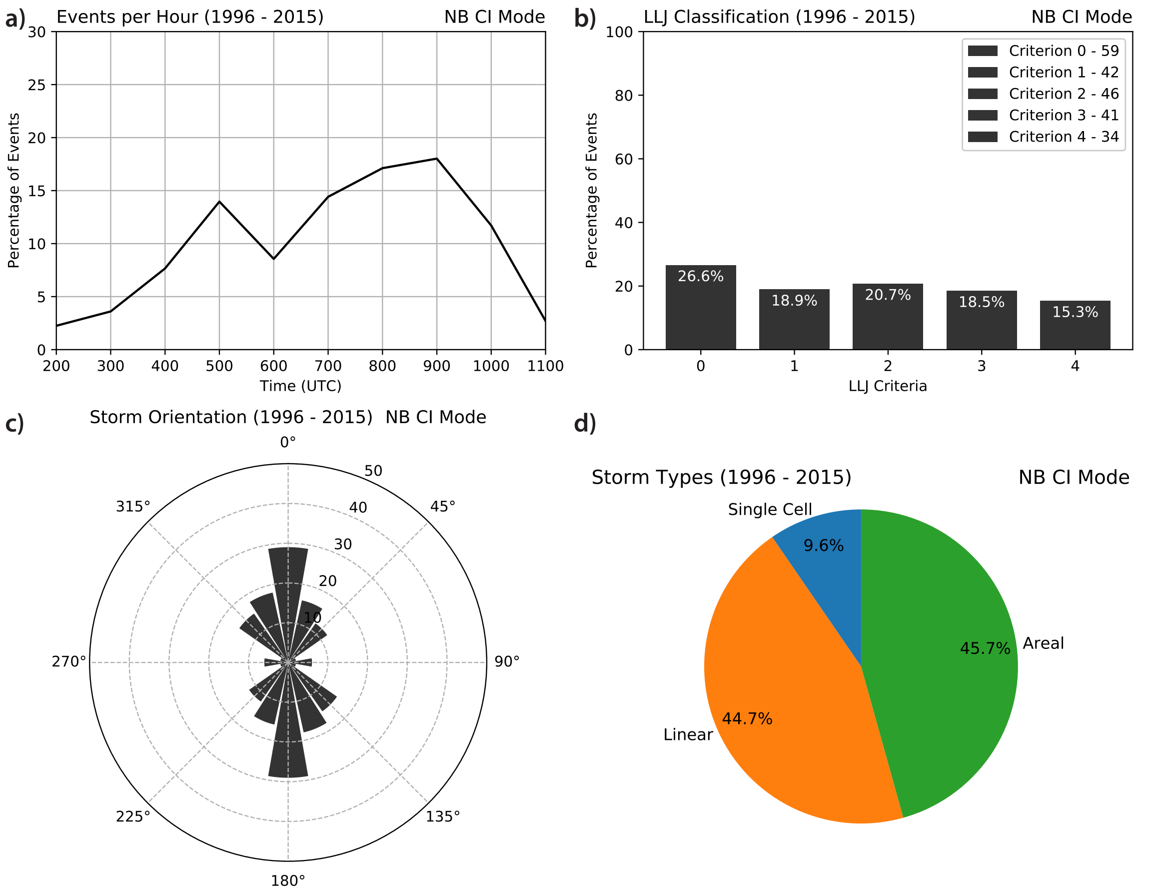

Figure 1.3: As in Fig. 1.1, but for NB CI mode events and (d) percentage of storm types (areal, linear, or single cell).

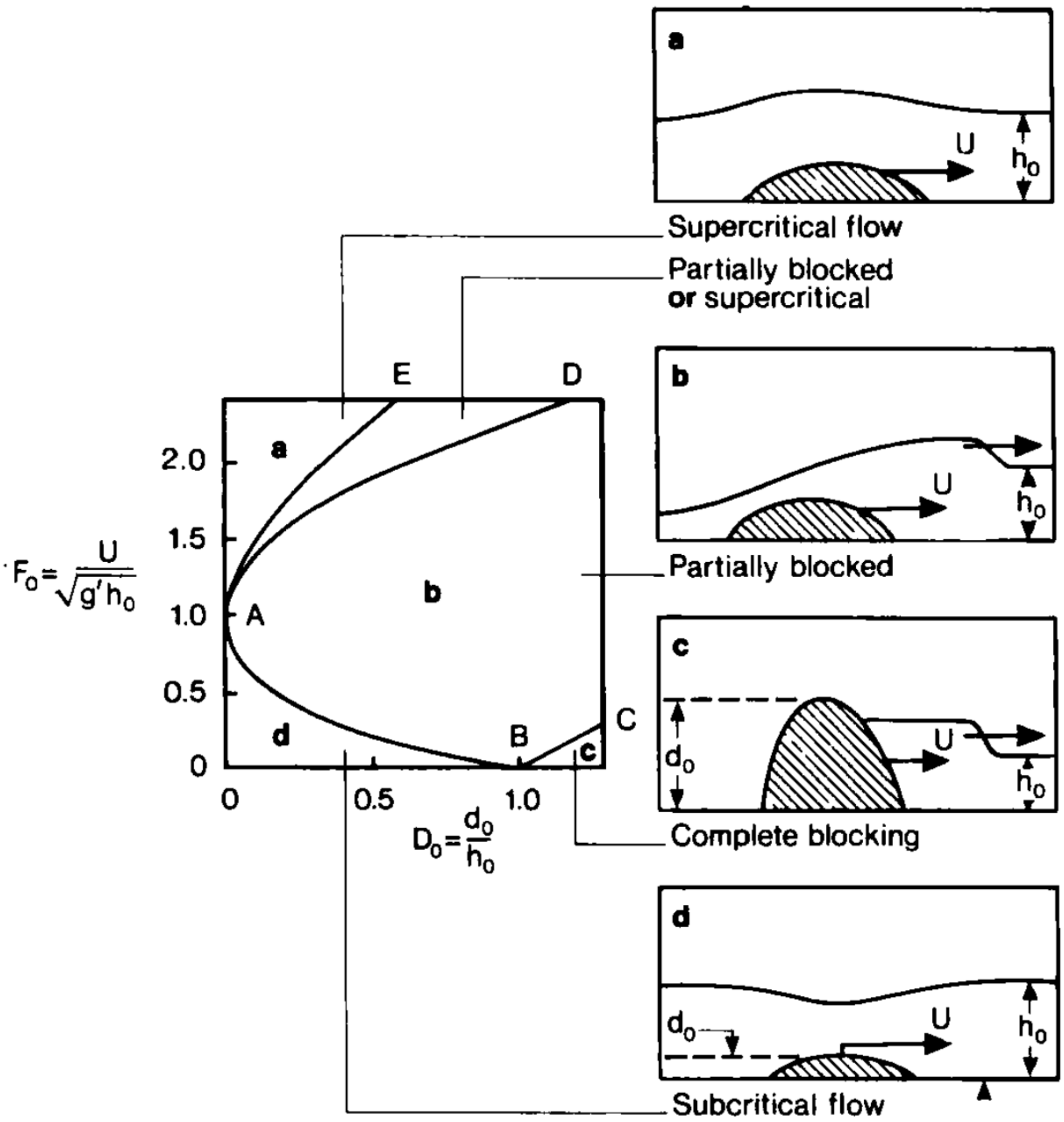

Figure 1.4: Flow regime for the two-layer atmosphere. Figure from Rottman and Simpson (1989). F_0 is the Froude number, D_0 is the non-dimensional height (ratio of the height of the obstacle d_0 to the inversion height h_0, and $g' = g(\rho_1 - \rho_2)/\rho_1$) where $\rho_1 > \rho_2$.

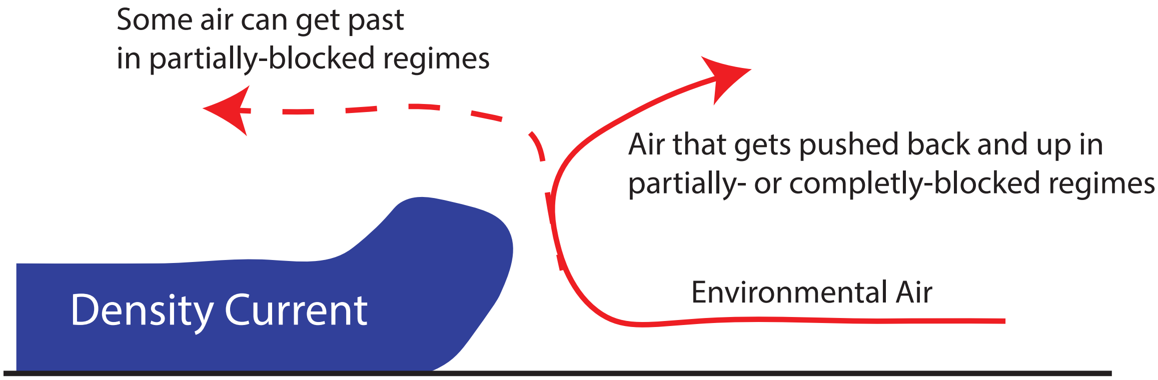

Figure 1.5: Illustration of the partially blocked flow regime (flow follows both the solid red and solid dashed line) and the completely blocked flow regime (flow follows the solid red line).

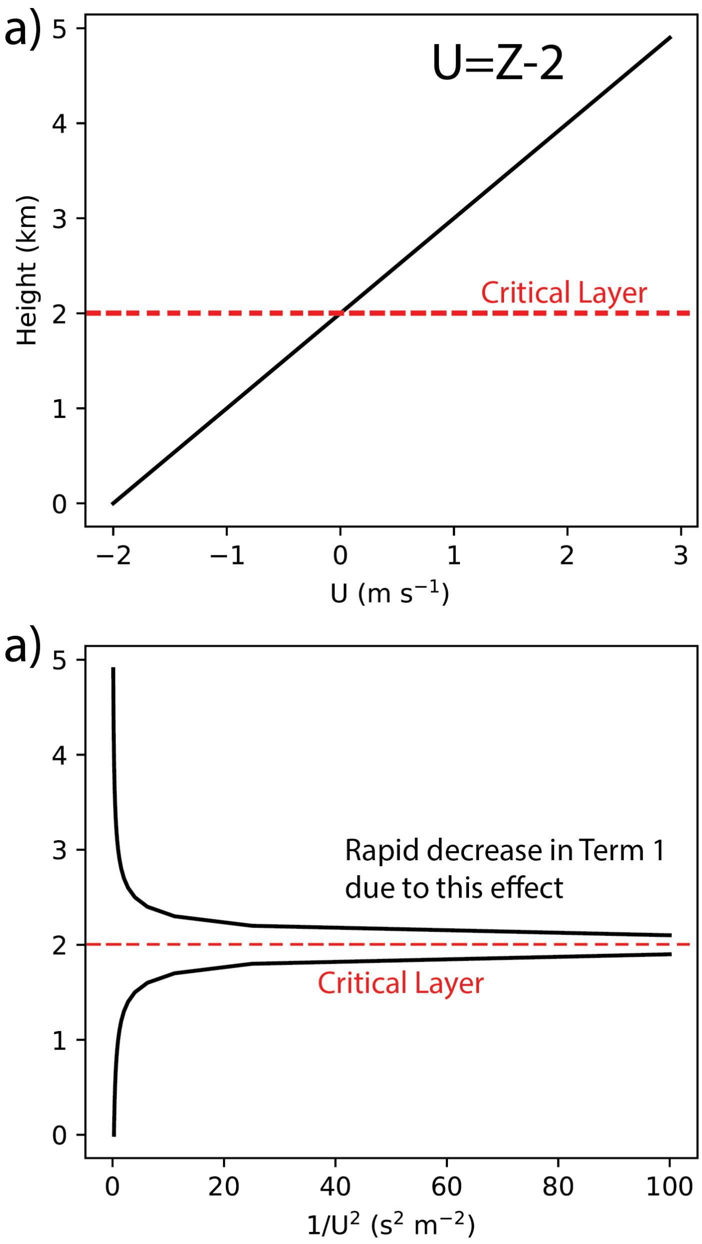

Figure 1.6: (a) Wind speed (m s^{-1}) as a function of height where $U = z - 2$ and (b), 1/U^2 as a function of height. The system-relative wind speed increasing as a function of height is seen in (a) (assuming that $c = 0$) and there is a critical layer at $z = 2$km AGL. The red dashed line denotes this critical layer. There is a rapid decrease with height of 1/U^2 above this critical layer and this effect contributes to the rapid decrease with height in the Scorer parameter.

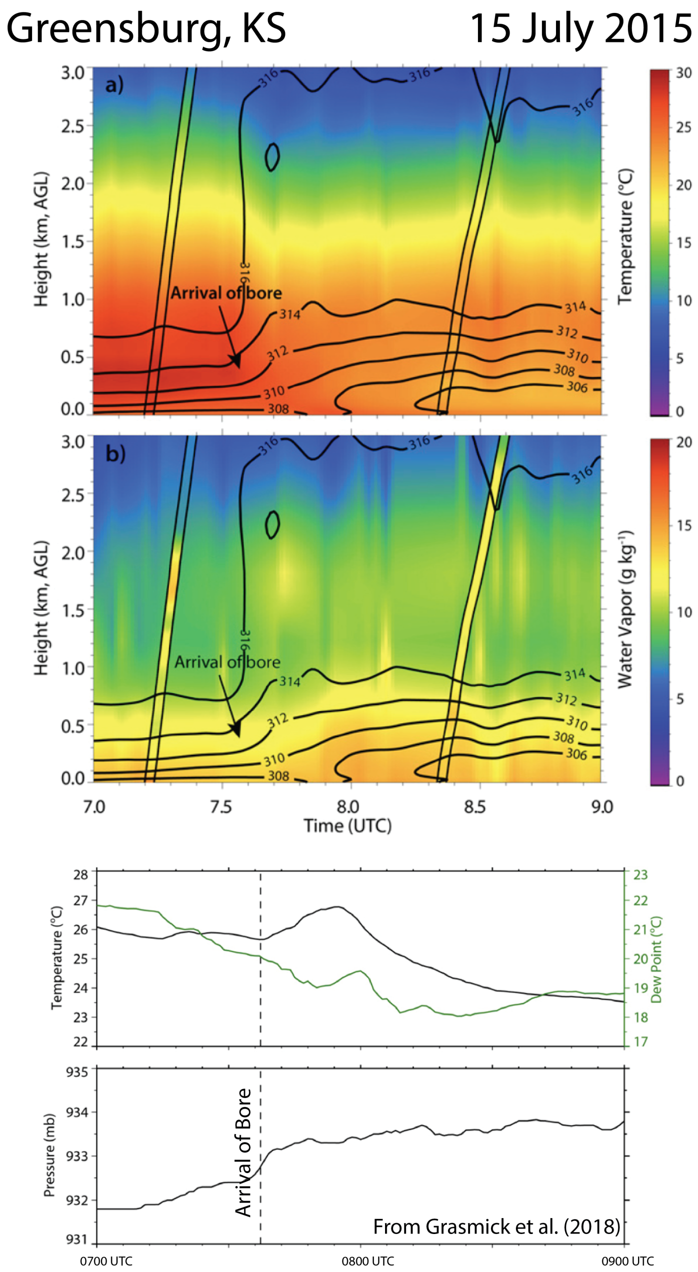

Figure 1.7: (a) AERI temperature (°C) and (b) AERI water vapor mixing ratio (g kg^{-1}) on 15 July 2015 at Greensburg Kansas. (c) Temperature (black line) and dewpoint (green line) and (d) pressure (hPa) at Greensburg, KS. The vertical black dashed line denotes the time of bore passage. Figure from Grasmick et al. (2018).

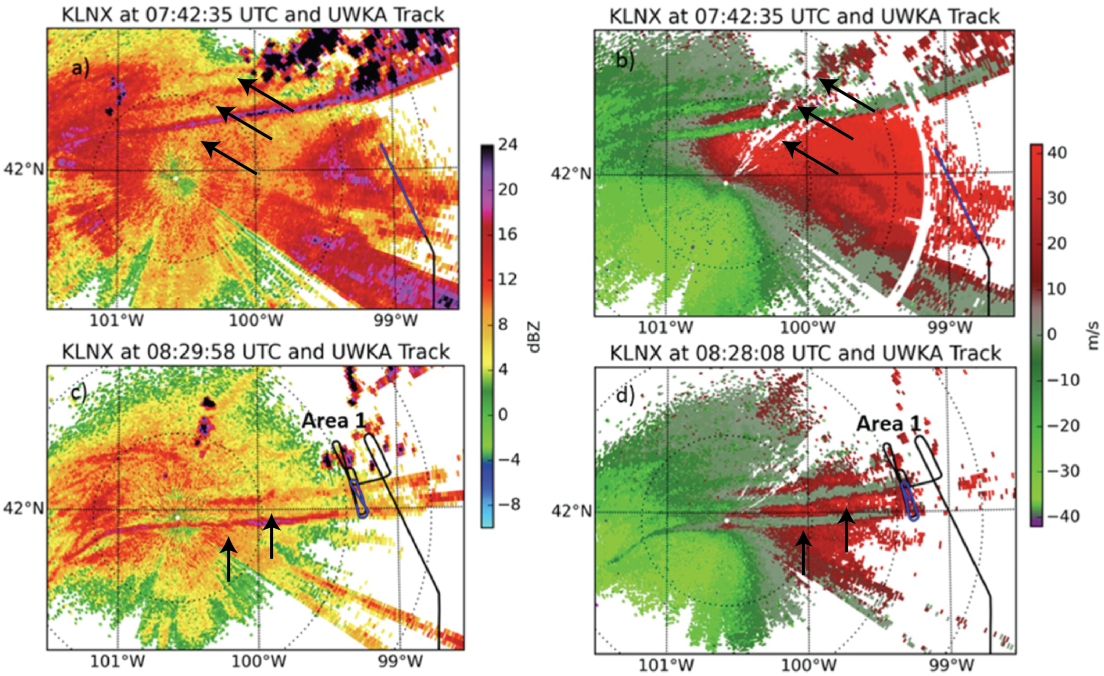

Figure 1.8: (a),(c) Radar reflectively factor (dBZ) and (b),(d), radial velocity (m s^{-1}) for KLNX (North Platte, Nebraska). In (b) and (d), red colors indicate velocity away from the radar and green colors indicate velocity towards the radar. The black arrows point to the parallel fine lines indicating the bore.

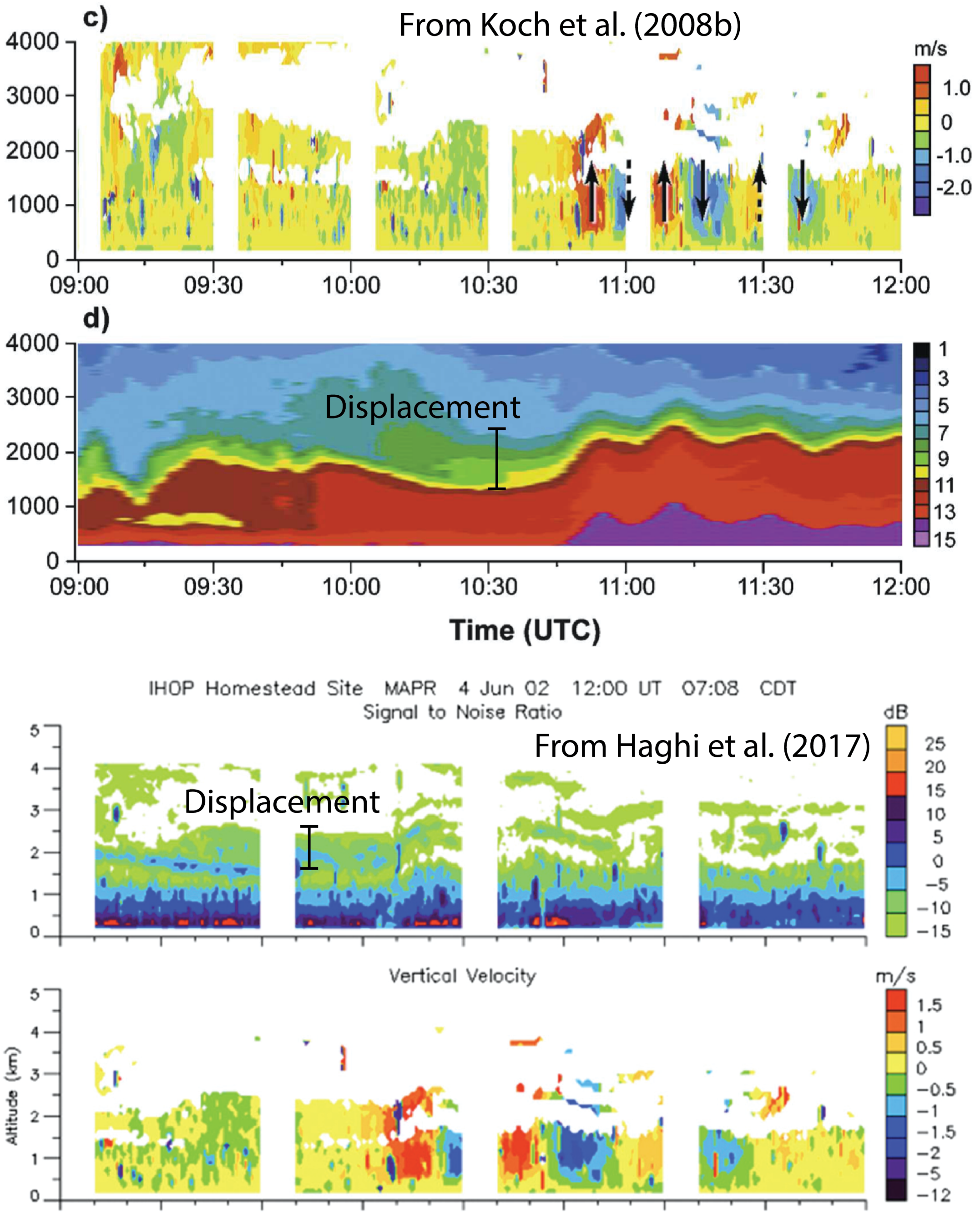

Figure 1.9: (a) Vertical velocity (m s^{-1}) and (b) mixing ratio (g kg^{-1}). (c) Signal-to-noise ratio (dB) and (d) vertical velocity (m s^{-1}). The sustained net displacement is denoted in panels (b) and (c). (a) and (b) from Koch et al. (2008a). (c) and (d) from Haghi et al. (2017).

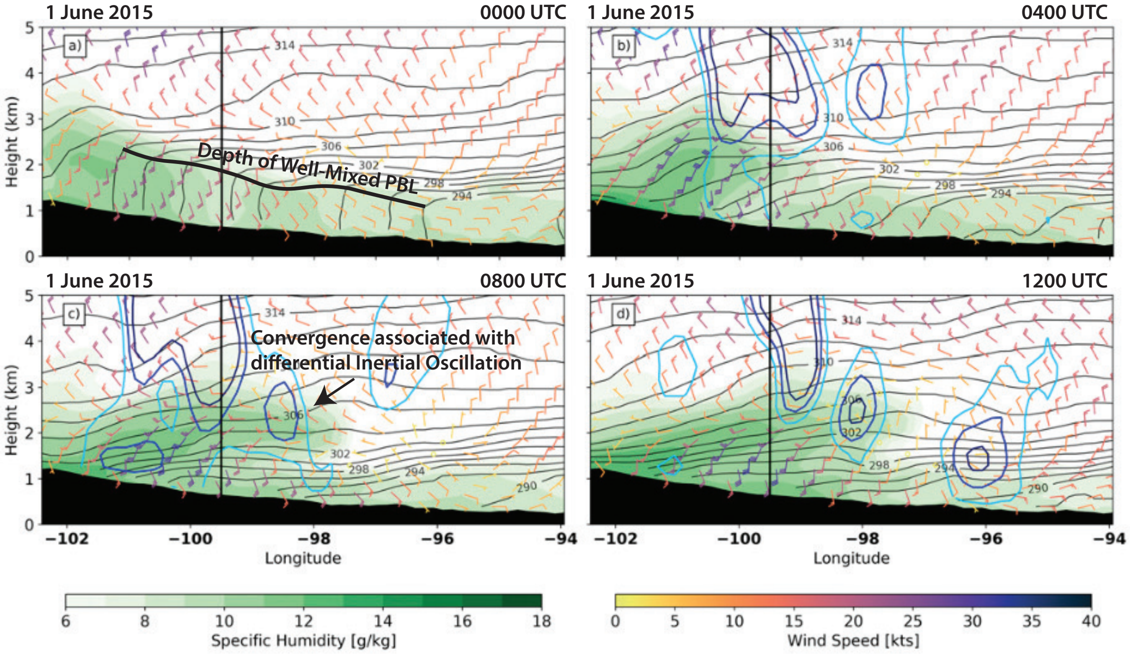

Figure 1.10: Specific humidity (g kg^{-1}; color-filled), potential temperature (black contours), and wind speed (colored barbs) on 1 June 2015 at (a) 0000 UTC, (b) 0400 UTC, (c) 0800 UTC, and (d) 1200 UTC. The horizontal convergence is contoured in blue.

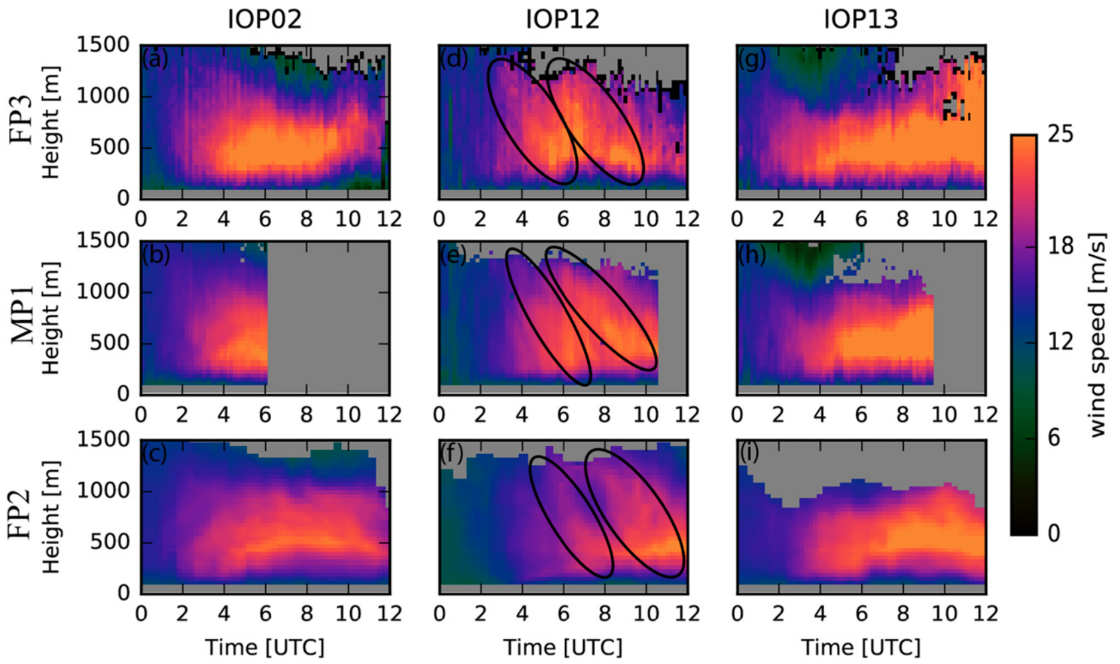

Figure 1.11: Wind speed (m s^{-1}) observed during PECAN on 3 June 2015 (IOP02), 20 June 2015 (IOP12), and 22 June 2015 (IOP13). The black ovals indicate the diagonal striations. Figure from Smith et al. (2019).

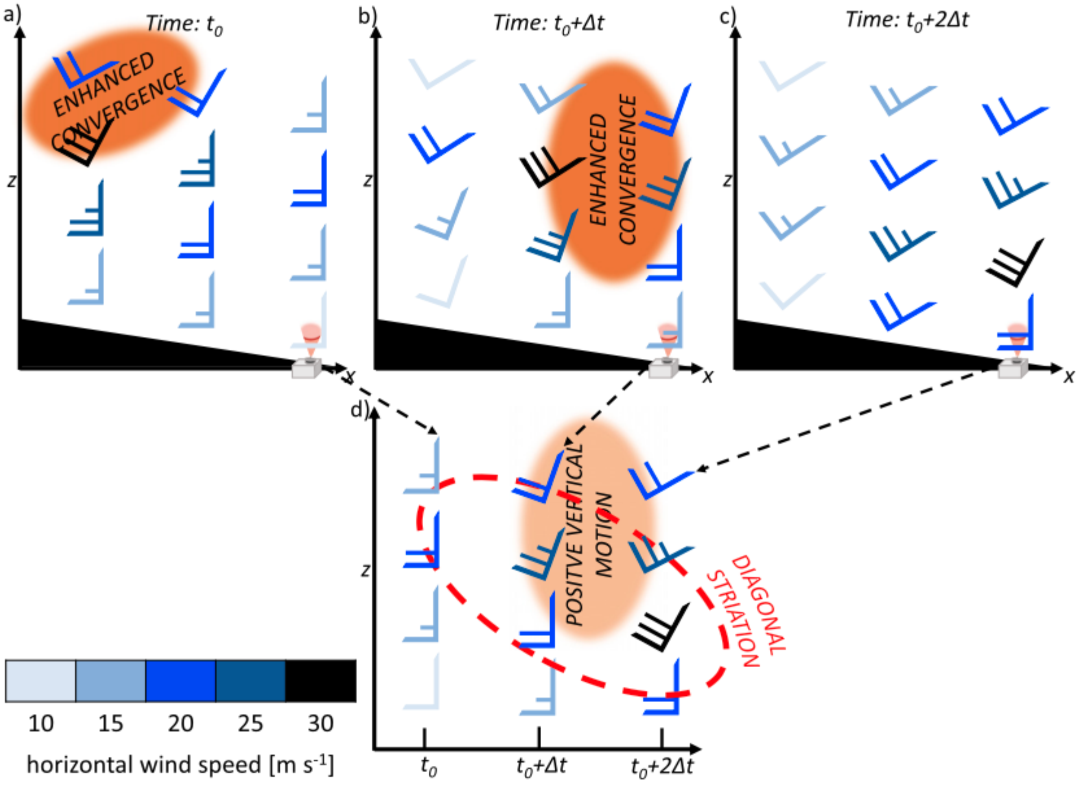

Figure 1.12: (a) - (c). Schematic of the development of the diagonal striation. A full barb is 10 m s^{-1} and the enhanced convergence is outlined in the dark-orange ovals. (d) A point profile observed from a Doppler lidar. Note the collocation of the diagonal striation and the enhanced vertical velocity. Figure from Smith et al. (2019).

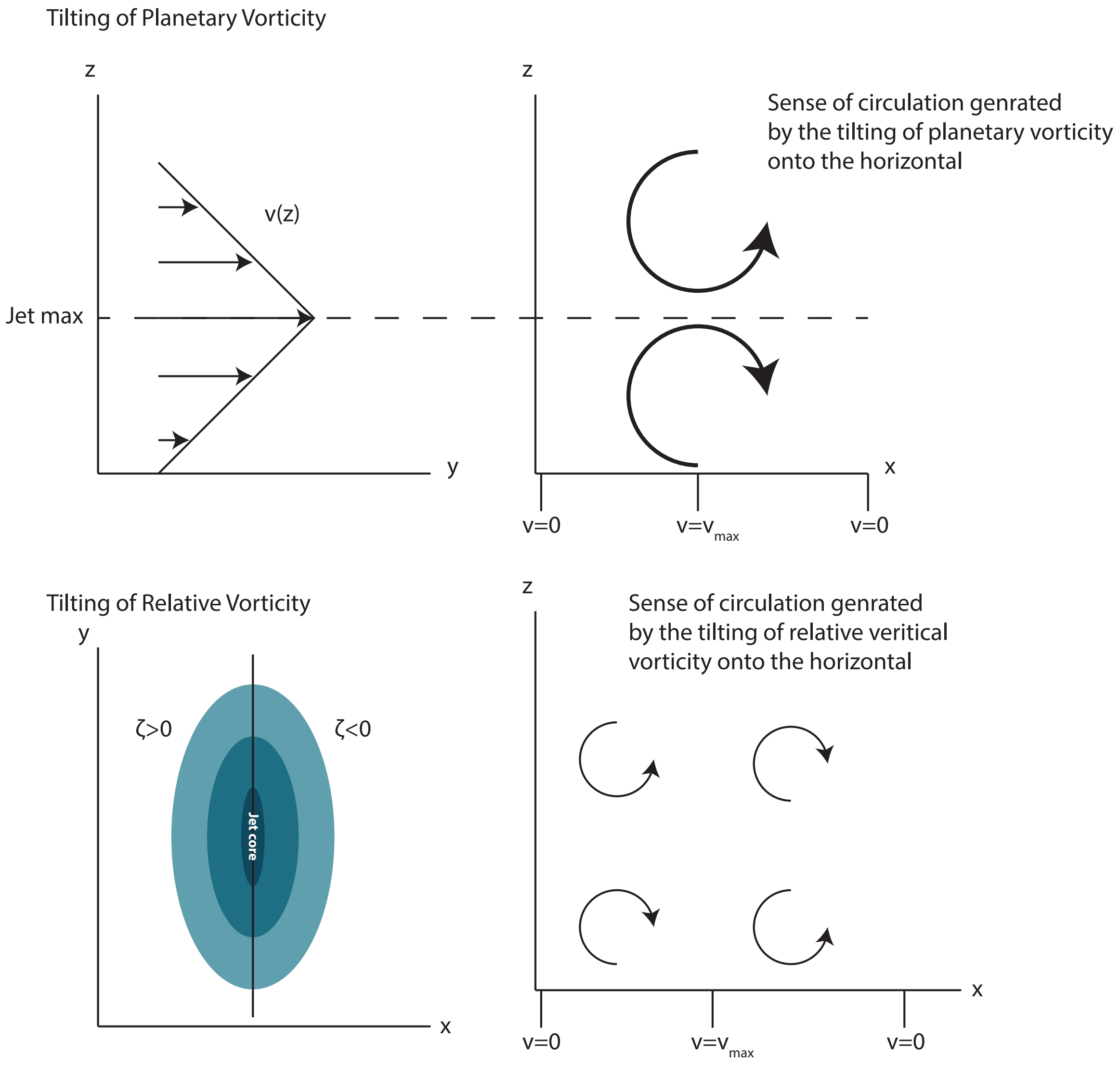

Figure 1.13: Top row: illustration of the tilting of planetary vorticity onto the horizontal. Bottom row: illustration of the tilting of relative vertical vorticity onto the horizontal. Curved arrows indicate the sense of the circulation, and the colors in the bottom row indicate the wind speed (darker colors indicate stronger wind speeds).

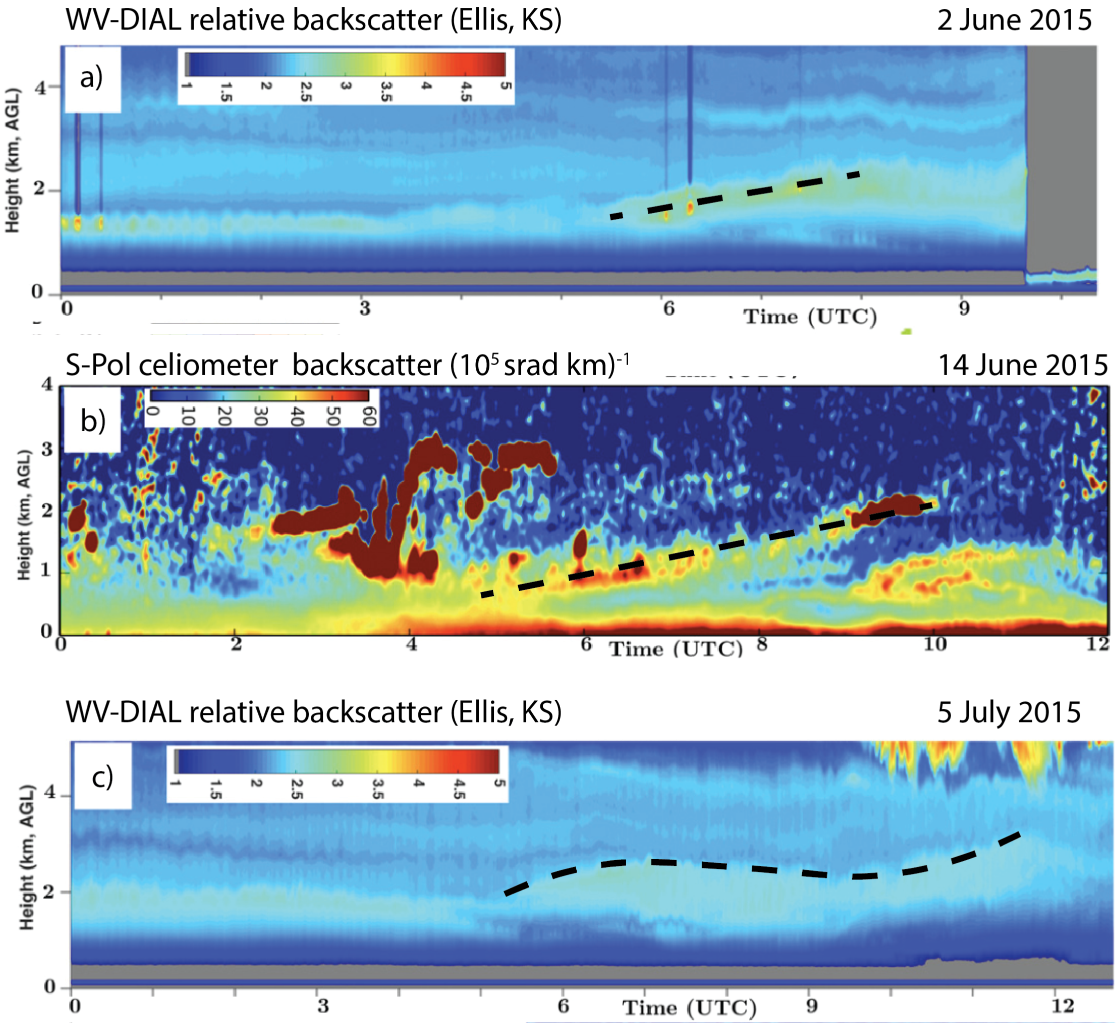

Figure 1.14: (a) 2 June 2015, WV-DIAL backscatter (b) 15 June 2015 celiometer baskscatter at S-Pol, and (c) 5 July 2015 WV-DIAL backscatter. The dashed line indicates the implied vertical motion. Figures from Shapiro et al. (2018).

a) 2 June 2015 at 0000 UTC (HRRR)

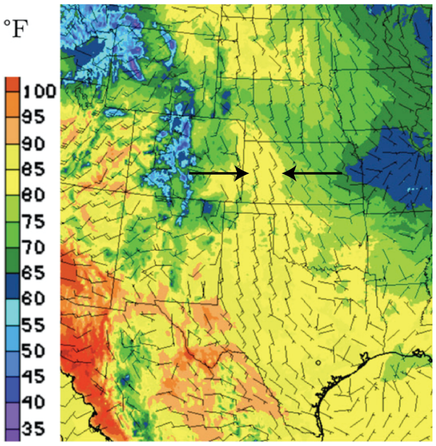

b) 14 June 2015 at 0000 UTC (HRRR)

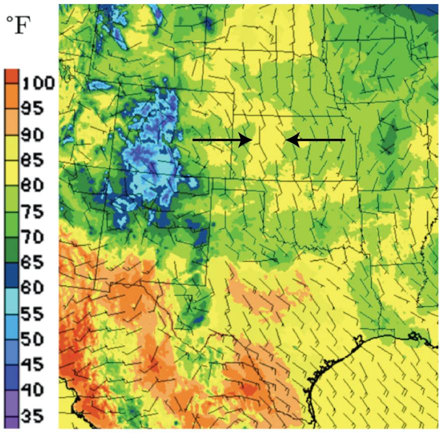

c) 5 July 2015 at 0000 UTC (HRRR)

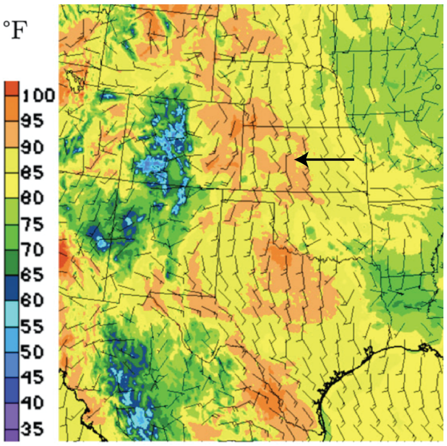

Figure 1.15: HRRR Surface Temperature (°F) at 0000 UTC for (a) 2 June 2015, (b) 15 June 2015, and (c) 5 July 2015. The black arrows indicate the temperature gradient (points to warmer temperatures). Figures from Shapiro et al. (2018).

a) Cyclonic PV Anomaly (Thorpe 1986)

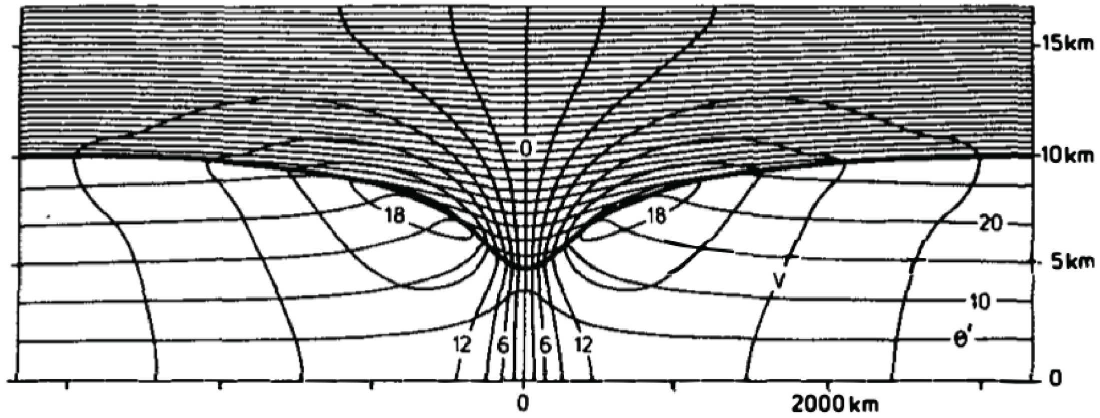

b) Anticyclonic PV Anomaly (Thorpe 1986)

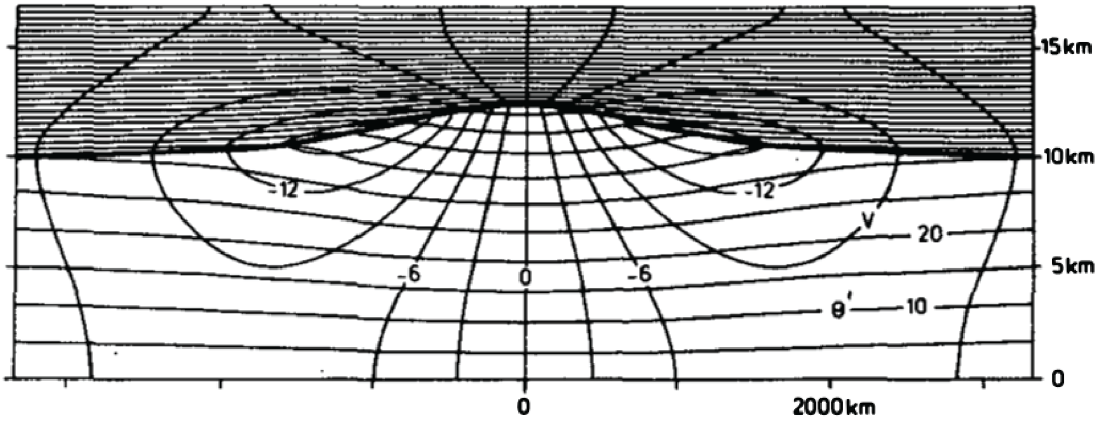

Figure 1.16: Wind speed (contoured; m s^{-1}) and potential temperature (quasi-horizontal contours (K)) for (a) a cyclonic PV anomaly and (b) and anticyclonic PV anomaly. The bold line indicates the dynamic tropopause. From Thorpe (1986) and appeared in Hoskins et al. (1985).

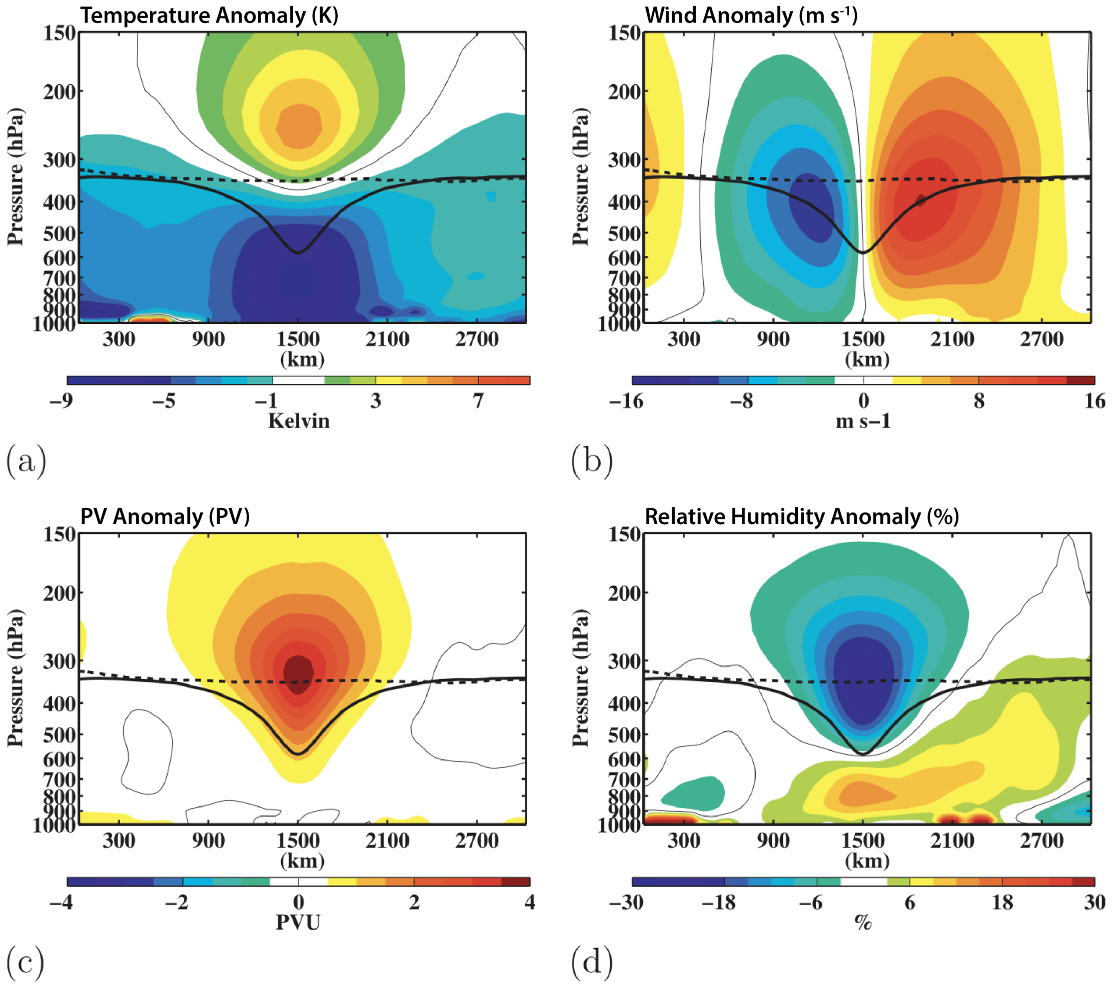

Figure 1.17: West-east cross section of the composite (a) temperature anomaly (K), (b) wind speed anomaly (m s^{-1}), (c) PV anomaly, and (d) relative humidity anomaly (%). Figure from Cavallo and Hakim (2010).

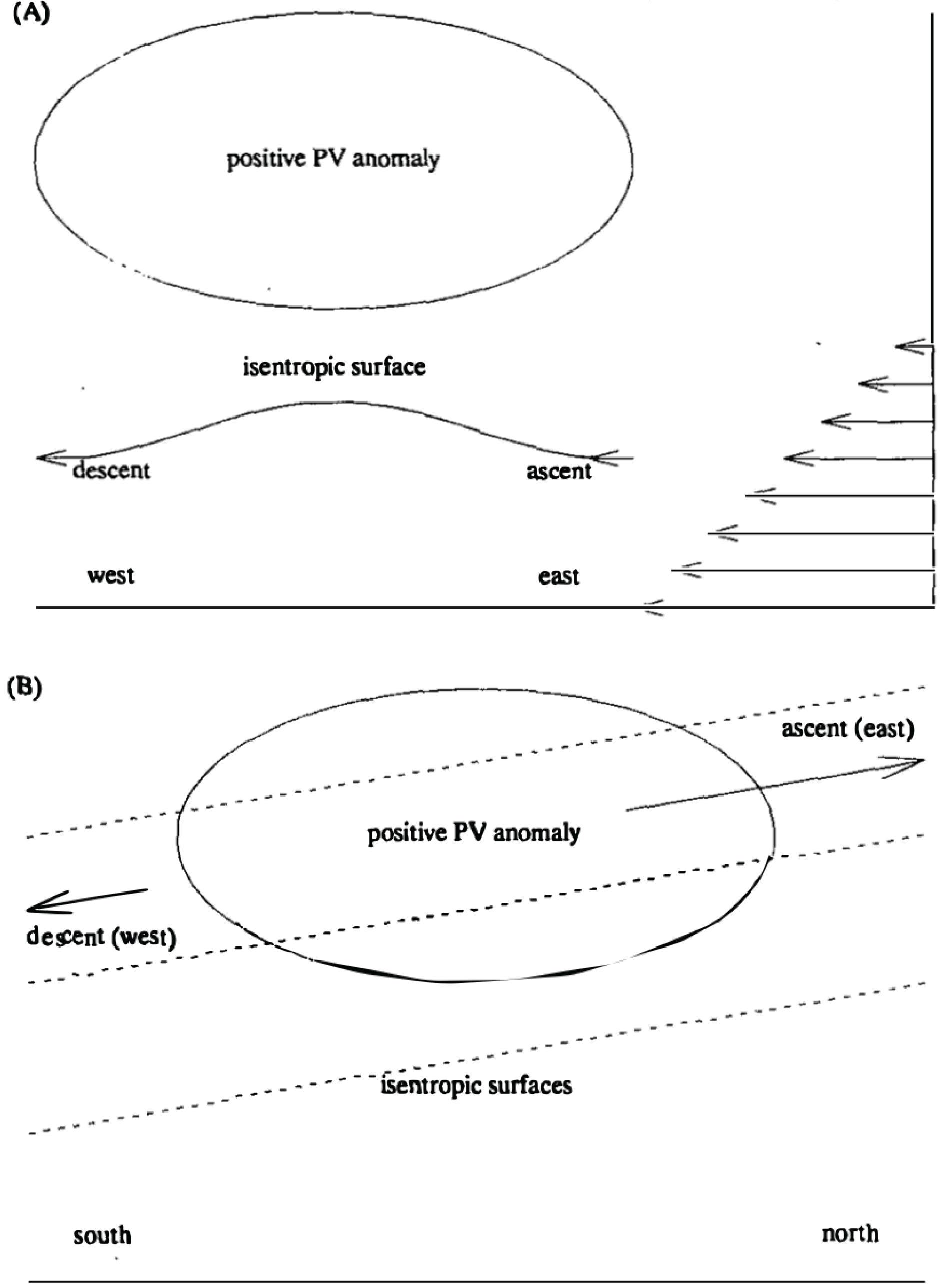

From Raymond and Jiang (1990)

Figure 1.18: (a) West-east cross section of a cyclonic PV anomaly (oval), and isentropic surface near the PV anomaly (below the oval) and the westerly vertical wind shear (the arrows on the right of the panel). (b) A south-north cross section of the same PV anomaly in (a). The dashed lines denote the isentropes. Ascent is downshear (east) of the cyclonic anomaly. Figure from Raymond and Jiang (1990).

Chapter 2

Methods

The gravity wave and LLJ initiation mechanisms will be tested using Cloud Model 1 (CM1; Bryan et al. (2003)), and the PV anomaly initiation mechanism will be tested using the PV inversion technique outlined in Davis and Emanuel (1991). A detailed description of each of these will be found in the following subsections. The goal is to understand how each of these initiation mechanisms can act independently to modify a typical nocturnal environment. Is the modification of the environment enough for CI to occur?

2.1 Idealized Nocturnal Atmospheric Profile

To understand the effect of each of the three initiation mechanisms on a typical nocturnal environment, we must have an environment representative of the NB CI mode events. Proximity soundings from the 20-year climatology in Reif and Bluestein (2017) are used to create a composite sounding. Of the 222 NB CI mode events in that climatology, 208 had a proximity sounding. The proximity sounding is the sounding that is closest in space to the CI location. Because the 1200 UTC soundings are used, the convection had to occur later during the night (i.e., after 0600 UTC). These 208 soundings were examined, and "bad soundings" were removed. These "bad" soundings include those with missing data above a pressure level (usually around 600 hPa), contaminated soundings, and those with too little low-level moisture to warrant inclusion in the composite (Fig 2.1). After filtering out the "bad" soundings, there were 108 soundings left. These remaining 108 soundings were used to create the typical nocturnal environment (Fig. 2.2).

Table 2.1: Low- and mid-level lapse rates (K km^{-1}) and the depth of the low-level lapse rate (km AGL) for the low lapse rate (WT; weak temperature), average lapse rate (AT; average temperature), and high (strong) lapse rate (ST; strong temperature) environments, and the maximum wind speed (m s^{-1}) and its depth for the weak winds (WW), average wind (AW), and strong wind (SW) environments.

Parameter	WT	AT	ST	WW	AW	SW
Low-Level Lapse Rate (K km^{-1})	0.5	11.5	17.5	–	–	–
Mid-Level Lapse Rate (K km^{-1})	0.5	3.5	6.5	–	–	–
Depth of low-level lapse rate (km)	2	0.9	1.4	–	–	–
Wind Maximum (m s^{-1})	–	–	–	3.5	10	16.5
Height of Wind Maximum (km)	–	–	–	1	1	1

The process to create the composite sounding is based on Parker (2014), which includes an adjustment to the height to account for differences in the surface elevation (from Gal-Chen and Somerville (1975)). This adjustment is given by

$$z^* = H\frac{z - z_{sfc}}{H - z_{sfc}} \tag{2.1}$$

where z^* is the adjusted height, z_{sfc} is the surface elevation, and H is 12 km. Pressure is then calculated using the hypsometric equation, assuming a surface pressure of 1000 hPa. This calculation allows for the composite to be averaged over pressures rather than heights. After this adjustment, the sounding is interpolated to 175 pressure levels between 1000 hPa and 50 hPa (the same levels for all 108 soundings). Once that interpolation and averaging are completed, the data are averaged over these pressure levels, creating the composite sounding for NB CI mode events.

This composite sounding represents the average nocturnal environment for the NB CI mode events. A better representation of the nocturnal profile would be to create a composite for LLJ-related events and gravity-wave-related events. However, one would need to be able to state which mechanism initiated each event. The uncertainty of which mechanism initiated each event due to the radar data's resolution, the availability of surface and upper air data, and the availability of infrared satellite data make creating these separate composites challenging. Nonetheless, these mechanism-specific composites would aid in the understanding of how conducive each environment is to CI.

These idealized numerical simulations will be conducted over nine environments to test the three initiation mechanisms' effect on various environments, not just on the typical nocturnal environment. There are three variations on the initial wind speed and three variations on the initial temperature. The mean and standard deviation of the potential temperature, the lapse rate, and the u- and v-wind components are computed from these 108 soundings (assuming the curves follow a Gaussian-like distribution; Fig. 2.4). These nine environments are created from the mean and standard deviation (see Fig. 2.3 for a visual of the mean and standard deviation of the variables in the nine environments).

Using the mean and ± 1 standard deviation temperature profile resulted in a shift of the curve. There was little-to-no change in the lapse rates of these shifted temperature profiles. Because the static stability is more important when assessing a parcel's CI potential (i.e., strong stability will inhibit parcels lifted from that layer or below), the temperature was computed using the mean and ± 1 standard deviation lapse rates. This difference in the temperature profile is seen in Figure 2.5.

The characteristics (depth of the stable layer, mid-level $\frac{\partial \theta}{\partial z}$, etc. . .) are listed in Table 2.1. Note that the mid-level lapse rate of 0.0035 K km^{-1} corresponds well with the value used in the Shapiro et al. (2018) analysis of the LLJ.

2.2 Idealized Numerical Simulations: Cloud Model 1

CM1 is a three-dimensional, non-hydrostatic cloud model used for idealized numerical simulations. This study will utilize CM1 to simulate the effects of gravity waves (specifically atmospheric bores) and the nocturnal LLJ on typical nocturnal environments. For both mechanisms, the atmosphere and the soil are dry. This lack of moisture will allow us to simplify the simulations further and avoid erroneous convection that might be produced. To keep the simulations and their analyses as simple as possible, we are primarily concerned with analyzing vertical motion. *The goal is not to produce CI in these models, but to analyze if the ascent produced in these dry environments is enough for CI in a moist environment.* While moisture can have a large impact on the potential for CI to occur, that impact will be discussed using analyses of composite and real soundings, not CM1 simulations. Early tests of the simulation were conducted with moisture. For the gravity wave simulations, the initial dam break produced large vertical velocity. CI formed almost instantaneously, inhibiting bore generation and limiting the analysis of the bore's potential for CI. In the LLJ simulations, the CBL was shallower, but the LLJ did not develop properly (i.e., there was no jet maximum and the vertical motion was zero). Based on these effects impacting the analysis of vertical motion associated with each mechanism, the simulations were kept dry. The specific configurations will be described in detail in the following subsections.

2.2.1 Atmospheric Gravity Waves

Atmospheric bores can be generated when a density current moves through the low-level stable atmosphere (Crook 1988; Koch et al. 1991; Knupp 2006; Haghi et al. 2017). In these simulations, there is an initial cold block that has a constant potential temperature perturbation. This dam-break problem will result in a density current that moves through the low-level stable layer defined by the composite sounding, generating a bore in these idealized simulations. The initial cold block has a constant potential temperature perturbation (similar to that done by Hutson et al. (2019)).

There needs to be some way to trap the wave energy from leaking upwards (Crook 1988). A rapid decrease in the Scorer parameter with height can do this. To satisfy this necessary condition, the wind profile is constructed to promote this decrease and is given by:

$$v(z) = v_{max} * \sin(2z) * e^{\frac{z}{-\pi/3}} * 1.75 \tag{2.2}$$

where v_{max} is the maximum wind speed denoted in Table 2.1, and z is the height in km (Fig. 2.7). The factor of 1.75 is an adjustment to get the maximum wind speed close to v_{max}.

This wind profile and the stability profile supports a rapid decrease in the Scorer parameter at 1.5 km above the surface (Fig. 2.9). This wind profile is similar to, but not the same as, the wind profile in Crook (1988). This profile is based on the typical nocturnal environment, except that the wind direction is unidirectional and southerly. Which terms contribute most to this rapid decrease in these profiles? The Brunt-Väisälä Frequency rapidly decreases at 900 m AGL (the height of the inversion; Fig. 2.81). There is a rapid decrease at 1.5 km in both Term 1 and Term 1 of equation 1.1. Based on this rapid decrease of the Scorer parameter near 1.5 km AGL, wave trapping is expected below this level.

Because of the short wavelength of atmospheric bores (10-20 km), a horizontal grid spacing of 500 m is chosen to resolve these waves. Previous studies have suggested that a horizontal grid spacing of less than 4 km is necessary to resolve atmospheric bores (e.g., Koch et al. 2008a; Martin and Johnson 2008; Chipilski et al. 2018, and the horizontal grid spacing here is similar to that used in the modelling studies of Crook (1988) and Haghi and Durran (2020). Furthermore, a fine vertical grid spacing (25 m) is chosen to resolve fine-scale features in the vertical (see Table 2.2 for more details on the model setup).

The simulation is run for three hours. Due to this limited duration and the relatively small domain size, the cold block is placed at the north edge of the domain. Otherwise, the bore would propagate out of the domain, and the domain would need to be larger (increasing the computation time and file size) to accommodate the bore. Open lateral boundary conditions are used to avoid reflection of features (waves, density currents, etc...) off these lateral boundaries. Rayleigh damping exists at the top of the model (Klemp et al. 2008), starting at 12 km above the surface, preventing waves from reflecting off the model top.

There is no boundary-layer scheme, no surface-layer scheme, no convective scheme, no radiation scheme, and no microphysics scheme in these simulations, and the simulations are dry. This lack of parameterization schemes and moisture keeps the simulation as idealized as possible to identify bores' effect on the nocturnal environment. Due to the simplicity of simulating with no physics parameterizations, some important features are not simulated. These features include cooling due to radiation loss, the spatiotemporal evolution of the LLJ, and temperature and moisture advection. However, the effect of some of these features is present in these simulations. There is a stable layer and an LLJ, but the model is initialized with them already present. A reasonable simulation of atmospheric bores does not require a correct representation of the spatiotemporal evolution of the LLJ, only that there is an LLJ. Neglecting the spatiotemporal evolution of the LLJ will not significantly impact the simulation of the atmospheric bores.

Finally, the model is initialized with 50-m thick layers of passive tracers at three levels: between 100 and 150 m, between 675 and 725 m, and between 1475 and 1525 m. The addition of these passive tracers will help in the analysis of vertical motion and the net displacement of parcels associated with bores' passage. These tracers will act as a scattering layer, and the net displacement of parcels can be analyzed using the net displacement of these passive tracers.

2.2.2 Nocturnal Low-Level Jet

One important feature of the LLJ is the inertial oscillation of the ageostrophic wind as turbulent mixing shuts down. To simulate this feature, we need to run these simulations over one diurnal cycle to capture this shutdown at sunset. In these LLJ simulations, all the parameterization schemes are turned on (except for the convective parameterization). The radiation scheme must be turned on to simulate the diurnal cycle. In CM1, a microphysics parameterization must be used in conjunction with the radiation scheme. To avoid complications due to water vapor, all moisture (in the atmosphere and the soil) is

Table 2.2: CM1 model specifications for the gravity wave simulations

Parameter	Value
Horizontal Grid Points (x and y)	1000
Vertical Grid Points	120
Horizontal Grid Spacing	500 m
Vertical Grid Spacing	25 m (stretched to 650 m starting at 2 km to 15.5 km)
Coriolis Parameter	None
PBL Scheme	None
Microphysics Scheme	None
Radiation Scheme	None
Convection Parameterization	None
Lateral Boundary Conditions	Open
Cold Block $\theta^{'}$	-10 K (constant)
Cold Block Diameter	200 km
Cold Block Depth	1.5 km

Table 2.3: “Cropland/Grassland Mosaic” used in the CM1 simulations. Note that the soil moisture availability is set to zero. The original value is in parenthesis.

Albedo (%)	18
Soil Moisture Availability ($\times$ 100%)	0.00 (0.25)
Surface Emissivity (%)	0.98
Roughness length (cm)	14
Thermal Inertia ($\times$ 4.184 $\times$ 10^2 J m^{-2} K^{-1} $s^{-1/2}$)	4
Factor for Albedo Modification with Snow	2.56
Surface Heat Capacity (J m^{-3} K^{-1})	25 $\times$ 10^5

removed. The governing equations are similar to those without moisture, even though the microphysics parameterization scheme is active (Bryan 2016). A representative land surface is also needed. According to the United States Geological Survey, two common land use categories over the Great Plains are “agriculture” and “grassland” (available at https://www.usgs.gov/apps/landcarbon/categories/land-use/download/). This study will utilize the “Cropland/Grassland mosaic” land surface type (Table 2.3).

The Yonsei-University (YSU; Hong et al. (2006)) PBL scheme is a non-local scheme, meaning that variables at any level within the PBL can affect that variable. In the case of a local scheme, only the variables at levels adjacent to a point affect the variables at that point. This non-local aspect is generally considered favorable in representing the convective boundary layer since they account for countergradient fluxes (i.e., those opposite to the direction of the downward heat fluxes). The advantage of the YSU scheme is that it explicitly represents the entrainment at the top of the PBL. However, it tends to overmix the daytime PBL, especially in the warm season, resulting in PBLs that are too deep and too dry (Cohen et al. 2015). Smith et al. (2018) tested three schemes and showed that the simulation of the LLJ is less sensitive to the choice of the PBL scheme than the grid spacing. They showed that the quasi-normal scale elimination scheme (QNSE; Sukoriansky et al. (2005)), a local scheme, performed the best in simulating the SBL and the LLJ. An improvement to this study would be to add the QNSE scheme to CM1 for more accurate simulations of the SBL and the LLJ, but adding a new PBL scheme to CM1 is outside the scope of this study.

The surface layer is the lowest portion of the PBL (closest to the surface), and in these simulations, a surface-layer scheme is necessary to account for fluxes between the atmosphere and the surface. CM1 has two surface-layer schemes, one based on the MM5 scheme which is based on Monin-Obukhov similarity theory, and a revised version of that scheme to better account for strongly stable and unstable conditions (Jiménez et al. 2012). Because of this more-accurate representation of variables at night under strongly stable conditions, the revised surface layer scheme is chosen. A summary of the parameterization schemes and model parameters is given in Table 2.4.

The sloping terrain is thought to be an important in determining the LLJs location (Holton 1967; Shapiro and Fedorovich 2010; Shapiro et al. 2016), but an LLJ can still be simulated without an explicit representation of the sloped terrain (Shapiro et al. 2018). To keep this simulation simple, there is no slope to the surface. Adding the slope would complicate the analysis and simulations too much for a proper analysis. However, the buoyancy gradient due to differential heating along the slope is simulated. This gradient is achieved by placing a "heating pad" at the lowest three model levels during the daytime. A sinusoidal weighting function is applied during the day, and there is no heating at night. A schematic of this heating is shown in Fig. 2.6. Shapiro et al. (2018) showed that a surface temperature gradient of 1 K $(100 \text{ km})^{-1}$ over the Great Plains can exist and is important to vertical motion over the LLJ. This gradient will be simulated by applying this heating pad. The lack of PBL schemes and this arbitrary heating will likely result in unintended consequences in these simulations. These consequences and their potential impact on the results will be discussed in Chapter 5.

Table 2.4: CM1 model specifications for the low-level jet simulations

Parameter	Value
Horizontal Grid Points (x)	300
Horizontal Grid Points (y)	304
Vertical Grid Points	220
Horizontal Grid Spacing	3000 m
Vertical Grid Spacing	25 m (stretched to 450 m starting at 4 km to 18.25 km)
Coriolis Parameter	Yes
PBL Scheme	YSU
Surface-Layer Scheme	“Revised” surface-layer scheme (Jimenez et al. 2012)
Microphysics Scheme	Morrison double-moment scheme
Radiation Scheme	RRTMG
Convection Parameterization	None
Lateral Boundary Conditions	Open
Land Use Index	5 (Cropland/Grassland Mosaic)

The simulation begins at 12 UTC and ends at 12 UTC the next day, resulting in one diurnal cycle. There is a jet-like profile defined in the initial conditions, but it is horizontally homogeneous. Differential heating associated with the heating pad creates horizontal inhomogeneity during the daytime, creating horizontal temperature and pressure gradients. The lateral boundary conditions are open to avoid features coming back into the domain and interacting with itself, and Rayleigh damping is applied in the vertical above 12 km.

The model domain is 900 km by 900 km horizontal, a longitudinal extent representative of the Great Plains. Smith et al. (2018) showed that there was no significant difference in simulations of the wind field when using a fine grid spacing (1 km) than when using a coarser grid spacing (4 km). The wind maximum's location and strength were poorly represented with a 1 km spacing than by the 4 km spacing, though the jet's strength was underestimated using both grid spacings. They concluded that there was no direct benefit to using the 1 km grid spacing over the 4 km grid spacing. There was an improvement to the temporal evolution and vertical structure of the LLJ when using finer vertical grid spacing. Based on their study's results, these simulations of the LLJ use a 3 km horizontal grid spacing and a 25-m vertical grid spacing (stretched to 450 m starting at 4 km AGL).

The average lapse rate of 3.5 K km^{-1} was too strong for any substantial vertical motion at night, so the mid-level lapse rate is reduced from those in Table 2.1. In these simulations, the low lapse rate is 1 K km^{-1}, the average lapse rate is 2 K km^{-1}, and the high lapse rate is 3 K km $^{-1}$. These lapse rates fall within the -1 to 0 standard deviation for nocturnal environments, so they represent typical environments.

Twenty-seven simulations are conducted. There are nine simulations for the parameter space (three wind and three lapse rate), and three different heating rates are tested. These simulations allow us to test how the strength of the LLJ is affected by static stability and how vertical motion changes as a result of that strength and static stability. The effect of the baroclinic zone strength is examined by testing the three different heating rates. The heating applied at the surface is chosen to generate a baroclinic zone representative of one over the Great Plains. As a result, the heating rate is not the typical heating rate over the Plains. During the daytime, there is strong mixing throughout the convective boundary layer. The gradual heating with time and the mixing in the simulations act to smooth out the temperature gradient. For example, even if a surface heating rate of 10 K d^{-1} is specified, the temperature will not increase by 10 K because of this mixing. Because the goal is to simulate the temperature gradient, a stronger-than-observed heating is necessary to overcome this mixing. Just as there are likely unintended consequences associated with the lack of PBL schemes, this strong heating may also result in unintended consequences, which will be discussed in Chapter 5.

2.3 PV Inversion

Originally, CM1 was going to be used to create a PV anomaly and diagnose the flow using the idealized numerical simulations. The idea was to generate a PV anomaly diabatically by including a heating bubble in the simulation. However, features such as gravity waves throughout the entire domain resulted from this methodology. These features complicated the simulation to the point where diagnosing vertical motion related to the PV anomaly itself could not be done. Since the goal was to see how a PV anomaly would modify the atmosphere, a simpler approach was needed.

2.3.1 Inversion Technique

PV inversion, a technique described by Hoskins et al. (1985) and Davis and Emanuel (1991), is used to obtain the wind field and potential distribution given an initial PV field. To invert the field, we need a balance condition, a base-state, and we need to solve the problem globally (i.e., solve the entire domain at once). The method outlined by Davis and Emanuel (1991) will be used to invert the PV field and is described here.

Two nonlinear equations are solved iteratively. We will use the Charney (1955) balance condition (also used by Davis and Emanuel (1991)) and is given by the following:

$$\nabla^2\Phi^{(\nu+1)} = \nabla \cdot \; f\nabla\Psi^\nu + 2\left[\frac{\partial^2\Psi^\nu}{\partial x^2}\frac{\partial^2\Psi^\nu}{\partial x^2} - \left(\frac{\partial^2\Psi^\nu}{\partial x\partial y}\right)^2\right] \tag{2.3}$$

where f is the Coriolis parameter, Φ is the geopotential, Ψ is the streamfunction, and ν represents the iteration (we are solving at $\nu+1$). In the case of the first iteration, the initial guesses of Φ and Ψ are used at ν. The initial guesses of Ψ and Φ are taken to be the base state in this study (discussed in Sections 2.3.2 and 6.2). After the first iteration, the previous iteration values of Φ and Ψ are used for ν.

The other equation is the PV distribution and is given by:

$$q = \frac{g\kappa\pi}{p}\left[\left(f+\nabla^2\Psi\right)\frac{\partial^2\Phi}{\partial\pi^2} - \frac{\partial^2\Psi}{\partial\pi\partial x}\frac{\partial^2\Phi}{\partial\pi\partial x} - \frac{\partial^2\Psi}{\partial\pi\partial y}\frac{\partial^2\Phi}{\partial\pi\partial y}\right] \tag{2.4}$$

To make this easier, Equation 2.4 is solved for $\nabla^2\Psi$. This results in

$$\nabla^2\Psi^{(\nu+1)} = \frac{1}{\frac{\partial^2\Phi^{(\nu+1)}}{\partial\pi^2}}\left(\frac{qp}{g\kappa\pi} + \frac{\partial^2\Psi^\nu}{\partial\pi\partial x}\frac{\partial^2\Phi^{(\nu+1)}}{\partial\pi\partial x} + \frac{\partial^2\Psi^\nu}{\partial\pi\partial y}\frac{\partial^2\Phi^{(\nu+1)}}{\partial\pi\partial y}\right) - f \tag{2.5}$$

where g is the acceleration due to gravity, κ is 2/7, π is the Exner function, and p is pressure. Note that ν represents a major iteration, which is how many times Ψ and Φ are updated. Minor iterations are those that are used when solving the Poisson operator in Equations 2.3 and 2.5. The finite differencing methods used to solve the Poisson operators are discussed in Appendix A.

The iteration process is described as follows. First, Equation 2.3 is solved given an initial guess of the streamfunction. Next, Equation 2.5 is solved using the updated geopotential. Once the two equations have been solved, the iteration process continues. The geopotential is updated again using the previous iteration of Ψ, and then that new Φ is used to update Ψ.

It should be noted that after each updated variable is obtained, a successive-overrelaxation is applied to that variable as follows:

$$\Phi^{(\nu+1)} = \alpha\Phi^{(\nu+1)} + (1-\alpha)\Phi^\nu \tag{2.6}$$

In this study, $\alpha = 0.7$. According to Davis and Emanuel (1991), this successive-overrelaxation helps the system converge faster.

This process is repeated until the system converges to some condition. The convergence condition used in this study is when the difference between the new iteration and the previous iteration is less than some condition. In Davis and Emanuel (1991), this convergence condition is 1 $\mathrm{m}^2\ \mathrm{s}^{-2}$, and for Ψ, this condition is $1\times10^4\ \mathrm{m}^2\ \mathrm{s}^{-1}$. After 475 iterations, the difference between the new Φ and the previous Φ is 0.11, and the difference between the new Ψ and the previous Ψ is 1371. While both of these are an order of magnitude less than the convergence condition in Davis and Emanuel (1991), a lower convergence condition is necessary in this study due to the highly idealized nature of the field and the smaller grid spacing. A better convergence condition is a percentage difference due to the variation in the fields. In this study, the convergence condition is when this percent difference is less than 0.2% for both Φ and Ψ, and it is based on where this difference starts to level off for both variables (Fig. 2.10).

To solve the Poisson operators, Neumann boundary conditions are applied to the top and bottom as follows:

$$\frac{\partial \Phi}{\partial \pi} = f_0 \frac{\partial \Psi}{\partial \pi} = -\theta. \tag{2.7}$$

Dirichlet boundary conditions are applied to the lateral boundaries. These boundary conditions are specified by the base-state fields.

Once the system of equations converges, then we can compute the wind field and potential temperature from the following:

$$u = -\frac{\partial \Psi}{\partial y} \tag{2.8}$$

$$v = \frac{\partial \Psi}{\partial x} \tag{2.9}$$

$$\theta = -\frac{\partial \Phi}{\partial \pi} \tag{2.10}$$

2.3.2 Anomaly Creation

Creating the PV anomaly itself is important to the success of the inversion technique. For example, if the background lapse rate is weak and a strong anomaly is inserted, then the inversion may become numerically unstable. To keep this process as simple as possible, there is no low-level stable layer and the magnitude of the PV anomalies must allow for the inversion technique to maintain stability. Five tests are performed. A weak anomaly in a weak, average, and high lapse-rate environment, an average anomaly in an average lapse-rate environment, and a strong anomaly in a high lapse-rate environment. The lapse rates are the lapse rates of the average nocturnal environment (see Table 2.1) and the anomalies are 1, 2, and 3, PVU (representing the range seen in Table 1.2). Due to numerical instability associated with inverting the flow of a strong anomaly in a weak lapse-rate environment (and other scenarios with strong gradients), only five anomalies are tested instead of nine.

The environment is constructed to maintain the Neumann conditions at the top and bottom boundaries. There is no wind inside the domain, which does pose problems when defining the initial streamfunction. However, since the entire field is zero and vertical gradients of the streamfunction do not matter except for the Neumann condition, the initial streamfunction is horizontally homogeneous and satisfies the Neumann conditions. The domain is much larger than the anomaly, so the geopotential and streamfunction fields at the lateral boundaries are not impacted by the anomaly.

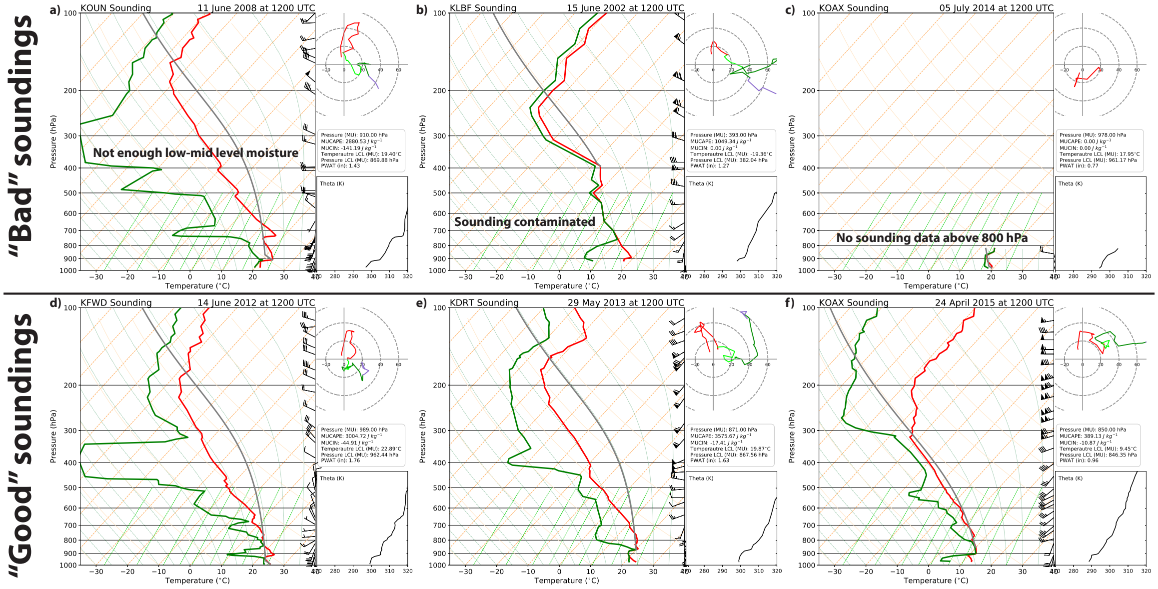

Figure 2.1: (a) (b) and (c) are examples of "bad" soundings not included in the composite. (d), (e), and (f) are examples of "good" soundings included in the composite.

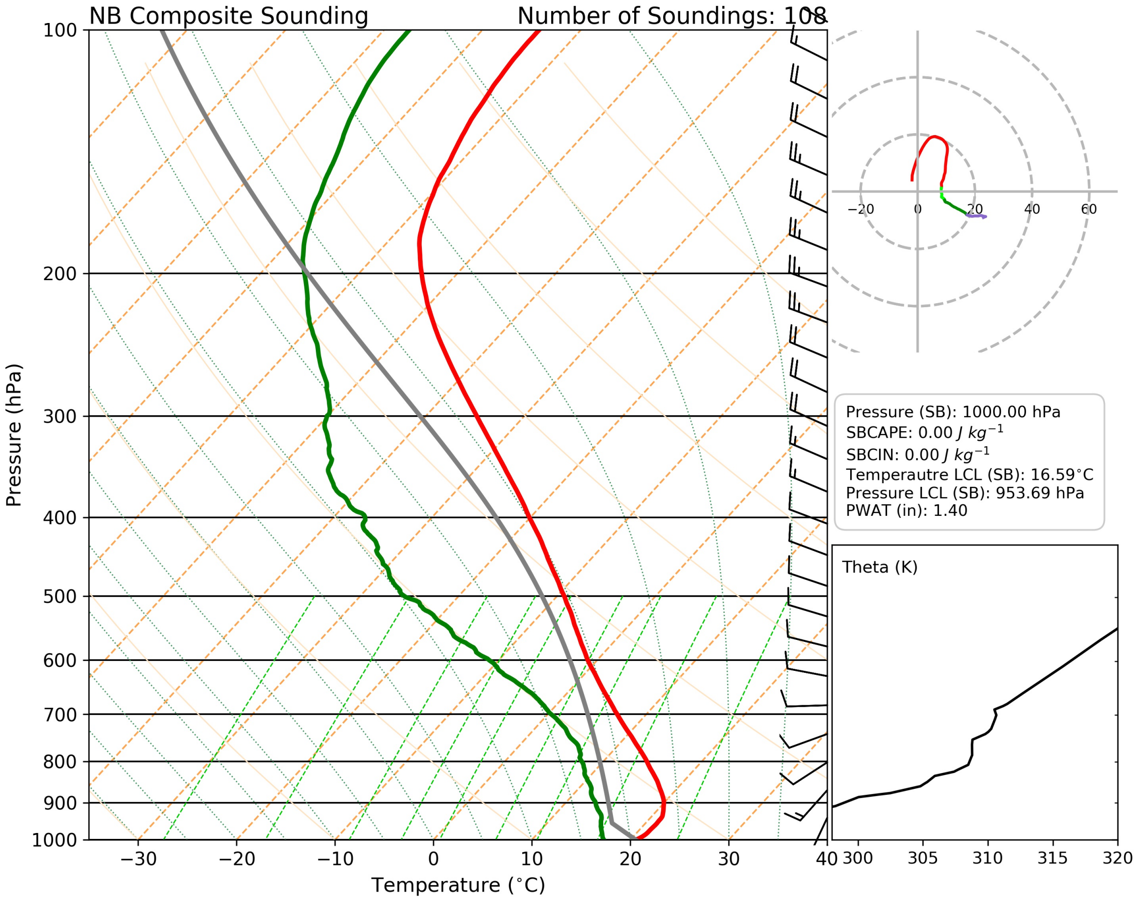

Pressure (SB): 1000.00 hPa
SBCAPE: 0.00 $J\ kg^{-1}$
SBCIN: 0.00 $J\ kg^{-1}$
Temperautre LCL (SB): 16.59°C
Pressure LCL (SB): 953.69 hPa
PWAT (in): 1.40

Figure 2.2: The NB CI mode composite sounding. The hodograph is in m s^{-1}.

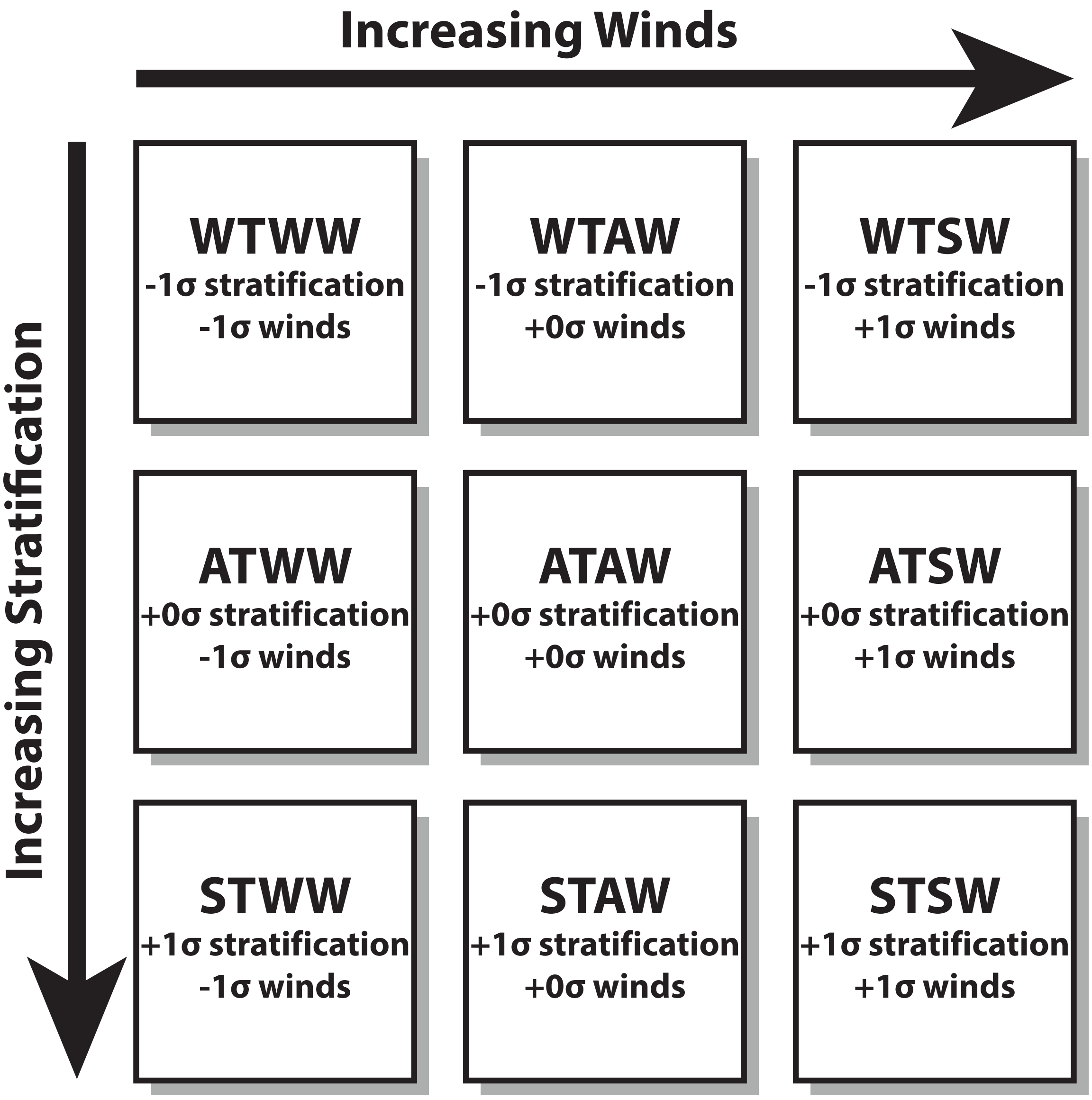

Figure 2.3: The nine nocturnal environments created. The strength of the winds increase from left to right and the environmental stratification increases from top to bottom.

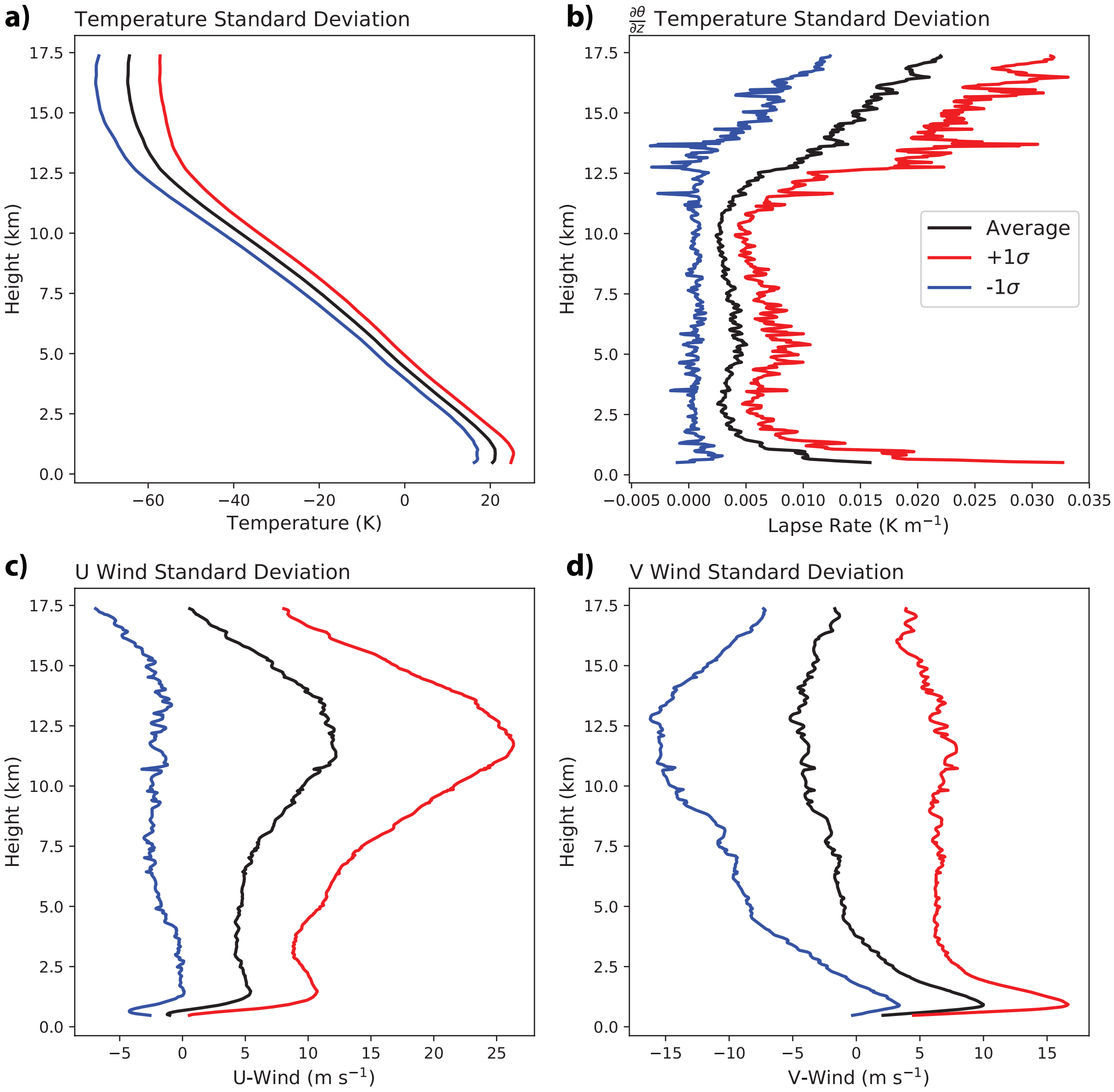

Figure 2.4: The +1 σ (red curves), average (black curves), and -1 σ (blue curves) for (a) temperature, (b) $\frac{\partial\theta}{\partial z}$, (c) u-wind component, and (d) v-wind component from the composite sounding in Fig. 2.2.

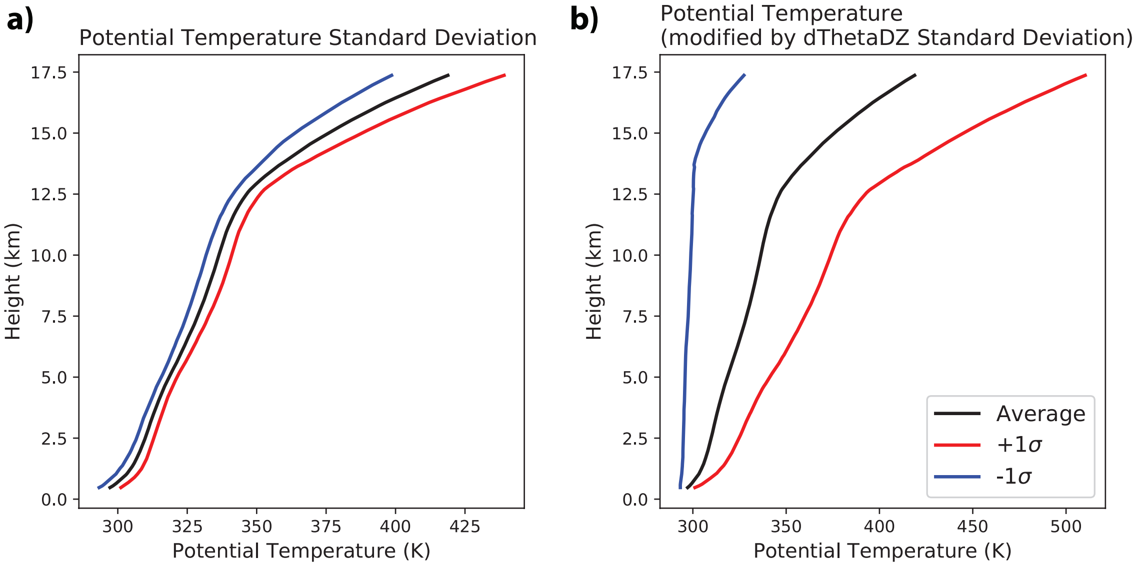

Figure 2.5: (a) Potential temperature computed from the ±1 σ temperature, and (b) potential temperature computed from the ±1 σ lapse rates. Lines are as in Fig. 2.2.

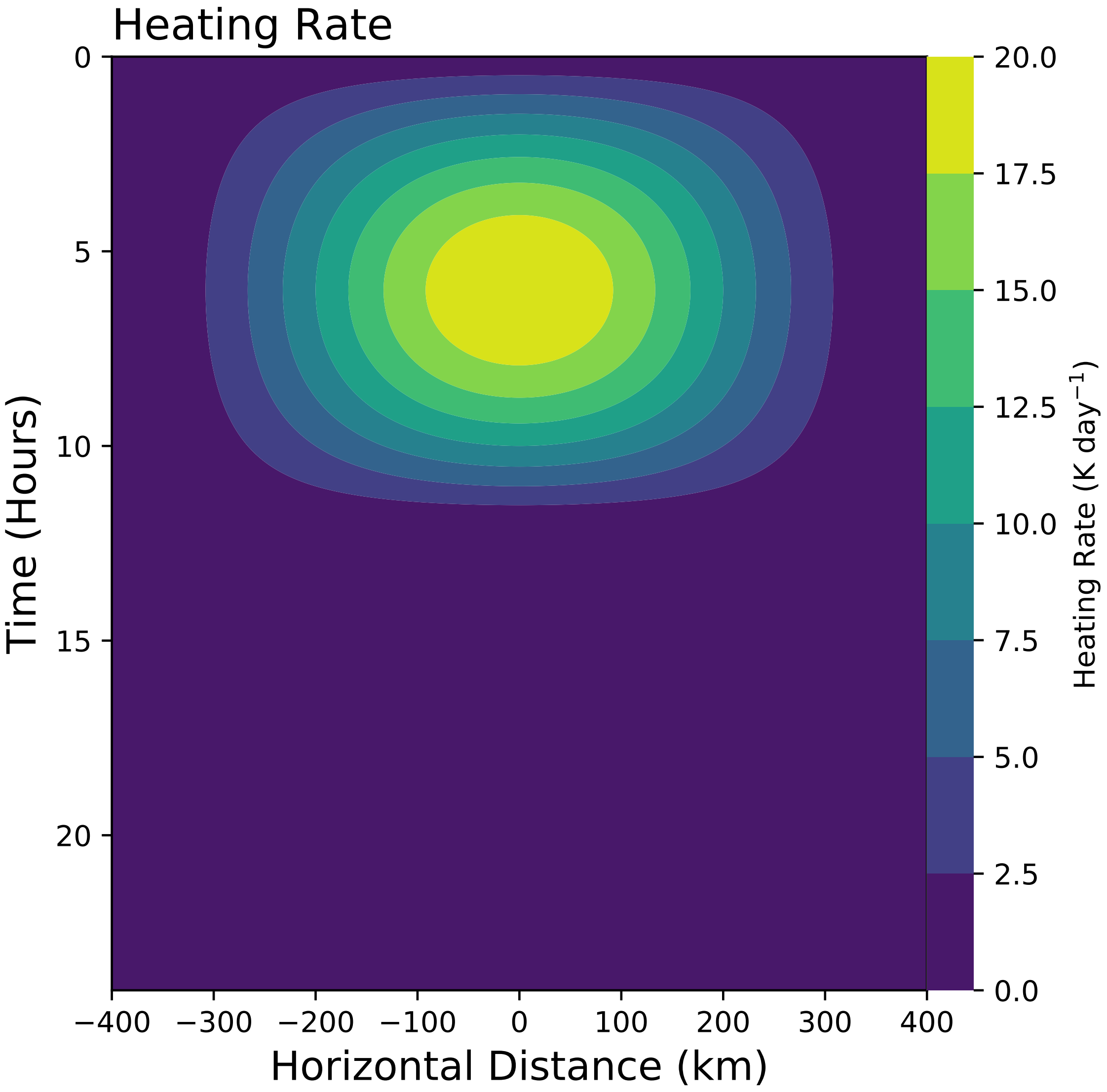

Figure 2.6: Heating rate (K day^{-1}) for the average-heating LLJ simulations. Time increases from top to bottom starting at 1200 UTC and the horizontal distance is on the x-axis.

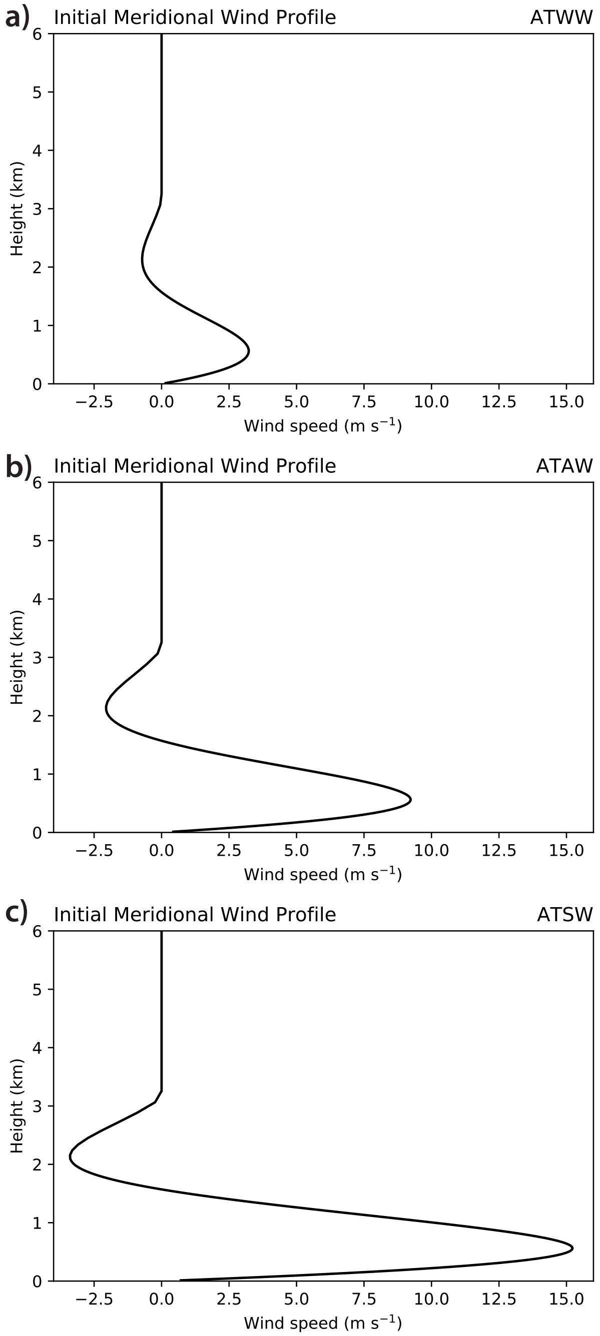

Figure 2.7: Initial meridional wind profiles for (a) WW, (b) AW, and (c) SW gravity wave simulations.

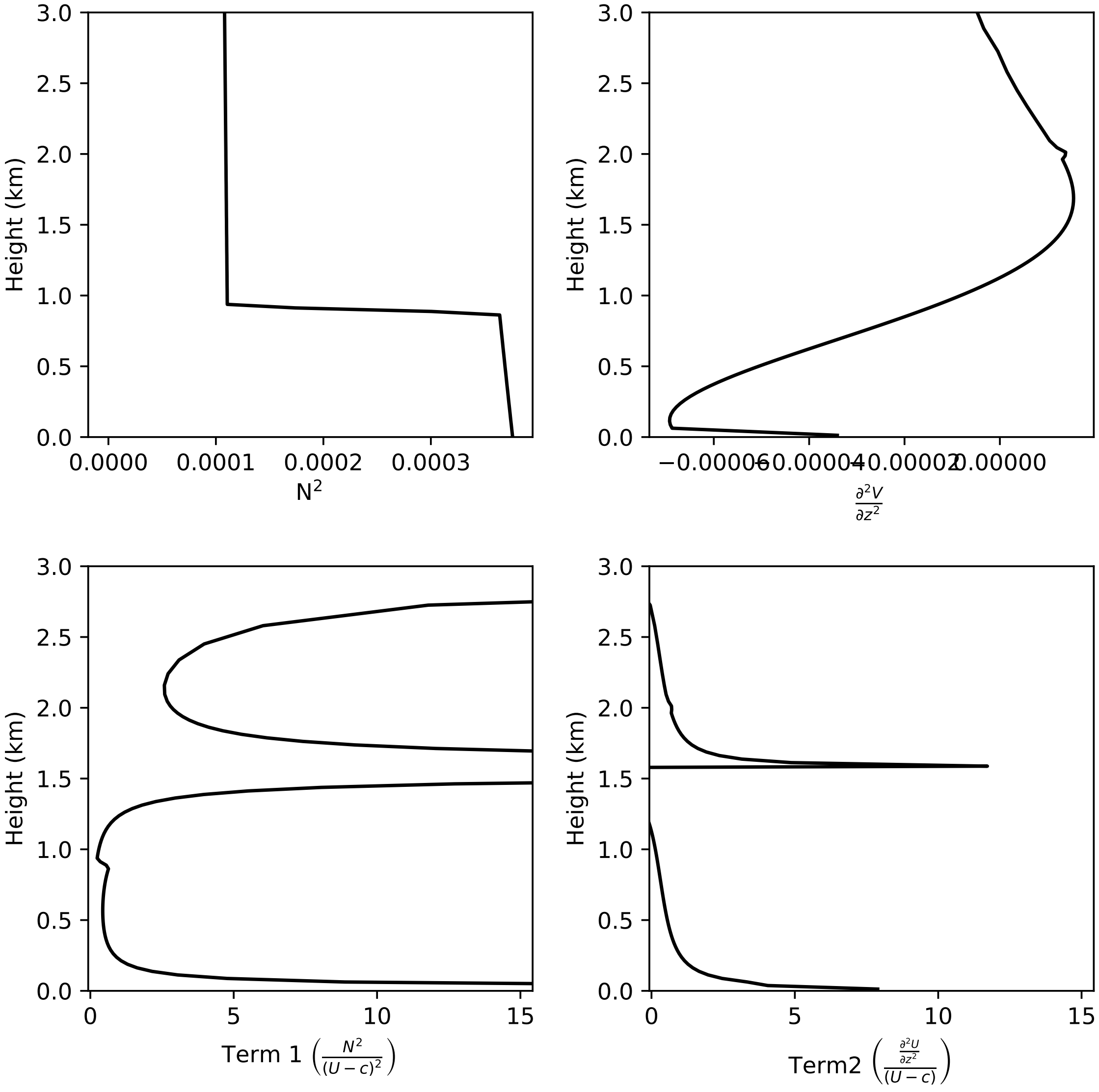

Figure 2.8: Terms used to calculate the Scorer parameter in the ATAW simulation. (a) N^2, (b) $\frac{\partial^2 U}{\partial z^2}$, (c) Term 1 of Equation 1.1, and (d) Term 2 of Equation 1.1.

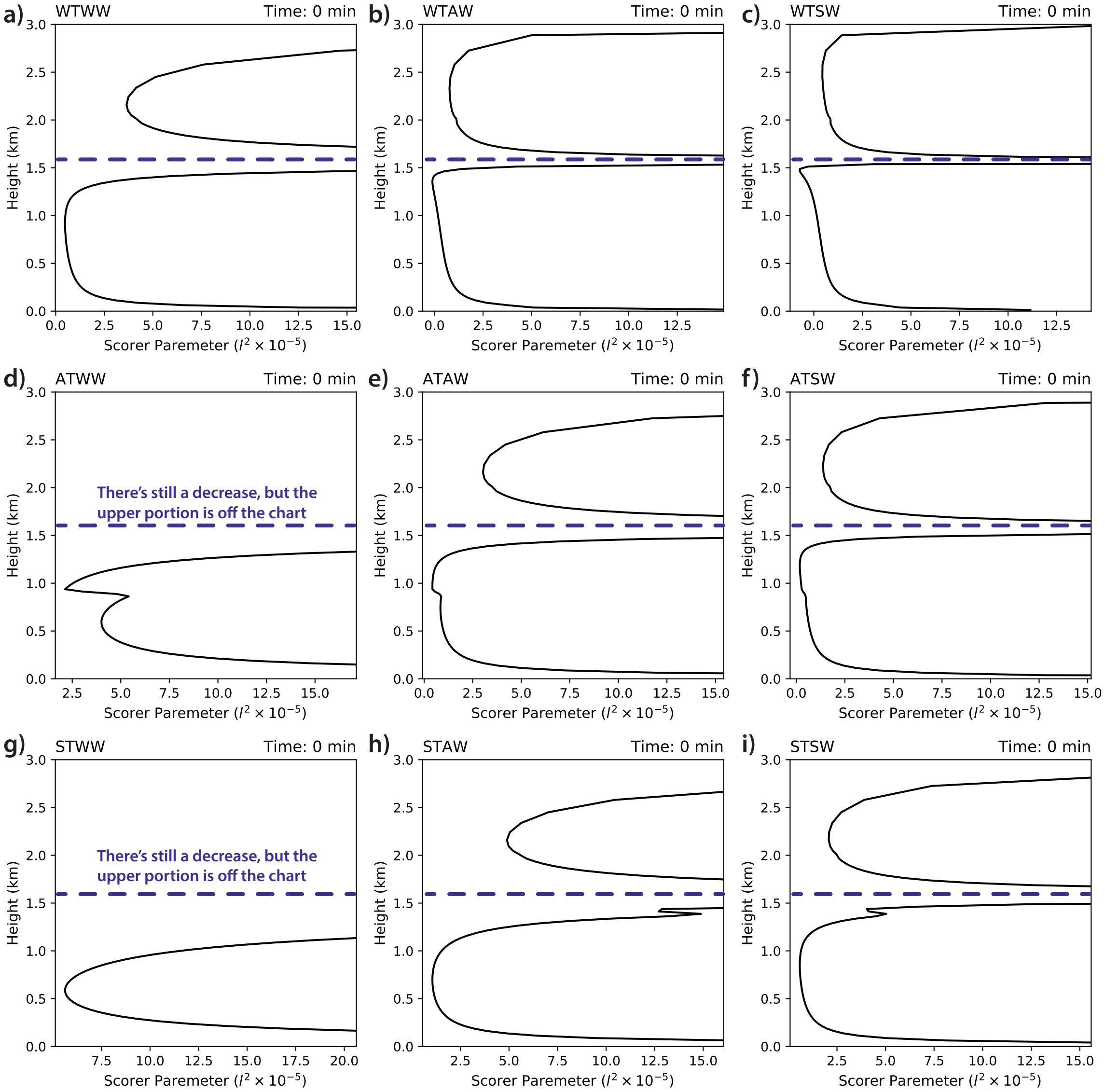

There's still a decrease, but the upper portion is off the chart

There's still a decrease, but the upper portion is off the chart

Figure 2.9: Scorer Parameter for (a) WTWW, (b) WTAW, (c) WTSW, (d) ATWW, (e) ATAW, (f) ATSW, (g) STWW, (h) STAW, and (i) STSW gravity wave simulations. The blue dashed line indicates the rapid decrease in the Scorer parameter.

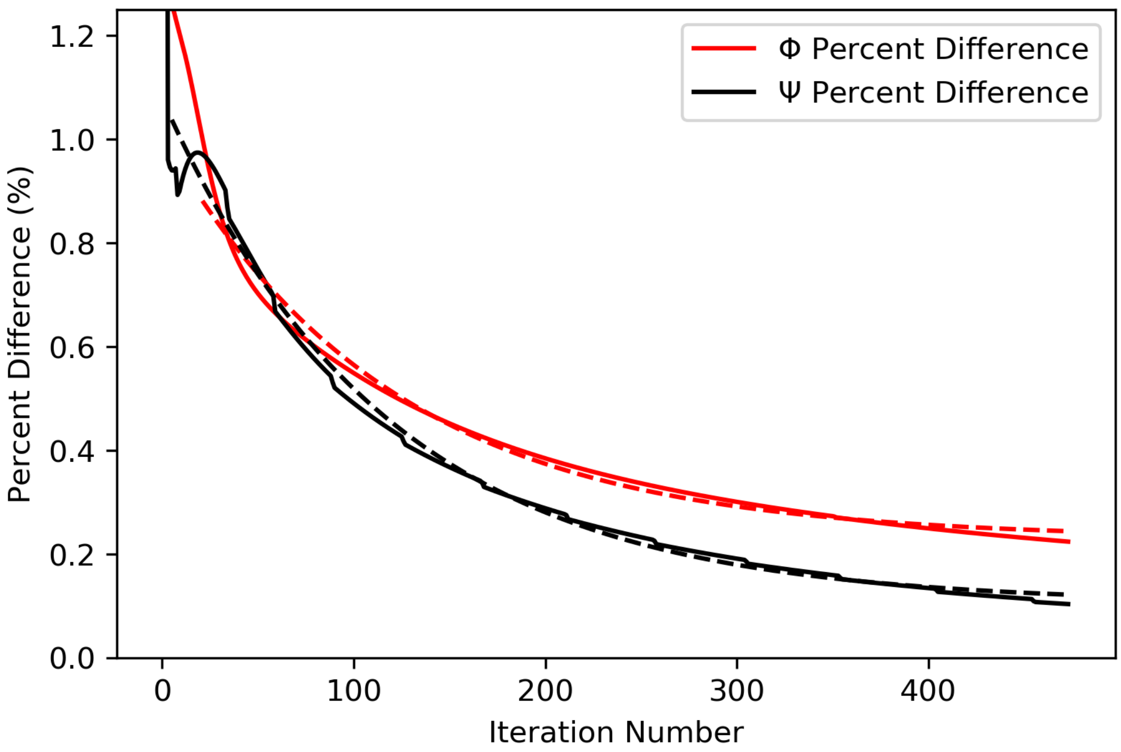

Figure 2.10: Percent difference between the current iteration and the previous iteration as the iteration number increases. Φ is the red curve and Ψ is the black curve. The dashed curves represent an exponential fit.

Chapter 3

Sounding Analysis

The typical nocturnal environment in the composite sounding (Fig. 2.2) is not conducive to CI. There is no CAPE, and the 100 hPa deep inversion near the surface prevents any surface parcel from rising (Fig. 2.2). Given that CI can occur at night without any strong forcing, what modifications to this composite profile are necessary to make it more conducive for CI? To explore this question, the low-level moisture profile will be modified to examine the impact on the profile through the generation of CAPE and the reduction of CIN. These changes will also let us examine how much lift is necessary to lift a parcel to its level of free convection (LFC). Real soundings will then be examined to see how features such as temperature inversions and shallow layers of moisture averaged out of the composite sounding affect the net displacement necessary to cause CI in that environment.

Features that are important to CAPE in these environments can be shallow and subtle. When the composite sounding was created, these features get averaged out, and only the most common features in the most common locations remain (including the near-surface inversion and the LLJ). This compositing is the reason why there is no CAPE in the composite sounding. Observed nocturnal soundings do have CAPE, though in many cases there is CAPE for elevated parcels rather than surface-based parcels and there is generally high CIN. A Gaussian modifier (Equation 3.1; shown below) is applied to the dewpoint temperature to modify the composite sounding to simulate the effects of a shallow layer of enhanced moisture. This modification will generate the elevated CAPE seen in observed nocturnal soundings. The Gaussian modifier is given by

$$f(p) = ae^{-\frac{1}{2}\left(\frac{p-\mu}{\sigma}\right)^2} \tag{3.1}$$

where a is the magnitude of the modification, μ is the center of the modification and σ is the standard deviation. In this modification, the standard deviation is 75 hPa and the magnitude is dependent on the dewpoint depression ($T - T_d$). The modification is based on a percentage of this depression. For example, a modification of 50% means that the dewpoint depression is reduced by 50% (5°C to 2.5°C). If the dewpoint exceeded the temperature at any level via this modification, the dewpoint was set to the temperature.

The goal is to modify the moisture profile at various levels and show how the added moisture will increase the CAPE and reduce the net displacement needed for parcels to reach their LFC. At night, the low-level moisture can be increased by processes including the advection of moisture from the west by the LLJ (Gebauer et al. 2018; Reif and Bluestein 2018), from pre-existing convection over the Rockies that has decayed (Reif and Bluestein 2018), or moisture transport northward by the LLJ (e.g., Tollerud et al. 2008). The goal is not to replicate these processes in this analysis, but to show how a simple modification of the moisture profile affects the nocturnal sounding.

3.1 Modifications to the Composite Sounding

The dewpoint temperature was modified at three levels: centered at 900 hPa, centered at 800 hPa, and centered at 700 hPa. The 900 hPa and 800 hPa levels could represent the height of the LLJ max depending on how deep the LLJ is. In all three cases, CAPE increased as the dewpoint depression decreased to zero. As the dewpoint depression decreased, the lifted condensation level (LCL) decreased (see Fig. 3.1 for visual examples of a 50% reduction in the dewpoint depression). This decrease in the LCL shifts the parcel profile (denoted by the gray line) to the right, increasing the CAPE. Above the LFC, there are relatively steep mid-level lapse rates (a temperature decrease with height of $7-8$ K km^{-1}). As that dewpoint depression decreases to zero, then the low LFC and steep mid-level lapse rates result in CAPE of more than 1000 J kg^{-1}.

The dewpoint depression is 6.94°C at 900 hPa, is 6.63°C at 800 hPa, and 6.65°C at 700 hPa. For parcels lifted from 900 and 800 hPa, only a 10% decrease in the dewpoint depression is needed to achieve positive CAPE. For parcels lifted at 700 hPa, a 40% decrease in the dewpoint depression is needed. This decrease in the dewpoint depression corresponds to an increase in the mixing ration of 0.49 g kg^{-1} for parcels lifted at 900 hPa, an increase of 0.39^{-1} for parcels lifted at 800 hPa, and an increase of 1.22 g kg^{-1} for parcels lifted at 700 hPa. In vertical cross-sections shown by Reif and Bluestein (2018) and Gebauer et al. (2018), the westward advection of moisture by the LLJ could cause this magnitude of increase in the mixing ratio.

The necessary reduction in the dewpoint depression for a parcel to have a net displacement necessary to reach the LFC of less than 1000 m is 75% for a 900 hPa modification (CAPE = 1367), 55% for an 800 hPa modification (CAPE = 337), and 60% for a 700 hPa modification (CAPE = 61). These modifications correspond to an increase in the mixing ratio by 4.3 g kg^{-1} at 900 hPa, 2.3 g kg^{-1} at 800 hPa, and 1.9 g kg^{-1} at 700 hPa. Again, typical processes at night (e.g., the eastward advection of moisture by the LLJ) could explain this increase. While these net displacements are still large (though the trend is towards zero as the dewpoint depression decreases to zero), it is important to remember that this simple modification of the dewpoint temperature does not account for all of the processes that modify the environment.

The nearly 100-hPa deep inversion in the composite sounding and the relatively dry air contributes to this larger net displacement. If the temperature could be cooled somehow, that would reduce the net displacements necessary for parcels above that layer of cooling. For example, a moist absolutely unstable layer (MAUL) could form throughout a layer due to sustained ascent (e.g., Bryan and Fritsch 2000; Trier et al. 2017). This process also modifies the temperature, which is not adjusted in this simple analysis. A more realistic modification to the sounding would be to cool the temperature and increase the moisture.

This process will result in lower LFCs and CIN (resulting in lower net displacements necessary), thereby increasing the potential for CI. Let us examine what the profile would be like with a MAUL between 800 and 700 hPa. While the CAPE in the modified profile is low, the net displacement required to lift a parcel to its LFC is only 50 hPa. Due to the instability associated with a MAUL, that parcel could start at any level between 800 and 700 hPa. This deeper layer of instability increases the potential for CI due to the larger "sweet spot" for ascent. The sustained ascent from features discussed in the next few chapters could modify the environment in this way, making it more conducive for CI.

3.2 Real Soundings

Even small modifications to the low-level moisture can drastically increase the CAPE in the composite sounding. However, real soundings have features such as shallow layers of enhanced moisture and temperature inversions that might be averaged in the composite sounding. These features can make real environments even more conducive to CI than the modified composite sounding. We will now examine the net displacements necessary for parcels to reach their LFC in real soundings. These real soundings are not modified but provide examples of this low-level moisture maximum and illustrate the displacements necessary for CI in these optimal environments. Parameters such as CAPE and CIN for the three real soundings are shown in Table 3.1.

The 1200 UTC KOUN sounding on 9 June 2001 (Fig. 3.2a) has a nearly saturated layer between 900 and 850 hPa and relatively steep lapse rates between 800 and 700 hPa. There is an inversion between 700 and 550 hPa, which acts to reduce the CAPE for the most-unstable parcel. The most-unstable is lifted from the nearly saturated layer near 900 hPa and has 1188 J kg^{-1} of CAPE and only -1.5 J kg^{-1} of CIN. The net displacement needed for that parcel to reach its LFC is 542 m. However, the most-unstable parcel is not the one with the smallest net displacement. A parcel lifted from 850 hPa (near the top of the enhanced moisture) only needs 454 m to reach its LFC, but only has 696 J kg^{-1} of CAPE.

There is also a shallow layer of enhanced moisture in the 1200 UTC KBLF sounding on 17 July 2009 (Fig. 3.2b). The moisture content in this layer is less than the one in the previous sounding. In this case, there is no strong inversion above this layer of enhanced moisture, but a parcel needs to be lifted over 700 m to reach its LFC. Compared to that of the previous sounding, the relatively dry layer contributes to increased CIN for the most-unstable parcel and a higher net displacement. Unlike in the previous sounding, the most-unstable parcel has the lowest net displacement to reach its LFC, but there is only 754 J kg^{-1} of CAPE.

The 1200 UTC KLBF sounding on 16 July 2010 has extremely steep lapse rates and a shallow layer of moisture near 850 hPa (Fig. 3.2c). There is nearly 4000 J kg^{-1} of MUCAPE in this sounding and little CIN. The steep lapse rates and the shallow layer of moisture between 900 and 850 hPa create a conducive environment for CI to occur. Small inversions above the LFC increase the CIN, and as a result, the net displacement needed to achieve this CAPE is nearly 900 m. However, a parcel lifted from above this most-unstable parcel would need to be lifted only 709 m to achieve 2750 J kg^{-1} of CAPE. This amount of CAPE is atypical for these NB CI mode events. Given enough forcing, one might expect some severe storms associated with this sounding, especially severe hail. However, there were no severe reports, and the convective mode was multicellular and short-lived. In the 1200 UTC Omaha, NE sounding (not shown), there was an inversion aloft, and the enhanced layer of moisture is not present. The convection likely occurred in an environment where there was less CAPE, but just enough moisture for the environment to be conducive to CI. This case illustrates the importance of small-scale features important to CI in these events and how the standard observation network might not capture the necessary information to predict these events accurately.

Typical net displacements for atmospheric bores is between 500 m and over 1 km (Table 1.1), and the net displacements for the LLJ can be up to 1 km Shapiro et al. (2018). A small modification of low-level moisture to the NB CI mode composite sounding can result

Table 3.1: CAPE (J kg^{-1}), CIN (J kg^{-1}), displacement to LFC (m) and starting parcel pressure (hPa) for real NB CI mode soundings

Sounding	CAPE (J kg^{-1})	CIN (J kg^{-1})	Displacement (m)	Starting Pressure (hPa)
9 June 2001 1200 UTC KOUN (Most Unstable)	1188	-1.56	542	891
9 June 2001 1200 UTC KOUN (Lowest Displacement)	696	-6.33	454	850
17 July 2009 1200 UTC KLBF (Most Unstable)	536	-19.75	716	745
17 July 2009 1200 UTC KLBF (Lowest Displacement)	–	–	–	–
16 July 2010 1200 UTC KLBF (Most Unstable)	3869	-8.4	896	864
16 July 2010 1200 UTC KLBF(Lowest Displacement)	2750	-23.85	709	811

in these vertical displacements lifting a parcel to its LFC. Soundings from real cases need net vertical displacements of around 500 m for parcels to achieve their LFC. Based on this analysis of observed soundings and modified composite soundings, net vertical displacements of 500 m is the threshold to determine whether or not the mechanism can result in CI.

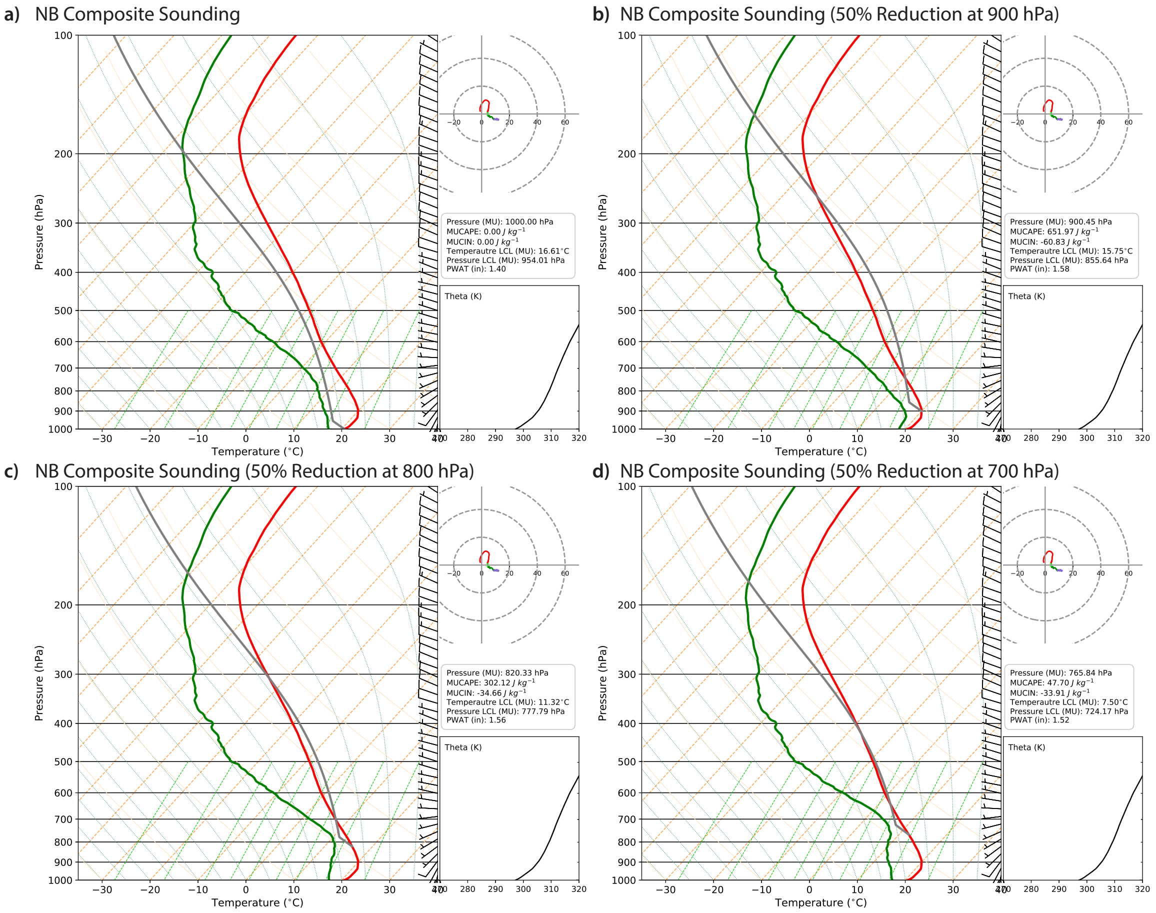

Figure 3.1: (a) The NB composite sounding. (b) as in (a), but a 50% reduction in the dewpoint depression at 900 hPa, (c) as in (a), but a 50% reduction in the dewpoint depression at 800 hPa, and (d) as in (a), but a 50% reduction in the dewpoint depression at 700 hPa

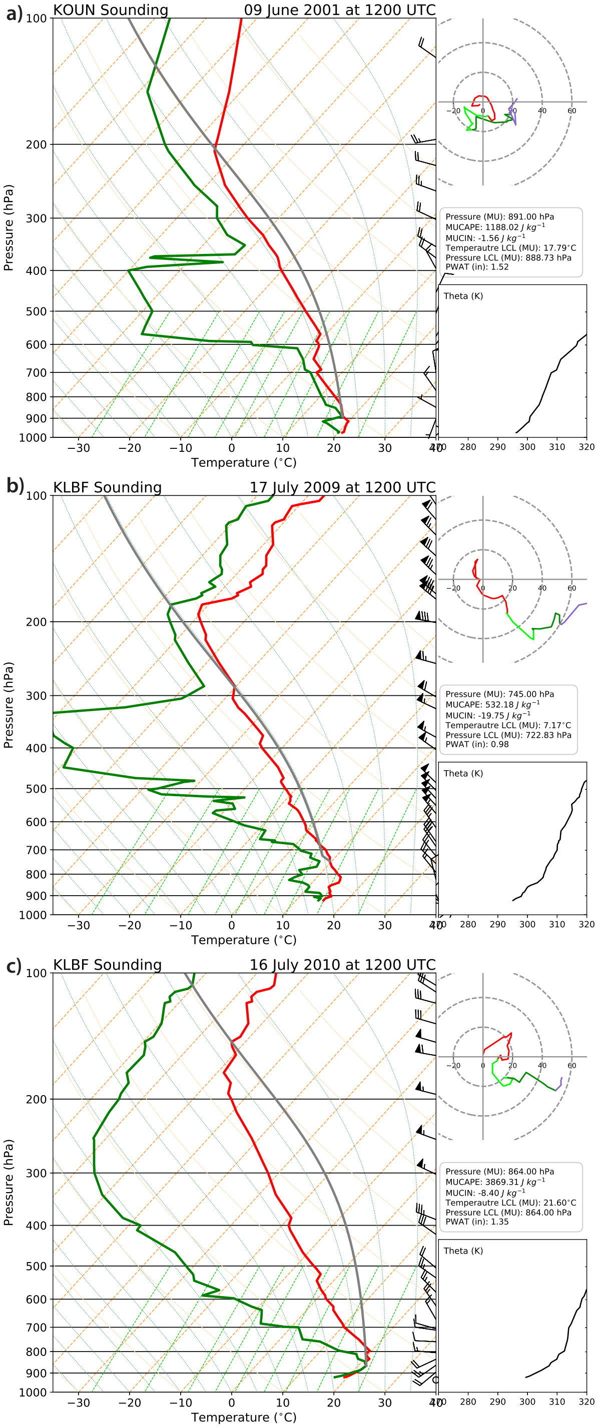

Figure 3.2: a) 1200 UTC KOUN sounding on 9 June 2001, b) 1200 UTC KLBF sounding on 17 July 2009, and c) 1200 UTC KLBF soundings on 16 July 2010.

Chapter 4

Atmospheric Gravity Waves

Atmospheric gravity waves were simulated in the nine environments that represent typical nocturnal conditions over the Great Plains. In these simulations, the gravity waves are generated like those over the Great Plains: a density current propagates through a preexisting stable layer. In this case, a density current is generated from a circular cold block, replicating the density current generated by an MCS. Depending on the environmental conditions, bores may or may not be generated ahead of that density current. The characteristics of these gravity waves, and how these gravity waves interact with and modify the environment will be examined. The potential for CI associated with the net displacement by bores will be discussed in each of the nine environments.

4.1 Gravity Wave Characteristics

4.1.1 Average Nocturnal Environment (ATAW Simulation)

The analysis will begin with examining the modification of the typical environment by gravity waves in the ATAW simulation. This simulation will serve as the "control" simulation. Two hours into the simulation, a bore-like feature is generated ahead of a relatively shallow (<250 m deep) density current (Fig. 4.1a). The purpose of this subsection is to show that the bore-like feature that is generated by the density current is in fact a bore.

The bore-like feature propagates around 60 km ahead of the density current 2 hrs after it was generated, and its wavelength is between 10 and 15 km, similar to the wavelength of observed bores. Another characteristic similar to observed bores is the quasi-permanent net displacement of the isentropes during the bore's passage. This displacement is determined by following a single isentrope. During and after the bore-like feature passes, the average height of that isentrope is approximately 150 m higher than when it started. This net displacement is smaller than that seen in the studies presented in Table 1.1. This difference is likely the result of a weak density current and strong ($>$10 K km^{-1}) near-surface stability reducing.

The passage of a density current is characterized by an immediate drop in the surface temperature while the passage of a bore is characterized by little-to-no change or even an increase in the surface temperature. During the first 1.5 - 2 hours when there was no bore-like feature, there was a drop in the surface temperature collocated with the density current (Fig. 4.1b). After the bore-like feature formed, the temperature either did not change or increased during its passage. These characteristics in the surface temperature further indicate that this feature is a bore and is generated after 1.2 – 2 hrs into the simulation.

This feature shares many similarities to bores, but is the environment conducive to bore formation? The ATAW flow regime is partially blocked (Fig. 4.1c), a regime conducive to the generation of atmospheric bores. This flow regime is common over the Great Plains at night (e.g., Haghi et al. 2017), so it is not too surprising that the average environment here is also partially blocked. While the environmental conditions are important to the partially-blocked flow, the density current was constructed to ensure that the ATAW environment is partially blocked. That same density current will then be applied to the other eight nocturnal environments.

4.1.2 Parameter Space of Nocturnal Environments

The low-lapse-rate (WT) environments are nearly neutrally-stratified throughout the domain. Recall that a bore forms as a density current moves through a stable layer, so if there is no stable layer, a bore should not be generated. In these WT simulations, there is a density current, but no indication of a bore (Fig. 4.2). As the environmental shear increases, the depth of the density current decreases from 1000 m to $<$ 500 m. Reif et al. (2020)

showed that the vertical velocity decreases as the depth of the density current decreases, and this decrease is seen here.

The depth of these density currents is larger than those in the AT or ST simulations (nearly 500 m compared to 250 m and 100 m, respectively). This decrease in the density current's depth as the stratification increases is also shown in Seigel and van den Heever (2012) and Reif et al. (2020). Parsons (1992) showed that the depth of a density current from a dam-break solution such as this one is nearly 4/9 the depth of the initial cold block. The depths of the density currents in these simulations correspond well to this predicted value. The net displacement of parcels associated with the density currents in the WT simulations will not be analyzed because this study focuses on the ascent associated with gravity waves. For a summary of the characteristics of observed and simulated density currents, the interested reader can see Reif et al. (2020).

A rapid decrease with height of the Scorer parameter promotes conditions favorable for wave trapping below the layer of that decrease (Crook 1988). In these simulations, the wind profile is designed to promote a decrease in the Scorer parameter above the inversion, trapping the energy below. Two variables affect the Scorer parameter in these simulations: the environmental stratification and the derivative of the vertical wind shear with height (hereafter referred to as the curvature of the wind profile). However, Haghi and Durran (2020) were able to simulate an atmospheric bore in an environment where the wave duct was not the result of a rapid decrease with height of the Scorer parameter. While their study calls into question the use of the Scorer parameter as a way to examine bores, the simulations presented in this study have atmospheric bores. Our analysis of the net displacement of the bores are not impacted because bores were generated in these simulations.

In the average-lapse-rate (AT) and the strong-lapse-rate (ST) simulations, there is a low-level stable layer topped by a less-stable upper layer. This two-layer stratification has a high N^2 topped by a lower N^2, so this term in the Scorer parameter should decrease rapidly (almost discontinuously) at the top of the inversion layer. The stratification is constant with height in the WT simulations, so there is no decrease of N^2. This term does not contribute to a decrease in the Scorer parameter in the WT simulations.

The initial wind profile is sinusoidal (Equation 2.2) and is similar in shape to the wind profile in Crook (1988). The only change in the wind profile among the weak winds (WW), the average winds (AW), and the strong winds (SW) simulations is the magnitude of the wind. Due to the sinusoidal wind profile, the second derivative will be the same for all three simulations, just scaled by that constant factor. The simulations with the strongest (weakest) constant will have the largest (smallest) decrease due to this term. Based on the influence of these two terms, one might expect the SW simulations to have the "best" bores when compared to the bores in the WW or the AW simulations.

Vertically-propagating gravity waves tilt upstream with height. Atmospheric bores are vertically-trapped gravity waves, so their isentropes should be vertically stacked. In all of the simulations with bore-like features (AT and ST simulations), the isentropes are approximately vertically stacked. There is a weak upstream tilt with height most notable in the leading crest, which may indicate that the wave energy is not perfectly trapped (Fig. 4.3). However, because this tilt is so subtle, there is likely still a significant amount of wave energy trapped below the layer where the Scorer parameter decreases. As time progresses, this tilt decreases (becomes more vertically-oriented) and in the simulations with stronger winds (not shown here), this tilt is non-existent.

In the AT simulations, a bore-like feature develops after 1.5 hr in the SW simulations. In the ATWW simulation, there is no clear wave-like feature that propagates ahead of the density current (Fig. 4.2d), but there is a single wave that propagates ahead and potentially a second wave that develops after 3 hrs. In the ATAW and ATSW simulations (Figs. 4.2e-f), there are well defined waves in the potential temperature. The wavelength of these bores is about 20 km for the ATWW bores, 10.9 km for the ATAW bore, and 13.9 km for the ATSW bore (at 260 min; Fig. 4.4). As the shear increases (WW to SW), the bores become better defined. This increased definition could be the result of the more favorable conditions for wave trapping due to an more rapid decrease with height of the Scorer parameter.

There was no critical layer mentioned in Crook (1988) and the wind direction typically opposed bore motion. In these simulations, this effect is also seen here. There is no place where the wind velocity and the bore velocity are in the same direction (i.e., the dot product of the two velocities is negative) (Fig. 4.5). However, this lack of a critical layer assumes a constant bore speed throughout the depth of the troposphere. If one gets above the bore and assumes the bore speed is zero there, there would be a critical layer. This effect is the same for all simulations with atmospheric bores.

The density current is very shallow ($\approx$100 m) in the ST simulations, but there are bore-like features in all three (WW, AW, and SW) ST simulations (Figs. 4.2g-i). The most pronounced bore is in the SW simulations and the least pronounced is in the WW simulation, similar to the bores in the AT simulations. The amplitudes of these bore-like features are not as pronounced as those in the AT simulations. This weak amplitude is likely due to the weak and shallow density current in these simulations or the very strong near-surface stratification. The wavelength of the STWW bore is about 20 km, the wavelength of the STAW bore is 16 km and the wavelength of the STSW bore is about 12.6 km.

The surface temperature decreases rapidly at the leading edge of the density current in the WT simulations (Figs. 4.6a-c), even after the other simulations developed bore-like features. The surface temperature in the AT (Figs. 4.6d-f) and ST (Figs. 4.6g-i) simulations either does not change or increase as the bore passes. The temperature then decreases as the density current passes, further indicating that atmospheric bores are produced in these simulations. The magnitude of this warming is around 0.5°C in the AT simulations and as large as 1.5°C in the STSW simulation.

The flow regime for the AT simulations is partially-blocked (Fig. 4.7), but the flow-regime for the ST simulations is borderline partially-blocked/subcritical. The steeper inversion height (1.2 km compared to .8 km) and the shallower density current results in the non-dimensional height being too low to be in the partially-blocked flow regime. However, a bore-like feature is still generated, particularly in the STSW environment. The speed of the density current is estimated 3 hr into the simulation and the depth of the density current is estimated earlier in the simulation (in the first hour). The depth used is 600 m. It is possible that the density current is slower 3-hr into the simulation. If the density current is faster, then the Froude number would increase, making the flow-regime more solidly partially-blocked.

To test how the bore would be modified if it were generated by a stronger density current, the initial cold block depth was increased from 1.5 km to 2 km and the negative potential temperature perturbation was increased from -10 K to -15 K. The flow regime for these bores is still partially blocked (not shown). The effect of the stronger and deeper density current is to increase the non-dimensional height. The response in the ATWW simulations is a single leading wave that is 40 km ahead of the density current (Fig. 4.8a), but aside from this single wave, there is no indication of a bore. However, the bores in the ATAW and ATSW simulations (Figs. 4.8b-c) and in all of the ST simulations are deeper than those generated by weaker density currents. The bores in the ATAW and ATSW simulations are not as wide as those generated by a deeper density current, however, and their wavelength is shorter. The bores in the ST simulations (Figs. 4.8d-f) generated by a stronger density current are more well defined, have a relatively consistent wavelength (20 km), and have a higher amplitude.

Generally, the surface warming ahead of the density current is similar to those generated by a weaker density current, but the time duration of warming is shorter (Fig. 4.9). This short duration is likely due to the narrower bore generated by the stronger density current.

Between three and five simulations produced atmospheric bores (the possible bores in the STWW and STAW simulations are weak and short-lived). These simulated bores share many characteristics of observed bores. These characteristics include a wavelength of 10-15 km, no temperature decrease as the bore passes, and propagate ahead of the density current.

4.2 Atmospheric Bores Moving in Directions Less Conducive for Wave Trapping

Due to the system-relative winds, the most favorable location for wave trapping should be where the density current moves purely southward. This direction is where the most rapid decrease in the Scorer parameter with height occurs. In all simulations with bores, the most pronounced near-surface warming occurs at x = 0 (the purely southerly motion), and the horizontal extent of this warming decreases as one moves away from this location. The leading edge of the density current and the bore at 12 m AGL is denoted on Fig. 4.10. The propagation ahead of the density current can clearly be seen, and the bore appears to be radially symmetric. However, there are slight variations in the field such as the bore's distance from the density current as one moves away from x = 0 (see Fig. 4.11 for a schematic of the angles used in this study). What happens to the structure and characteristics of the density current and bores as the angle from the most-optimal wave trapping increases?

The characteristics of the density current in the WT simulations do not change much between 0° (x = 0) and 45°. The depth of the 45° density current head is similar than the depth of the 0° density current in the WW and AW simulations, but it deeper in the SW simulation (Figs. 4.12a-c). The surface temperature still drops at the density current, and there is no surface warming and no indication of bores (Figs. 4.12d-f). The speed of the 45° density current is approximately the same as the speed of the 0° density current.

The Scorer parameter decreases similarly in the environment, but as the angle increases from 0° (i.e., a different reference frame), the magnitude of this decrease is reduced because of the apparent reduction of the environmental wind speed. The 45° angle should result in a nearly 30% reduction in the system relative wind speed. When the magnitude of the winds is weak, this decrease of the Scorer parameter associated with the angle difference is not as substantial as when the winds are stronger (e.g., 30% of 3 is less than 30% of 16). A slightly faster-moving density current can offset this small decrease at 45°, so one might not expect any major differences in the bores between 0° and 45°.

In the AT simulations, a bore-like feature is generated on the southwestern edge (45° angle). The 45° bore in the ATWW simulation (Fig. 4.13a) looks nearly identical to the 0° bore. In the ATAW and ATSW simulations (Figs. 4.13b-c), the structure of the 45° bore is different from the 0° bore. The isentropes of the 0° bore are at a more constant height than the isentropes of the 45° bore, which decrease with height as the bore passes (though there is still a net increase). The wavelengths of the 45° bores are a little shorter than those of the 0° bores (13.75 km compared to 15 km in the ATSW simulation), but the difference is small. The 45° bore is also shorter by about 10 km than the 0° bores. The isentropes of the 45° bores are also vertically-stacked, indicating that these are vertically-trapped waves.

The surface temperature patterns of the 45° and 0 ° bores are nearly identical in the ATWW simulation (Fig. 4.13d). In the ATAW and ATSW simulations, the 45° bore has weaker surface warming, and the time it occurs is less than that of 0° bore (Figs. 4.13e-f). Overall, the 45° bores in the ATAW and ATSW simulations are still bores, but based on the less uniform isentropes with height and reduced surface warming, they are not as well-defined as the 0° bores.

In the ST simulations, the bore is still weak (Figs. 4.14a-c). Like the bores in the AT simulations, the bore's characteristics are nearly identical in the WW simulation when viewed from 45°. The small reduction in the system-relative environmental wind speed does not have much impact and is likely offset by a faster-moving density current. There are no major differences in the characteristics of the isentropes between the 0° bore and the 45° bore in the AW or the SW simulations. The 60° bore is similar to the bore viewed from 0°.

The surface temperature change associated with the 45° ST bores (Figs. 4.14d-f) is similar to that of the 0° bore, but weaker in magnitude There is still pronounced surface warming associated with the 0° bore in the STSW simulation (Fig. 4.14f). The 60° bore (not shown) does not have any surface warming ahead of the density current. This decrease in the surface warming and the structure of the isentropes as the angle increases from 0° indicate that the bore is not as pronounced as the conditions for wave trapping decrease, corresponding well with the real WRF simulation results by Blake et al. (2017).

Consider the flow regime for the 0° bores (Fig. 4.7). The term that is most affected by the off-angle direction is the system-relative wind speed. The density current's depth also decreases as the system relative wind speed and vertical wind shear decrease, but not as much as the system relative wind speed itself decreases. *In these highly-idealized simulations, increasing the angle from 0° (i.e., from south to southwest or southeast) results in the flow regime becoming more subcritical.* One could use this chart to estimate where the partially-blocked flow regime ends. For example, the AT simulations need at least a 50% reduction (e.g., 60° angle from south) in the system relative-wind speed to be pushed out of the partially blocked flow regime. In the ST simulations, it is difficult to estimate the density current's depth after the bore was produced, but it is likely that a smaller reduction (maybe 30% - 50%) is needed. That angle corresponds to at least 45%.

Overall, as the angle between the most-optimal curvature of the winds and the density current propagation direction increases, the bore looks less organized, but still remains a bore. There are no horizontal inhomogeneities in the temperature field and the simulations are designed to have favorable bore conditions. Small reductions in the system-relative wind speeds due to the rotation around the density current do not impact the bore too much as the conditions are still favorable by design. In the real atmosphere, there can be large horizontal homogeneities in the wind and environmental stratification. These inhomogeneities can result in a smaller range of angles the bore can form at (e.g., the bore may only form on the southerly moving component and not the southwesterly or southeast moving component).

4.3 Impact of Westerly Wind Shear

4.3.1 Hypothesis

Parsons et al. (2019) averaged the meridional and zonal wind over the Atmospheric Radiation Measurement (ARM) sites over central Oklahoma to southern Kansas during IHOP_2002 (Weckwerth et al. 2004). They noted a low-level westerly wind maximum around 1 km AGL that results in the positive advection of moisture, increasing the CAPE and reducing the CIN. This westerly component of the LLJ is widely known to modify the environment through the advection of moisture (e.g., Reif and Bluestein 2017; Gebauer et al. 2018 and low-level warm advection (e.g., Parish et al. 2020). However, while acknowledging that the westerly wind maximum is important for making conditions more favorable for CI, Parsons et al. (2019) do not address the impact this westerly wind shear has on bore production and bore characteristics.

The base simulations were rerun with the inclusion of linear westerly wind shear. The wind increases from 0 m s^{-1} at 500 m AGL to 3 m s^{-1} at 2 km AGL. Consider the Scorer parameter again. The total wind can be proven down into its u and v components where

$$\vec{V} = u\hat{i} + v\hat{j}. \tag{4.1}$$

The effect that including linear westerly wind shear has on the Scorer parameter will now be examined. The second derivative of the wind is

$$\frac{\partial^2 \vec{V}}{\partial z^2} = \frac{\partial^2 u}{\partial z^2}\hat{i} + \frac{\partial^2 v}{\partial z^2}\hat{j}. \tag{4.2}$$

In this case of linear westerly wind shear, the second derivative should have no impact on the Scorer parameter. However, this does not mean that the bore's characteristics will be similar by including this shear, only that conditions for wave trapping are unaffected.

This westerly shear could promote more of an RKW balance (Rotunno et al. 1988) on the eastern edge of the density current, possibly resulting in a deeper density current (Fig. 4.19). The horizontal vorticity generated by the westerly wind shear is opposite in sign to the vorticity that is baroclinically generated at the leading edge of the density current. The upward branch of the horizontal vorticity generated by the environmental wind shear and the horizontal vorticity that is baroclinically generated at the leading edge of the density current act together to increase the vertical velocity and the depth of the density current head. This balance would affect the flow regime discussed earlier by increasing the non-dimensional height. On the eastern side of the density current, the westerly shear is hypothesized to increase the Froude number and the non-dimensional height (due to this more favorable RKW balance). On the western side of the density current, the westerly shear is hypothesized to decrease the Froude number and the non-dimensional height (towards subcritical flow).

Because of the circular nature of the density current and atmospheric bores, the westerly wind shear noted in Parsons et al. (2019) could result in differential advection with height of the density current (and possibly the bore). One consequence of this differential advection of the bore is the superposition of the waves. For example, if the bore gets sheared by half a wavelength, then the combined effect might reduce the wave's amplitude behind the leading crest. If the bore gets advected by a full wavelength, then the amplitude of the waves might increase. This superposition's impact on the bore's characteristics and the net vertical displacement is unknown but will be explored in this study.

4.3.2 Atmospheric Bore Characteristics in the Presence of Linear Westerly Vertical Wind Shear

When westerly vertical shear is added, the characteristics of the 0° bores in the AT and ST simulations (Figs 4.15 and 4.16) look nearly identical to the 0° bores in the simulations without vertical shear. These characteristics include a nearly identical pattern of the potential temperature with height and nearly identical surface warming. A parcel will travel horizontally 40 km over 4 hours, assuming a wind speed of 3 m s^{-1}. In the simulation, this distance is related to an angle of around 10° from the center (i.e., 10° from south), so it is unlikely that the inclusion of this weak westerly shear will have any major impact on the density current or bores when viewed from 0°.

However, the 45° bores have different characteristics when vertical shear is added, except for the bores in the WW simulations (Figs. 4.17 and 4.18). Those bores look nearly identical to the bores without shear. The 30% reduction of the apparent wind speed appears to have a minimal impact on the WW bores. The 45° bores in the AW simulations tend to be slower than those without vertical shear. This difference is small (<10 km by 2 hours into the simulation), but the bore's extra width can impact the mean net displacement of air parcels. In many of the simulations (e.g., ATAW and STSW), adding vertical shear resulted in a higher amplitude leading wave than the same bore without vertical shear and could impact the maximum vertical displacement.

4.3.2.1 Comparison of 45° bore to -45° bore

In the WT simulations, the density current is initially deeper during the first hour of the simulation. The density current becomes shallow (<500 m deep), so the westerly wind shear's impact on the density current is minimal. The vertical wind shear starts at 500 m AGL, so while the -45° density current has a more favorable RKW balance (Fig 4.19), the shallow nature of the density current prevents this favorable balance from being realized. In the AT and ST simulations, the density current is shallow (< 500 m AGL) due to the strong near-surface stability (Fig. 4.20). One could argue that the -45° density current in the ATSW simulation is deeper than the 45° density current, but this difference is small (< 50 m). One density current is not significantly stronger or different from the other.

The -45° bores in the AT simulations have different patterns in the potential temperature with height than that of the 45° and 0° bores (Fig. 4.21). For example, in the ATAW simulation, the -45° has a single leading wave and no noticeable second wave. The 45° bore has two waves, but the second one is stronger, and the 0° bore has no dominant wave and multiple crests associated with it. In the ATWW simulation, the 45° bore has a stronger leading wave and no notable secondary wave, the -45° bore has a stronger second wave and a weaker leading wave, and the 0° has two waves of similar amplitude. The three bores in the ATSW simulation have similar characteristics. The displacement of the isentropes of the -45° and 45° bores decrease as one approaches the density current from upstream, but the displacement associated with the 0° bore is quasi-constant.

In the ST simulations, the -45° bores in the WW and AW simulations were farther ahead of the density current, but the -45° bore in the SW simulation was closer to the density current (by 10 km at 120 minutes) (Fig. 4.22). There were not many notable differences between the -45° bore and the 45° or 0° bores in the WW or AW simulations, except perhaps that the 0° and -45 ° bores in the STAW simulation had shorter leading waves by approximately 60 m (Figs. 4.22d-f). The -45° bore in the STSW simulation has better defined waves behind the leading crest than the 0° bore and a similar pattern to the 45° bore.

The surface warming associated with the -45° bore is not notably different than that of the 45° bore (Figs. 4.23 and 4.24). This similarity is likely because the overall structure of the bore is not notably different from that of the 45° and -45° bores and the surface wind is still 0 m s^{-1}. In general, the inclusion of this weak vertical wind shear had no impact on surface warming.

Typically, the -45° bore is farther ahead of the density current than the 45° bore. This distance results in a wider bore and could result in a higher mean net displacement. There are also differences in the patterns of the waves between the -45° and 45° bores. The wavelengths of the 45° and the -45° tend to be more variable than the 0° bore (Fig 4.25).

The shearing of the atmospheric bore causes the waves to move more easterly as the height increases (see schematic in Fig. 4.26). This shear results in a superposition of a few waves, slightly increasing the amplitude while weakening the amplitude of others. This differential advection of the waves can be seen in the horizontal cross section of potential temperature. The crests in the inset in the lower portion of Fig. 4.26 are offset and at a different angle (denoted by the black lines).

4.4 Vertical Velocity and Net Displacement

The net vertical displacement of air parcels is important to CI. In Chapter 3, it was shown that vertical displacements as low as 200 m (or possibly lower) could cause CI in the most optimal environments. In those tests, the parcel's LFC was between 900 and 750 hPa, but that height depended on the environment. Typically, atmospheric bores will be associated with net displacements in the lowest 2-3 km of the atmosphere (i.e., from the surface to approximately 700 hPa). These levels correspond well with the LFCs in the sounding analysis. These gravity wave simulations are conducted in dry environments, so CI will not occur. However, the net vertical displacement of air parcels can be analyzed.

4.4.1 Vertical Velocity

The magnitude of vertical velocity is not enough to determine whether or not CI will occur, but examining the vertical velocity of these simulated bores offers a direct comparison to the vertical velocity of observed bores in previous studies. Because there are no bores in the WT simulations, they will not be described here. However, the interested reader is referred to Reif et al. (2020) for a summary of vertical velocities associated with density currents.

As the environmental stratification increases, it becomes more difficult to push a parcel upwards, so the magnitude of the vertical velocity should decrease. This effect is seen in these simulations. Regardless of whether or not there is a bore or a density current, given the same initial forcing (i.e., the cold block), the magnitude of the vertical velocity decreases as the stratification increases.

The magnitude of the vertical velocity associated with atmospheric bores is commonly between 1 and 3 m s^{-1}. In the AT simulations, the magnitudes of the vertical velocities were around 0.5 m s^{-1} (Fig. 4.27), lower than that seen in previous studies. However, this study's environment represents an average nocturnal environment, and the density current is not as strong as those seen in the real environment (see Reif et al. (2020)). The maximum vertical velocity was around 0.2 m s^{-1} in the ST simulations (Fig. 4.28). This low vertical velocity is attributed to the strong stratification (17 K km^{-1}) near the surface.

At 220 min into the ATAW simulation, and at 500 m AGL, the maximum vertical velocity is 0.39 m s^{-1}. The average vertical velocity for that bore is 0.027 m s^{-1}. The average and mean vertical velocity for all bores are computed from 30 km ahead of the bore to 50 km behind the leading edge. Across the bore's width, the positive average vertical velocity indicates that a parcel experiences a positive net vertical displacement. In general, as the wind increases (WW to SW), the vertical velocity increases. This increase is likely due to a stronger bore as a result of the more favorable wave trapping due to the enhanced wind. The average vertical velocity in the ST simulations (at 120 min) is comparable to that of the AT simulations. While the maximum is weaker than in the AT simulations, the bores tend to be wider in the ST simulations, so there are more positive vertical velocities, increasing the average (Fig. 4.29). Similar averages applied to a wider bore will result in a lower net displacement associated with the wider bore. Note that an earlier time was chosen because the bores in the ST simulations tended to form earlier, and the bore is better defined at the earlier time.

The vertical velocity following an isentrope may provide a more accurate assessment of the vertical velocity an air parcel will experience. For the AT simulations, the 306 K surface is selected. The maximum vertical velocity is 0.45 m s^{-1} and the average vertical velocity is 0.027 m s^{-1} (Table 4.1; Fig. 4.30). Due to the increased stratification in the

ST simulations, the 320 K surface is analyzed. The maximum vertical velocity is weak in all ST simulations (< 0.2 m s^{-1}) (Fig. 4.31) due in part to the increased stratification than the stratification in the AT simulations. While the maximum vertical velocity is weak, the bores' width is wider than those in the AT simulations. Because of the wider bores in the ST simulations, a similar average should result in a lower net displacement than those in the AT simulations.

In the AT simulations, the average vertical velocity was higher when analyzed from a constant height above the ground than the vertical velocity when analyzed on an isentropic surface. When analyzed at a constant height, this higher vertical velocity is likely due to the density current (which is between 40 and 50 km behind the bore's leading edge at this time). This density current is associated with a higher vertical velocity closer to the ground (see ATWW simulation). The isentrope is displaced higher, so the density current's vertical velocity is not felt as much at the higher altitudes. The density current in the ST simulations is more than 50 km behind the bore's leading edge, so this farther density current does not impact the computed vertical velocities.

The vertical velocity patterns of the 45° bores at 500 m AGL in all simulations are nearly identical to that of the 0° bores (Figs. 4.32 and 4.33). There is a tendency for the vertical velocity to be slightly weaker for the 45° bore (in the ATAW, STAW, and STSW simulations), but the overall patterns in w of the 45° bores and the 0° bores are the same.

When westerly shear is added, the 45° bores in the AT simulations have stronger vertical velocities (sometimes 20-25% higher). This stronger vertical velocity is related to the leading wave's stronger vertical velocity (Fig. 4.34). The 45° bores' vertical velocities in the ST simulations are similar with and without vertical wind shear (Fig. 4.35). Just as there was little change in the isentrope pattern of the 0° bore when shear was added, there is little change in the vertical velocity pattern of the 0° bores with shear than those without vertical shear.

Table 4.1: Maximum and Average Vertical Velocity for simulations with atmospheric bores. The bore speed is also noted.

Simulation (220 min for AT, 120 min for ST)	ATWW	ATAW	ATSW	STWW	STAW	STSW
Maximum Vertical Velocity (m s^{-1}; Isentropic)	0.23	0.45	0.46	0.11	0.19	0.29
Maximum Vertical Velocity (m s^{-1}; 500 m AGL)	0.24	0.39	0.34	0.09	0.16	0.25
Average Vertical Velocity (m s^{-1}; Isentropic)	0.018	0.027	0.036	0.017	0.027	0.032
Average Vertical Velocity (m s^{-1}; 500 m AGL)	0.020	0.027	0.030	0.015	0.024	0.93
Bore Speed (m s^{-1})	14.2	12.9	15.4	17.5	17.5	10.4

The vertical velocity patterns of the -45° bore in the westerly shear simulations are similar to the pattern in the isentropes, and there is no clear "stronger" bore in the shear simulations (Figs. 4.36 and 4.37). For example, in the ATWW simulation, the -45° bore has a weak vertical velocity followed by a strong vertical velocity (again, similar to the isentropes). This vertical velocity is weaker than that of the 45° bore in the same simulation. However, in the STSW simulation, the -45° bore has the highest vertical velocity at the leading edge, and there is no difference between the 45° and 0° bores in that simulation. While it is clear that the vertical wind shear impacts the structure of the bores, especially those not moving perpendicular to the shear, the effects of the shear do not seem to favor one bore over the other consistently.

When the bores are initialized by a stronger cold pool, the vertical velocity is stronger associated with each bore. In the ATAW and ATSW bores at 240 min, the maximum vertical velocities are greater than 1 m s^{-1}, more than twice as strong as those initialized by a weaker density current (Fig. 4.38), and is more typical of the vertical velocity of observed bores. In the ST simulations, the maximum vertical velocity is also stronger for the bores initialized by a stronger density current (Fig. 4.39). These stronger vertical velocities correspond to a higher-amplitude bore in all simulations.

4.4.2 Net Vertical Displacement

All of the simulated bores are associated with a positive average vertical velocity, but analyzing the vertical velocity alone cannot accurately determine the net displacement or the potential for CI. One of the most common ways to analyze the net displacement is through the vertical displacement of the scattering layers (Koch et al. 2008a; Parsons et al. 2019) or the displacement of the isentropes (Knupp 2006; Chipilski et al. 2018). While there are no scattering layers in these idealized simulations, passive tracers are placed ahead of the bore and act like a scattering layer. The displacement of these passive tracers and the displacement of the isentropes will be used to analyze the net vertical displacement associated with the bores. The net displacement by the density current (WT simulations) will not be analyzed here.

To analyze the net displacement associated with the isentropes, the height of the isentropic surface was computed for the 0° bore and the 45° bore. The maximum and mean vertical displacements were computed from the bore's leading edge to 40 km behind the leading edge. The maximum and average height of the isentropic surface is then subtracted by the height of the same isentropic far upstream (>100 km) of the bore (Fig. 4.40). This difference should result in the net displacement by the bore itself.

In the AT simulations, the bore's net displacement (at 160 min) is approximately 250 m and the net displacement increases as the potential temperature increases (i.e., as the height increases) until about 314 K (Figs. 4.41a-c). This increase indicates that the magnitude of the displacement increases up to a point throughout the bore's depth. There were no significant differences between the maximum displacement between the 0° bores and the 45° bores, but the mean displacement was 20 m less for the 0° bores than that of the 45° bores. In the ATSW simulation, the 45° bore has a higher-amplitude second wave than the 0° bore. This second wave explains the difference in the maximum and mean net displacements.

In the ST simulations, the overall maximum and mean net displacement (100 and 50 m, respectively) is lower than that in the AT simulations (Figs. 4.41d-f). As the wind speed increases in these simulations, the net vertical displacement increases. Otherwise, the net displacement's patterns are similar to those in the AT simulations with one exception: the 0° bore in the STSW simulations has a higher maximum net displacement by 100 m and a higher mean net displacement by 40 m than the displacement by the 45° bore. At low levels (lower isentropes), this difference can be explained by the density current's influence (50 m behind the bore's leading edge). The density current is right at the edge of the calculation domain for the 0° bore is just outside of the calculation domain for the 45° bore, explaining this difference at the lower heights. There is not as much of a downward dip in the isentropes at higher levels as one approaches the density current from upstream, which would result in an overall larger net displacement, especially in the average.

Passive tracers were placed at three heights (150 m, 700 m, and 1.5 km) in the southern half of the domain. In the AT simulations, the tracer with the highest net displacement was the one that started at 700 m AGL. Its net displacement was 250 m, corresponding well with the analysis using the displacement of the isentropes (Fig. 4.42), but is smaller than the net displacements typically seen with observed bores (around 500 m; Table 1.1). The tracer at 150 m experienced a smaller net displacement, again corresponding well with the isentropic analysis. At these levels, the patterns of the tracers were identical to that of the isentropes, indicating that the vertical displacement of parcels in these dry simulations is primarily from the displacement of the isentropes. This makes sense because in the absence of diabatic effects, parcels should remain in their isentrope as it is a conserved variable.

In the ST simulations, the displacement of the passive tracers is again similar to that of the isentropes (Figs. 4.42d-f). The maximum net displacement is around 100 m and the average is around 20-30 meters. Interestingly, the mean displacement of the tracers near the surface was approximately 0 m, indicating that the near-surface parcels do not get lifted, but the parcels aloft do. This lifting of more elevated parcels in the AT and ST simulations is important because in the nocturnal environment, parcels need to be lifted from above the near-surface stable layer minimize the negative buoyancy due to that stable layer.

Because the passive tracer analysis yielded similar results to the isentrope analysis and the pattern of the passive tracers was nearly identical to that of the isentropes, it is a reasonable assumption that the net displacement using isentropes provides the best estimate of the net displacement in these simulations. Due to the difficulty in initializing passive tracers at different horizontal locations, the passive tracer analysis for the 45° bore was not conducted. Based on the similarity to the isentrope analysis, one can safely assume that an analysis of the bore at 45° using passive tracers would yield similar results as the isentrope analysis.

The net displacement of air parcels associated with a bore generated by a stronger density current is larger than that generated by the weaker density current (Fig. 4.43). In the AT simulations, the 0° bore has a maximum net displacement of 350 m and an average of between 150 m and 250 m. This maximum net displacement is 100 m larger, and the mean net displacement is 50 m larger. The maximum and mean net displacements are nearly twice as high in the ST simulations for those generated by the stronger density currents than those generated by the weaker density currents. For example, in the STAW simulation, the maximum and mean net displacement are around 80 m and 60 m, respectively, while those generated by the stronger density current are 140 and 100 m, respectively. Given the optimal environment in the model simulations, the stronger density current generates stronger bores with larger net displacements.

4.4.2.1 Inclusion of Westerly Wind Shear

Overall, adding westerly wind shear to the AT or ST simulations did not alter the maximum or minimum net displacement of the 0° bores (Figs. 4.41 and 4.44). However, adding westerly wind shear did affect the 45° bore. The 45° bores in the ATWW simulations with vertical shear has a lower mean (by 50 m) and max (by 50-70 m) at 80 min than those without vertical shear. By 140 min, the 45° bore with vertical shear had a higher maximum (by 25 - 50 m) than the one without vertical shear. The mean net displacement increased in 45° bore in the STWW and STAW simulations by about 10 m when vertical shear was added but decreased by about 10 m in the STSW simulation. However, at 200 min in the STSW simulation, the 45° bore had a higher net displacement by about 10 m than the 45° without vertical wind shear. *The effect of shear on the 45° bore was variable.* At times, the bores had a higher net displacement, and at other times, it had a lower net displacement.

The -45° bores in the AT simulations have a larger mean and maximum net vertical displacement than the displacement of the 0° or 45° bores (Fig. 4.46). This difference can be as large at 10-20% (25-50 m). This larger displacement is the result of a higher amplitude leading wave in the ATAW and ATSW simulations and a larger amplitude second crest in the ATWW simulation. This larger leading wave may be related to the superposition of the waves and the larger second crest may be related to the superposition effect or its proximity to the density current (though the density current is in a similar position relative to the bore in all AT simulations). The mean net displacement is larger in the ATSW simulation. This larger mean displacement is due to the higher amplitude first and second waves in the -45° bore than in the 45° bore. The amplitude of the -45° and 45° bores is higher than the amplitude of the 0° bore.

In the STWW and STAW simulations at 120 min, the 45° bore had a higher maximum and mean net displacement by about 10 m than the -45° bore, but the -45° bore had the higher mean net displacement by 5 – 10 m in the STSW simulation (Fig. 4.47). That difference is due to the slightly higher amplitude leading wave in the 45° bore than the -45° bore. However, later in the simulation (by 220 min) the -45° bore in the STAW simulation had the highest mean and maximum net displacement. This variation is consistent with that of the AT simulations where the effects of the vertical wind shear did not seem to favor one side over the other.

The inclusion of linear westerly wind shear does not impact the 0° bore significantly. In terms of the maximum and mean net vertical displacement, there is no favored side where there is a consistently stronger bore. Sometimes, in the same simulation, the -45° bore had a higher displacement and sometimes the 45° bore had a higher displacement (e.g., STAW). The linear wind shear does not increase the wave trapping condition anywhere around the bore, but the shear itself can cause differential advection of the waves. This superposition is most likely the reason for the variable structure, but more research is needed in that area.

4.5 Summary

Atmospheric bores are generated similar to how bores are formed in the real atmosphere in six of the nine simulations. These simulated bores' characteristics are consistent with observed bores: little to no change in the surface temperature and a semi-permanent displacement of the isentropes. The depth of these bores extends in the lowest few km of the atmosphere. They have a wavelength of 10-15 km and propagate faster than the density current.

By design, the most favorable location for wave trapping was the southern end, but because of the favorable conditions, bores were generated from -30° to 30°, a 120° swath around the density current. The characteristics of the bores did weaken as the angle from the optimal wave trapping increased, and this effect was more noticeable in the strong wind simulations than in the weak wind simulations.

Adding in westerly wind shear in the lowest 2 km changed the bores' characteristics at 45° and -45°. The bore was not favored one side of the density current over the other. Both sides produced notable bores. The wavelength of the 45° and -45° bores was non-uniform, but the wavelength of the 0° bore was more uniform. At times one side would have a higher net displacement than the other but then have a smaller displacement at another time. One possibility for this that was discussed is the superposition of the waves at different levels.

This superposition effect has not yet been observed or simulated to the author's knowledge, but it is worth further exploration.

The net vertical displacement in these simulations was around 250 – 300 m for the AT simulations and around 100 m for the ST simulations. These displacements are lower than the observed net displacements of between 500 m to 1 km (see Table 1.1), but the density current that formed these bores is weaker than many observed density currents. However, even in the most optimal environments, a 200-300 m displacement is sufficient to initiate convection (Fig. 3.2). Atmospheric bores are certainly a plausible method of CI for NB events, assuming that the bore is far enough ahead of the parent MCS/density current to be considered pristine CI.

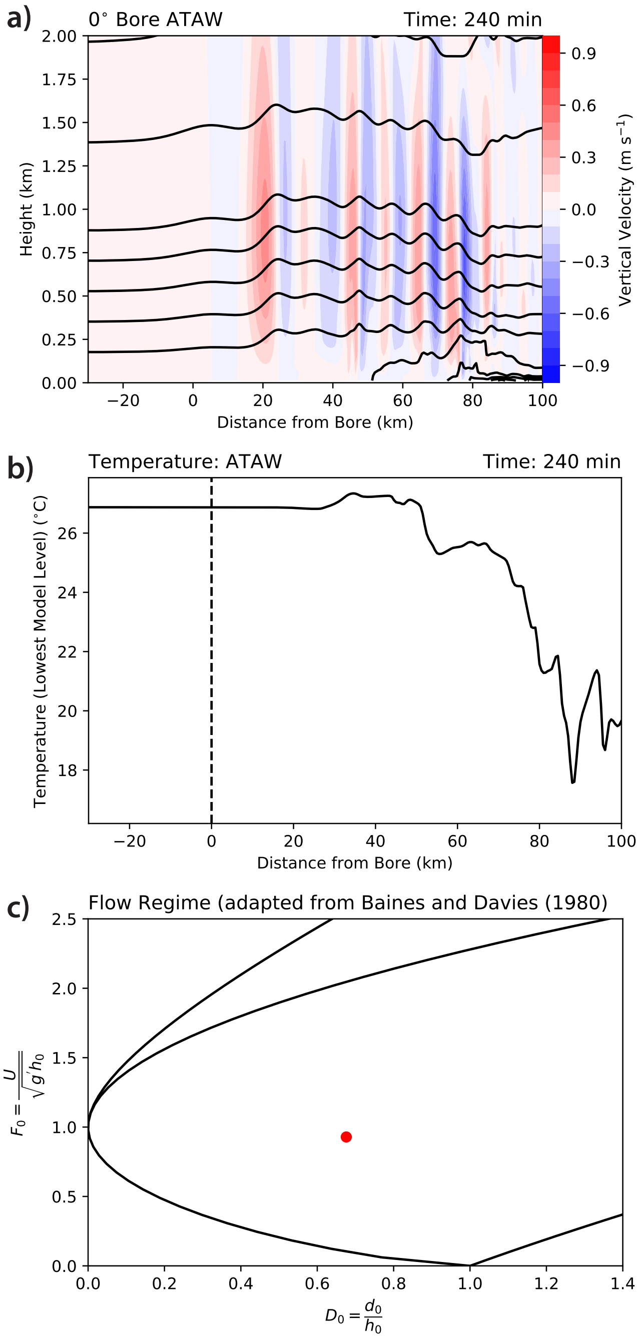

Figure 4.1: (a) Potential temperature (contoured every 2 K) and vertical velocity (color-filled) for the ATAW bore at 240 min. (b) Near-surface temperature for the ATAW bore at 240 min. The leading edge of the bore is denoted by the vertical black line. (c) The flow regime for the ATAW bore. Note that $g' = (\theta_{inv} - \theta_{sfc})/\theta_{sfc}$. The red dot is in the partially-blocked flow regime.

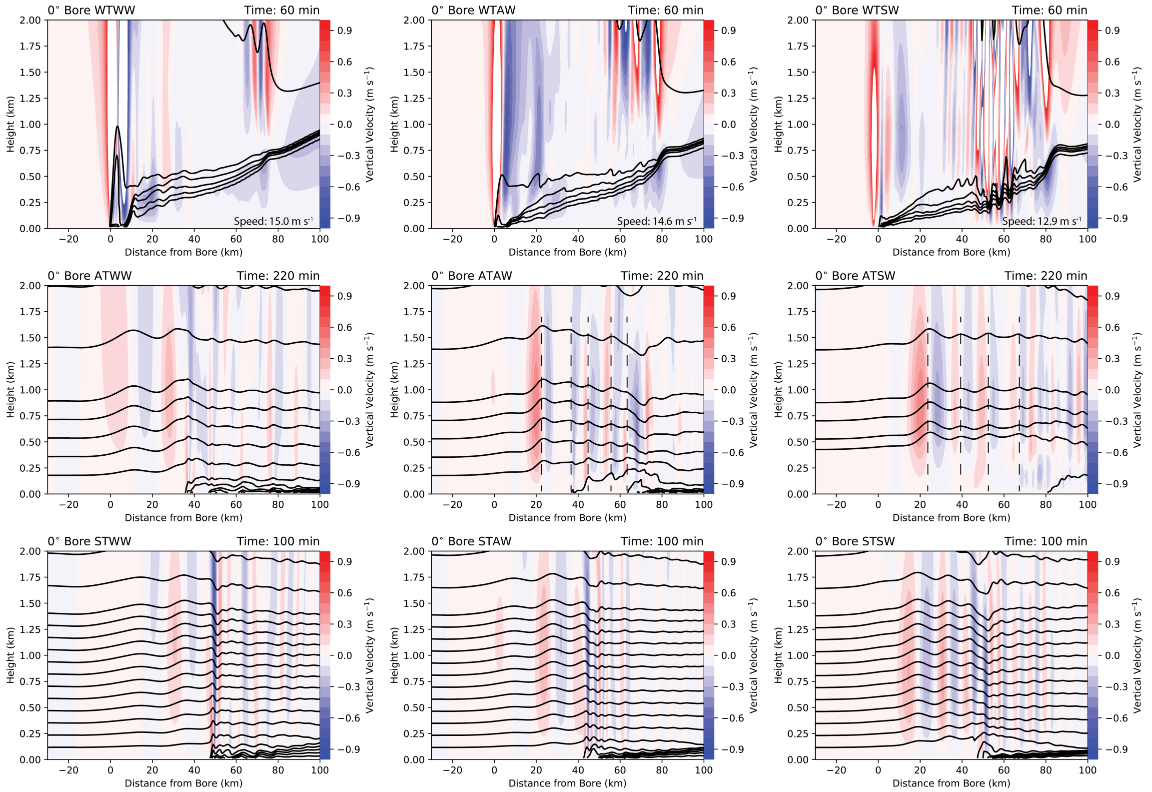

Figure 4.2: As in Fig. 4.1a, but for the (a) WTWW, (b) WTAW, (c) WTSW, (d) ATWW, (e) ATAW, (f) ATSW, (g) STWW, (h) STAW, and (i) STSW simulations. The WT simulations are shown at 60 min, the AT simulations are shown at 220 min, and the ST simulations are shown at 100 min.

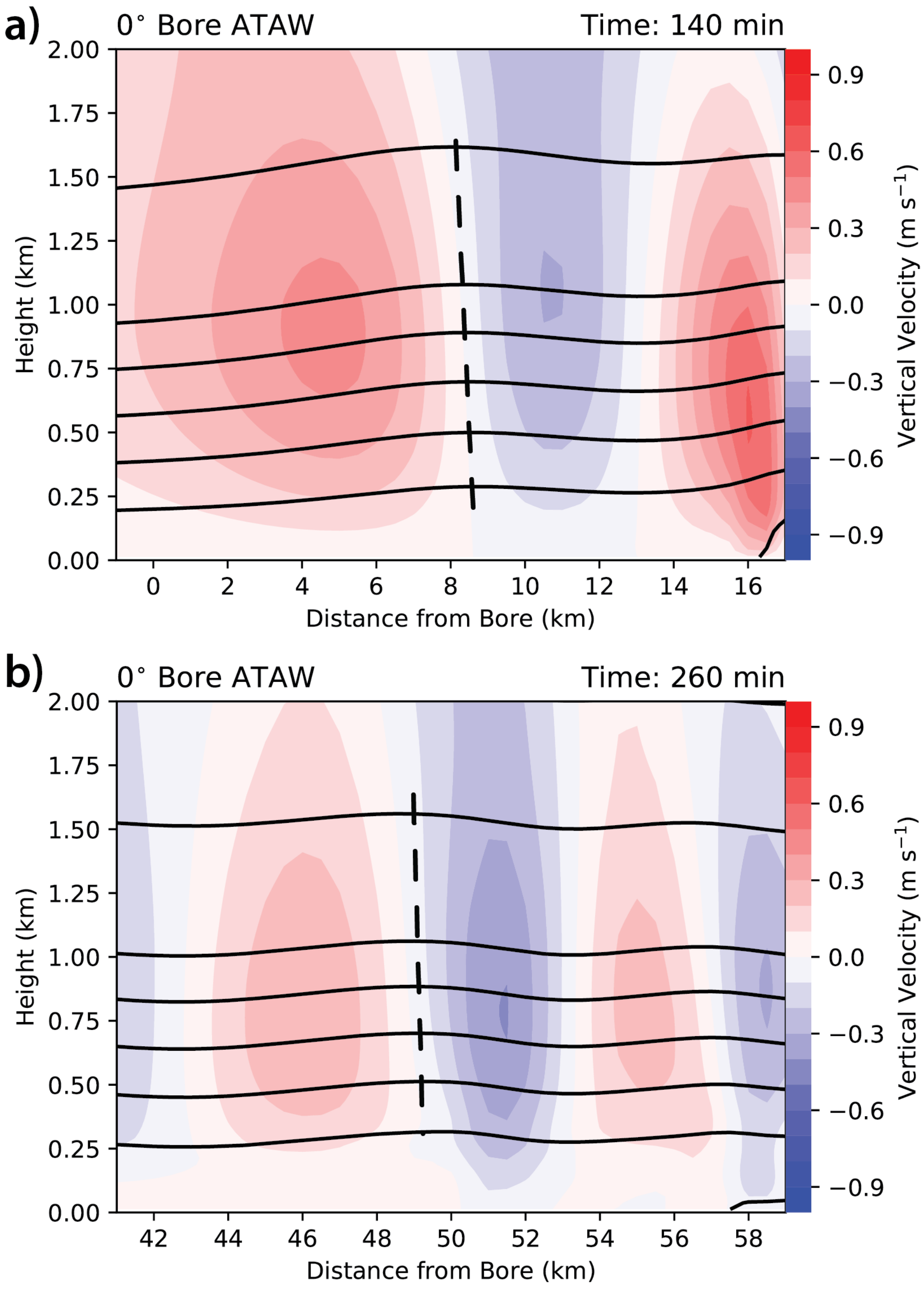

Figure 4.3: A zoomed-in image to one wave associated with the bore like feature in the ATAW simulation at (a) 140 min and (b) 260 min. The dashed line indicates the crest of the isentropes associated with this wave.

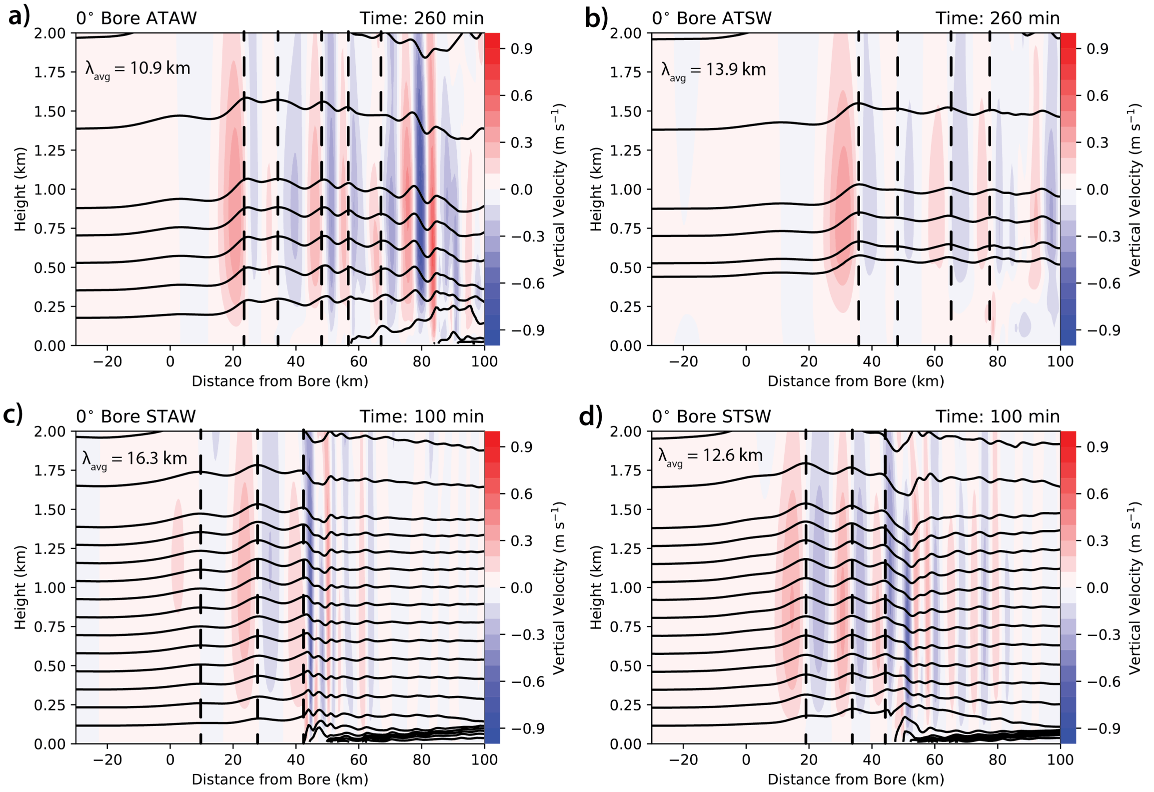

Figure 4.4: Vertical velocity (color-filled) and potential temperature (K; contoured every 2K) for (a) the ATAW bore and (b) the ATSW bore at 260 min and (c) the STAW bore and (d) the STSW bore at 100 min. The vertical dashed lines denote the crests of the bore and the average wavelength is denoted in the upper left of each panel.

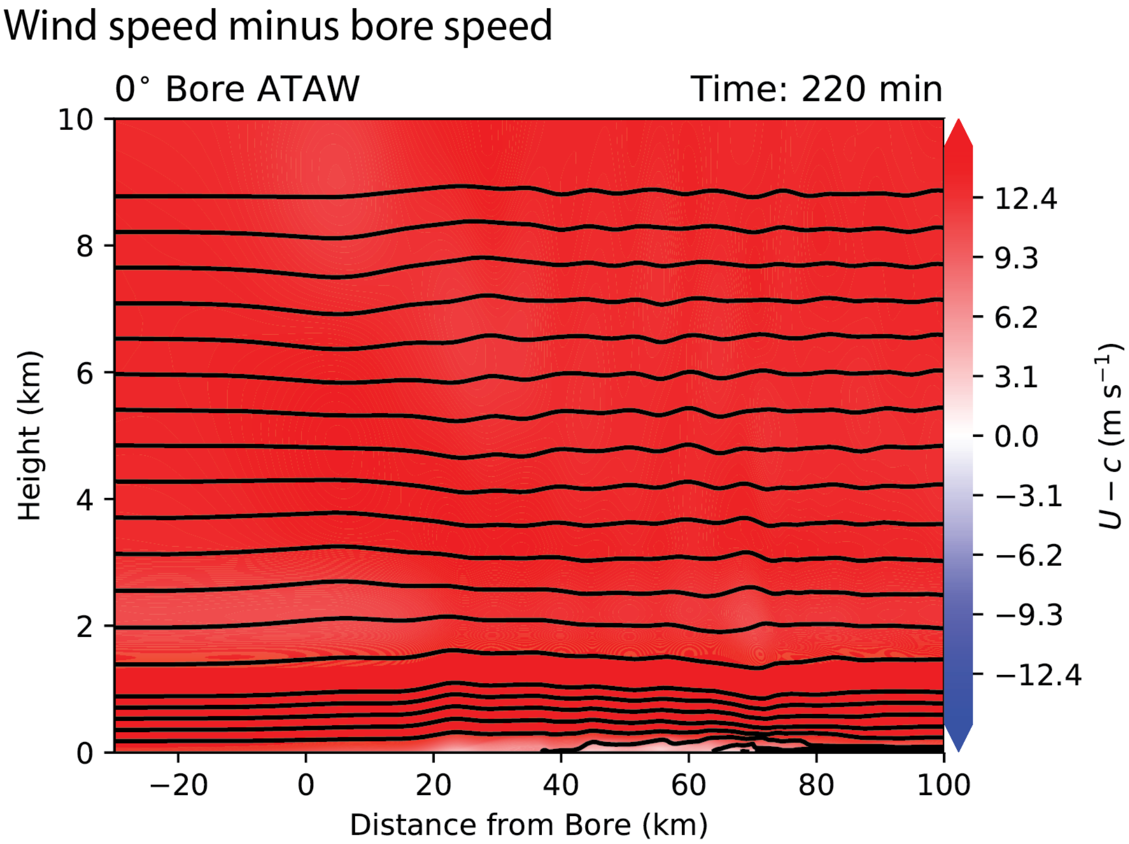

Figure 4.5: Wind speed minus bore speed for the ATAW simulation at 220 min. Red colors indicate positive difference and blue indicate negative. Isentropes contoured every 2K

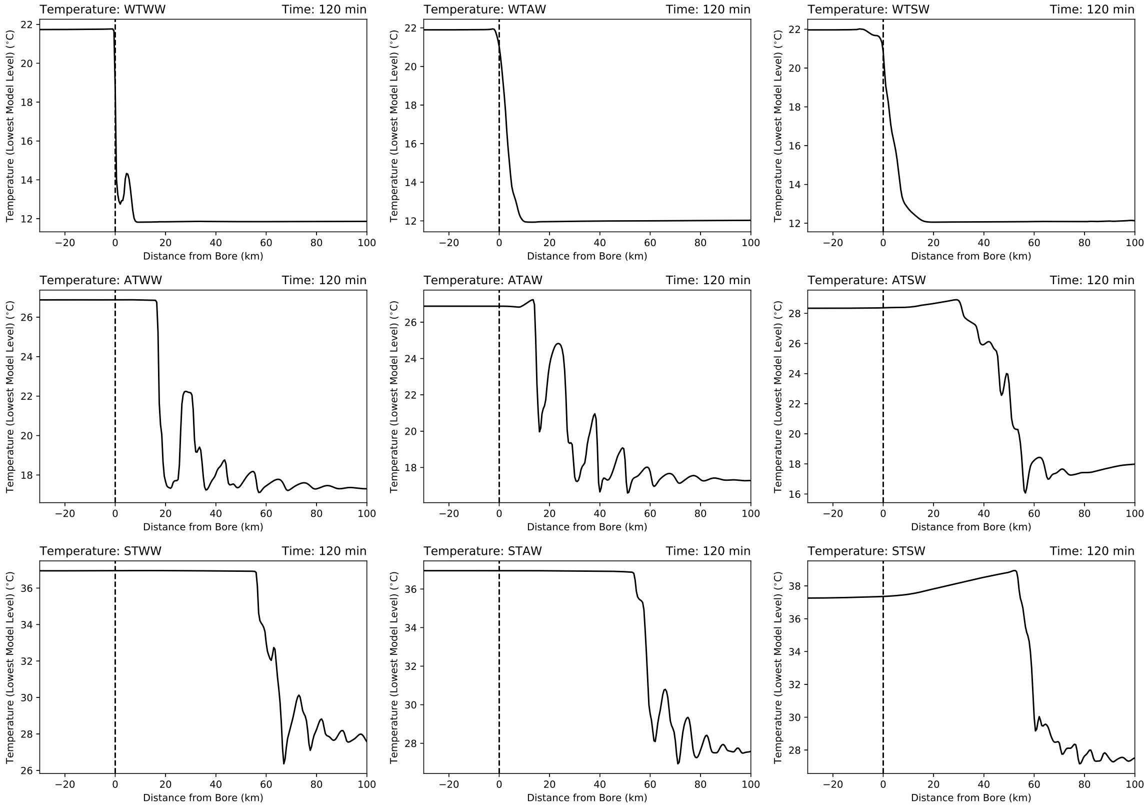

Figure 4.6: As in fig 4.2, but for the near-surface temperature at 120 min. The leading edge of the bore is dented by the vertical dashed line (In the WT simulations, this line denoted the density current).

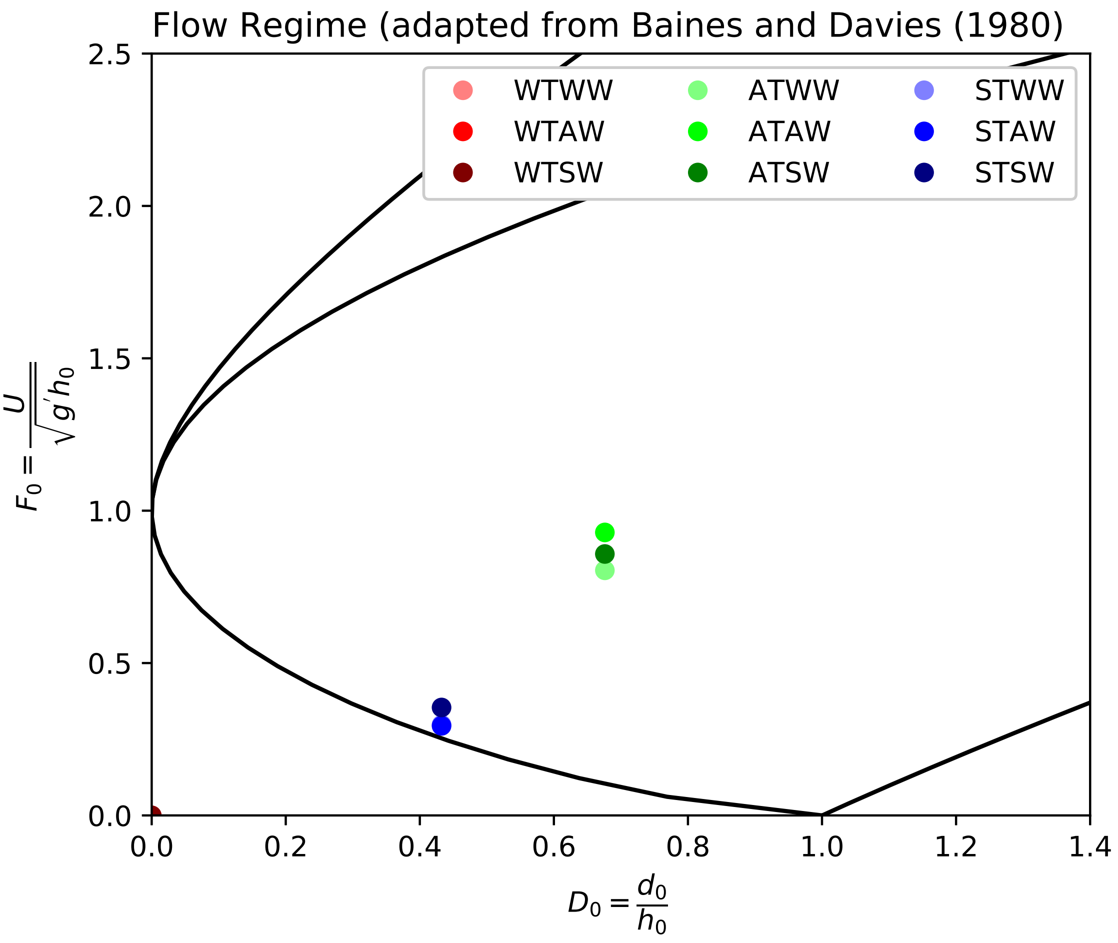

Figure 4.7: Flow regime for the nine simulations. $g' = (\theta_{inv} - \theta_{sfc})/\theta_{sfc}$. The red dots denote the WT simulations, the green dots denote the AT simulations, and the blue dots denote the ST simulations. The shade of the dots represent the strength of the wind speed. The flow regime for the red dots are at the origin because there is no stable layer, so it's technically undefined.

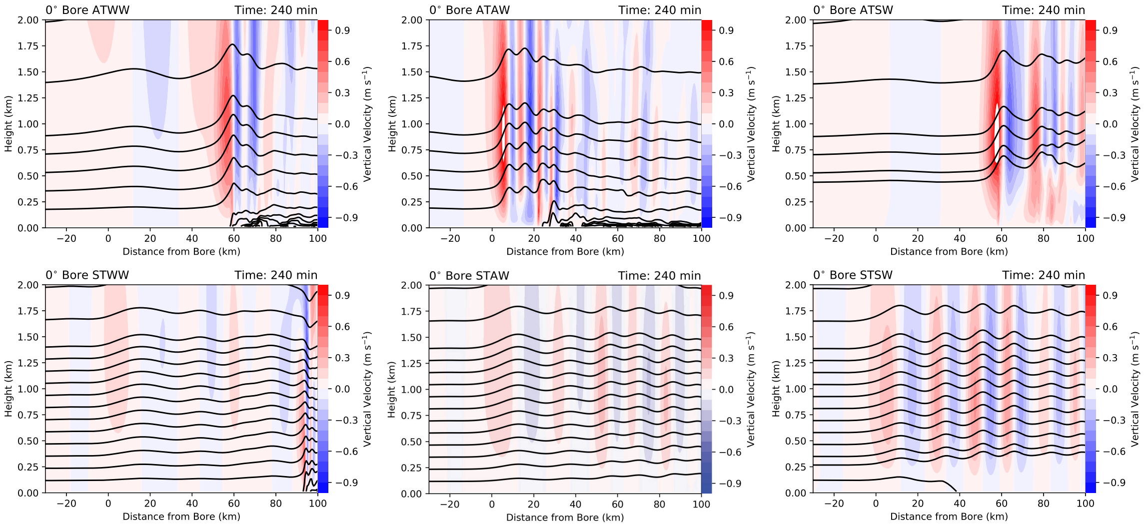

Figure 4.8: As in Fig. 4.1a, but for the a) ATWW, b) ATAW, c) ATSW, d) STWW, e) STAW, and f) STSW simulations at 240 min initialized by a stronger cold pool.

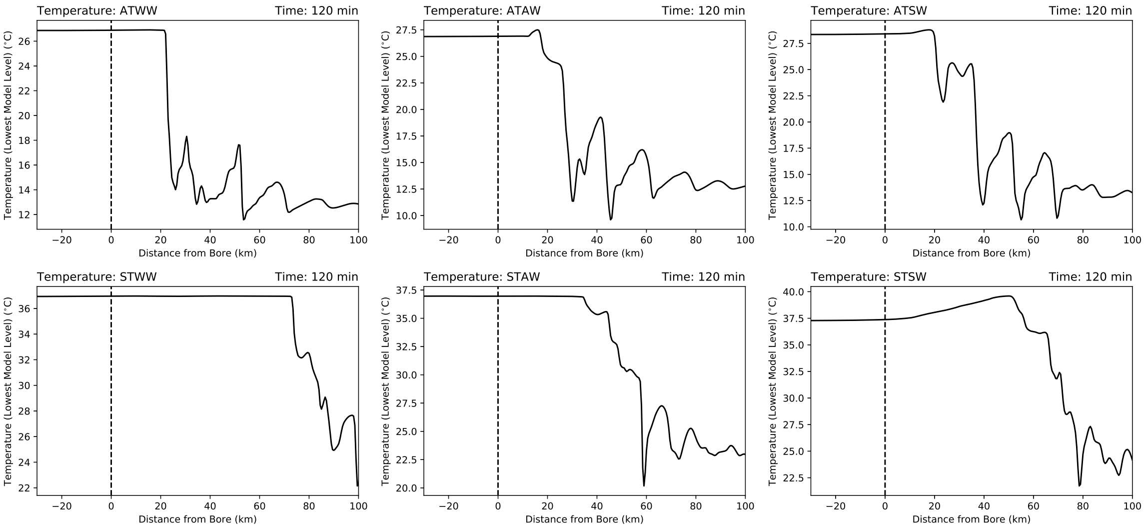

Figure 4.9: As in fig 4.8, but for the near-surface temperature at 120 min.

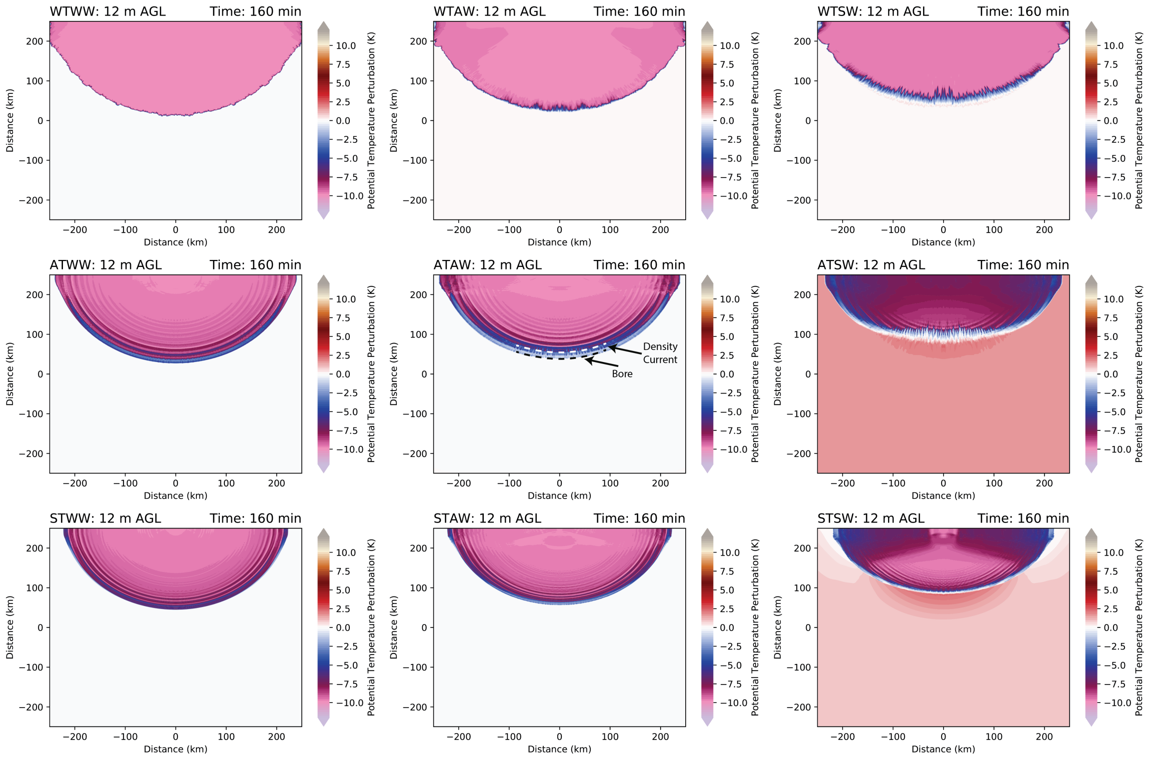

Figure 4.10: Horizontal cross-sections of potential temperature (color-filled) for the a) WTWW, b) WTAW, c) WTSW, d) ATWW, e) ATAW, f) ATSW, g) STWW, h) STAW, and i) STSW simulations. In e), dashed lines denote the density current (white line) and the bore (black line).

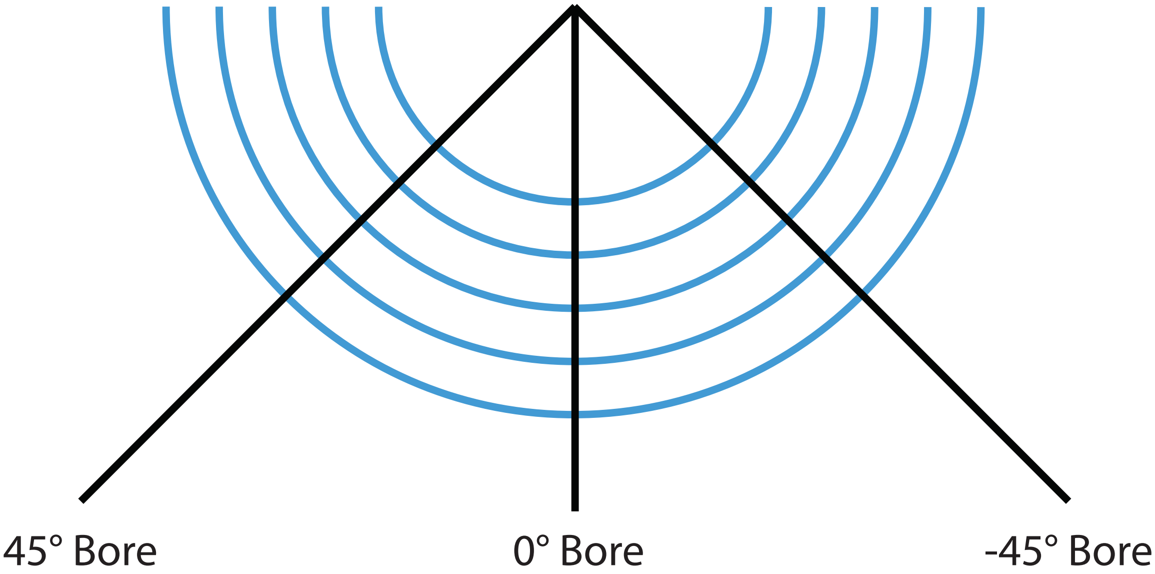

Figure 4.11: Illustration of the angles of the 45°, 0°, and -45° bores.

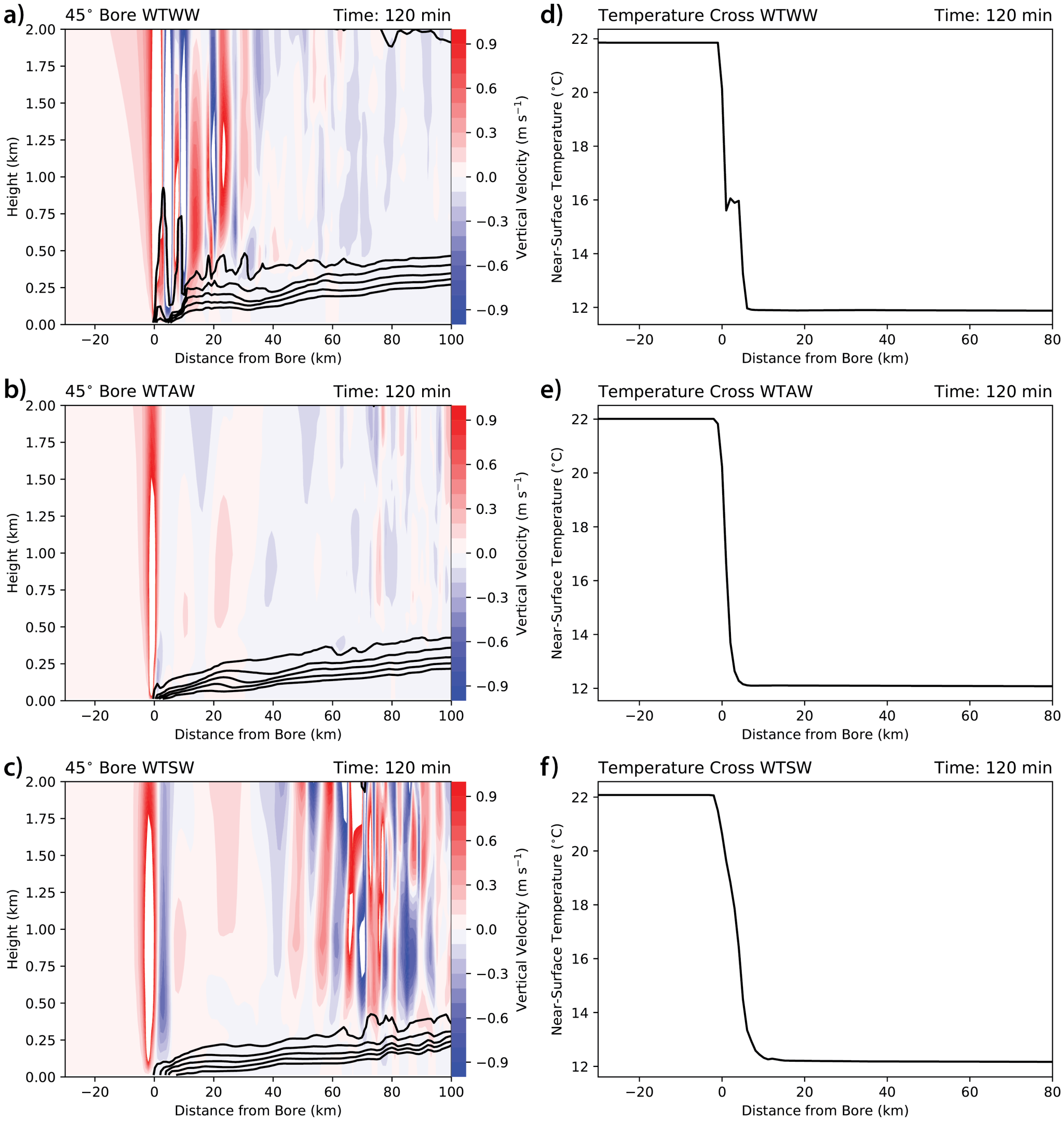

Figure 4.12: Potential temperature (black lines every 2K) and vertical velocity (color-filled) for the 45° bore for the a) WW, b) AW, and c) SW simulations at 120 min in WT environments. d), e), f) are the surface temperature corresponding to the panels on the left.

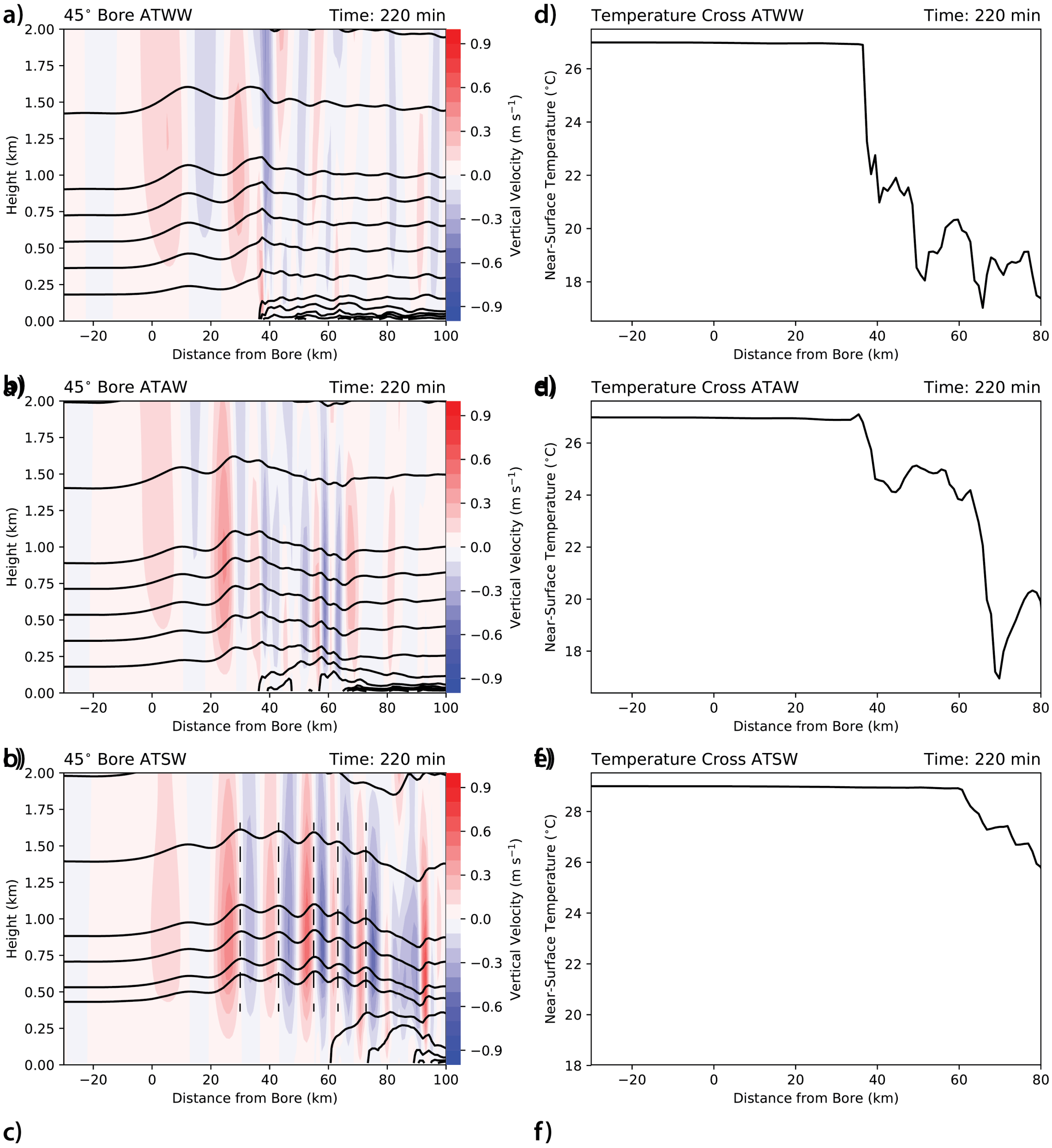

Figure 4.13: As in Fig. 4.13, but for AT environments at 220 min.

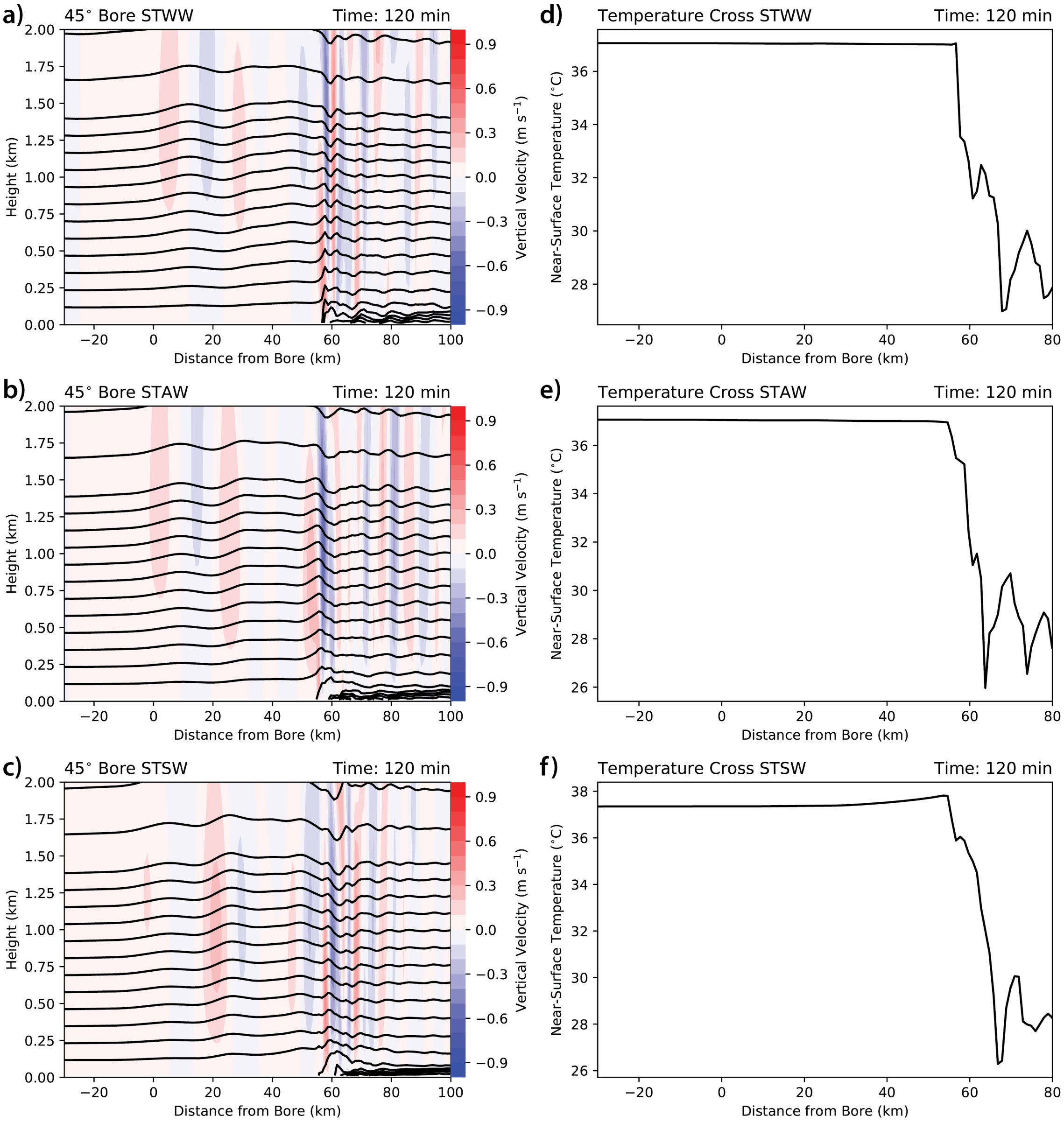

Figure 4.14: As in Fig. 4.13, but for ST environments at 120 min.

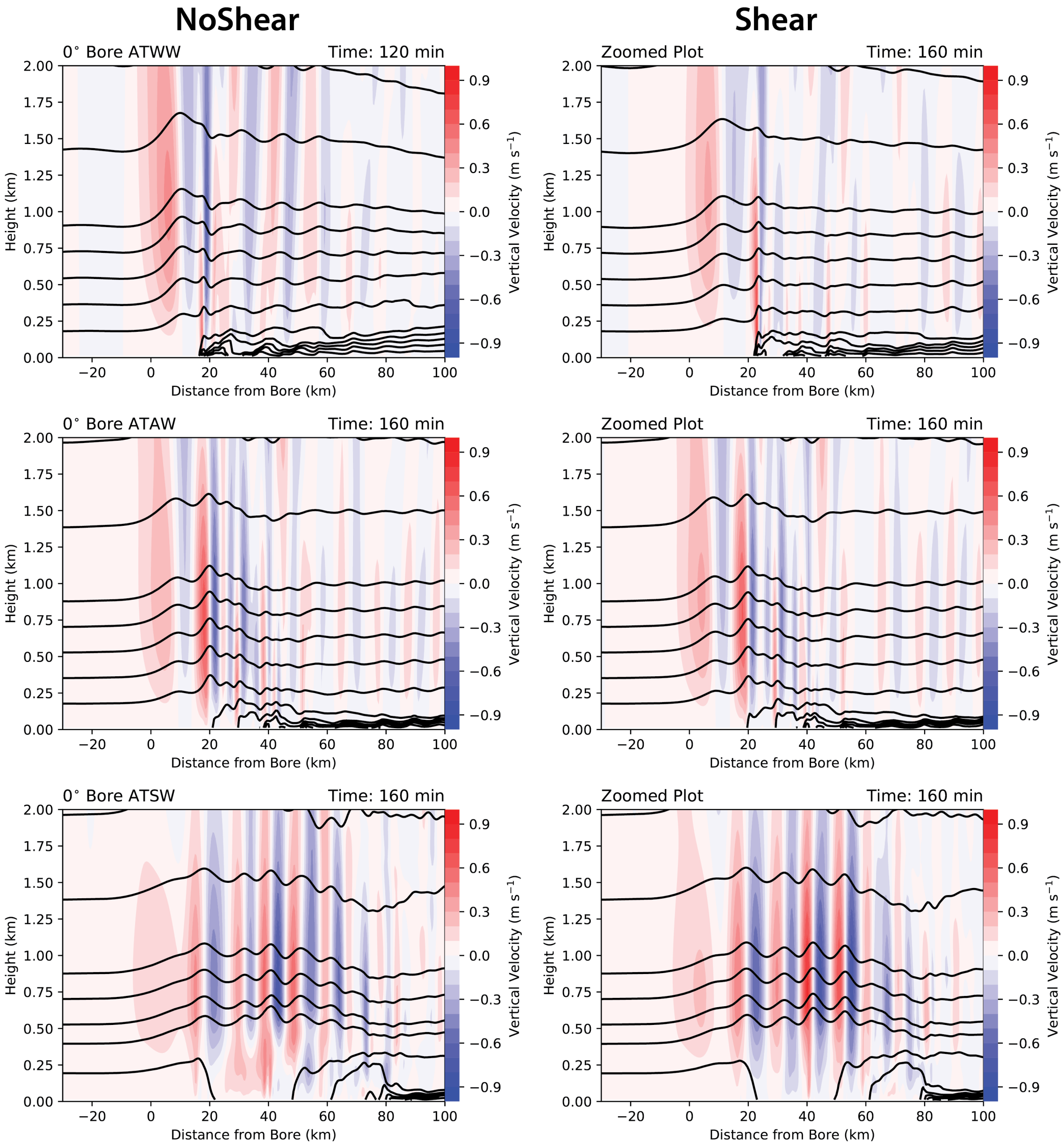

Figure 4.15: Comparison of the 0° bores in the AT simulations for a) - c), without vertical shear and d)- f), with vertical shear. Potential temperature is contoured every 2K and vertical velocity is color filled.

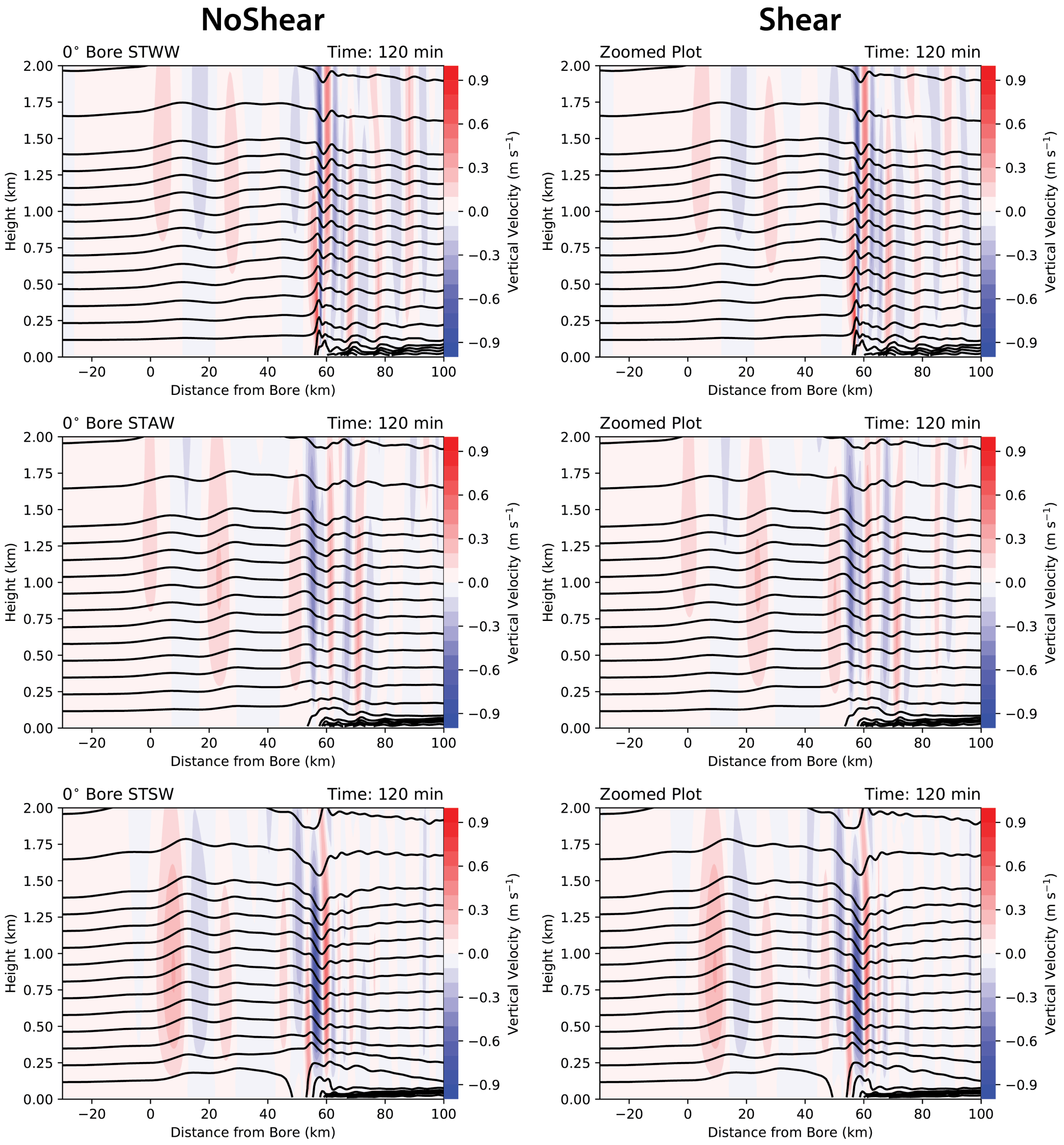

Figure 4.16: As in Fig. 4.15, but for the ST simulations

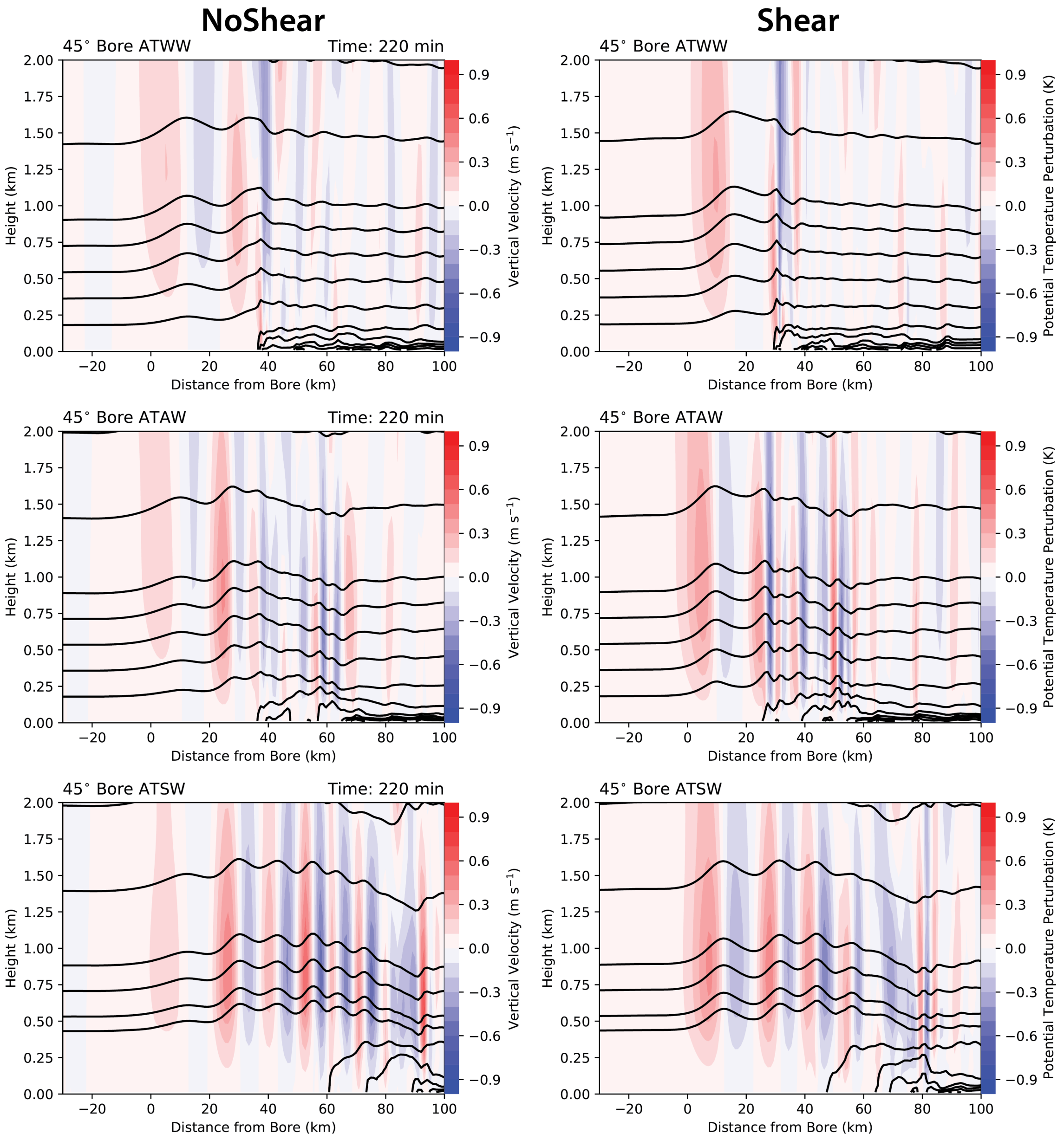

Figure 4.17: As in Fig. 4.15, but for the 45° bores.

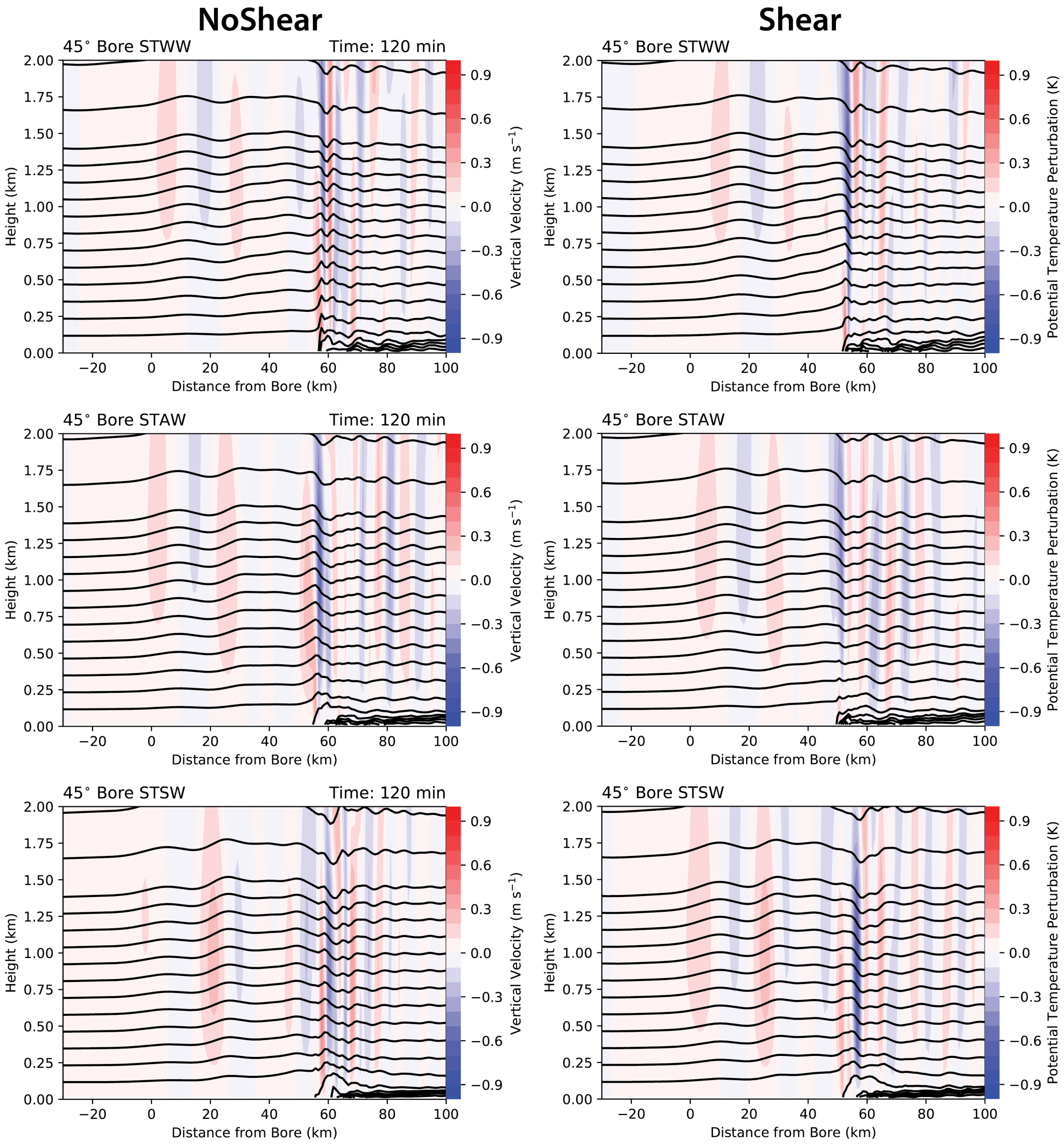

Figure 4.18: As in Fig. 4.17, but for the ST simulations.

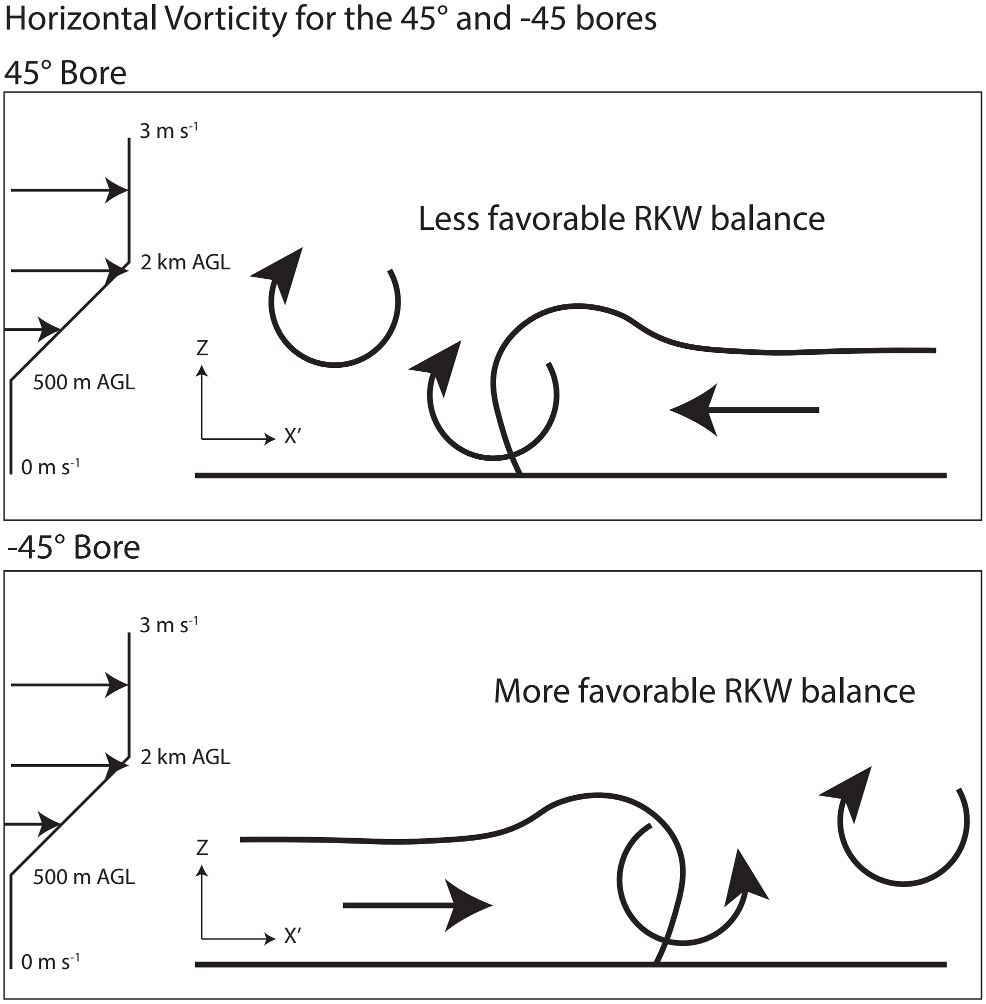

Figure 4.19: Two-dimensional illustrations the 45° (top) and -45° (bottom) density currents. Height is on the y-axis and the horizontal distance in the density-current-relative reference frame (X' on the figure) is on the x-axis. The arrow on the circles indicates the sense of the circulation. The circle at the density current head represents the baroclinically-generated horizontal vorticity. The circle outside o the density current represents the horizontal vorticity that is generated by the vertical wind shear. The arrow in the density current indicates its propagation direction. The westerly environmental wind speed is indicated by the lines and arrows on the left of the panels.

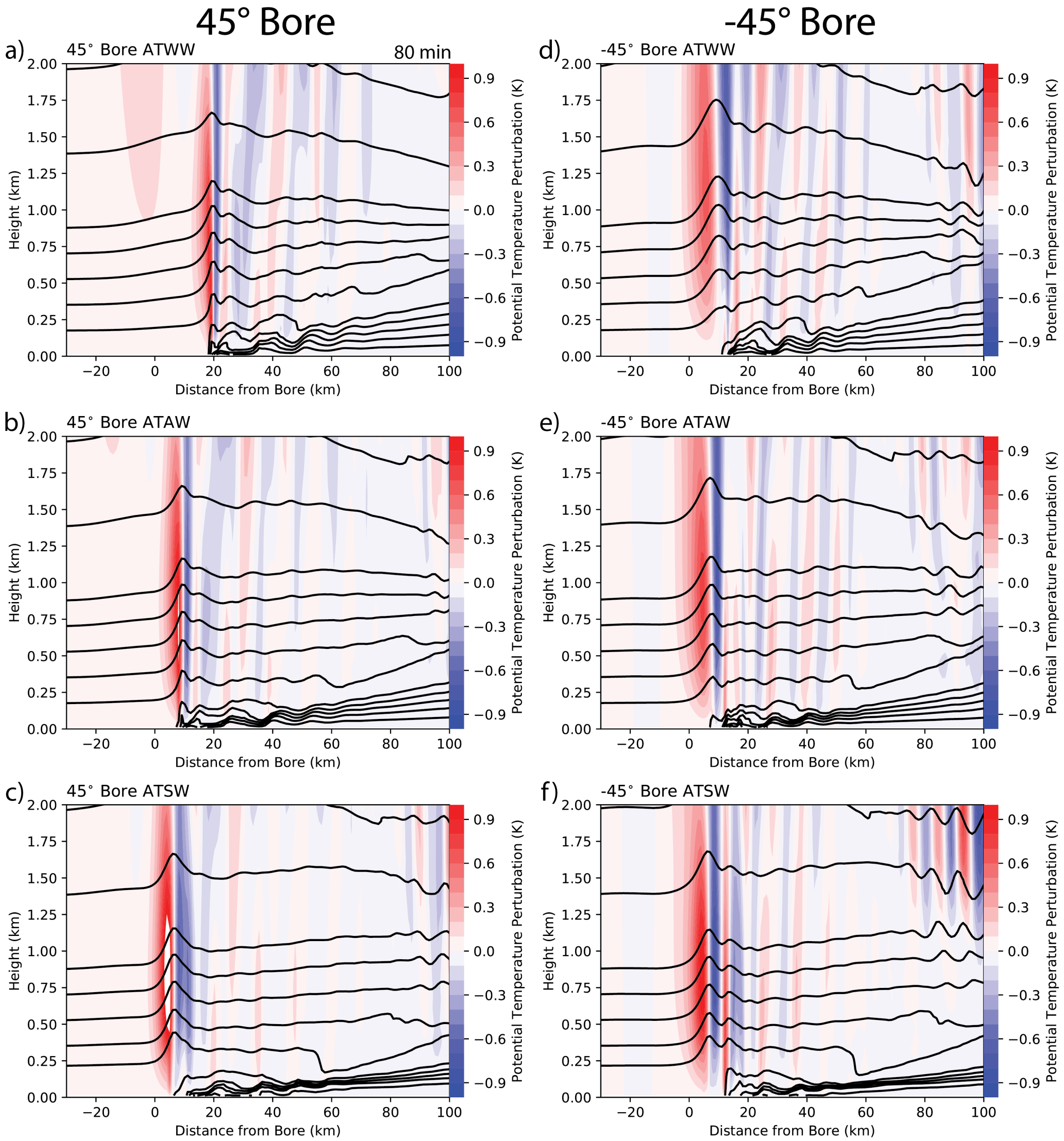

Figure 4.20: Comparison of the (a) - (c) 45° density currents, (d) - (f) -45° density currents.

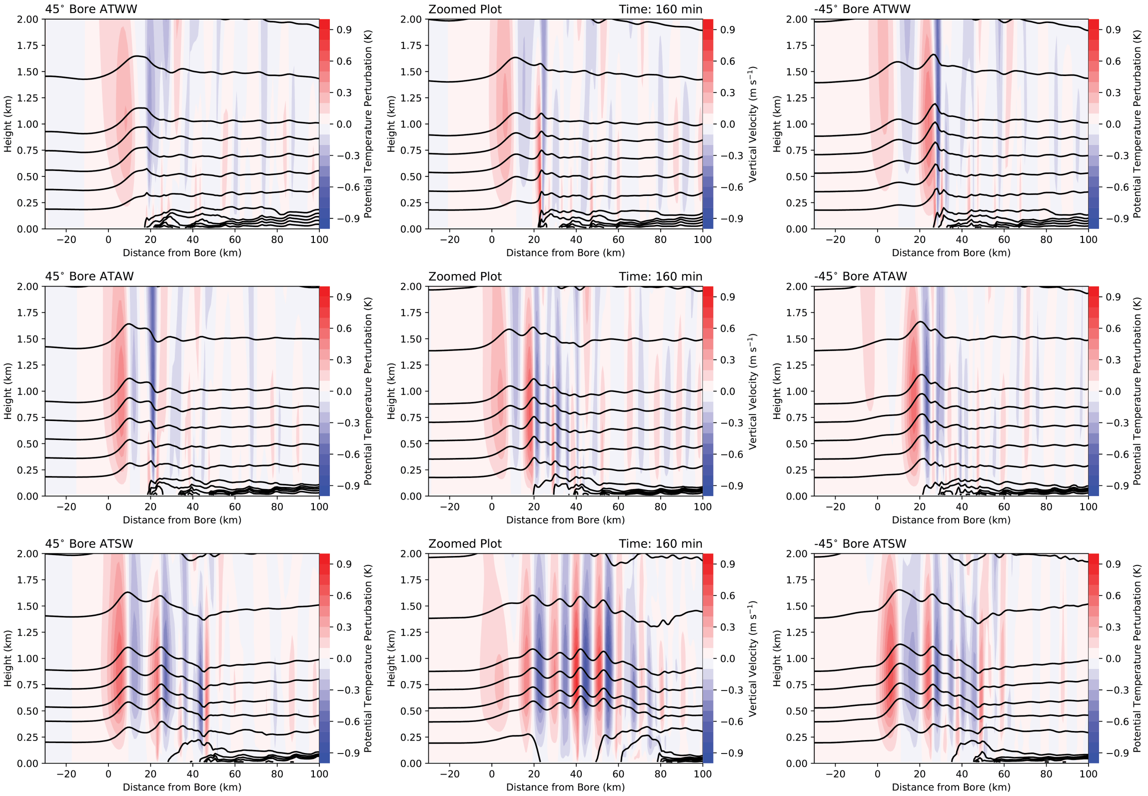

Figure 4.21: Comparison of the a) - c) 45° bores, d) - f) 0° bores, and g) - i) -45° bores in the AT simulations with vertical shear at 160 min.

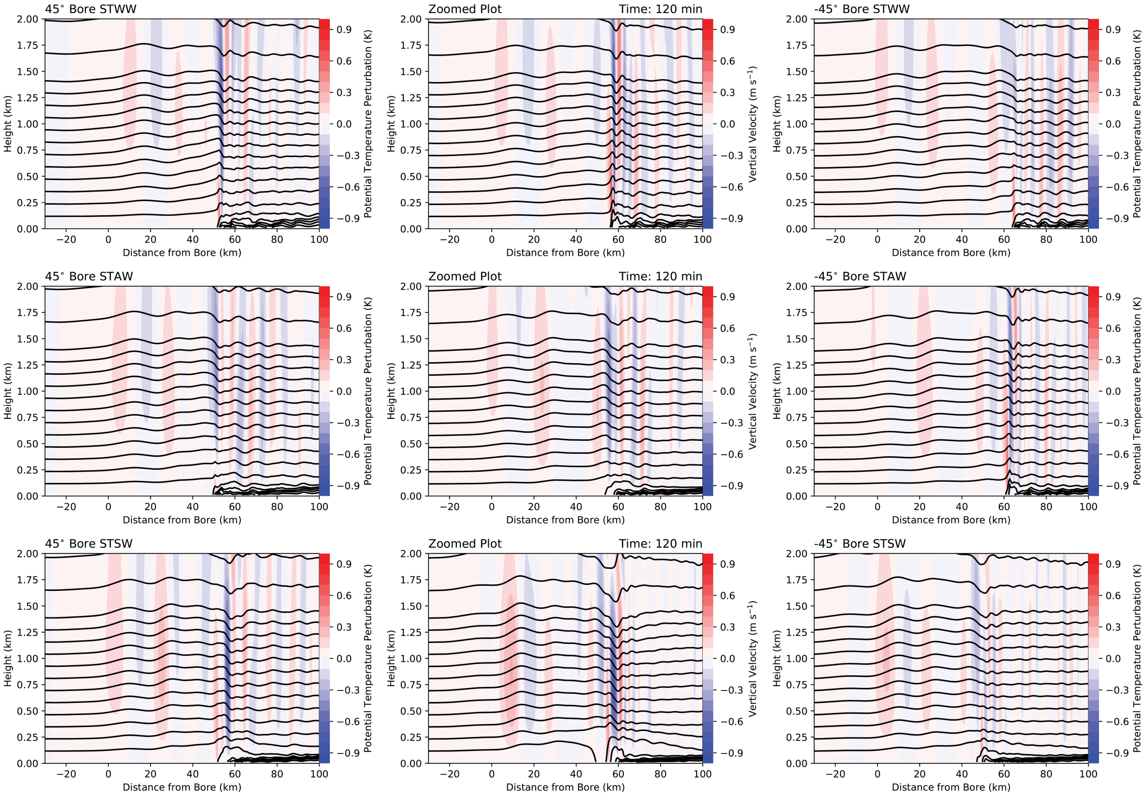

Figure 4.22: As in Fig. 4.21, but for the ST simulations at 120 min.

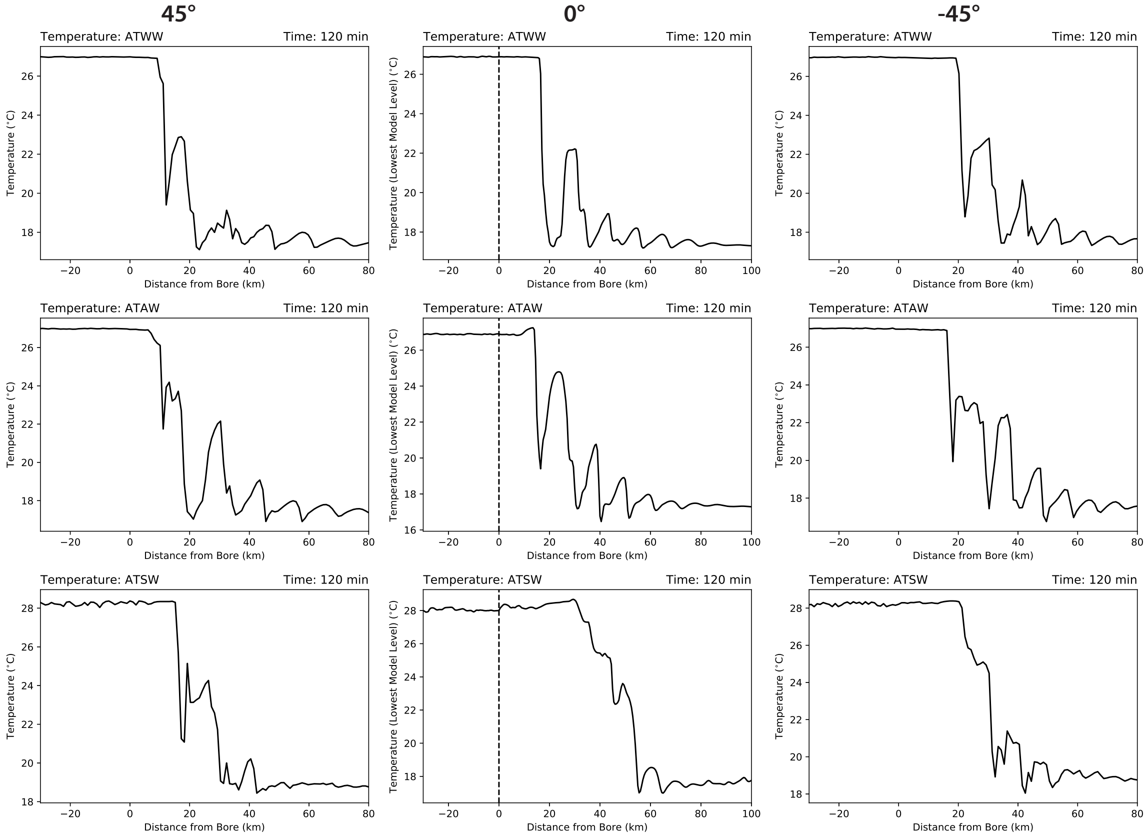

Figure 4.23: As in Fig. 4.21, but for the surface temperature (°C) in the AT simulations at 120 min.

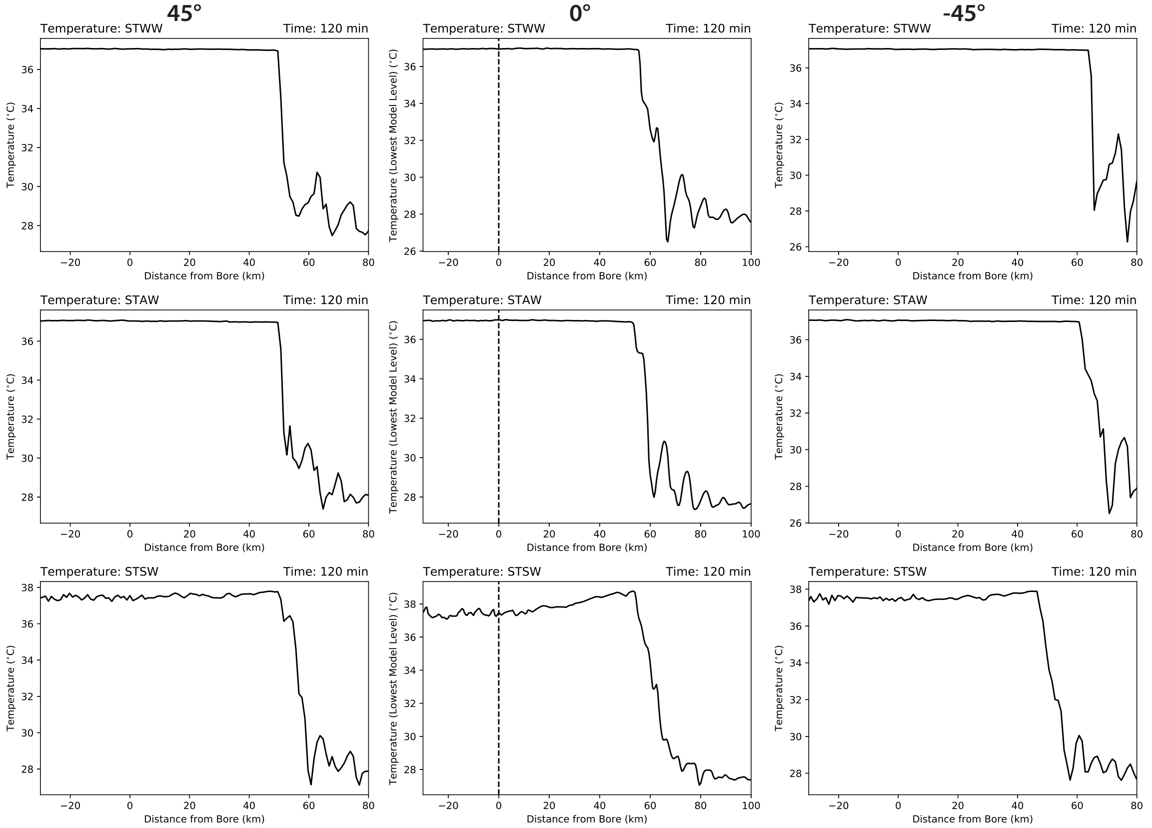

Figure 4.24: As in Fig. 4.23, but for the ST simulations with vertical wind shear.

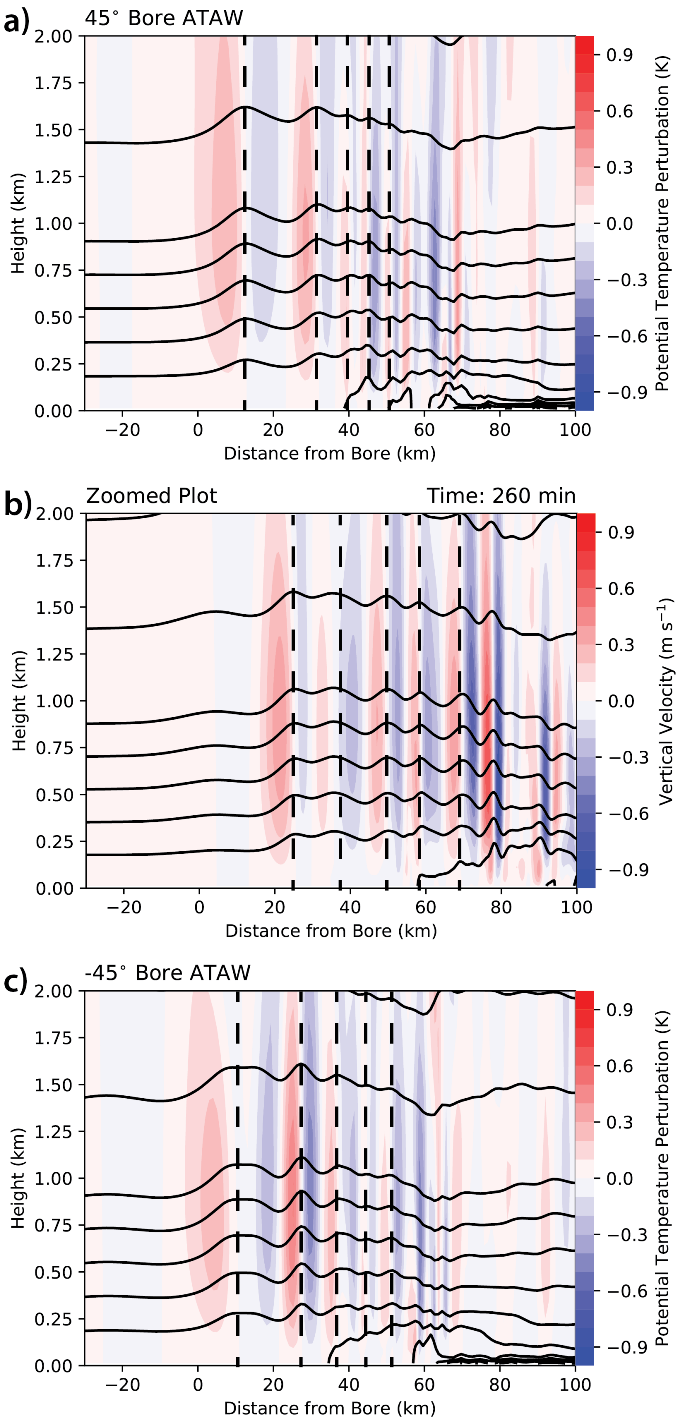

Figure 4.25: Potential temperature (contoured every 2K) and vertical velocity (color-filled) for the AT simulations with vertical wind shear at 260 min. The vertical black dashed line denotes the crests of the bores.

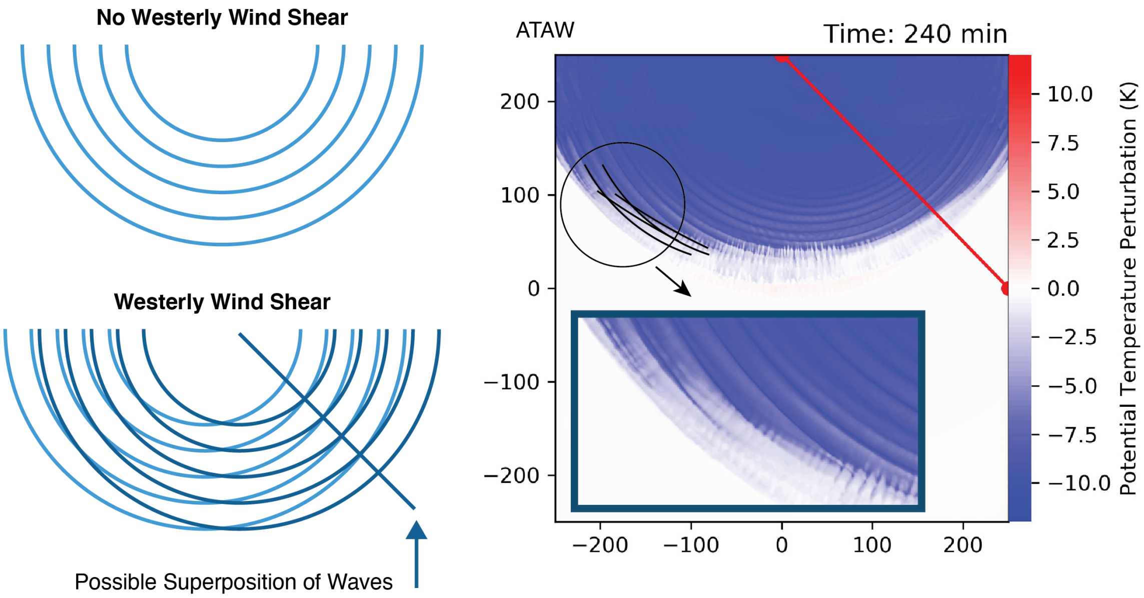

Figure 4.26: Illustration of the superposition of waves. The left if a schematic of the process and the right is the possible process in the ATAW simulation at 240 min. The different orientation of the waves is denoted by the lines in the circle. The inset is the same region just zoomed for clarity.

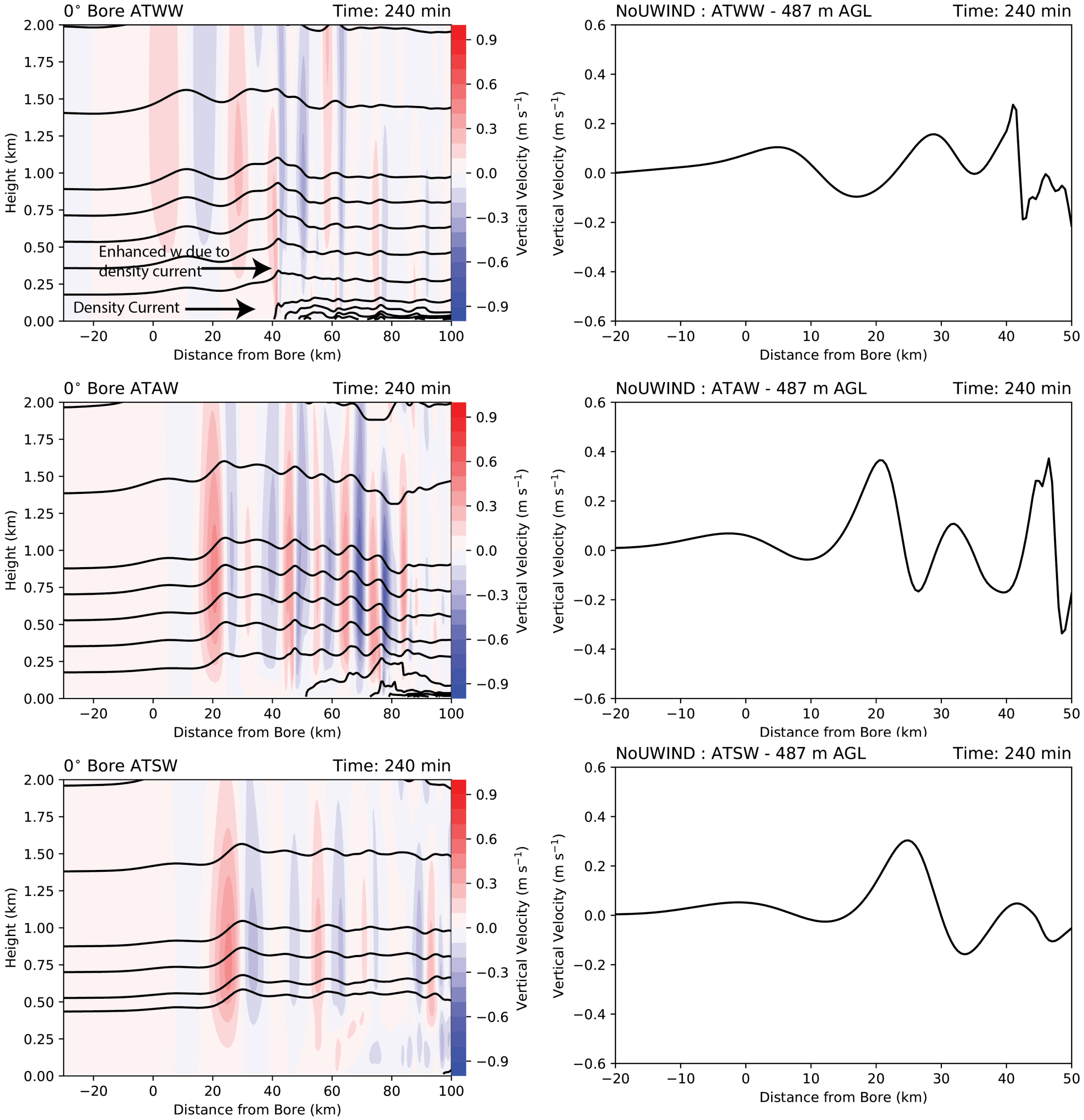

Figure 4.27: a) - c) Potential temperature (contoured every 2K) and vertical velocity (color-filled) for the 0 ° bores in the AT simulations at 240 min. The corresponding vertical velocity at 500 m AGL is shown on the right.

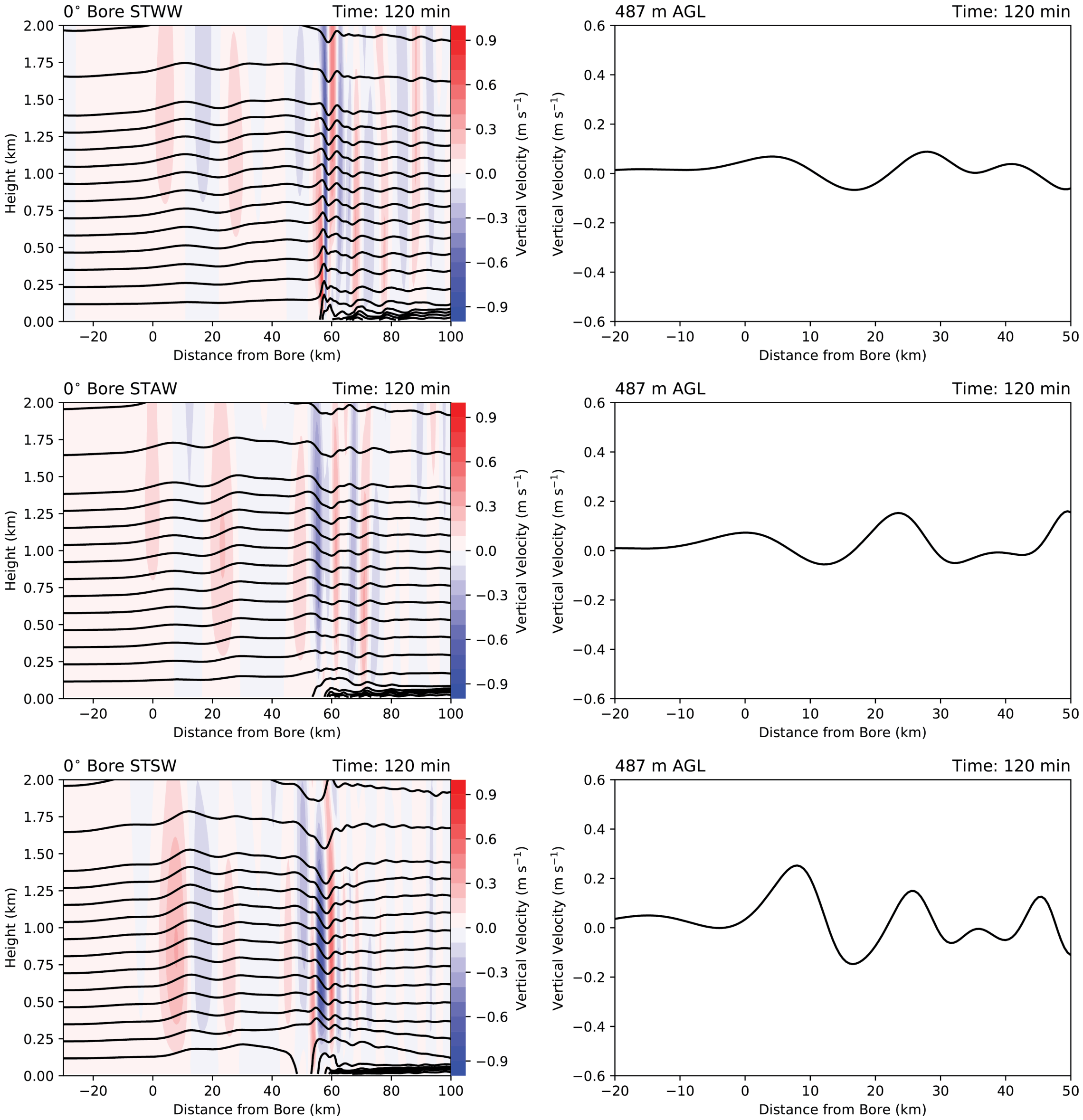

Figure 4.28: As in Fig. 4.27, but for the ST simulations at 120 min.

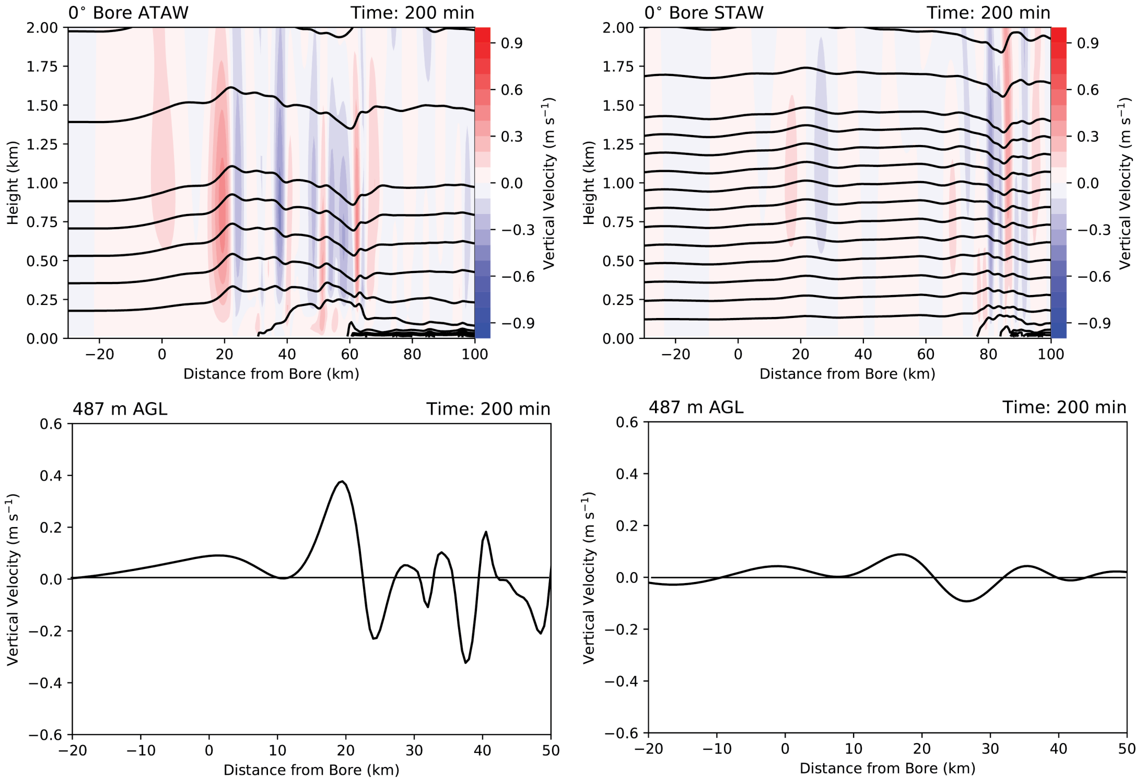

Figure 4.29: Comparison of the length of the bore in the a) ATAW simulation and b) STAW simulation without vertical shear. The vertical velocity associated with the bores is given in c) and d).

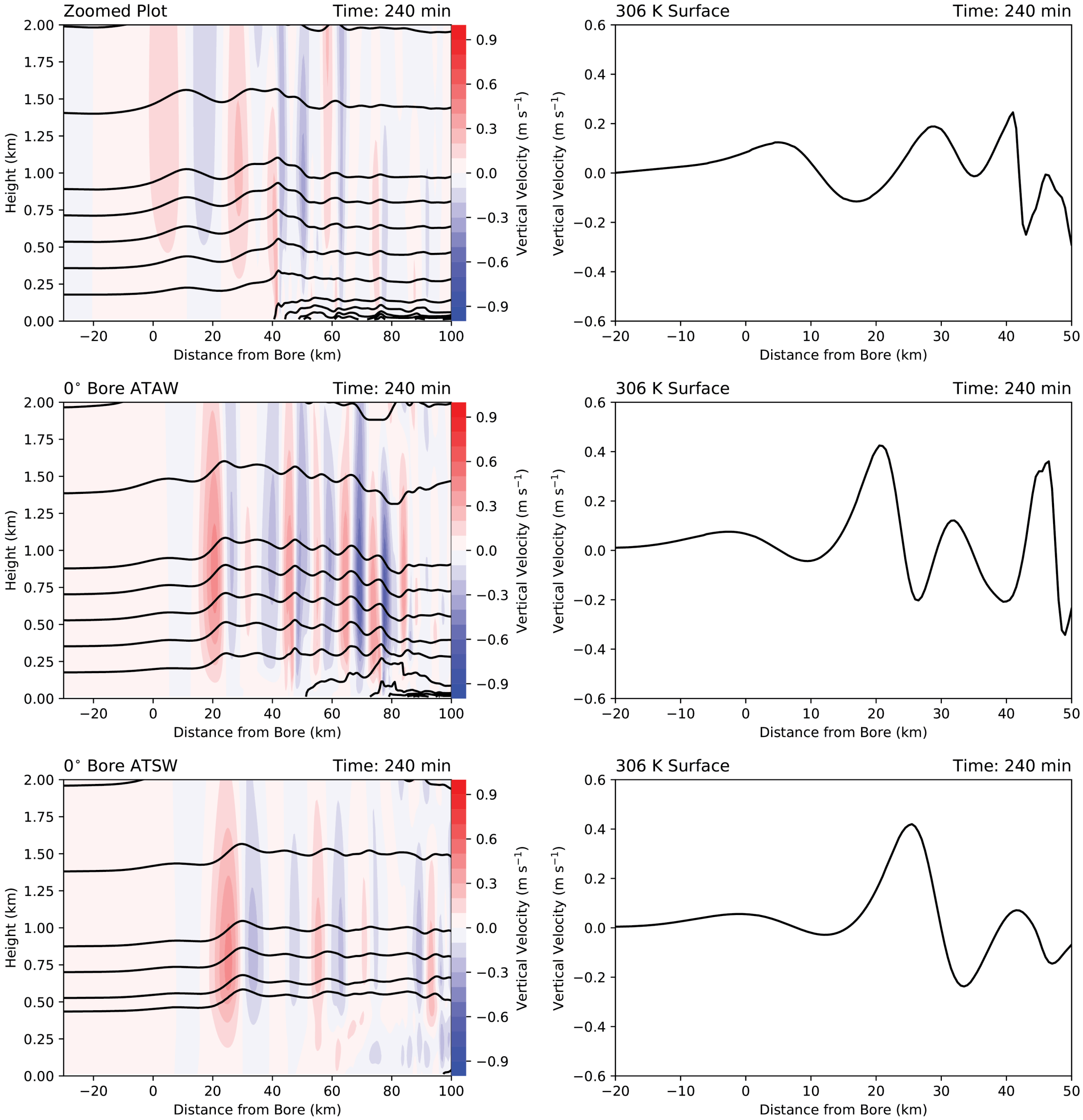

Figure 4.30: As in Fig. 4.27, but for the vertical velocity at the 306 K surface rather than at 500 m.

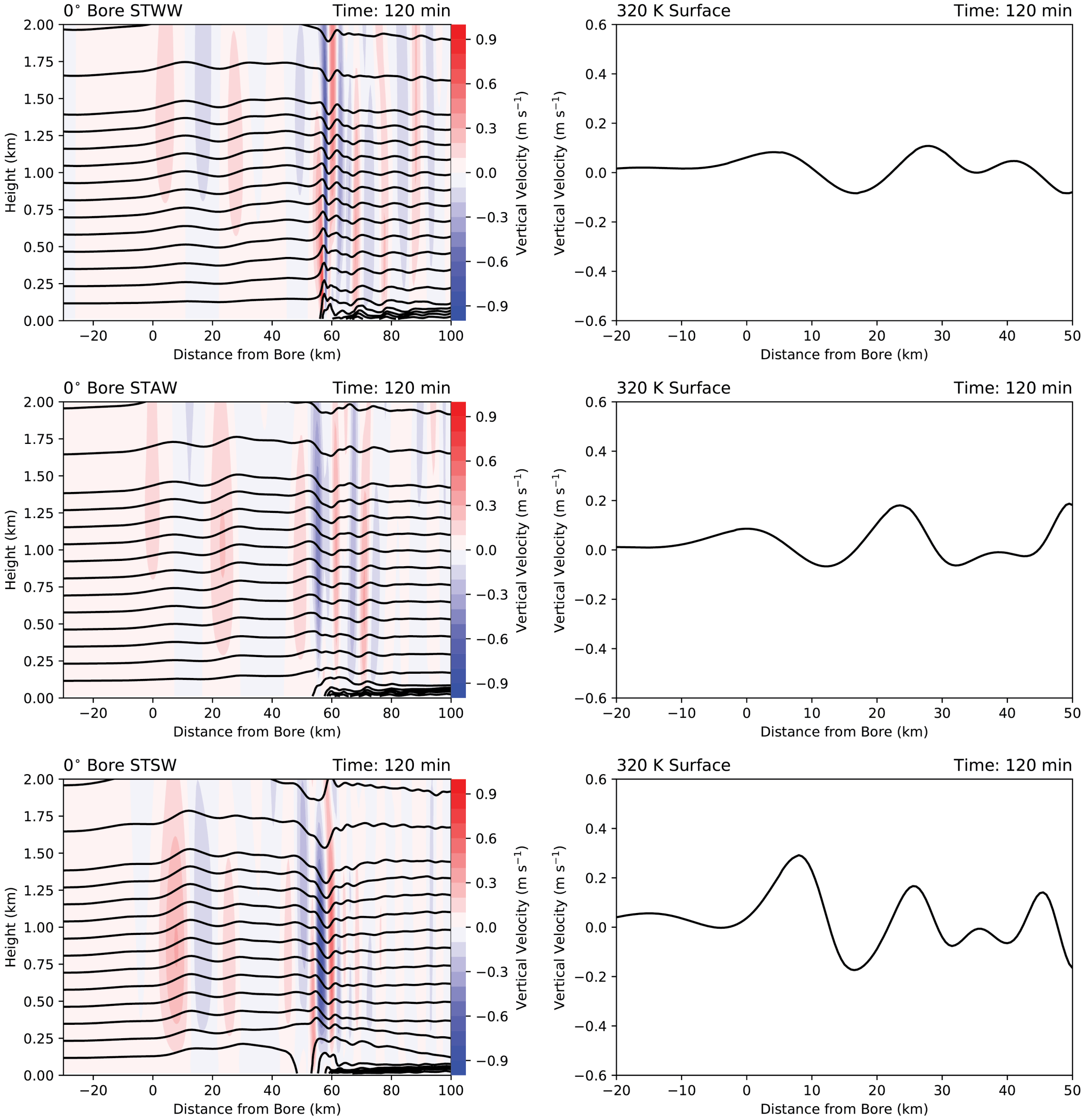

Figure 4.31: As in Fig. 4.30, but for the ST simulations at 120 min. The vertical velocity is shown on the 320 K isentropic surface.

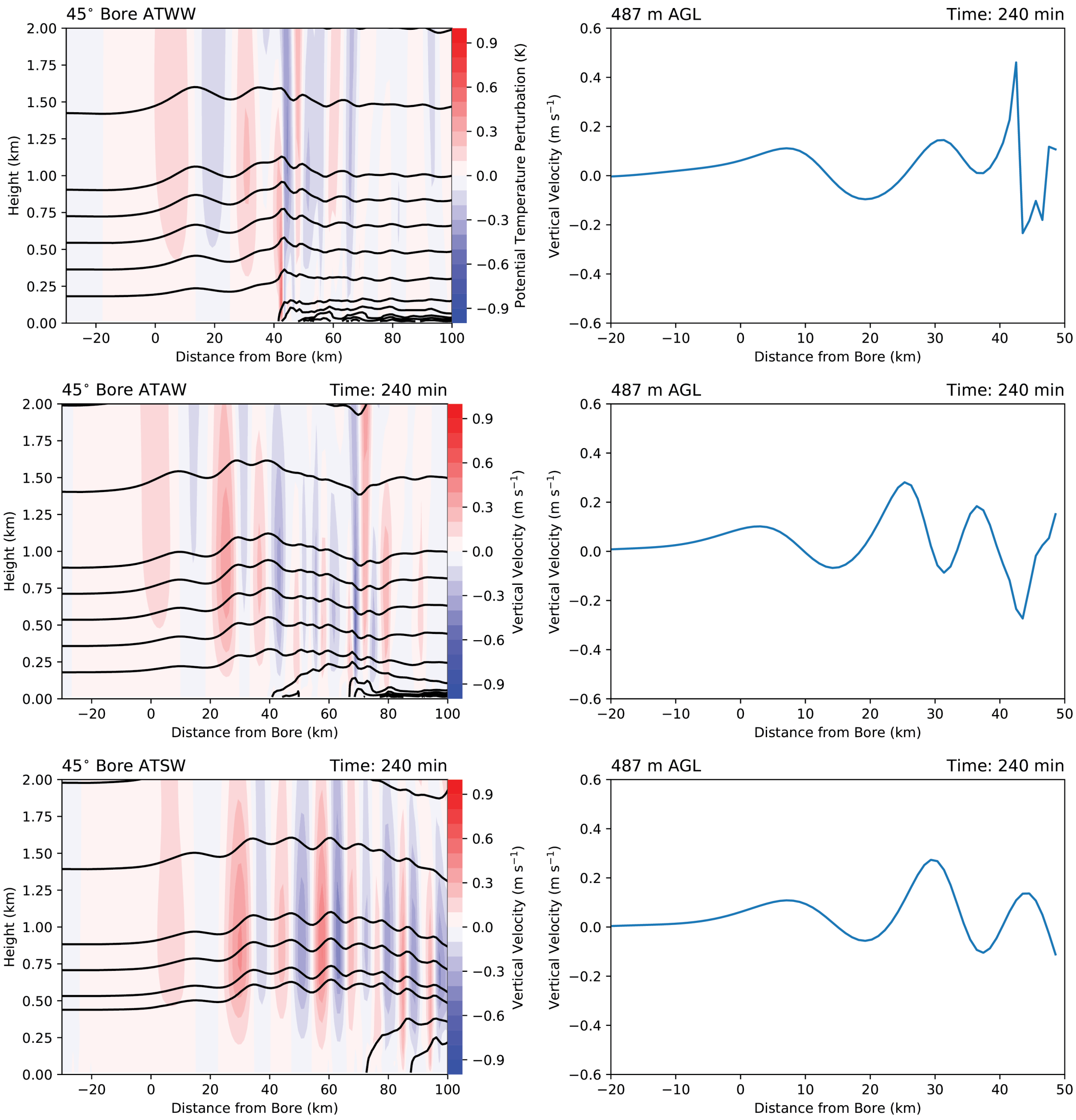

Figure 4.32: As in Fig. 4.27, but for the 45° bore without vertical wind shear.

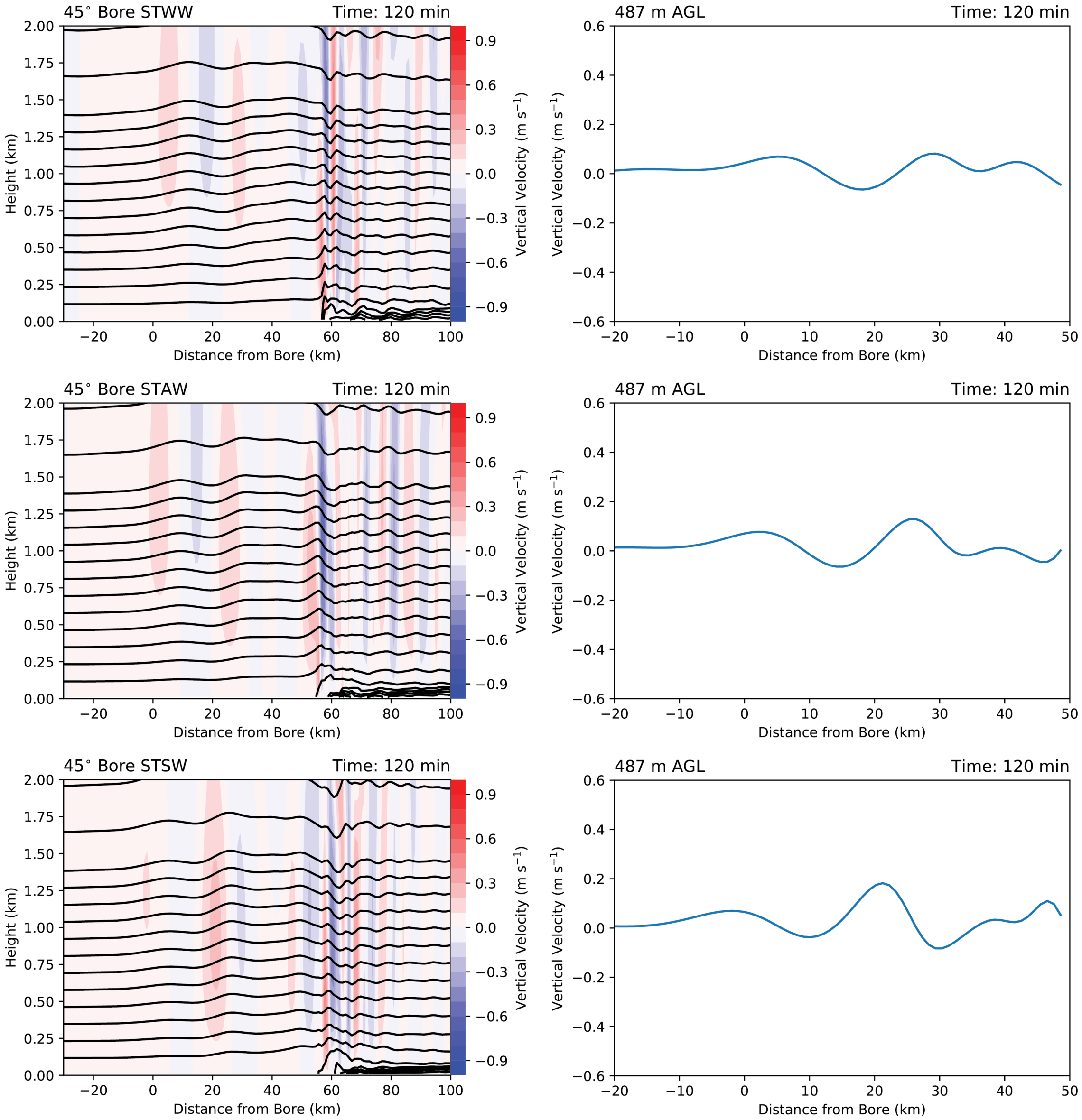

Figure 4.33: As in Fig. 4.32, but for the bores in the ST simulations.

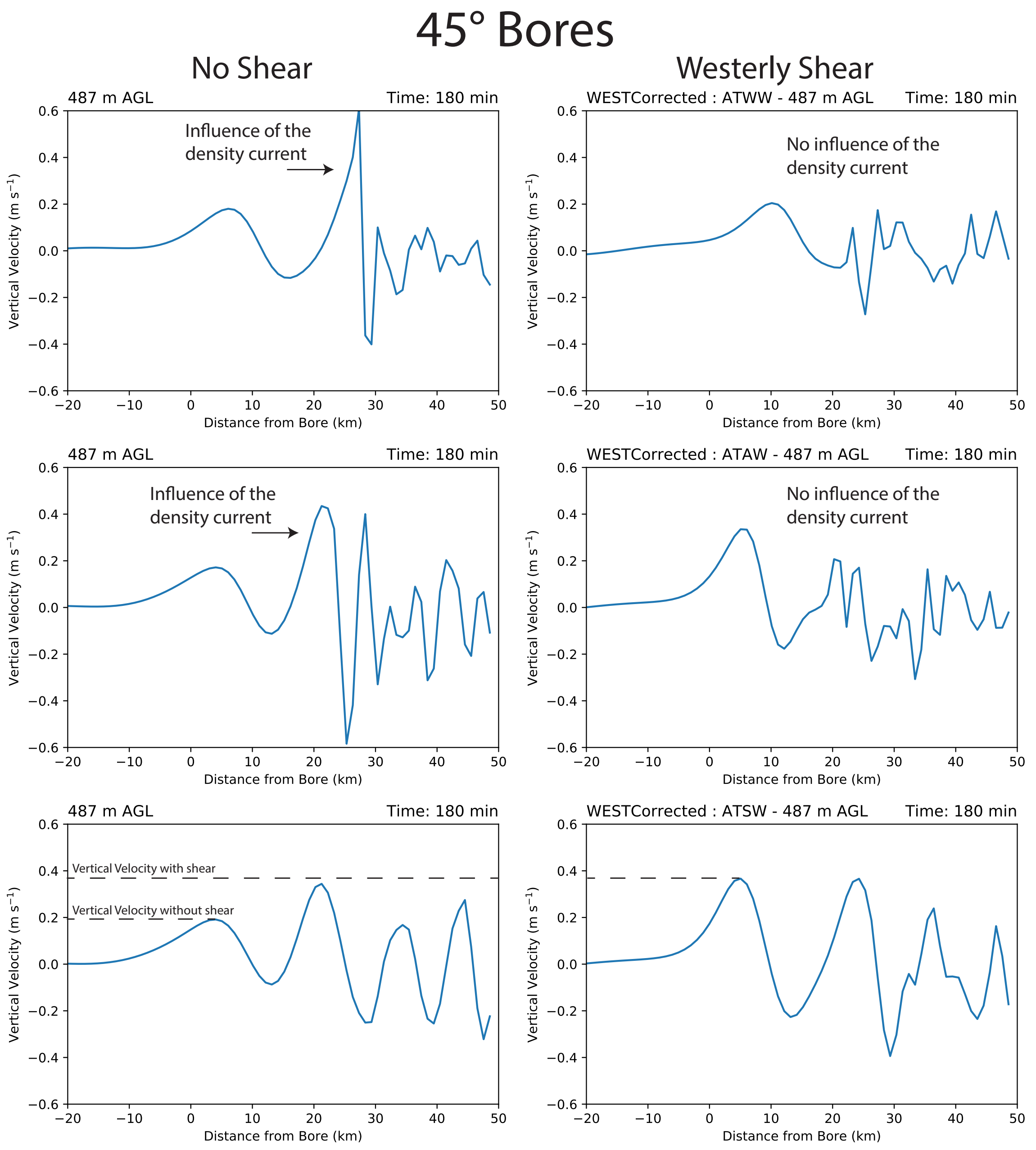

Figure 4.34: Vertical velocity (cm s^{-1}) for the 45° bores in the ST simulations for (a) - (c) AT simulations without vertical wind shear and (d) - (f) with vertical wind shear.

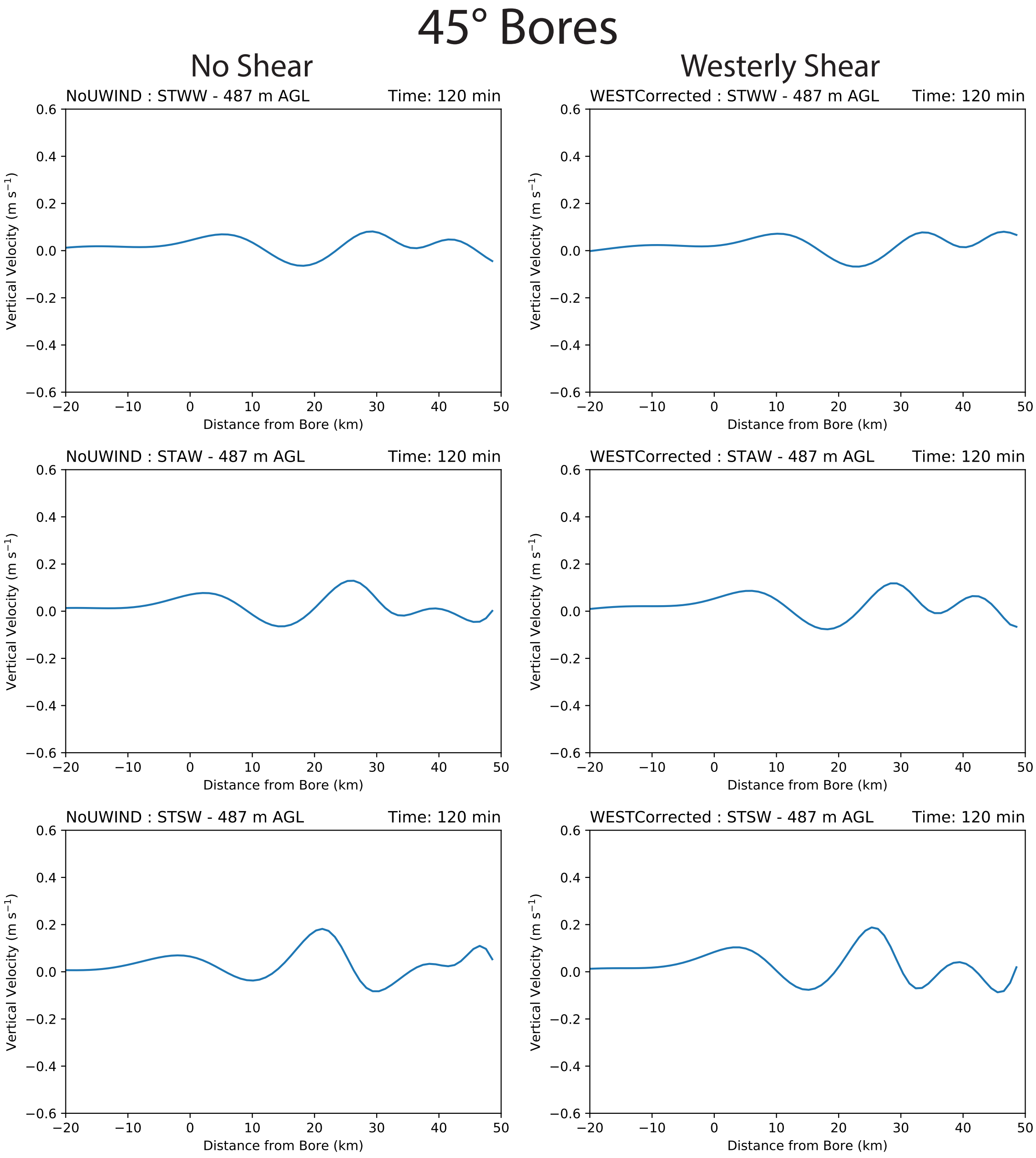

Figure 4.35: As in Fig. 4.34, but for the ST simulations.

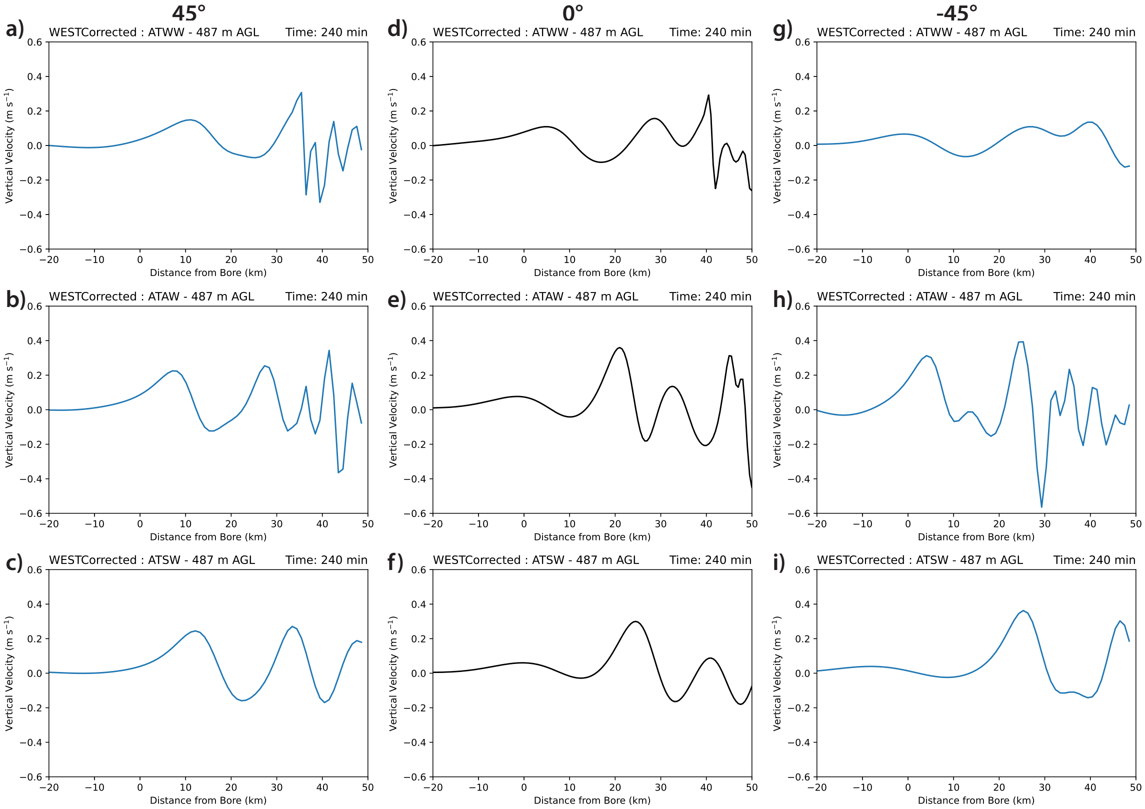

Figure 4.36: As in Fig. 4.21, but for the vertical velocity 500 m AGL at 240 min.

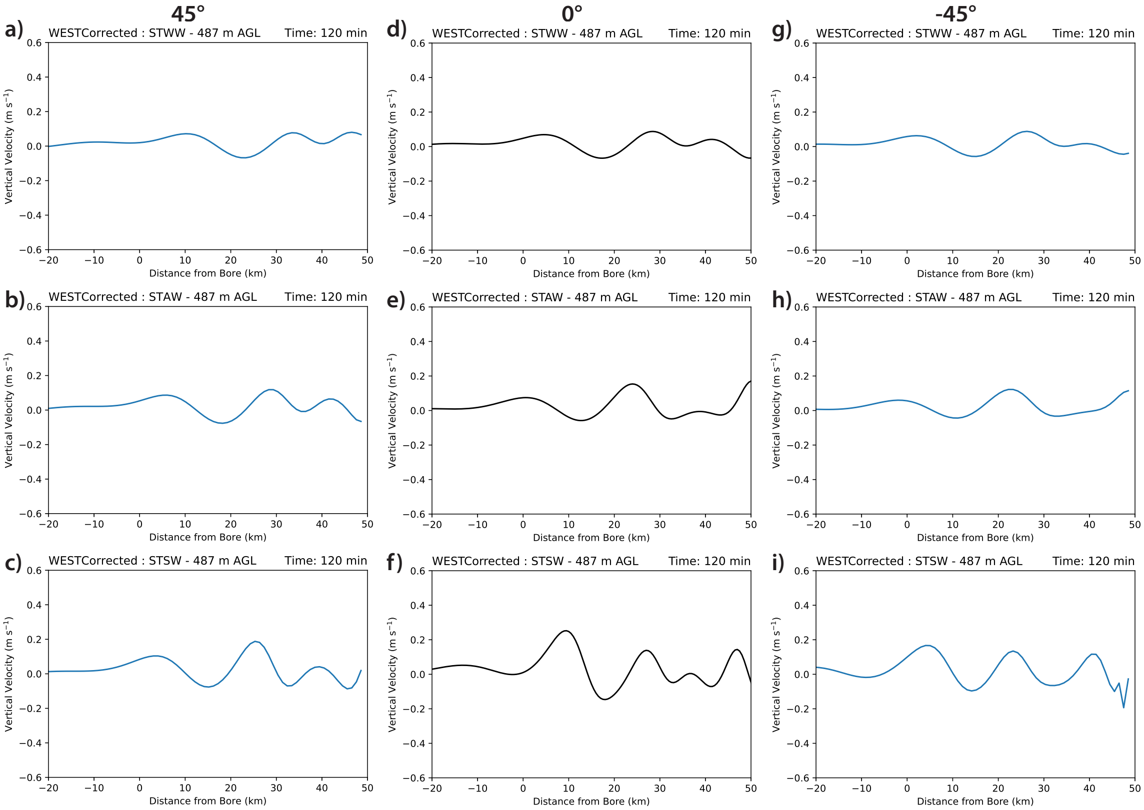

Figure 4.37: As in Fig. 4.36, but for the ST simulations at 120 min.

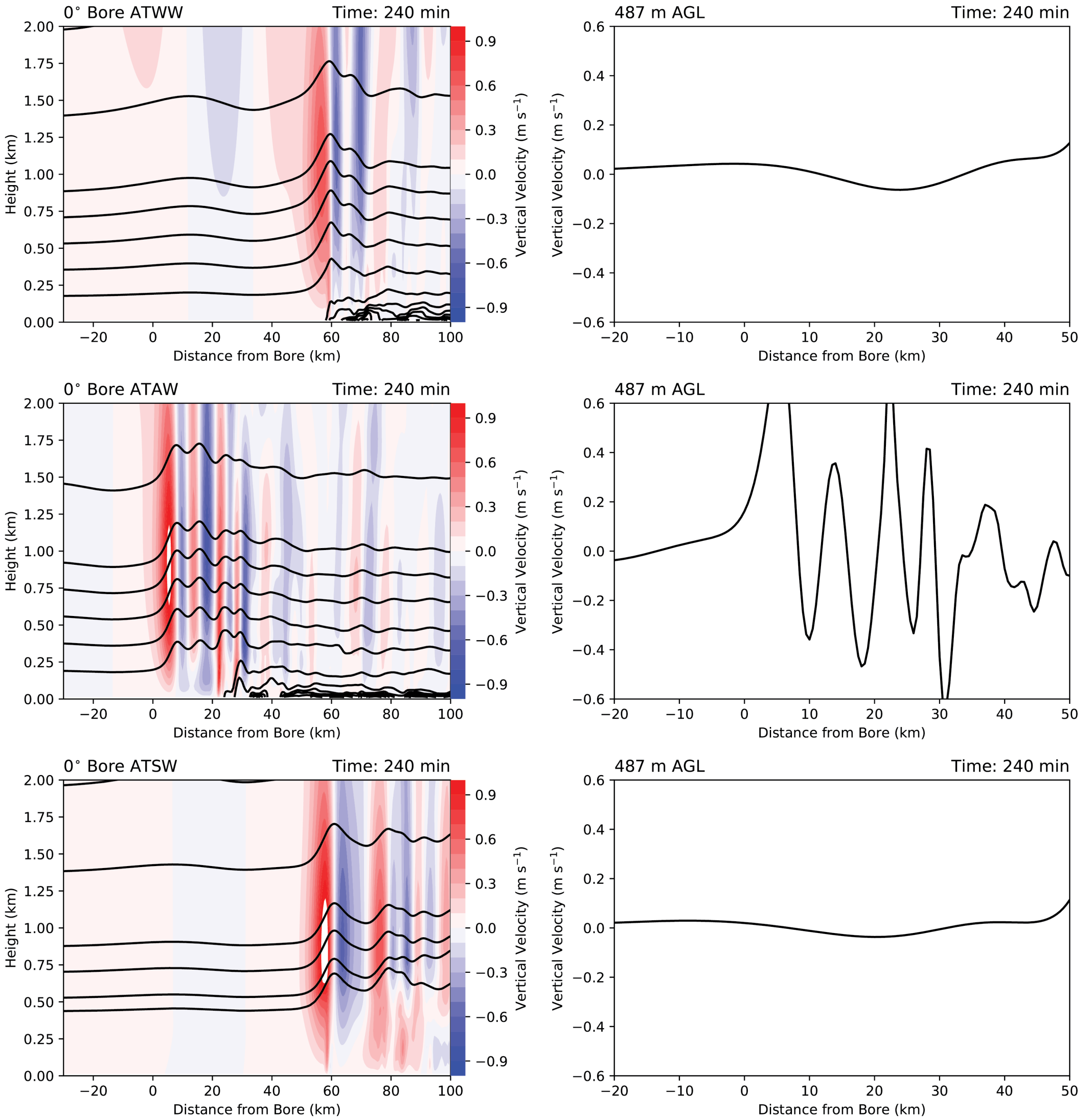

Figure 4.38: As in Fig. 4.27, but for simulations with stronger density currents.

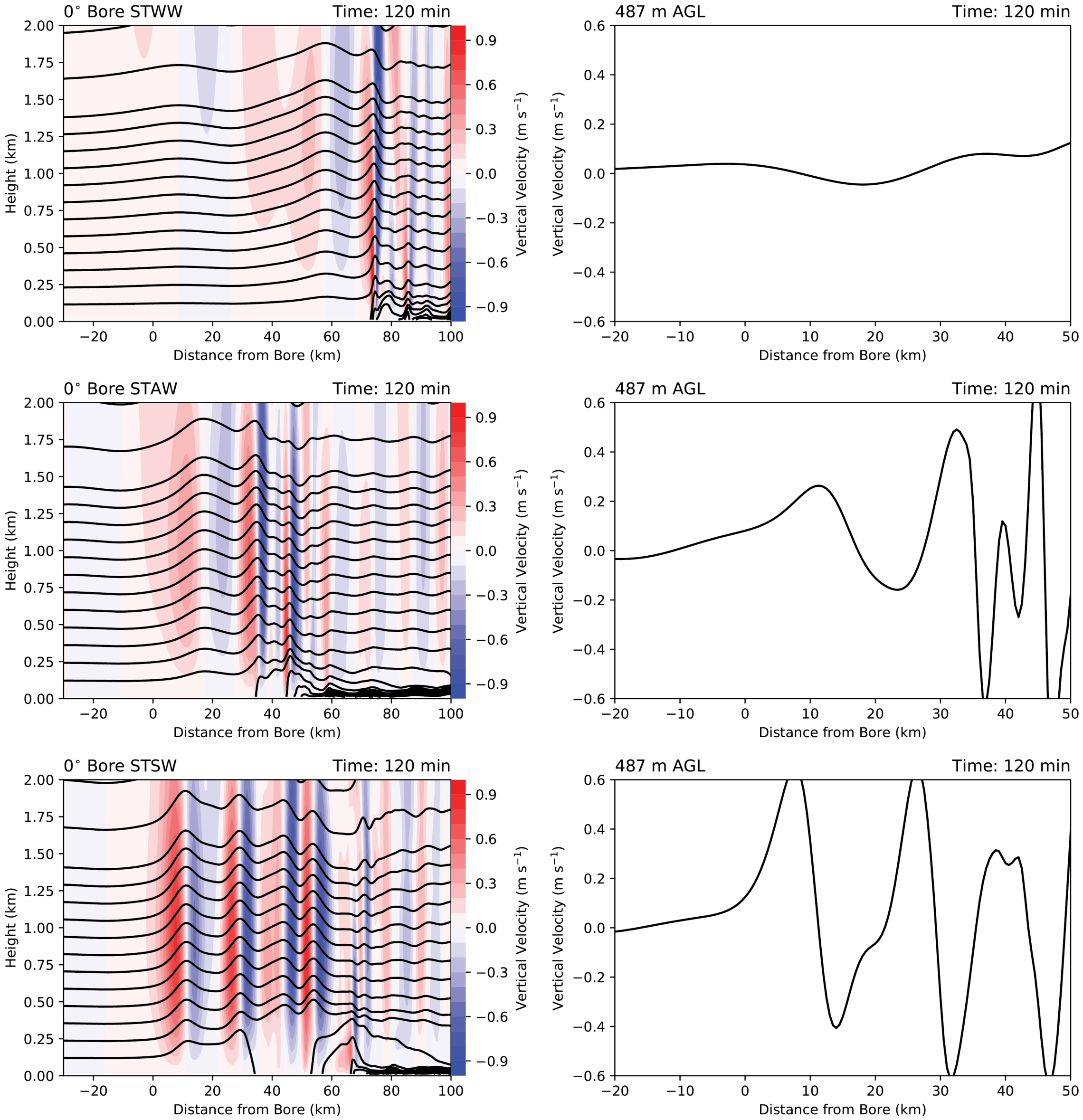

Figure 4.39: As in Fig. 4.38, but for the ST simulations.

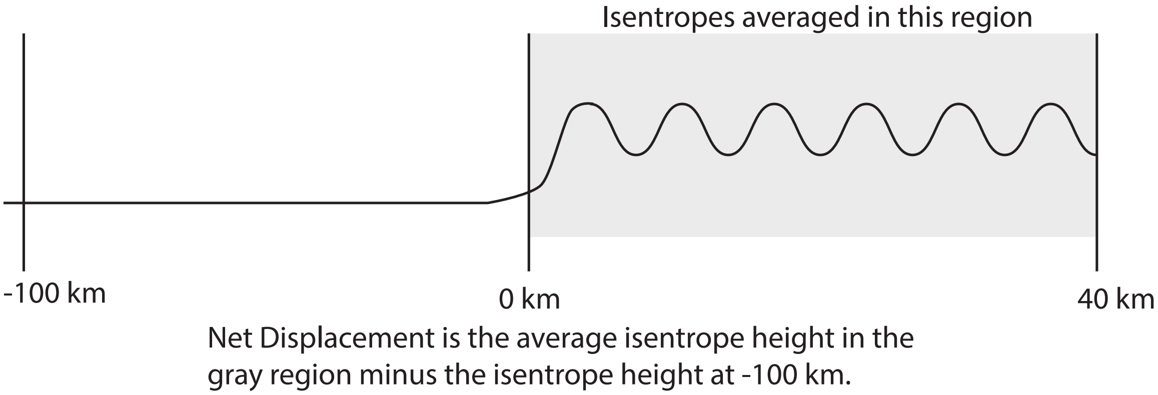

Figure 4.40: Illustration of how the net vertical displacement by the bore is computed.

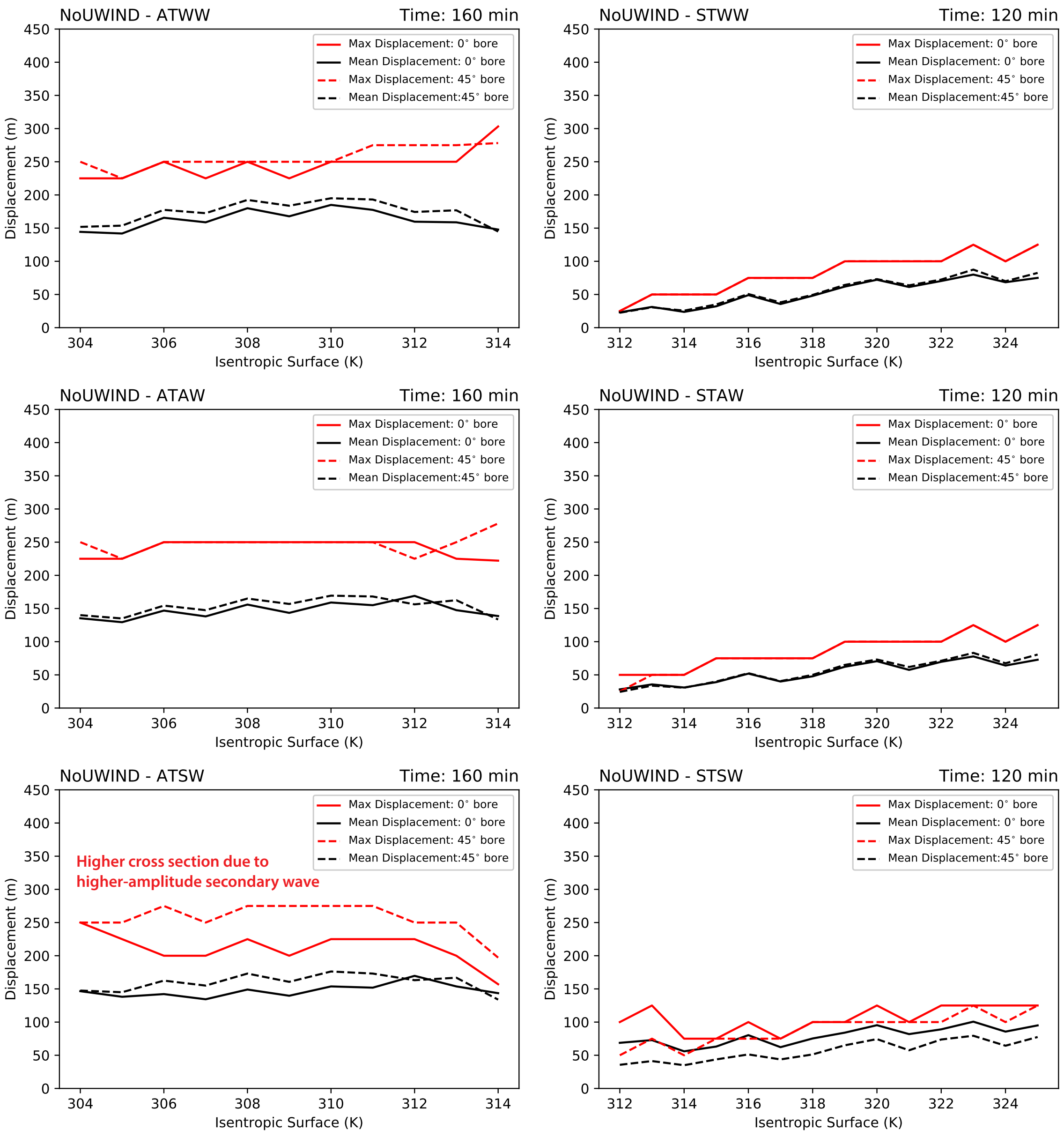

Figure 4.41: Net displacement for parcels associated with the 0^{-1} bore (solid lines) and the 45° bore (dashed line). The red lines are the maximum displacement and the black lines are the mean displacement. a) - c) is the AT simulation at 160 min and d) - f) is the ST simulation at 120 min.

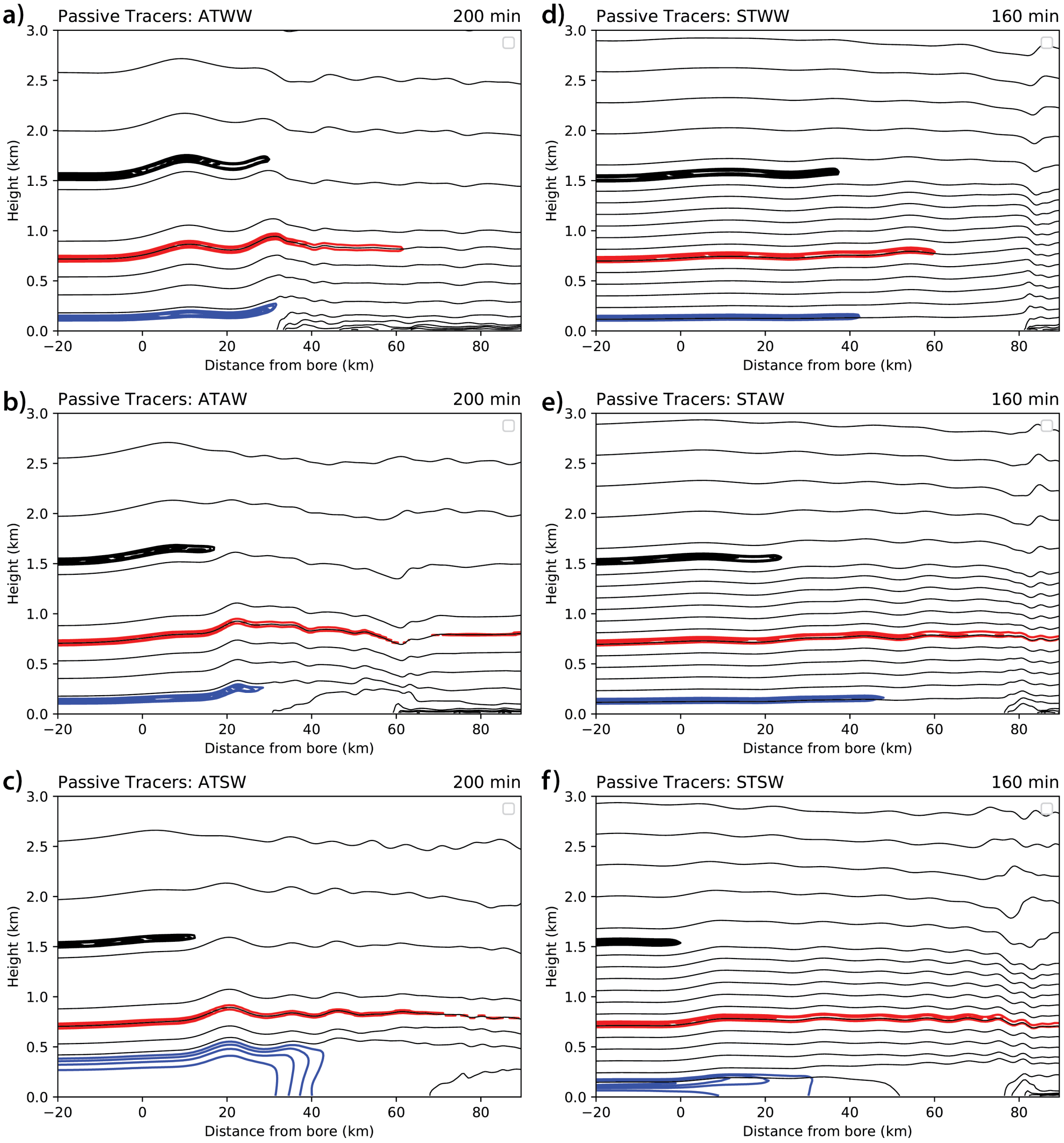

Figure 4.42: Passive tracers initialized at 125 m (blue curve), 700 m (red curve) and 1500 m (large black curve) and potential temperature contoured every 2 K (thin black lines) for the a) - c) AT simulations at 200 min and d) - f) ST simulations at 160 min.

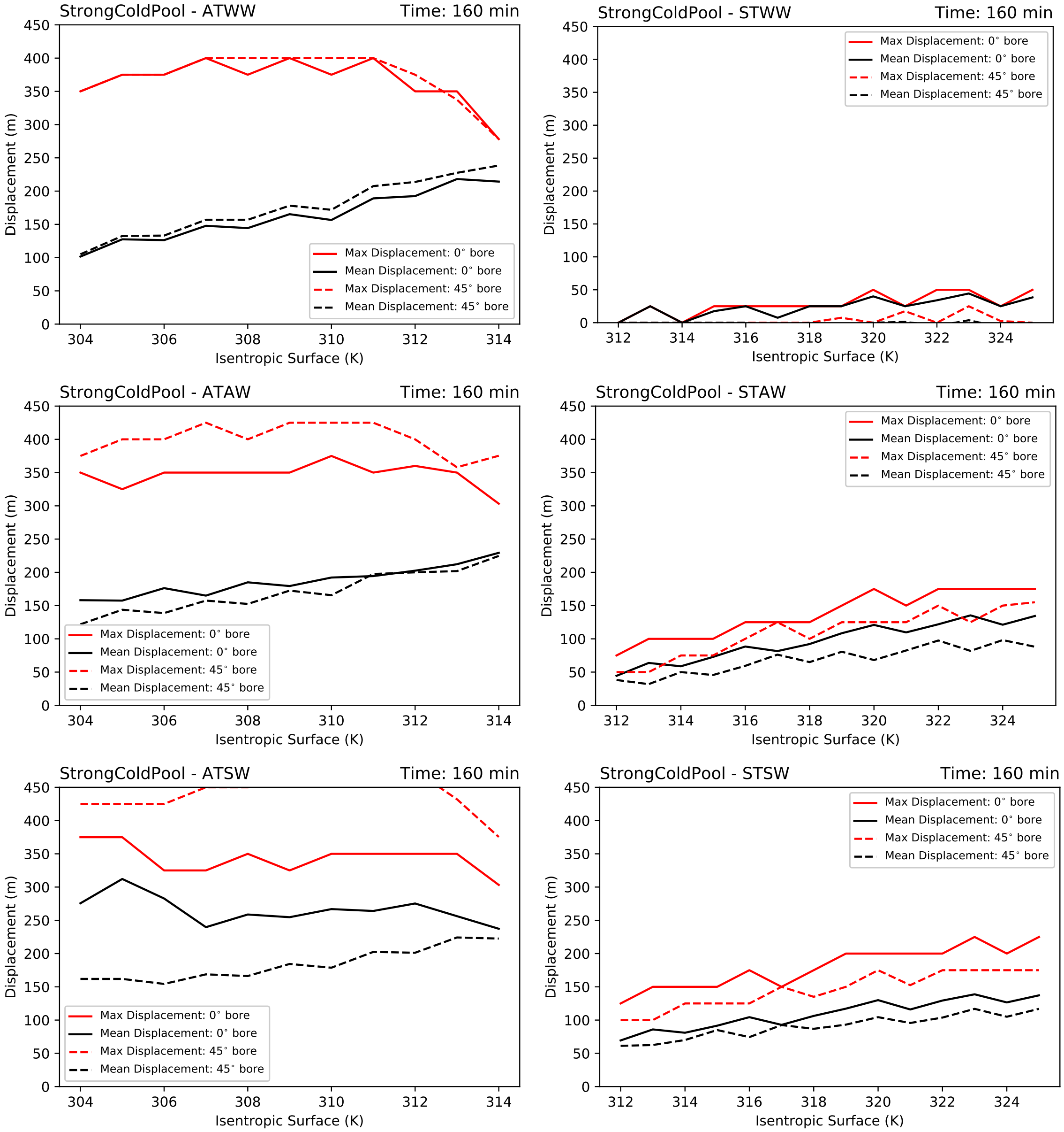

Figure 4.43: As in Fig. 4.41, but for the simulation with a strong cold pool.

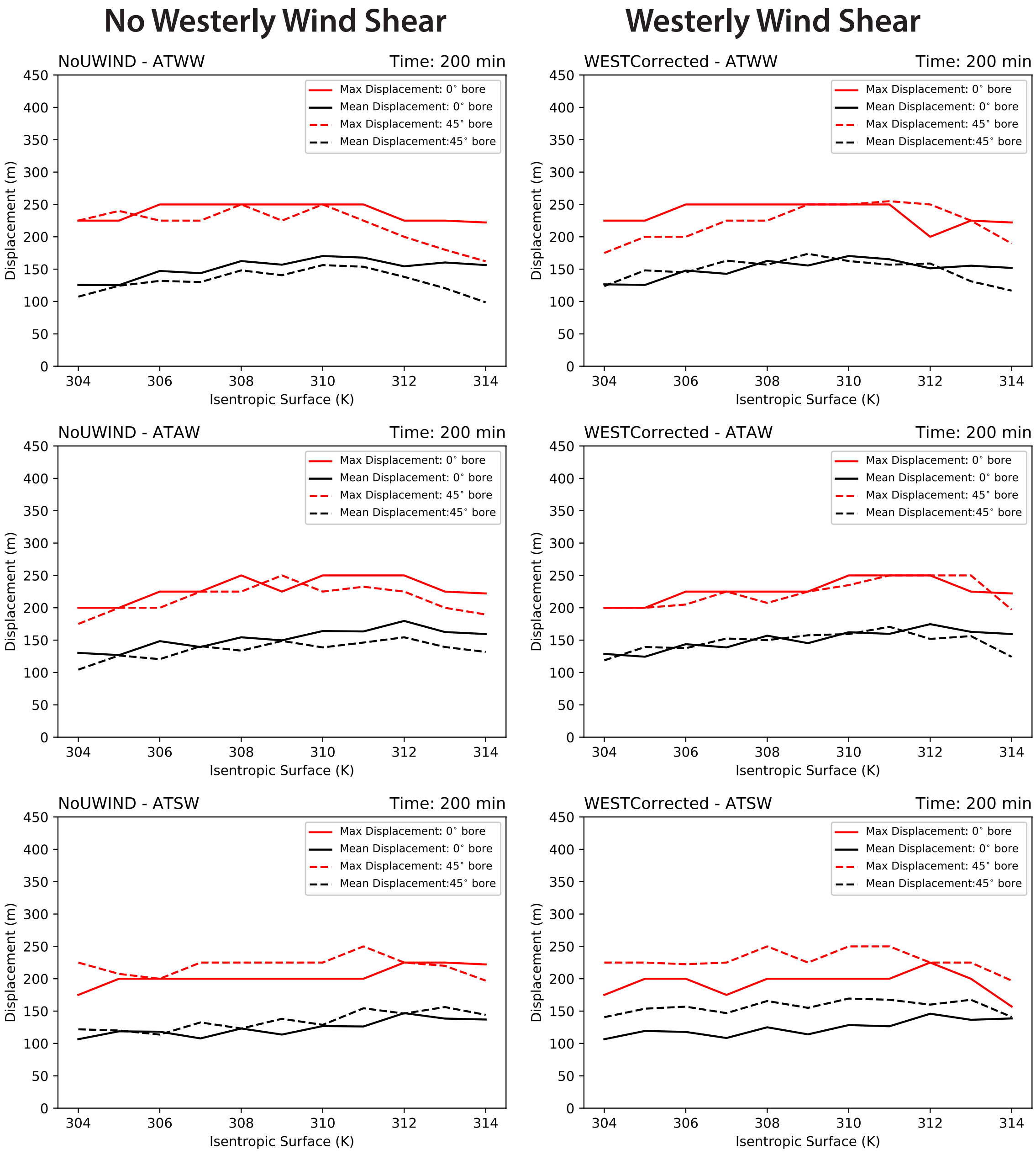

Figure 4.44: As in Fig. 4.41, but for (a),(b),(c), AT simulations without westerly wind shear at 200 min, and (d),(e),(f), AT simulations with westerly wind shear at 200 min.

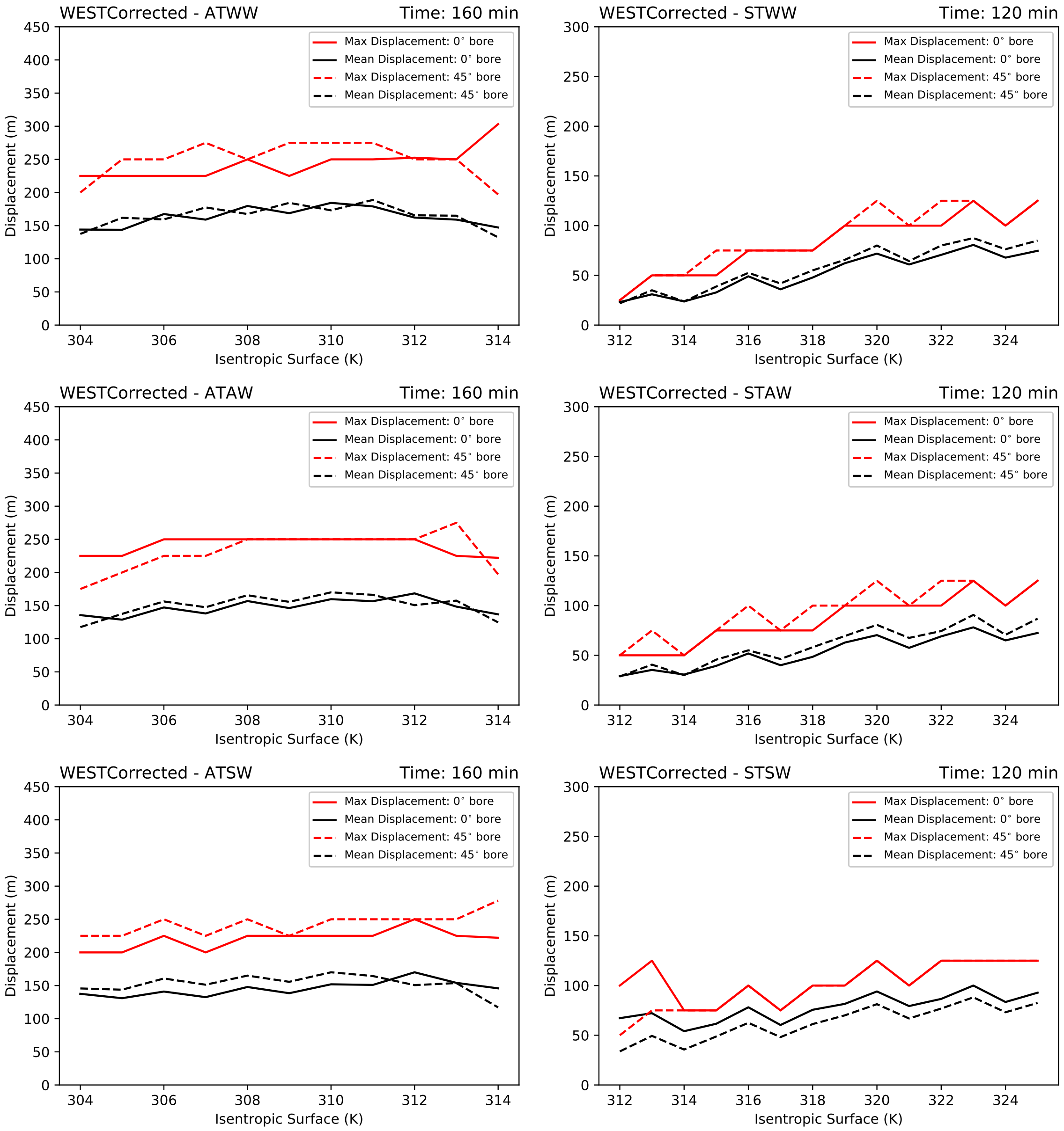

Figure 4.45: As in Fig. 4.41, but for (a),(b),(c), AT simulations with vertical wind shear at 160 min, and (d),(e),(f), ST simulations with vertical wind shear at 150 min.

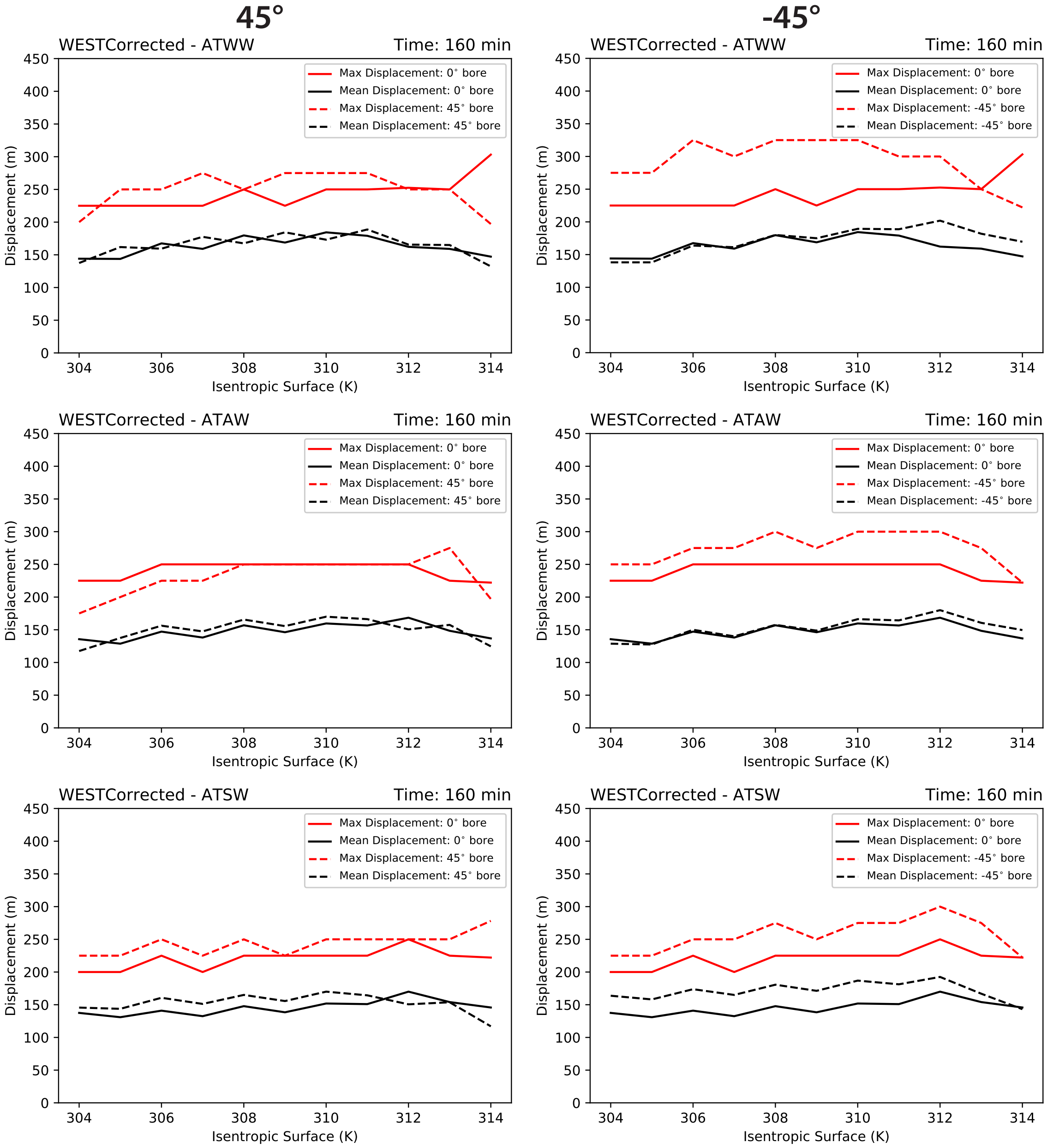

Figure 4.46: As in Fig. 4.41, but for (a),(b),(c) 45° bore in the AT simulations with westerly wind shear and (d),(e),(f), -45° bore in the AT simulations with vertical wind shear at 160 min.

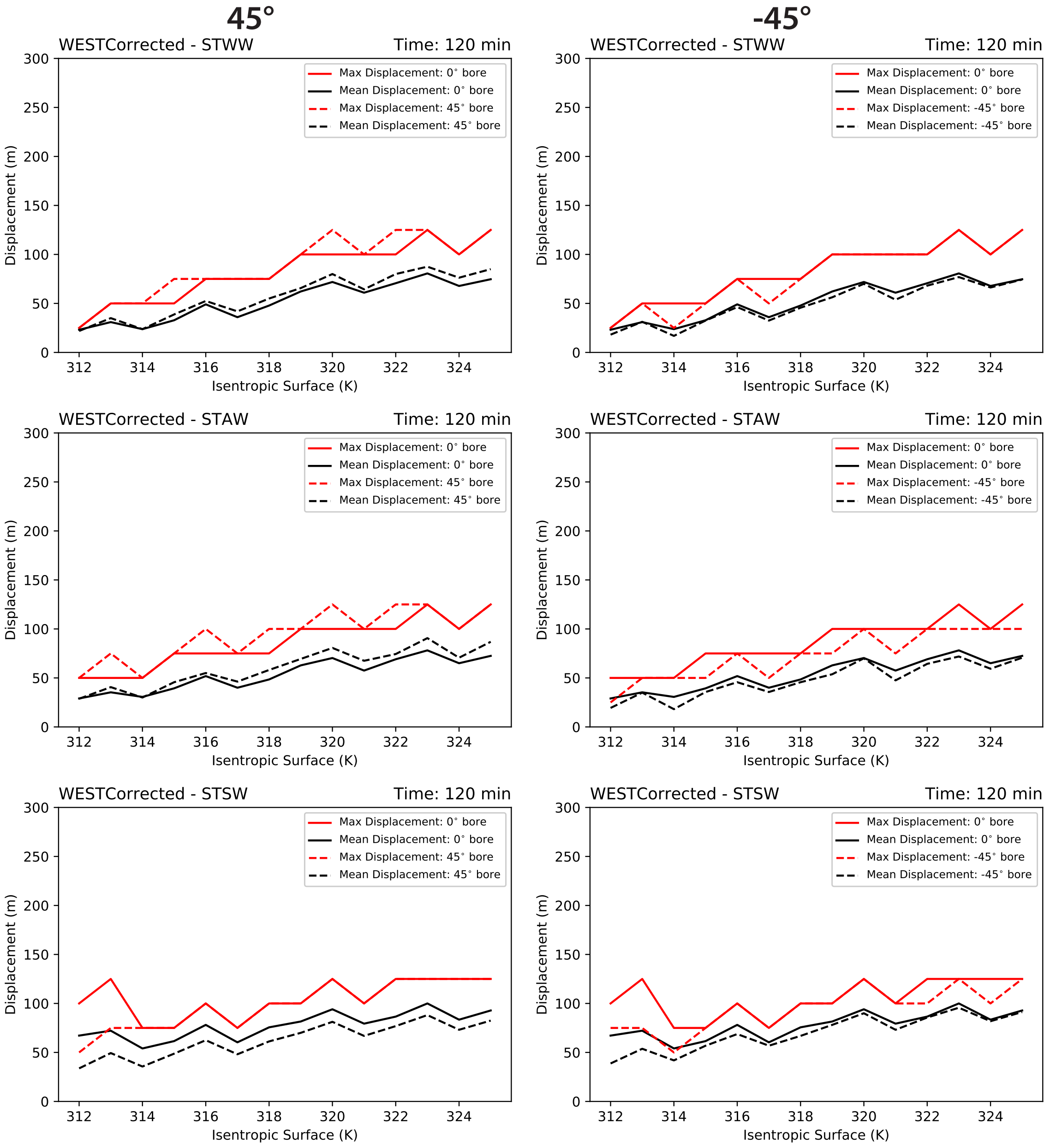

Figure 4.47: As in Fig. 4.46, but for the ST simulations with vertical shear at 120 min.

Chapter 5

Nocturnal Low-Level Jet

The LLJ was simulated over one diurnal cycle starting at 1200 UTC. The nine environments are similar to the conditions over the Great Plains but are modified from the environments in the GW simulations. The near-surface stable layer is the AT stable layer in Table 2.1 (11.5 K km^{-2} in the lowest 900 m), but the mid-level lapse rates are different. The WT simulations have a lapse rate of 1 K km^{-1}, the AT simulations have a lapse rate of 2 K km^{-1}, and the ST simulations have a lapse rate of 3 K km^{-1}. These lapse rates fall with the -1 to 0 standard deviation of lapse rates in the composite sounding, so they still represent typical nocturnal conditions. While the GW simulations had a modified wind profile from the typical nocturnal environment (i.e., the magnitudes and relative decreases were similar, just idealized as a sine wave), these LLJ simulations use the meridional wind directly from the composite sounding. Small-scale features can be averaged out in this composite sounding. For example, a sharp wind maximum at 250 m AGL in one sounding and a wind maximum at 1000 m AGL in another sounding get averaged together. Despite this averaging, the resulting wind profile in the composite sounding represents typical conditions over the Plains. The LLJ-related ascent that is to be simulated is the sustained mesoscale ascent due to the inertia-gravity wave response due to the release of the friction constraint at sunset (Shapiro et al. 2018), not the ascent due to elevated convergence associated with the laterally-varying inertial oscillation (Gebauer et al. 2018), though that CI mechanism for NB CI mode events is entirely plausible.

In the Shapiro et al. (2018) analytical model, the mesoscale ascent occurred in the presence of a surface buoyancy gradient. The buoyancy gradient is generated by applying a heating pad at the surface, as noted in Section 2.2.2 and Fig. 2.6. The surface is differentially heated, and after 12 hours into the simulation, a sinusoidal potential temperature gradient is generated at the surface. The magnitude of the surface potential temperature gradient depends on the strength of the surface heating and the mid-level stratification (which impacts the PBL depth). This potential temperature gradient generates the buoyancy gradient needed to cause this mesoscale ascent (Shapiro et al. 2018).

5.1 LLJ characteristics

5.1.1 Average Nocturnal Simulation and Average Heating (ATAW)

During the daytime (1200 UTC to 0000 UTC), the surface heats up due to two effects: the heating due to the incoming solar radiation from the radiation scheme and the heating due to the heating pad. The incoming solar radiation represents the late-May solar radiation as the model is initialized starting on 21 May (Fig. 5.1a). Late May insolation is used rather than June or July insolation because the surface heating due to the incoming radiation is stronger in July than in May, thereby increasing the depth of the PBL. Because there is additional heating related to the heating pad, the radiation scheme uses late May to prevent the PBL from being too deep. The total radiation at the surface (incoming and outgoing SW and LW) is maximized at noon, but after sunset, the net loss is about 250 W m^{-2} and decreases slightly to 200 W m^{-2} at sunrise (Fig. 5.1b). This net loss during the night is typical (e.g., Wallace and Hobbs 2006; their Fig. 9.9) and is important to the generation of the nocturnal stable boundary layer (SBL). Two effects directly impact the temperature: the surface heating pad and the heating from the radiation scheme. The heating pad is turned off at night, so the surface cooling is largely due to outgoing radiation. The heating pad at the surface generates the heterogeneity of surface temperature in the model. This horizontal heterogeneity in the surface temperature results in horizontal heterogeneity of the PBL as the day progresses. All other forcings such as heating due to radiation in the simulations are horizontally homogeneous.

The surface baroclinic zone generated in this simulation is about 0.6°C per 450 km (Figs. 5.2a-b). This gradient is weaker than the 4.5 K (450 km)$^{-1}$ gradient in the Shapiro et al. (2018) study. However, it was challenging to generate a baroclinic zone of more than a few degrees Celsius across the domain while maintaining a reasonable simulation throughout the day and night that simulates the jet's features such as a low-level wind maximum, the inertial oscillation, and the mesoscale ascent. These features are not replicated perfectly but are similar to the observed features.

The generated temperature gradient is characteristic of typical baroclinic zones over the Great Plains and can originate over the Plains via differential heating up the sloping terrain, warm advection northward from the LLJ, or both. In this simulation and many others presented here, the skin temperature profile is not smooth. The noise in this profile (see -200 km to 0 km in Fig. 5.2b) is related to the rising thermals that are generated during the late afternoon. However, the profile is smooth in many other simulations in this study. The differences that this smoothness has on the quality of the simulations will be discussed later.

The time evolution of the daytime boundary layer is characteristic of typical boundary layers (e.g., Stull 2012). A well-mixed convective boundary layer (CBL) is present by 0000 UTC (evidenced by the constant potential temperature). In this simulation, the boundary layer is deeper at the center of the domain than at the east and west edges. This difference is due to the heating pad's presence, which will result in the surface baroclinic zone needed to produce the ascent in Shapiro et al. (2018). The CBL grows to 3 km deep by 2100 UTC, has a near-surface suberadiabatic layer, and a capping inversion above the well-mixed layer. These characteristics are similar to observed CBLs (red curve on Fig. 5.3).

However, the stable boundary layer (SBL) is shallow and is characterized by a steep near-surface inversion (blue curve on Fig. 5.3). This near-surface inversion is uncharacteristic of observed SBLs. This "runaway" cooling has been noticed for a while (Louis 1979; Jiménez et al. 2012), and it is speculated that the low friction velocity (u_*) reduces the turbulent heat flux, decoupling the temperature of the atmosphere from the ground. This decoupling would cause the temperature at the surface to cool by radiation. These simulations use the YSU PBL scheme and the revised surface layer scheme (Jiménez et al. 2012). This revised surface layer scheme should limit this cooling effect, but it is still present in this simulation. CM1 has one PBL scheme and two surface-layer scheme (the revised and un-revised version). There were no combinations of the PBL and surface-layer schemes that did not include this "runaway" cooling given the current setup (i.e., with the heating pad and without moisture). While the inclusion of this "runaway" cooling may impact the structure of the SBL, it does not appear to have a significant impact on the time evolution and magnitude of features such as the LLJ or the vertical velocity. The maximum jet strength ranges from 15 - 20 m s^{-1} and reaches a maximum shortly before sunrise (e.g., Bonner 1968; Whiteman et al. 1997), there is an inertial oscillation (e.g., Blackadar 1957; Bluestein et al. 2018), and the vertical velocity is approximately 1 cm s^{-1}, its strength increases throughout the night, and is strongest between 0600 and 0900 UTC (e.g., Shapiro et al. 2018).

The temperature does decrease throughout the residual layer (the former CBL above the near-surface inversion) at night, which is characteristic of the nocturnal boundary layer (Fig. 5.4). This cooling may be related to the broad area of vertical motion near the center of the domain. This poor representation of the SBL is a limitation of the numerical simulations. This simulation can produce the mesoscale ascent noted in Shapiro et al. (2018), and the LLJ produced shares many characteristics with observed LLJs.

When the soil moisture is returned to normal, the surface does not heat up as fast due to the moisture's presence, and the CBL is not as deep (Figs. 5.5a-b). The entire CBL cools during the night, but the "runaway" surface cooling still exists. The surface cooling is similar to that without moisture, and the overall representation of the SBL remains poor. The LLJ in the simulation with moisture was virtually nonexistent (Figs. 5.5c-d). In these 3d simulations, capturing the nature of *both* the CBL and the SBL was impossible. Based on the similar characteristics of the LLJ, and the good representation of the CBL, the simulations without soil moisture were selected even though the representation of the SBL was poor. The purpose of this study is not to evaluate the representation of PBL schemes on idealized simulations of the LLJ. However, more option's for the PBL scheme could improve the representation of the CBL, the SBL, and the LLJ.

As the jet develops, an easterly wind develops in the lowest 2 km of the atmosphere, reaches its maximum strength around 0600 UTC, then weakens (i.e., becomes more westerly) (Fig. 5.6). This characteristic of the zonal wind is related to the inertial oscillation of the LLJ, which is captured in all 36 LLJs simulated in this study. At night in these simulations, there is no preferred location for forcing (i.e., the cooling due to the radiation budget is the same at all horizontal points). This lack of any preferred location combined with the easterly wind causes features such as the PBL/residual layer to be advected towards the west, evidenced by the westward motion of the deepest portion of the PBL. The mesoscale vertical velocity (discussed later) is also advected towards the west by this easterly zonal wind.

During the night, a westerly wind forms above the jet and near the surface west of the rising motion (Fig. 5.6). Rising air parcels cannot penetrate the capping inversion atop the residual layer, and according to mass continuity, they must move horizontally away.

The strongest portion of the LLJ occurs east of x = 0 (the location of maximum daytime heating) (Figs. 5.7 and 5.8). The meridional component of the wind develops a wind maximum near 1 km AGL, and the strength increases throughout the night. In the real atmosphere, the LLJ reaches its maximum strength before sunrise (typically around 0900 UTC). If this simulation were run out shortly past sunrise, the new CBL would mix out the nocturnal LLJ. While the simulated LLJ here is not identical to observed LLJs, it shares many similar characteristics such as the inertial oscillation, depth of the LLJ, and location of the LLJ maximum (around 1 km AGL or less).

During the late afternoon, rising thermals are generated throughout the CBL (Figs. 5.9a-b). These rising thermals are related to the noisy skin temperature profile. The thermals do not exist at night, but there is a persistent area of ascent that lasts throughout the night (Figs. 5.9c-d). This nighttime ascent starts near x=0. By 0300 UTC, the maximum vertical velocity strengthens to 6 cm s^{-1} before leveling off to 3 cm s^{-1} before sunrise. The ascent spans a horizontal distance of approximately 400 km, similar to that noted in Shapiro et al. (2018). This vertical velocity does decrease in strength as the night progresses but does not go away; it is persistent throughout the night.

While this simulation has some problems (e.g., the "runaway" cooling at night and the noisy PBL), it provides a reasonable simulation of the LLJ and replicates many of its observed features. The highly-idealized nature of this simulation prevents other observed features such as moisture fluxes (especially at the surface), the sloping terrain, inhomogeneities in the zonal wind field above the jet, and clouds from impacting the simulation. Differential heating associated with cloud cover could result in deeper CBL in some areas, potentially impacting how the jet develops. Daytime subsidence would limit the growth of the CBL, reducing the height of the CBL and the LLJ. While a more realistic jet profile would likely be achieved by including these effects, the idealized nature of the simulation would change. Here, the mesoscale ascent identified in Shapiro et al. (2018) is effectively isolated from the influence of these other effects.

5.2 LLJ Typical Nocturnal Environments

By 0000 UTC, there is sinusoidal profile of the skin temperature that is warmest in the center of the domain and coolest at the edges. The horizontal temperature gradient at the surface increases as the environmental stratification increases (Fig. 5.10). Given the same heating profile in all nine simulations, the mixing in the ST simulations is weaker due to the increased stratification. This reduced mixing likely results in a stronger temperature gradient. During the first few hours of the night, the warmest region of the skin temperature appears to move towards the east. Adiabatic warming due to subsidence increases the air temperature just above the surface, warming the surface through conduction, while adiabatic cooling due to the ascent decreases the air temperature, decreasing the skin temperature through conduction. The warm and cool skin temperatures are collocated with subsidence and ascent, respectively.

The daytime evolution of the boundary is similar among all nine average heating simulations (Fig. 5.11). The depth of the PBL is similar for each of the lapse-rate simulations. As environmental stratification increases, the depth of the PBL decreases. All nine PBLs have a well-mixed layer topped by a capping inversion. The weak wind (WW) simulations have a more "noisy" PBL structure. This noise is related to the zonal variation in the skin temperature and a combination of the weak wind. As the initial wind speed is increased, the field tends to look smoother, but it will be shown later that modifying the initial zonal wind also affects the smoothness of the skin temperature. The smoothness of the simulations may be related to the smoothness of the skin temperature at sunset. Perhaps the increased wind speed near the surface results in a stronger along-gradient motion of the wind speed, smoothing out the profile.

In the WT simulations, there are vertical pockets of enhanced PBL depth that appear to remain quasi-constant with time during the night, and they are collocated with enhanced "noise" in the skin temperature profile (Fig. 5.12). These pillars are less noticeable as the stratification increases, so these are likely related to the rising thermals of the daytime PBL. However, they are not advected westward as much as the structure of the PBL (defined by the maximum in PBL depth).

The time-evolution of the nocturnal boundary is similar in all nine simulations. The "runaway" surface cooling is in all of the simulations, and the deepest part of the nocturnal PBL is still advected to the west with time (as was shown in the ATAW simulation). Otherwise, there is no notable difference among all nine average heat simulations.

The zonal wind is stronger in the simulations with stronger environmental stratifications and initial meridional wind speeds (Fig. 5.13). In the simulations with stronger stratifications, the zonal wind speed increases faster than in the simulations with weaker stratifications. This difference is likely due to the shallower PBL depth. Because the air has a shorter distance to travel upwards before reaching the PBL top, it is deflected horizontally due to mass conservation before it would otherwise be. The longer this deflection occurs, the stronger the zonal wind becomes. After the zonal wind speed reaches its maximum at around 0600 UTC, it decreases faster in the simulations with the stronger stratifications. Other than this slight difference in the time evolution, the zonal wind characteristics are similar in all the simulations.

A stronger initial wind speed results in a stronger meridional wind during the night. This meridional wind increases faster as the stratification is increased (Fig. 5.14), and is smoother as the stratification and the initial wind speed increase. Otherwise, the general spatiotemporal evolution of the meridional wind is similar among all nine simulations. The maximum wind speed occurs at roughly the same height above the ground and the same horizontal location. There is a slight eastward shift in the maximum wind speed's horizontal location as the stratification is increased, but this difference is small (<25 km; see right column of Figs. 5.14c,f,i).

The clockwise-turning hodograph indicates that the inertial oscillation is present in all simulations (Fig. 5.15). The hodograph increases in size as the initial wind speed increases, indicating that the zonal and meridional components increased (as discussed in the previous paragraphs). As the stratification increases, the hodographs tend to decrease in size a little and the turning with time is slightly more pronounced. The hodograph's final point is farther to the right, indicating a stronger zonal wind at the final time as the stratification increases.

5.2.1 Different Baroclinic Zone Strengths

The timing and location of the surface baroclinic zone remain the same in these analyses, but the magnitude is altered. The simulations with an imposed heating of 20 K 12 hr^{-1} are the average heating simulation, the simulations with an imposed heating of 10 K 12 hr^{-1} are the weak heating simulations, and the simulations with an imposed heating of 30 K 12 hr^{-1} are the strong heating simulations.

Not surprisingly, the baroclinic zone becomes noisier as the strength of the surface heating increases. In the AT simulation (the middle row in Fig. 5.16), the gradient strength increases from less than 0.5 K / 450 km in the weak heating simulations to nearly 1 K /450 km in the strong heating simulations. The noise in the skin temperature profile increases as the heating increases. The WTSW and ATSW skin temperature profiles were smooth in the average heating simulations. They are smooth in the weak heating simulations and become noisy in the strong heating simulations (especially in the WTSW simulation). The smooth profiles in the average heating simulation were again smooth in the weak heating simulation, but the noisiness increases as the heating increases.

As expected, the simulations with the deepest PBLs have the strongest heating and the weakest mid-level lapse rates (the WT simulations) (Fig. 5.17). The simulations that have noisy skin temperatures also have noisy PBLs. The time-evolution of the PBL is independent of the surface heating. The deepest portion of the PBL still moves west with time, and it is the same location as the heating changes. Aside from the depth of the PBL and the noisiness related to the skin temperature, there are no notable changes as the heating increases.

As the strength of the heating increases, the magnitude of the zonal wind component increases, though this difference is only between 1 and 2 m s^{-1} (Fig. 5.18). The simulations with stronger heating have a more defined local maximum in the magnitude of the zonal wind, but the differences among the different heating simulations aside from the zonal wind's magnitude are small.

The differences in the meridional component as heating increases are similar to those of the differences in the zonal wind. As the heating increases from the weak heating to the strong heating, the strength of the meridional component increases between 1 and 2 m s^{-1} (Fig. 5.19), similar to that of the zonal wind. The depth and height of the wind maximum are similar among the different heating profiles, though the noisier profiles tend to have a more pronounced jet maximum. Overall, there are no significant differences in either type of wind profile as the heating is changed other than their magnitude.

This pattern of the zonal and meridional components is reflected in the hodographs. The hodographs get larger as the heating increases (Fig. 5.20), meaning that the zonal and meridional components of the winds increase. The inertial oscillation is present in all hodographs, which is a necessary characteristic of the LLJ. Other than the hodograph's size, there are no notable changes among the hodographs of the different heating simulations.

The effect of increasing the initial wind speed and environmental stratification on the LLJ and the vertical velocity is independent of the baroclinic zone's strength. The ST simulations produce the weakest rising motion, and the simulations with the stronger initial meridional wind produce the strongest jet-like profiles. While these features' magnitudes may depend on the buoyancy gradient's magnitude, their temporal evolution is nearly identical to that mentioned in the previous subsection. This discussion will focus on how the features such as the meridional wind component and PBL characteristics change as the strength of the heating pad changes.

In summary, altering the surface heating strength did not affect the time evolution of the PBL, the LLJ, or the rising motion. They remain the same regardless of the heating strength. However, these features' magnitudes increased, and the noisiness of the fields increased as the heating increased. This increase in magnitude is the only notable difference among the different heating simulations.

5.3 Influence of the initial zonal wind

The average heating simulations were rerun to include a 2 m s^{-1} initial zonal wind speed. This wind speed is chosen because it is near the average wind speed of the hodographs. The purpose of using this wind speed is to try and keep the zone of mesoscale ascent centered near x = 0, which would otherwise be advected towards the west, and see what differences there are between the two types of simulations. These simulations will be referred to as the UWIND2 simulations and the others as the NoUWIND simulations.

One notable difference is that while the time evolution of the skin temperature is generally the same (Fig. 5.21), the WW simulations are now smooth, and the AW and SW simulations are noisy (e.g., Fig. 5.22). In the WW simulations, the skin temperature decreases at x=0, becoming cooler than the surrounding environment. This cooler center is likely due to adiabatic cooling that results from rising motion centered at x=0 which cools the air and then the surface via conduction.

The time evolutions of the PBL (Fig. 5.23), the zonal wind (Fig. 5.24), and the meridional wind (Fig. 5.24) in the UWIND2 simulations are similar to those in the NoUWIND simulations. The most notable difference is the eastward shift in the features towards x=0. Minor differences in these UWIND2 simulations include the smooth structure of the WW simulations (see the smooth skin temperature in Fig. 5.21) and an increased magnitude of the zonal and meridional wind components. The zonal wind speed at 0800 UTC is 2 – 3 m s^{-1} larger than in the NoUWIND simulation (which is similar to the added wind speed in the initial conditions). The difference in the meridional wind speed is not as noticeable, but the speed in the UWIND2 simulations is about 1 m s^{-1} higher than in the NoUWIND simulations.

The hodograph is centered near 0-1 m s^{-1} during the night and is smaller in the UWIND2 simulations than in the NoUWIND simulations (Fig. 5.26). This hodograph represents the winds at x=0, so the eastward shift of the LLJ can explain this smaller hodograph. If the strongest winds get shifted towards the east, then the hodograph will be smaller because of this shift (apparent reduction of the wind speed).

The addition of the 2 m s^{-1} did not drastically change any of the profiles in comparison with those without the initial zonal wind. While the ascent was centered over x=0 in the WW simulations, this centering does not improve the quality of these simulations. For the rest of the analysis, the simulations without the initial zonal wind will be used.

5.4 Vertical Velocity

During the daytime, intense rising motion occurs in the PBLs in the WW and AW average heating simulation (e.g., Fig. 5.9b) and is a representation of rising thermals. These thermals are related to the noise that appears in the skin temperature, if not its cause. The strongest rising motion is in the center of the domain where the maximum heating is. As the stratification increases, the depth and horizontal extent of the rising motion decrease.

During the night, the rising thermals cease, and a nearly 400-km-wide area of ascent persists throughout the night (Fig. 5.27). This broad area of ascent moves westward with time (due to the increase in the eastward component of the zonal with time via the inertial oscillation). In general, the magnitude of the vertical velocity at night ranges from 1 – 3 cm s^{-1}. As the stratification increases, this magnitude of the vertical velocity associated with this nighttime ascent decreases.

The vertical velocity profiles are noisy in the NoUWIND WW simulations and are smooth in the UWIND2 WW simulation (Fig. 5.31). To alleviate the problem with the noisy vertical velocity field, it was smoothed using a Gaussian filter. Both sets of simulations are subjected to the average heating. To determine the impact the noisy vertical velocity field has on the magnitude of the vertical velocity, the smoothed vertical velocity fields from the UWIND2 WW simulations and the NoUWIND WW simulations will be compared. While these simulations cannot be compared directly, they are the most equivalent simulations to compare.

The average maximum vertical velocity in the UWIND2 ATWW simulation during the night is 1.2 cm s^{-2} while in the NoUWIND ATWW simulation, it peaks near 10 cm s^{-1} at sunset before decreasing to 2 cm s^{-1} by 0800 UTC (Fig. 5.32). This difference is related to the large pockets of high vertical velocity that are present due to the noise in the skin temperature, resulting in a higher vertical velocity. Based on the smoothness of the curve and the lack of these intense pockets of vertical velocity during the late afternoon and the night, the UWIND2 simulation is likely more representative of the average broad mesoscale ascent during the day.

A simple Gaussian filter applied to the vertical velocity was not enough to mitigate the effects of the noisy skin temperature. Averaging the vertical velocity over a 1 km deep and 100 km wide area may result in a better comparison. The average vertical velocities of the UWIND2 ATWW simulation and the NoUWIND ATWW is similar (around 1 cm s^{-1}) (Fig. 5.33. This average vertical velocity is more likely what a parcel will experience over that period of time. A parcel is extremely unlikely to experience the maximum vertical velocity throughout the night.

While the average vertical velocity profiles of the UWIND2 and NoUWIND simulations are similar in magnitude, there is still more noise in the NoUWIND simulation than in the UWIND2 simulation. This noise is likely unavoidable without rerunning all of the simulations to reduce the noise in the skin temperature (done most easily by changing the initial zonal wind). However, the good agreement in the average vertical velocity between the equivalent smooth and noisy simulations means that we can analyze the vertical velocity of the noisy simulations without having to tailor each simulation to have a smooth skin PBL. However, one cannot simply compare the UWIND2 and NoUWIND simulations directly because the initial conditions are different, albeit slightly.

In the NoUWIND average heating simulations, the average vertical velocity decreases as the stratification increases, and there are no notable changes in the average vertical velocity as the initial meridional wind speed increases. These average vertical velocities are listed in Table 5.1. The maximum average vertical velocity is 2 cm s^{-1} in the WT simulations, 1.25 cm s^{-1} in the AT simulations, and 1 cm s^{-1} in the ST simulations (Fig. 5.34). This vertical velocity is sustained over a few hours during the middle of the night. In all nine average heating simulations, the average vertical velocity is weak during the day. This weak daytime vertical velocity is due to the spatial averaging. As the night progresses, the vertical velocity increases, reaching its maximum sometime between 0500 and 0800 UTC. The magnitude of these vertical velocities is weaker than that in Shapiro et al. (2018), but the surface baroclinic zone is not as strong as in their study, so it should be weaker.

As the heating increases, the average vertical velocity increases. In the NoUWIND weak heating simulations (Fig. 5.35), the maximum average vertical velocity is 1 cm s^{-1} in the WT simulations and decreases to 0.5 cm s^{-1} in the ST simulations. The time evolution of the vertical velocity is similar to that of the average heating simulation. As the initial meridional wind speed is increased, there are no notable differences in the average vertical velocity.

The maximum average vertical velocity in the simulations subjected to the strongest surface heating exceeds 3.5 cm s^{-1} in the NoUWIND WW simulations, is 2 cm s^{-1} in the AW simulations, and is 1.5 cm s^{-1} in the SW simulations (Fig. 5.36). Other than the vertical velocities' magnitudes, the vertical velocities characteristics (including its time evolution) are similar among all three heating simulations.

The maximum average vertical velocity ranges from 0.5 to 4 cm s^{-1}, depending on the strength of the surface heating and the environmental stratification. Not surprisingly, the highest vertical velocities are in the environments with strong heating and weak stratification. The time evolution of this vertical velocity remains the same in all 27 simulations. The magnitude increases during the night, reaches a maximum around 0500 – 0800 UTC, and then decreases.

Table 5.1: Average vertical velocity (cm s^{-1}) computed using the integral of the average vertical velocity during the night (0000 UTC - 1200 UTC).

Average Vertical Velocity	Weak Heating (cm s^{-1})	Average Heating (cm s^{-1})	Average Heating (UWIND2) (cm s^{-1})	Strong Heating (cm s^{-1})
WTWW	0.62	2.2	1.37	3.90
WTAW	0.59	1.44	1.48	3.09
WTSW	0.55	1.33	1.14	3.00
ATWW	0.33	1.1	0.88	1.63
ATAW	0.42	0.98	0.66	1.69
ATSW	0.35	1.03	0.96	1.79
STWW	0.38	0.85	0.68	1.15
STAW	0.31	0.70	0.53	1.33
STSW	0.28	0.74	0.72	1.22

5.4.1 Relationship between vertical velocity and the LLJ

Shapiro et al. (2018) stated that “for the typical case where the homogeneous jet is southerly, the peak ascent would be on the western flank of the full inhomogeneous jet.” In all simulations presented, the zone of ascent is west of the LLJ maximum, consistent with Shapiro et al. (2018). There is no vertical velocity in the simulation when there is no heating pad applied to the surface (i.e., when the only heating is due to the radiation scheme). An LLJ develops and is quasi-horizontally homogeneous throughout the domain. However, when the heating pad is added (generating the buoyancy gradient), the zone of mesoscale ascent occurs west of the LLJ maximum as a result of the horizontal buoyancy gradient (Fig. 5.37).

There seems to be little connection between the initial meridional wind and the strength of the vertical velocity. The simulations with a stronger initial meridional wind develop a stronger jet-like profile during the night. However, as the strength of the baroclinic zone increases, the strength of the vertical velocity increases as does the wind speed of the LLJ. The strength of the heating impacts the depth of the PBL, the strength of the jet, and the magnitude of the average vertical velocity. Conclusions about the relationship between the initial meridional wind speed and the vertical velocity cannot be made in this study due to the simplified model conditions.

5.5 Net Displacement

The net displacement of air parcels will be assessed in two ways: integrating the average vertical velocity during the night and examining the displacement associated with passive tracers that start at three different heights. Shapiro et al. (2018) suggested that parcels can rise anywhere from 300 m to 1 km due to this persistent vertical motion, so we will compare that assessment using these idealized numerical simulations.

It is assumed that the duration of ascent is 12 hours and that parcels remain in this area the entire time. This assumption is good because the ascent's orientation is typically parallel to the jet's orientation so that parcels will remain in the jet for long periods. The horizontal extent of the ascent is 400 km. If the parcel moves east or west at 10 m s^{-1}, it takes just over 11 hours to traverse this horizontal distance.

The net vertical displacement is calculated via the integral of the average vertical velocity during the night. As the environmental stratifications increase in the NoUWIND average heating simulations, the net vertical displacement of air parcels decreases. The net displacement is also not sensitive to the initial meridional wind speed as the net displacements from the WW to SW simulations are similar. The one exception is the WTWW simulations, but this large net displacement results from the large vertical velocities from 0200 – 0400 UTC. The average net displacement is 500 m for the WT simulations, 320 m for the AT simulations, and 230 m for the ST simulations.

The pattern of the net displacement is similar among all three heating simulations. The net displacement decreases as the stratification increases, and there is little dependency of the net displacement to the initial meridional wind speed. As the heating increases, the net displacement increases due to the stronger vertical velocity during the night. The weakest net displacement is 135 m in the STAW weak heating simulation, and the largest net displacement is 1215 m in the WTWW strong heating simulations. The net displacements for the different simulations are shown in Table 5.2.

Table 5.2: Net displacements (meters) computed using the integral of the average vertical velocity during the night (0000 UTC - 1200 UTC).

Net Displacement Integral	Weak Heating (m)	Average Heating (m)	Average Heating (UWIND2) (m)	Strong Heating (m)
WTWW	273.8	684.0	602.9	1214.5
WTAW	255.8	500.5	645.2	936.2
WTSW	241.2	401.7	499.1	917.5
ATWW	148.0	336.4	385.8	501.5
ATAW	185.2	308.0	308.0	535.1
ATSW	151.3	320.0	424.5	554.7
STWW	166.0	255.1	301.7	346.6
STAW	134.9	220.1	230.3	405.8
STSW	122.1	229.3	–	536.4

These net displacements are computed from the average vertical velocity from the raw model data, not the fitted curve to the data (indicated by the dashed line in Figs. 5.34-5.36. The difference between the average vertical velocity computed from the data and the fitted curve is small, and the difference in the net displacement is small. Thus, the fitted curve is a good representation of the data.

In general, the net displacements range from 200 m to over 1200 m, and the average is between 400 and 600 m. These net displacements correspond well with those noted by Shapiro et al. (2018) for this type of LLJ-related ascent. However, while these simulations have a PBL parameterization and a surface-layer scheme (for a complete list of physics parameterizations, see Table 2.4), they remain dry, so CI cannot occur in these simulations. Processes associated with typical environments include moisture advection via the LLJ and moisture advection from decaying convection from the west. This ascent, combined with the increasing moisture in these environments, results in smaller displacement necessary to produce CI in these more optimal environments.

5.5.1 Passive Tracers

Passive tracers are initialized at three heights: 125 m, 700 m, and 1500 m (Figs. 5.38, 5.39, and 5.40). How these tracers evolve as a function of time, especially during the night, will provide insight on how a parcel may move in this environment.

The first, and perhaps most obvious, observation is that there are many simulations in which the passive tracers become well mixed throughout the PBL during the night. These tracers cannot penetrate the capping inversion into the free atmosphere; however, they remain in the residual layer. Analyzing the net displacement of parcels in the simulations where they are well mixed throughout the residual layer will result in the difference between the depth of the PBL and the starting height of the passive tracer.

However, there are some simulations (including the UWIND2 WW simulations) in which the tracers are not seemingly everywhere in the PBL, and that can give us a comparison with the net displacement using the integral of the average vertical velocity during the night (Fig. 5.41). Let us start with the NoUWIND average heating ATSW simulation. The net displacement for the tracers at 0800 UTC is 512.5 m for those starting at 700 m AGL.

This analysis is complicated because CM1 does not allow tracers to be put in at a specific time. The tracers must be initialized beginning at the start of the simulation. To mitigate the impact of the tracer's daytime net displacement on the analysis of their net displacement during the night, we examine the difference between the net displacement late at night (around 0900 UTC) and the net displacement at 0000 UTC of the tracers that have smooth profiles. This resulting displacement should result in the displacement that occurred during the night. For the ATSW simulation, this is 325 m. The integral of the average vertical velocity during the night is 320 m, so there is good agreement in this simulation. This net displacement is the one noted in Figs. 5.38 - 5.40 and in Table 5.3.

There is relatively good agreement between the displacement using the average vertical velocity and the displacement using the passive tracers. In most cases, the average net displacement is between 300 and 600 m. This displacement should be sufficient in these

Table 5.3: Net Displacement (m) computed using passive tracer position at 0800 UTC - 0000 UTC. The passive tracer starting at 700 m is the one used.

Net Displacement	Weak Heating	Average Heating	Average Heating (UWIND2)	Strong Heating
WTWW	–	–		–
WTAW	325	–		–
WTSW	200	–		–
ATWW	–	–		–
ATAW	200	–		–
ATSW	150	325		600
STWW	–	–		–
STAW	100	375		–
STSW	–	275	–	–

LLJ environments because the moisture advection from the south and the west should help make the environment more conducive for CI throughout the night. The persistent ascent throughout the night can cool the atmosphere and aid in the generation of a MAUL, so even small displacements can be enough to cause CI.

5.6 Analysis using the Sawyer-Eliassen Equation

Recall the Sawyer-Eliassen Equation

$$\begin{aligned}\frac{\partial^2 \psi}{\partial y^2}\left[-\frac{R}{f_0 p}\left(\frac{p}{p_0}\right)^{\kappa}\frac{\partial \theta}{\partial p}\right]+\frac{\partial^2 \psi}{\partial y \partial p}\left(2\frac{\partial u_g}{\partial p}\right)+\frac{\partial^2 \psi}{\partial p^2}\left(f_0-\frac{\partial u_g}{\partial y}\right)\\ =2\left[\frac{R}{f_0 p}\left(\frac{p}{p_0}\right)^{\kappa}\left(\frac{\partial \theta}{\partial y}\frac{\partial v_g}{\partial y}+\frac{\partial \theta}{\partial x}\frac{\partial u_g}{\partial y}\right)\right]-\frac{R}{f_0 p}\frac{1}{c_p}\frac{\partial}{\partial y}\left(\frac{dQ}{dt}\right)\end{aligned} \quad (5.1)$$

where Ψ is the streamfunction, p is pressure, θ is the potential temperature, u_g is the zonal geostrophic wind, and dQ/dt is diabatic heating. $2\frac{R}{f_0 p}\left(\frac{p}{p_0}\right)^{\kappa}\left(\frac{\partial v_g}{\partial y}\frac{\partial \theta}{\partial y}\right)$ represents changes in the across-front temperature gradient due to geostrophic stretching and deformation along the front. $2\frac{R}{f_0 p}\left(\frac{p}{p_0}\right)^{\kappa}\left(\frac{\partial u_g}{\partial y}\frac{\partial \theta}{\partial x}\right)$ represents in changes in the across-front temperature gradient due to the tilting of the along-front temperature gradient into the cross-front direction by the geostrophic shearing deformation. $-\frac{R}{f_0 p}\frac{1}{c_p}\frac{\partial}{\partial y}\left(\frac{dQ}{dt}\right)$ is the differential diabatic heating term.

We can apply this equation to the output simulations to see if the sign of the circulation is similar to that seen in the simulations. The difficulty in doing this is the noisiness of the model data in all simulations. This noise affects the second derivatives that need to be computed, which results in numerical instability. Smoothing the data can alleviate this problem, but the amount of smoothing needed to maintain some numerical stability reduces the computed data's value and the output magnitudes of the streamfunction.

Furthermore, pressure adjusts rapidly throughout the domain. This quick adjustment is due, in part, to the weak forcing put throughout the entire domain, as the only forcing that would result in horizontally-heterogeneous pressure changes is the heating pad at the surface. Otherwise, everything is horizontally homogeneous. This weak pressure gradient results in weak geostrophic winds, so the actual wind was used in this analysis.

The differential diabatic heating term is weak (1 K $(1000 \text{ km})^{-1}$ $(12 \text{ hr})^{-1}$) and will not contribute significantly to the magnitude in these simulations. However, while the magnitude is weak, the data still need to be smoothed because of its noisiness. Based on this smoothing needed to maintain computation stability and the relatively weak gradients in the model output, getting any quantitative results will be unlikely. However, we may still obtain a qualitative sense of the resulting circulation.

Because all of the simulations have similar characteristics, the smoothest data will be analyzed because the iteration process will converge more easily. In the chosen cases, the analysis using the Sawyer-Eliassen indicated rising motion west of x=0 and sinking motion on the other two sides (Fig. 5.42). While the magnitude of this vertical velocity is not the same as the model output (because of the amount of smoothing necessary), the sense of the circulation is similar.

5.7 Summary

The broad mesoscale ascent noted in Shapiro et al. (2018) was explored using idealized numerical simulations. The baroclinic zone at the surface was created via a heating pad during the daytime. The nine typical environments were subjected to three strengths of the heating pad, resulting in 27 simulations. The average heating simulations were also rerun to include a 2 m s^{-1} initial zonal wind. This addition resulted in 36 total simulations.

All 36 simulations produced LLJs, and all had persistent mesoscale ascent during the night. The magnitude of the ascent varied from 0.3 to 3 cm s^{-1}. The net displacement of air parcels during the night associated with this ascent ranged from 200 m to over 1 km. For a parcel to realize this net displacement, it must remain in that mesoscale area of ascent for a long duration. Given that the jet axis orientation and the mesoscale area of ascent are usually parallel to each other, it is not a terrible assumption to assume that these parcels can remain in this zone for several hours, at least. Future work involving these LLJ simulations will be to compute trajectories for parcels starting at night. The path of these trajectories will be similar to the actual trajectory of an air parcel, allowing us to obtain its three-dimensional coordinates as a function of time (tracking its horizontal and vertical displacements).

This mechanism is a plausible mechanism for NB CI mode events, and stronger baroclinic zones will like result in stronger ascent throughout the night. This mechanism is different from the horizontal convergence due to the differential veering of the LLJ identified in Gebauer et al. (2018) and provides an alternative explanation for LLJ-related ascent. The prevalence of this mechanism has not yet been determined, but the variety of ascent mechanisms associated with the LLJ illustrate its importance to nocturnal CI. The LLJ is common at night, and its influence on CI at night (with or without surface boundaries) cannot be understated.

The strong arbitrary surface heating in these simulations to generate a surface baroclinic zone likely resulted in unintended consequences in these simulations. For example, the surface cooling at night was more substantial than what would otherwise be simulated via radiation alone. The dry soil moisture could add to this increase in cooling during the night. The surface was decoupled from the atmosphere, resulting in the runaway cooling effect described by Jiménez et al. (2012). The forced heating and the lack of options of PBL schemes and surface-layer schemes prevent this effect from being mitigated. To mitigate this effect, local PBL schemes such as MYNN or QNSE would likely need to be added to CM1 as local schemes typically better represent the nocturnal PBL. However, adding these schemes to CM1 is outside the scope of this study.

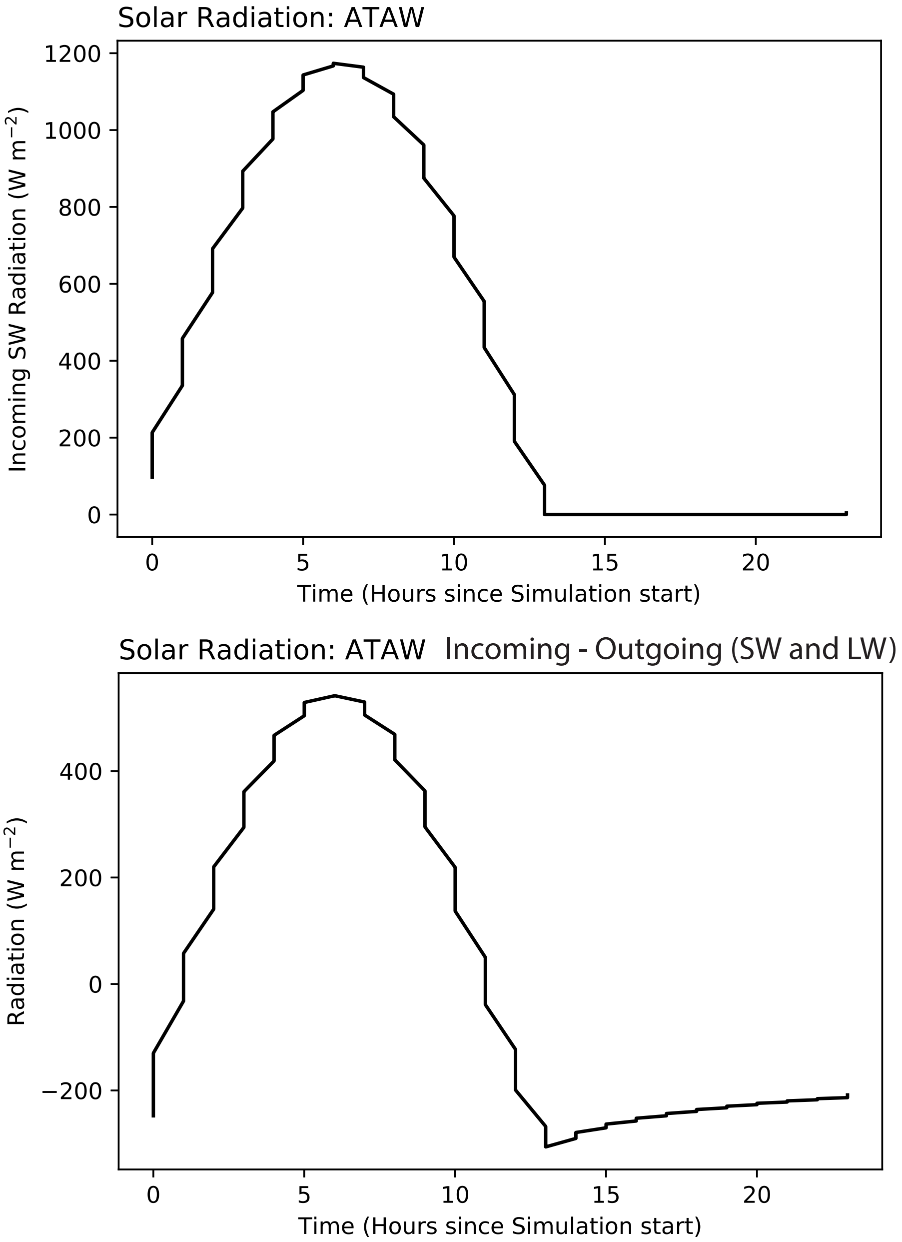

Figure 5.1: a) Incoming shortwave radiation (W m^{-2}) and b) Net radiation at the surface (incoming - outgoing) (W m^{-2}).

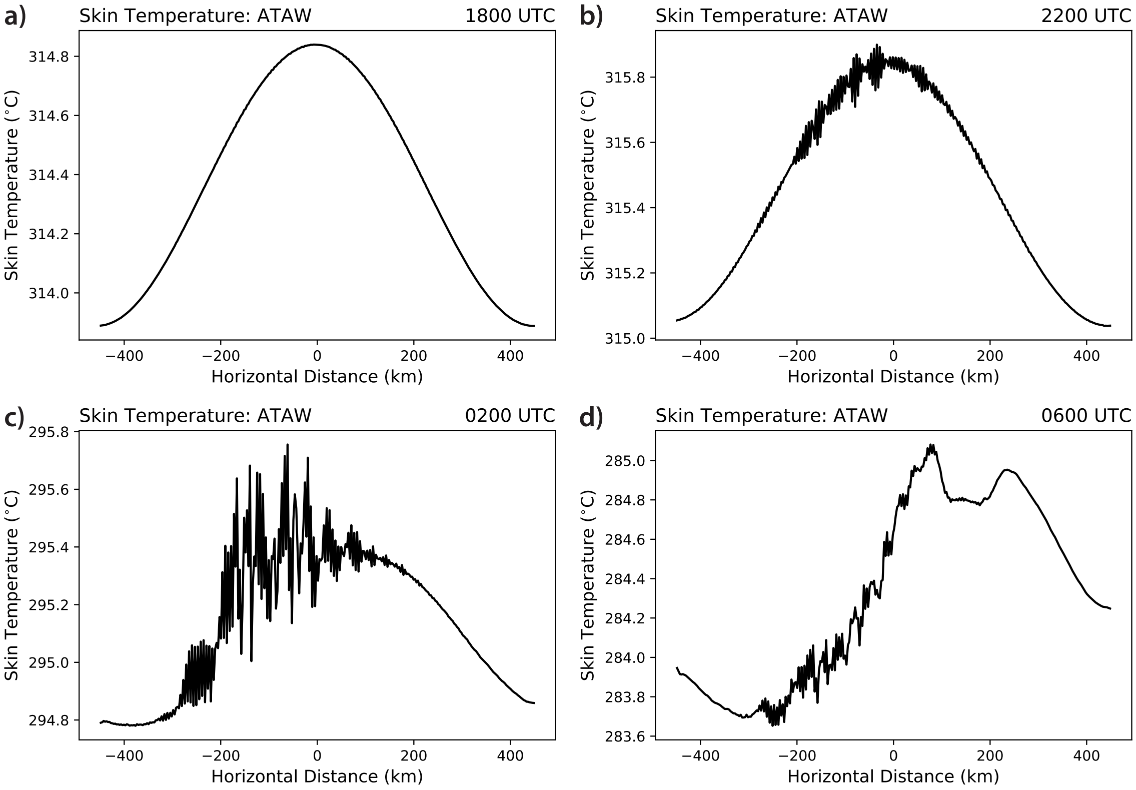

Figure 5.2: Skin temperature (°C) for the ATAW simulation at a) 1800 UTC, b) 2200 UTC, c) 0200 UTC, and d) 0600 UTC.

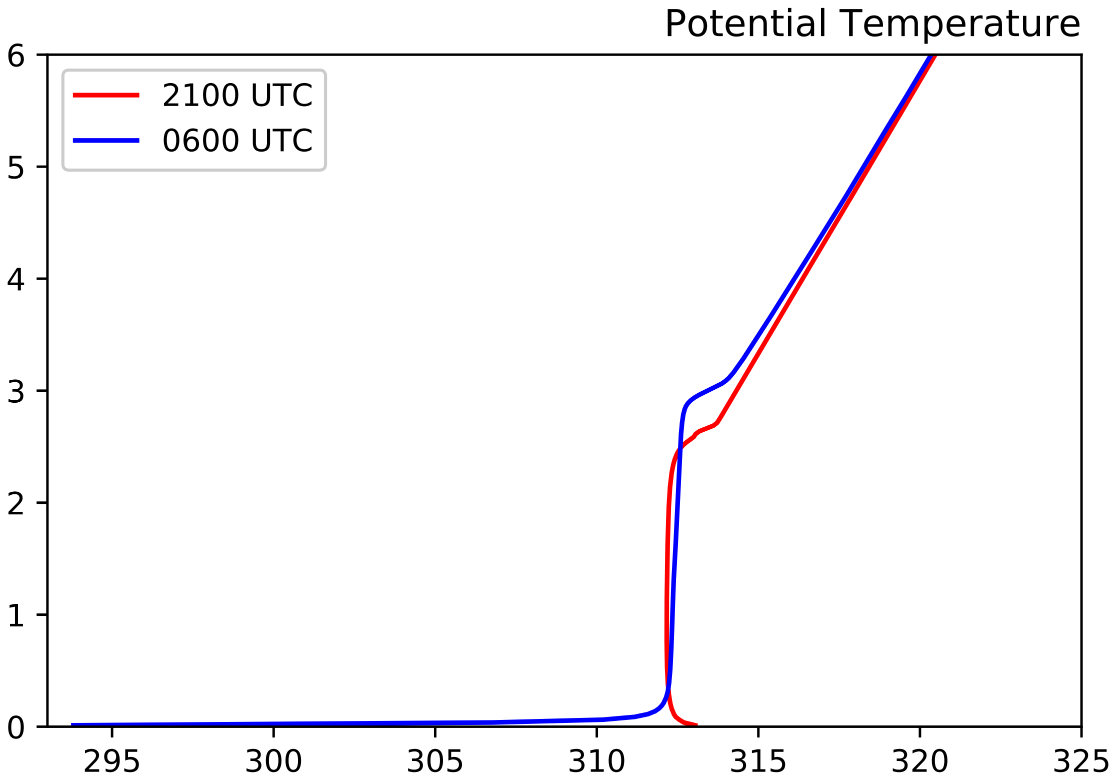

Figure 5.3: Potential temperature as a function of height at 2100 UTC (red curve) and 0600 UTC (blue curve).

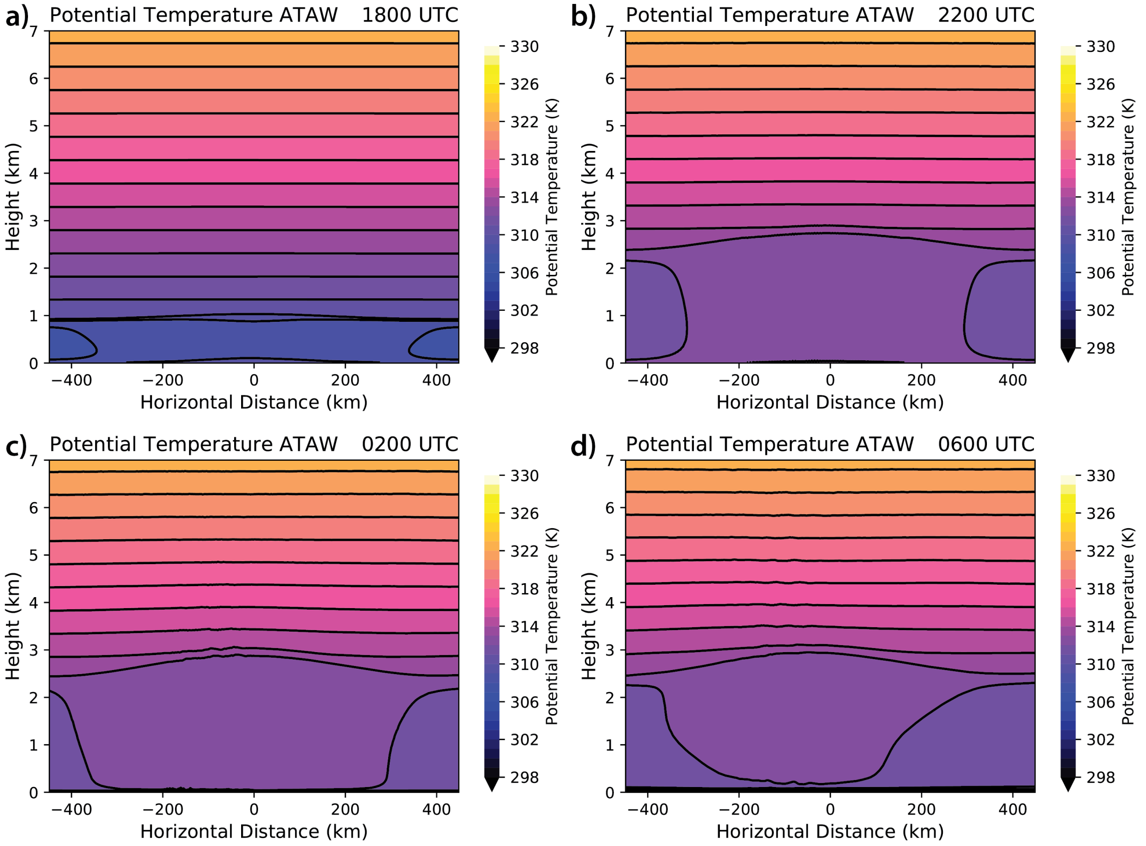

Figure 5.4: As in 5.2, but for potential temperature. Height is on the y-axis and the horizontal distance is on the x-axis.

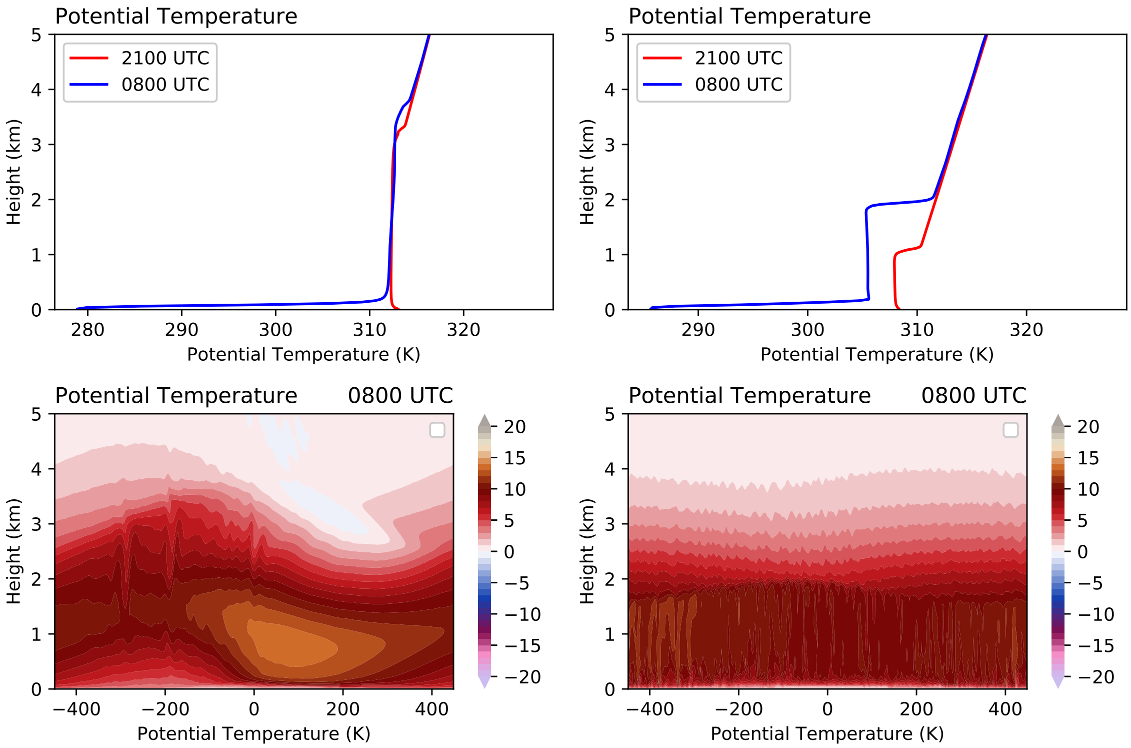

Figure 5.5: (a),(b) potential temperature at 2100 UTC (red curve) and 0800 UTC blue curve. (c),(d) meridional wind component (m s^{-1}). (a) and (c) have no moisture in the simulation. (b) and (d) have no moisture in the atmosphere, but include soil moisture.

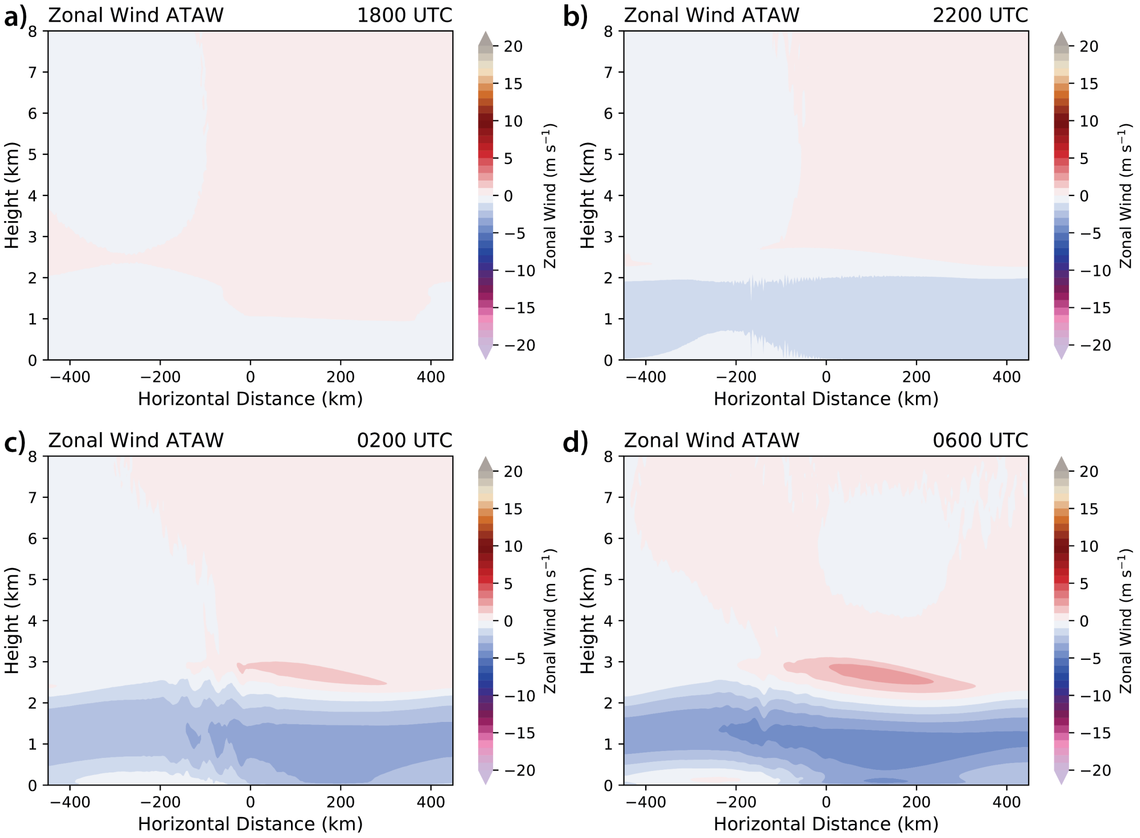

Figure 5.6: As in Fig. 5.4, but for the zonal wind component.

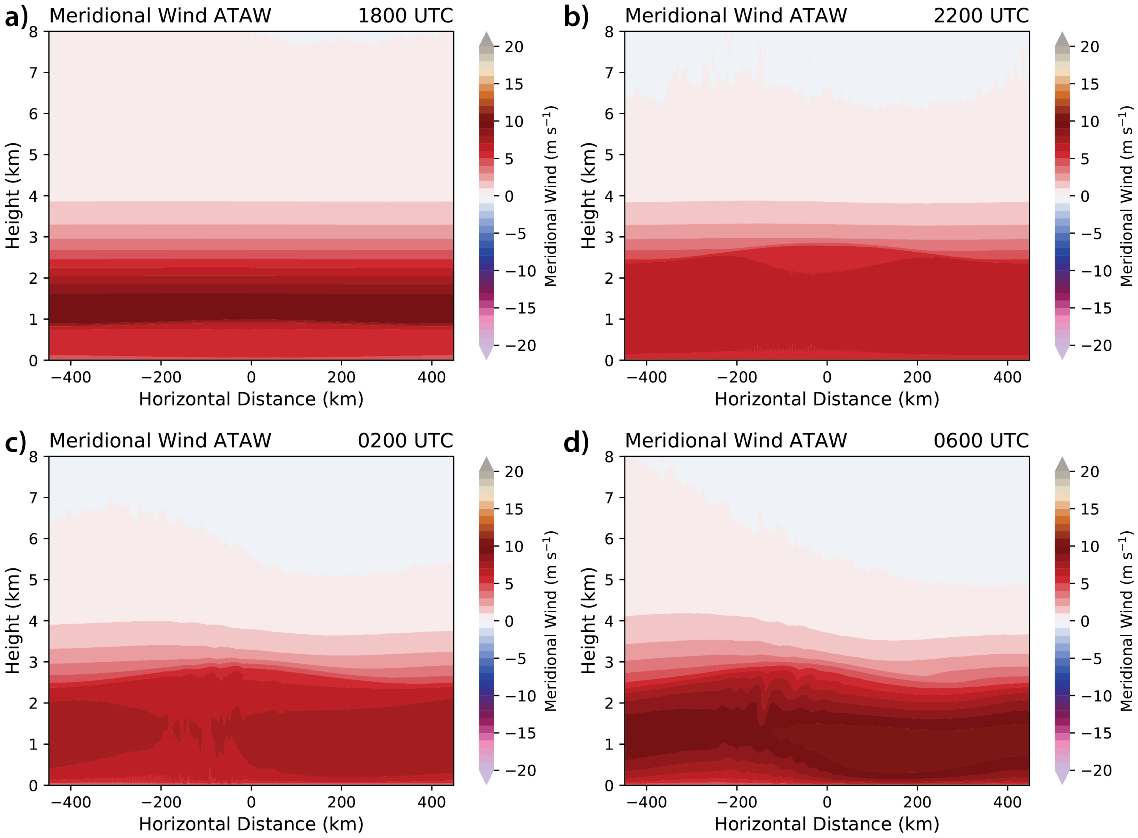

Figure 5.7: As in Fig. 5.4, but for the meridional wind component.

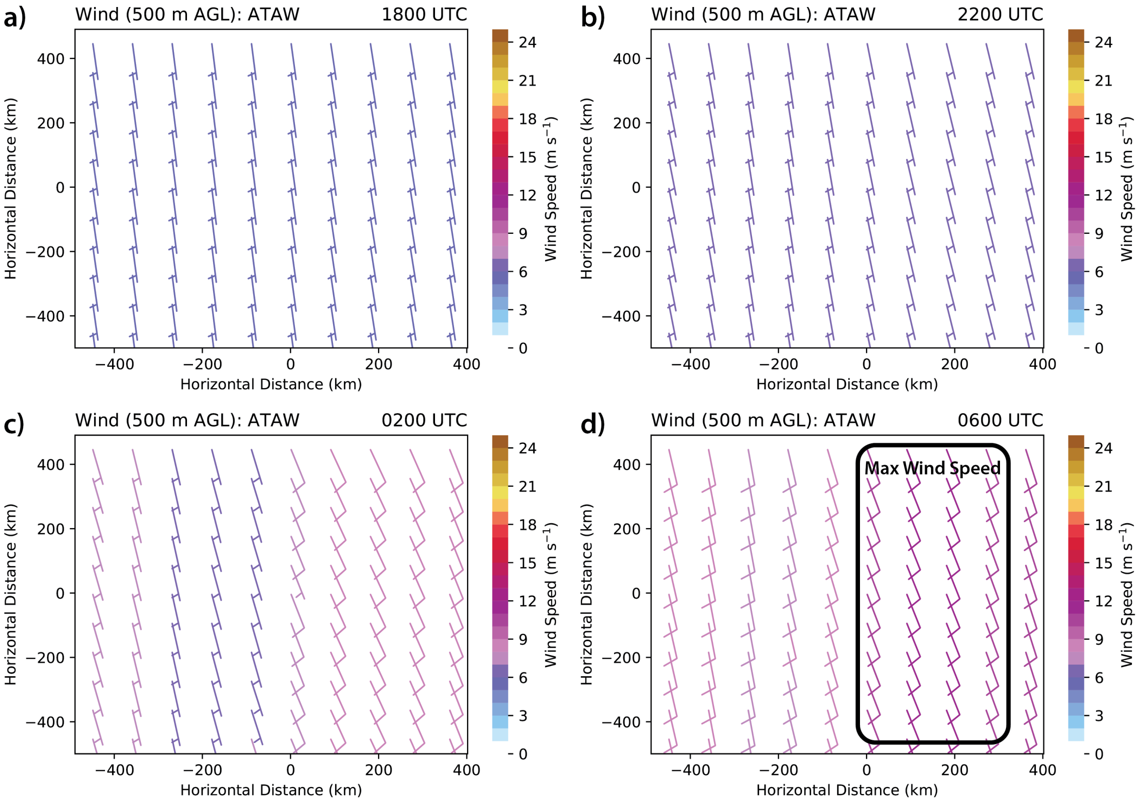

Figure 5.8: Wind barbs (full barb is 10 m s^{-1}) at 500 m AGL for (a) 1800 UTC, (b) 2200 UTC, (c) 0200 UTC, and (d) 0600 UTC.

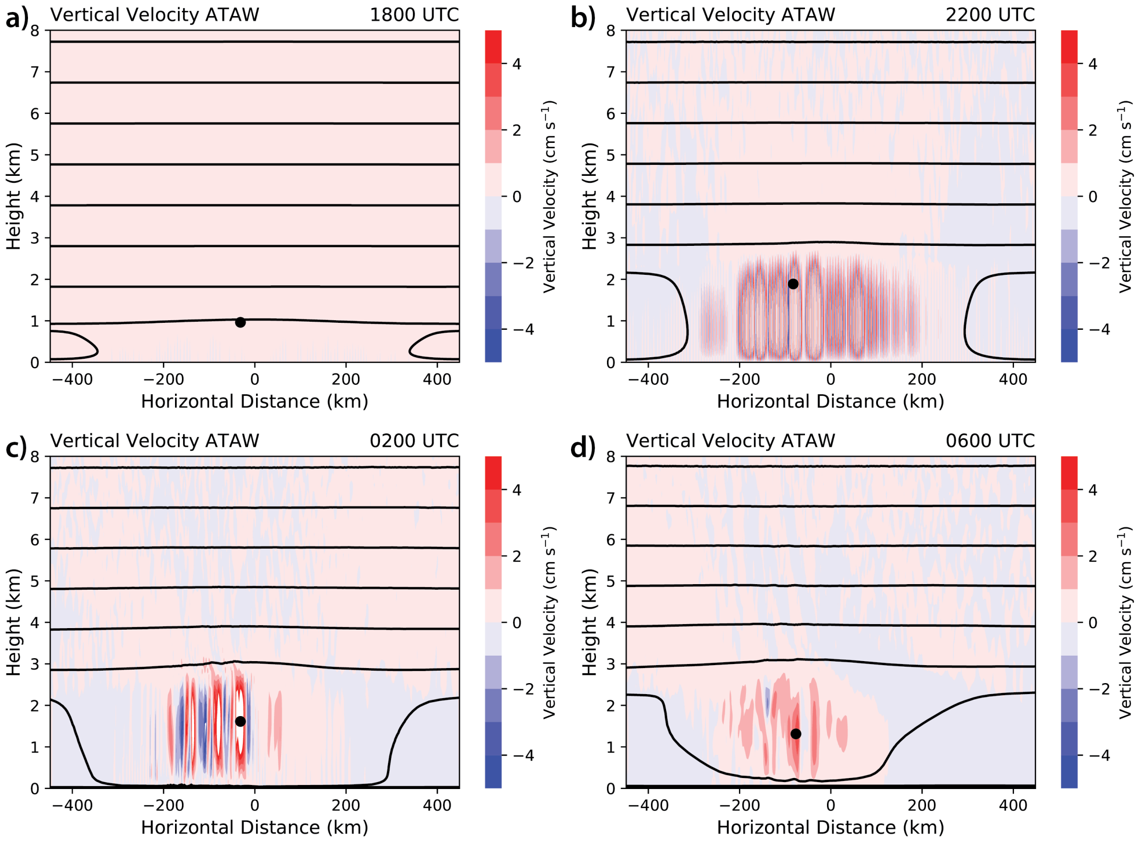

Figure 5.9: As in Fig. 5.4, but for the vertical velocity (color filled) and potential temperature (contoured every 2K).

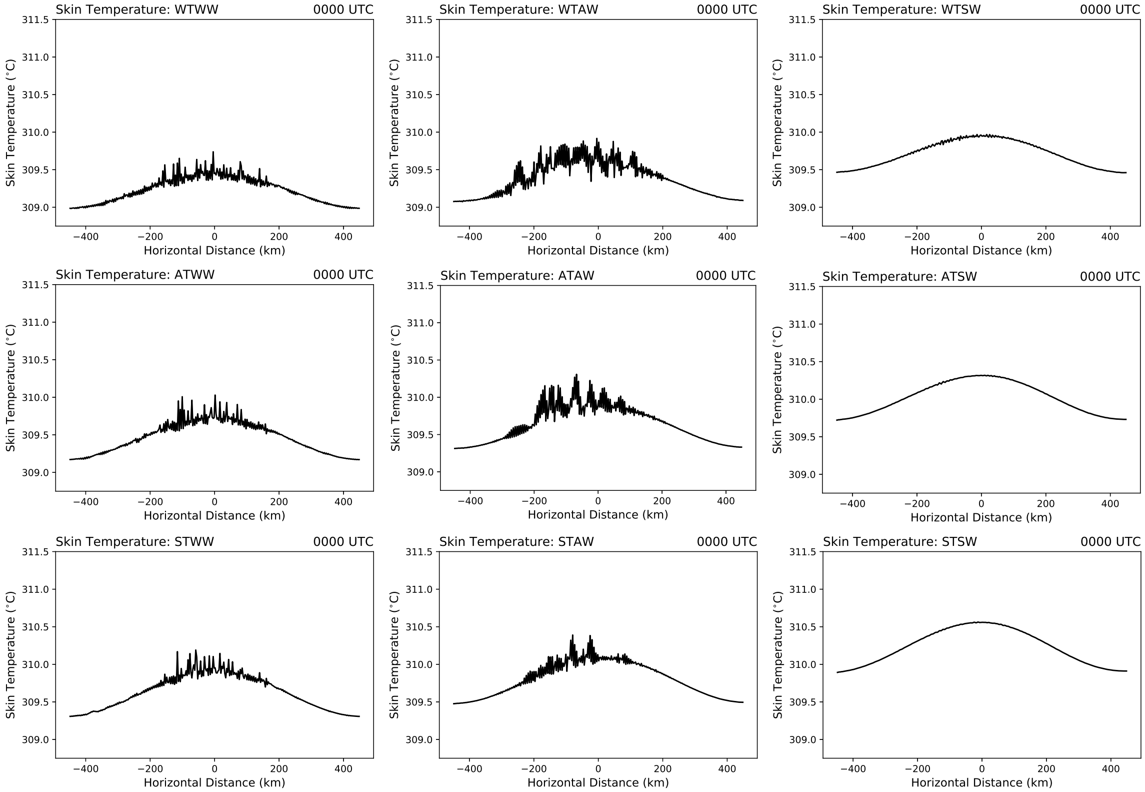

Figure 5.10: Skin temperature (°C) for the (a) WTWW, (b) WTAW, (c) WTSW, (d) ATWW, (e) ATAW, (f) ATSW, (g) STWW, (h) STAW, and (i) STSW simulations.

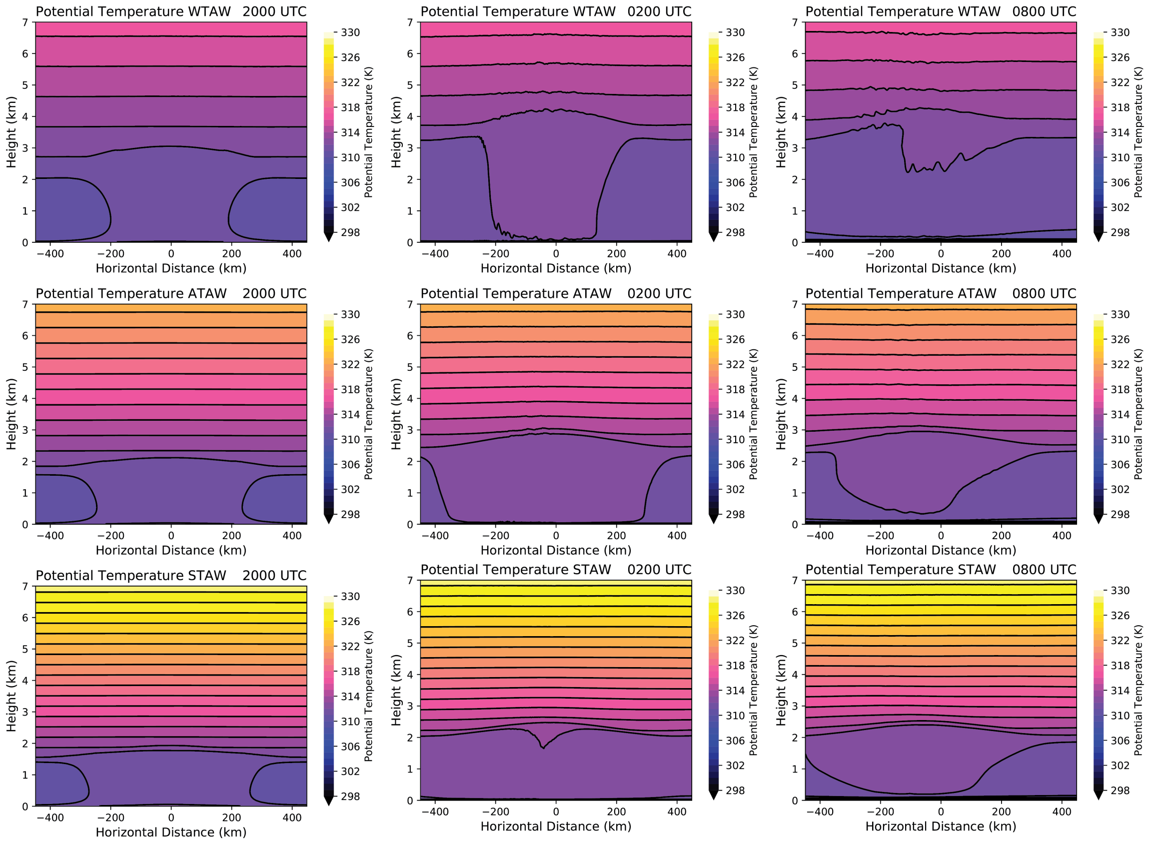

Figure 5.11: As in Fig. 5.10, but for potential temperature. Height is on the y-axis and the horizontal distance is on the x-axis.

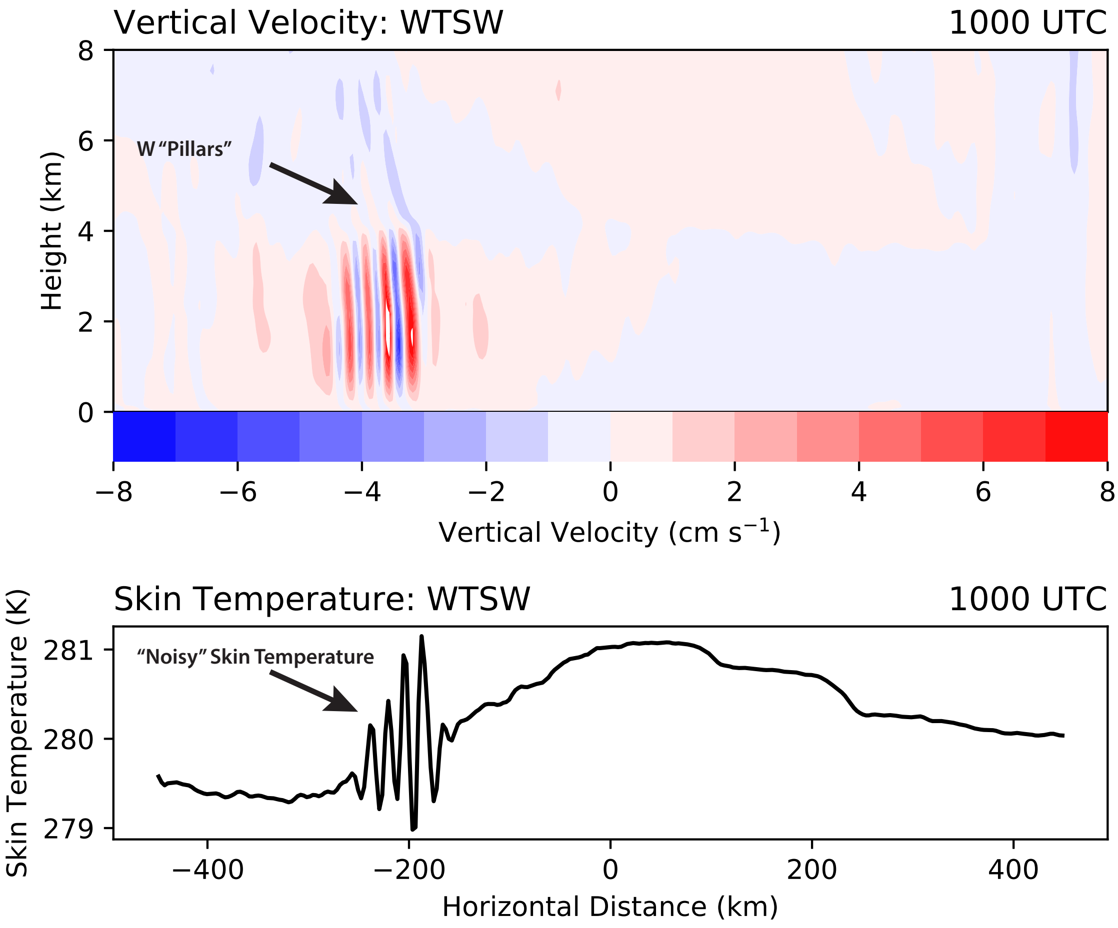

Figure 5.12: (a) Vertical velocity (color-filled; cm s^{-1}) and (b) skin temperature (°C). The "pillars" of vertical velocity correspond to the noisy skin temperature.

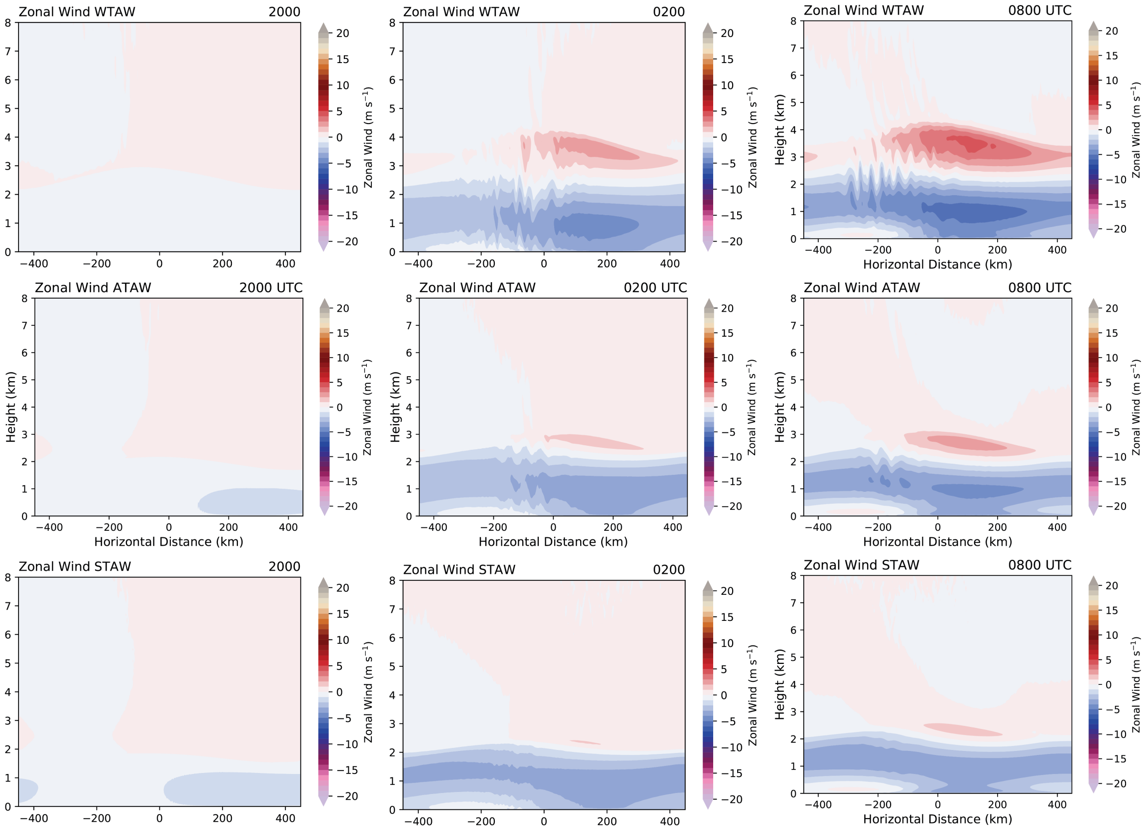

Figure 5.13: As in Fig. 5.11, but for the zonal wind component.

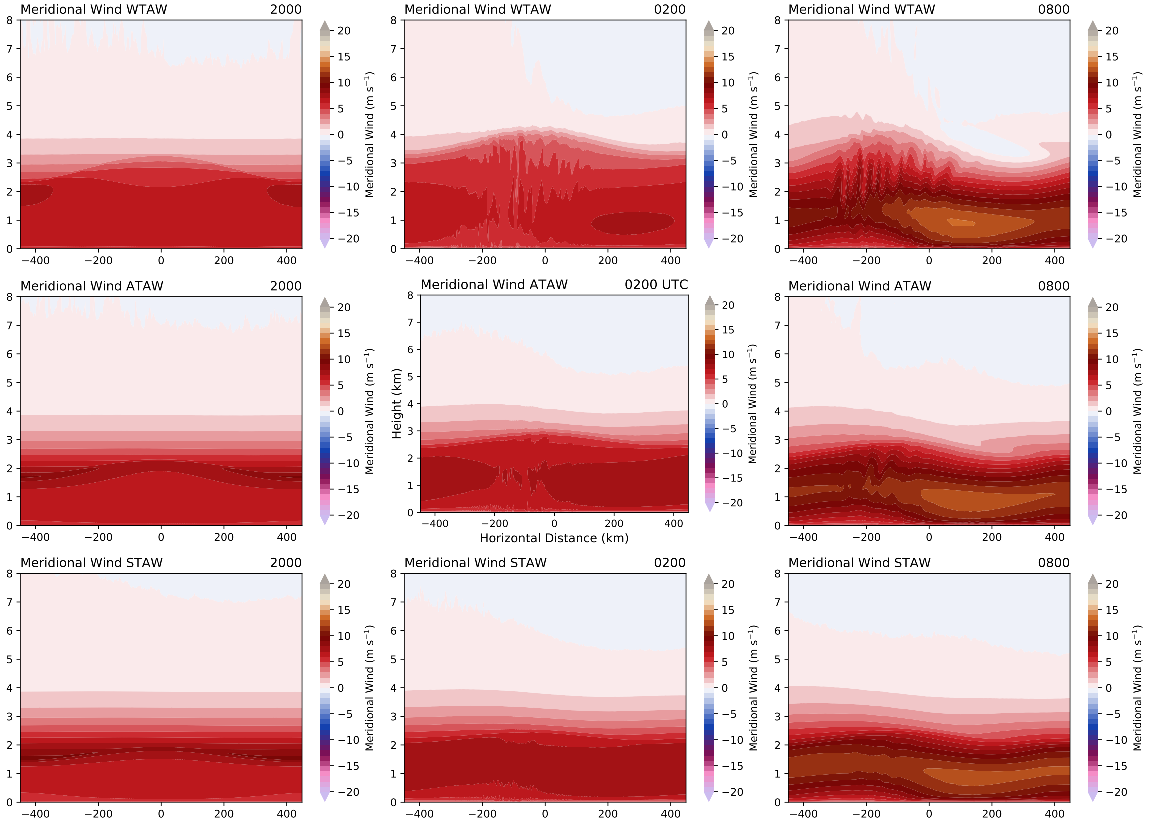

Figure 5.14: As in Fig. 5.11, but for the meridional wind component.

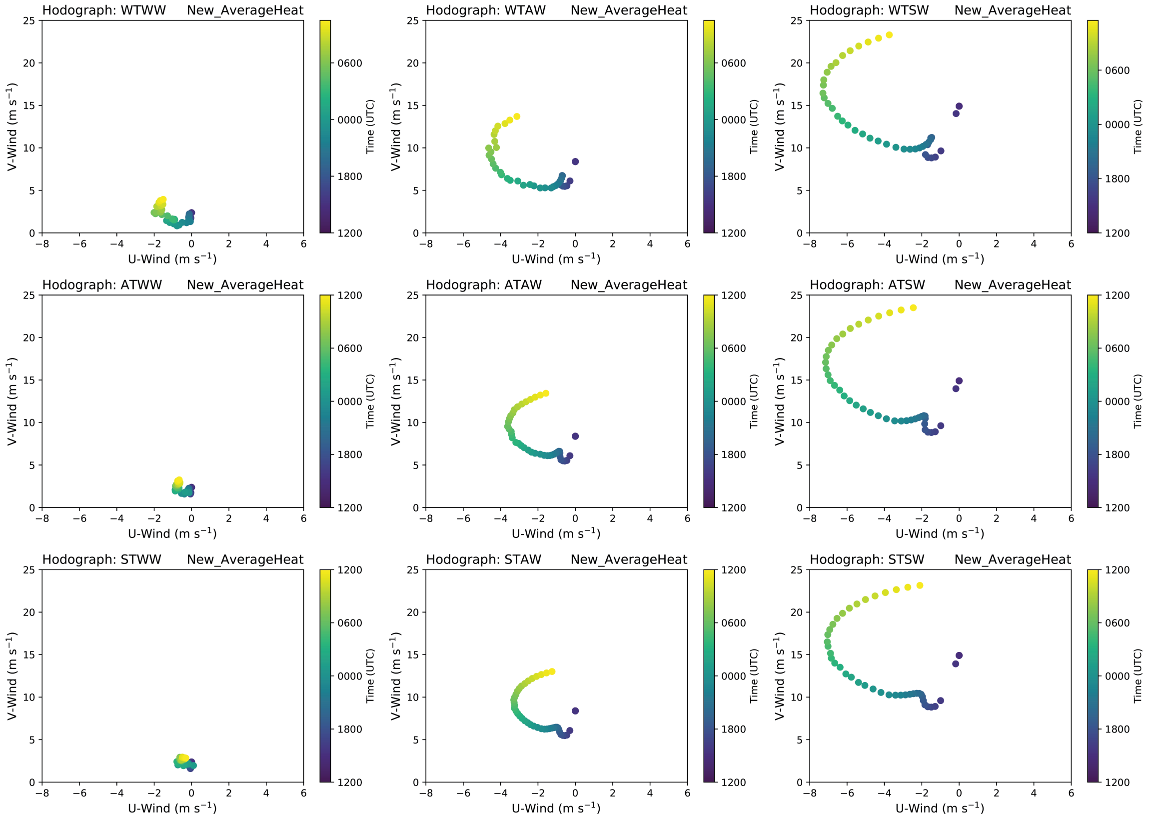

Figure 5.15: As in Fig. 5.11, but for the hodographs. The zonal wind is on the x-axis and the meridional wind is on the y-axis. The color of the dot gets lighter as time increase.

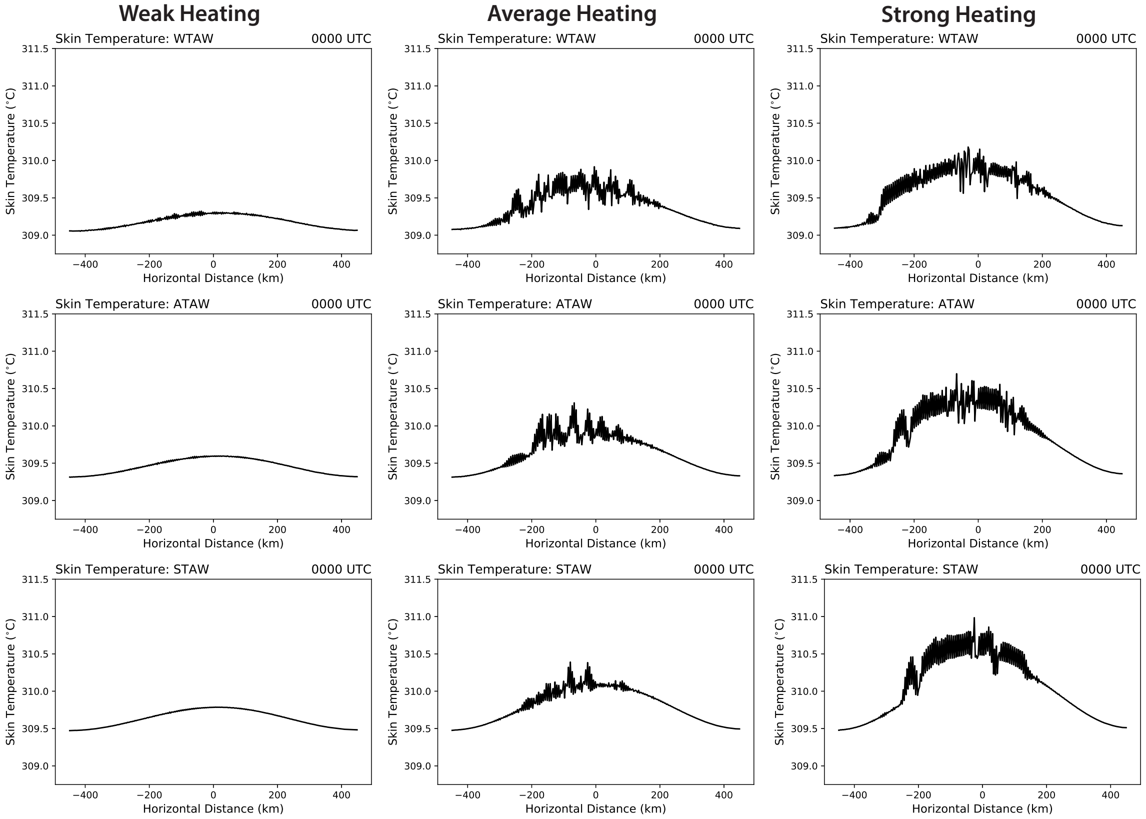

Figure 5.16: Skin temperature for the AW simulations for (a),(b),(c) weak heating (10 K hr^{-1} max), (d),(e),(f), average heating (20 K hr^{-1} max), and (g),(h),(i), strong heating (30 K hr^{-1} max). The mid-level stability in these simulations increases from top to bottom.

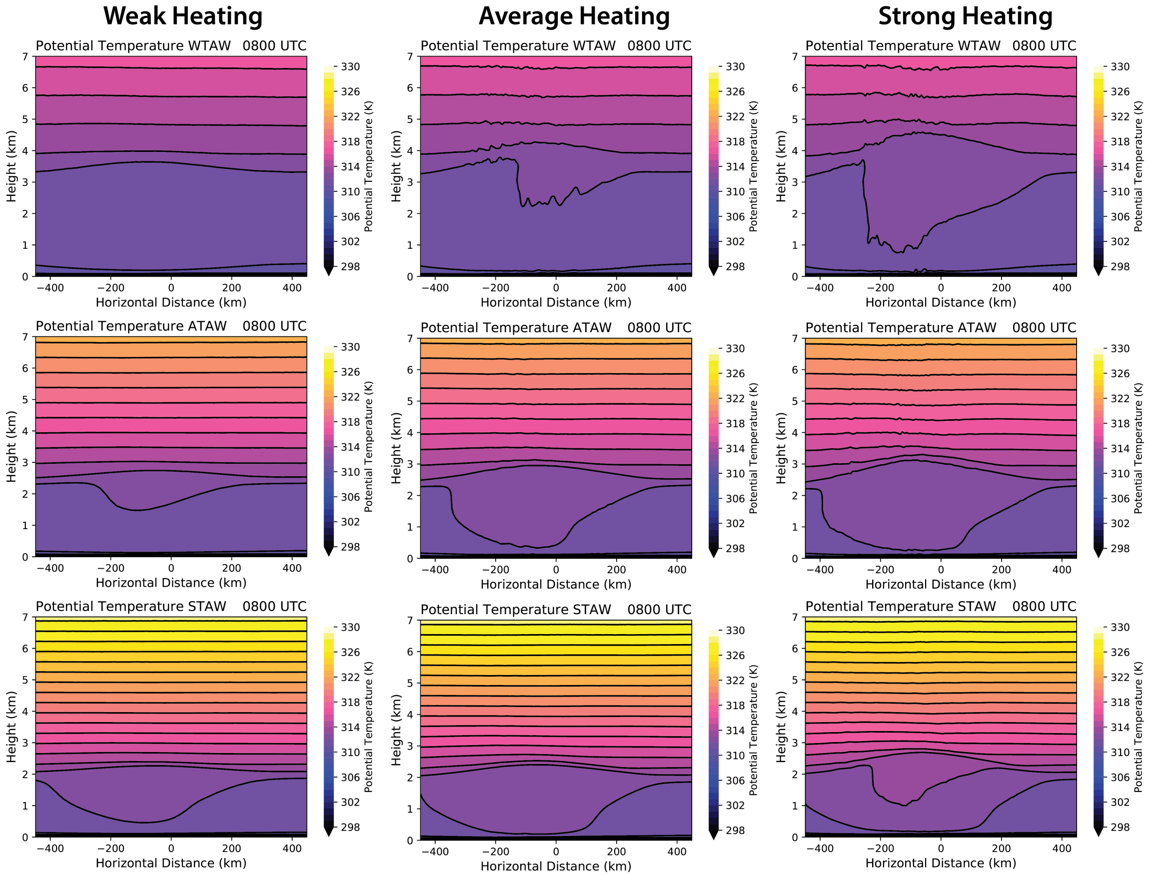

Figure 5.17: Potential temperature at 0800 UTC for the AW simulations for (a),(b),(c) weak heating (10 K hr^{-1} max), (d),(e),(f), average heating (20 K hr^{-1} max), and (g),(h),(i), strong heating (30 K hr^{-1} max). The mid-level stability in these simulations increases from top to bottom. Height is on the y-axis and horizontal distance is on the x-axis.

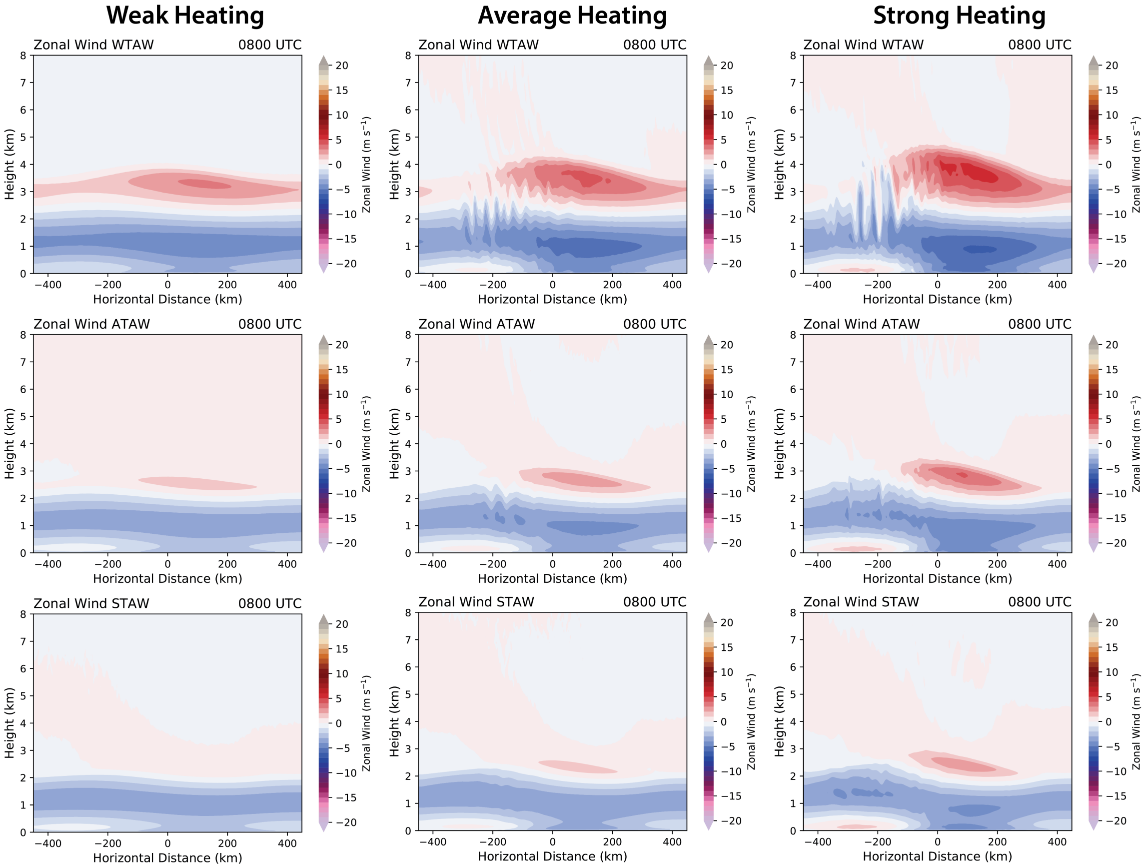

Figure 5.18: The zonal wind component at 0800 UTC for the AW simulations for (a),(b),(c) weak heating (10 K hr^{-1} max), (d),(e),(f), average heating (20 K hr^{-1} max), and (g),(h),(i), strong heating (30 K hr^{-1} max). The mid-level stability in these simulations increases from top to bottom. Reds represent westerly winds and blues represent easterly winds.

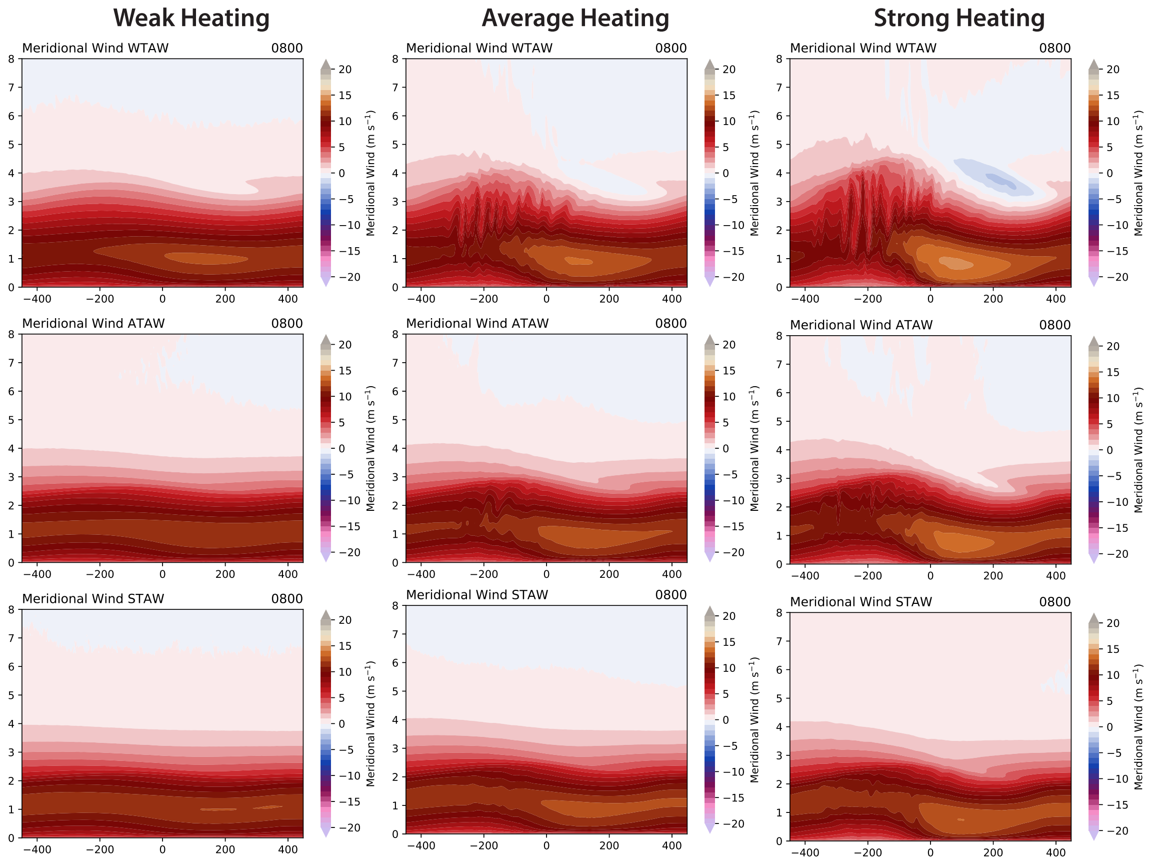

Figure 5.19: As in Fig. 5.18, but for the meridional wind component.

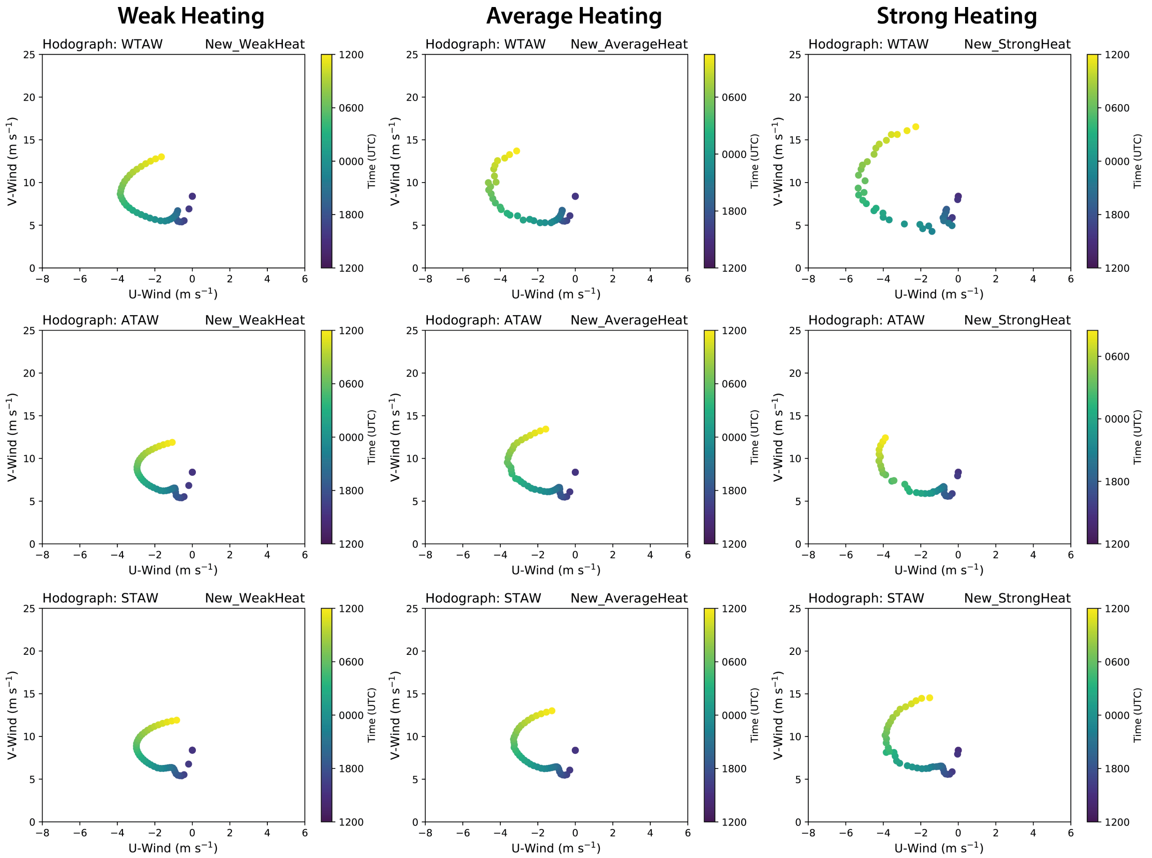

Figure 5.20: Hodographs for the AW simulations for (a),(b),(c) weak heating (10 K hr^{-1} max), (d),(e),(f), average heating (20 K hr^{-1} max), and (g),(h),(i), strong heating (30 K hr^{-1} max). The mid-level stability in these simulations increases from top to bottom. The zonal wind is on the x-axis and the meridional wind is on the y-axis. The color of the dot gets lighter as time increase.

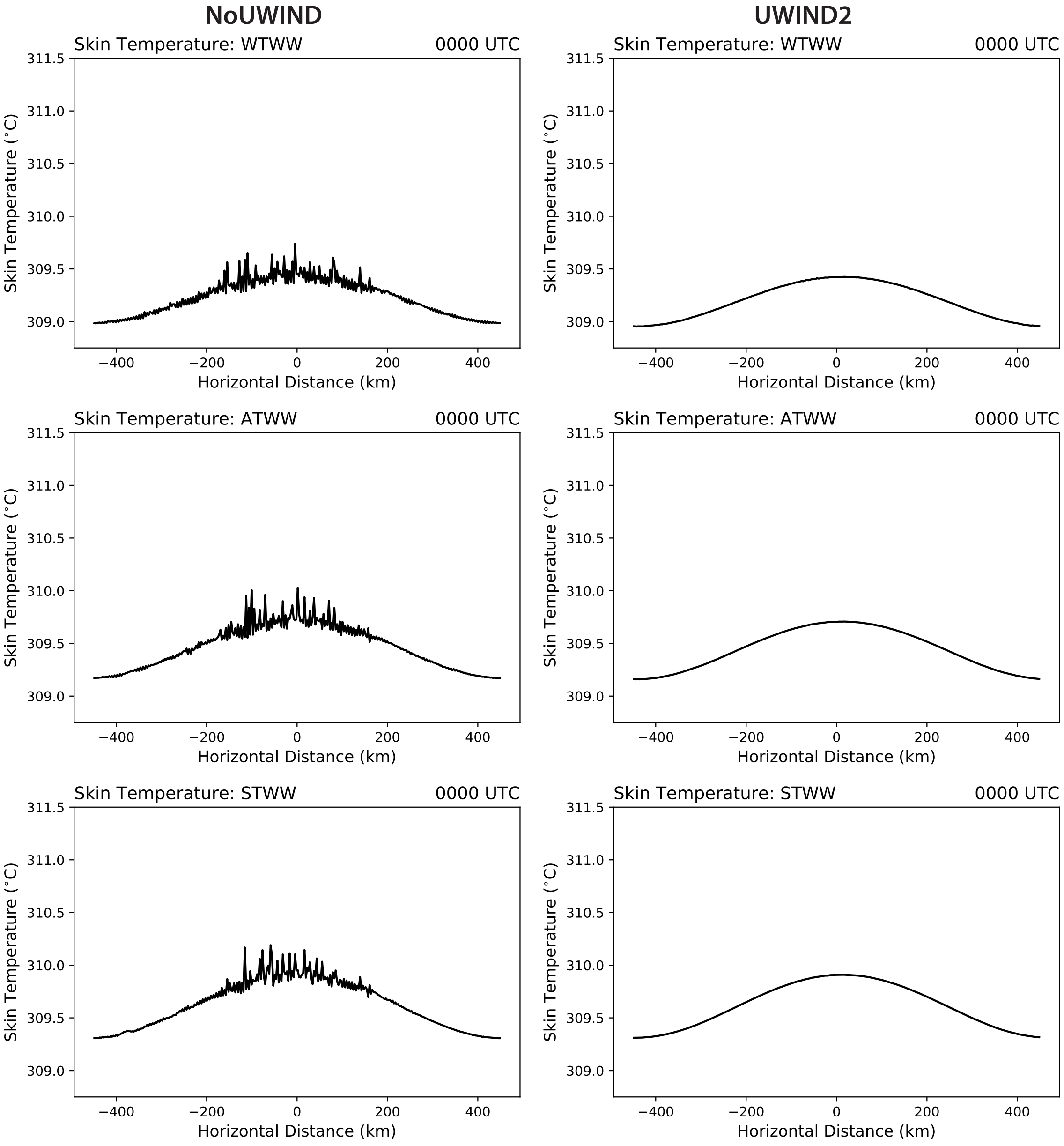

Figure 5.21: Skin Temperature (°C) at 0000 UTC for the WW simulations for (a),(b),(c), NoUWIND simulations and (d),(e),(f), UWIND2 simulations. Static stability increases from top to bottom.

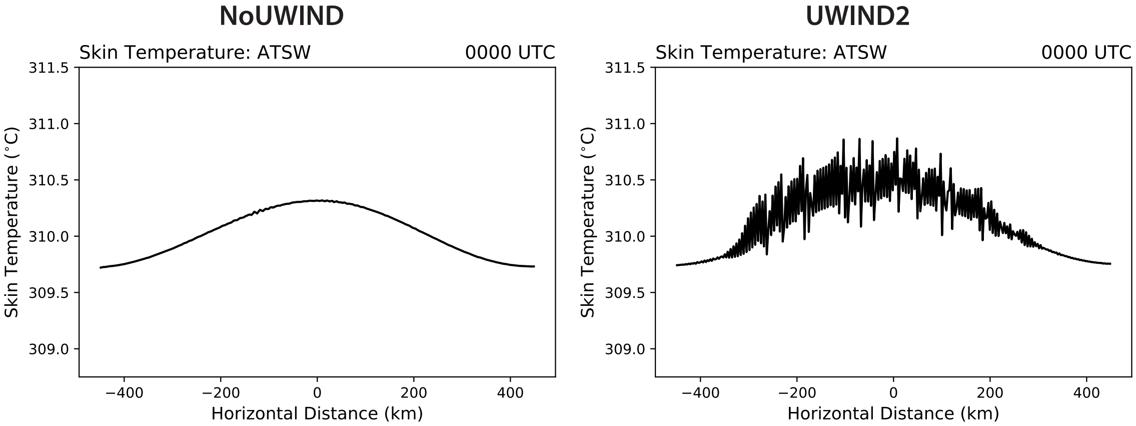

Figure 5.22: As in Fig. 5.21, but for the ATSW simulation.

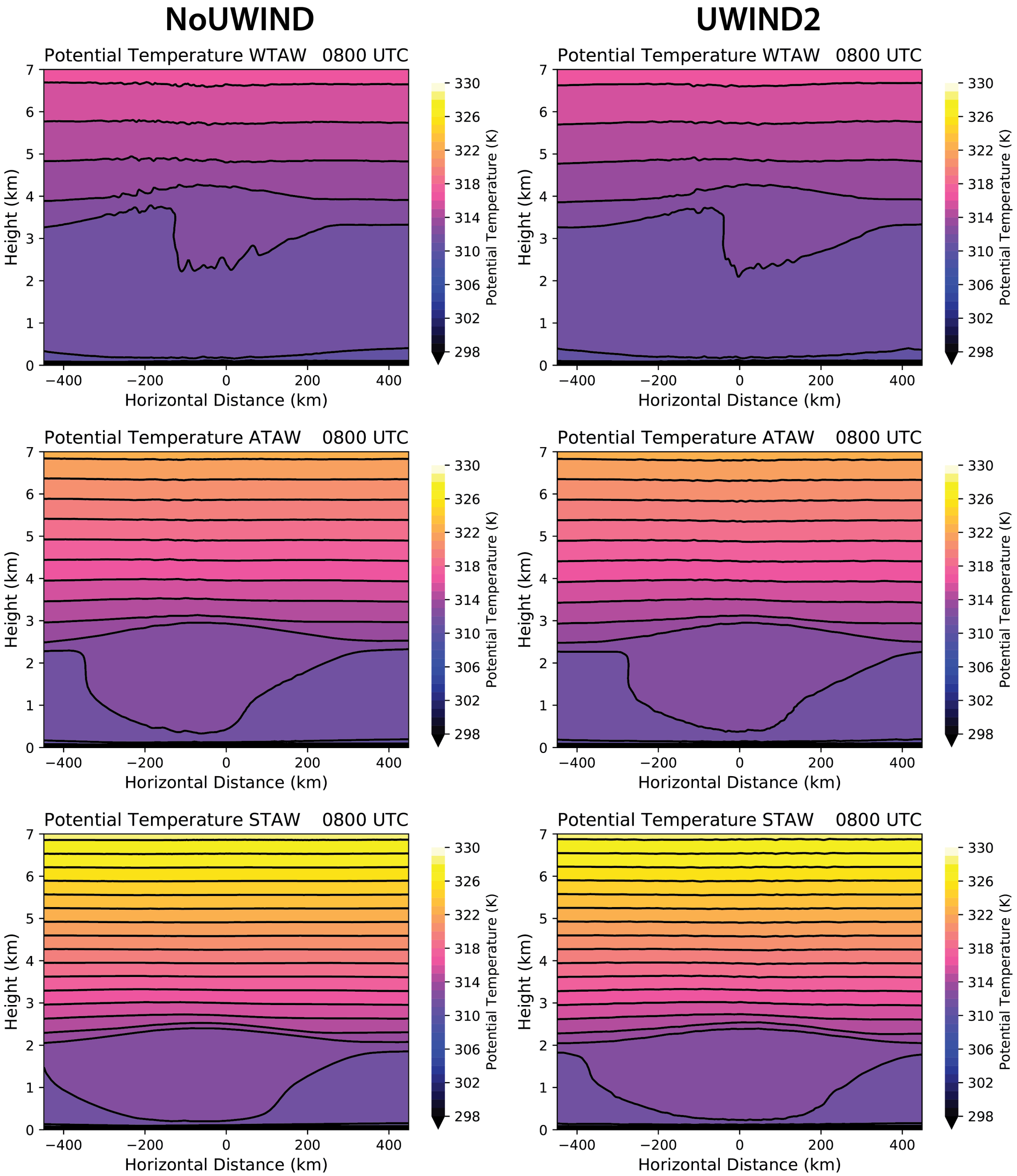

Figure 5.23: Potential temperature (K; contoured every 2 K) at 0800 UTC for the AW simulations for (a),(b),(c), NoUWIND simulations and (d),(e),(f), UWIND2 simulations. Static stability increases from top to bottom. Height is on the y-axis and horizontal distance is on the x-axis.

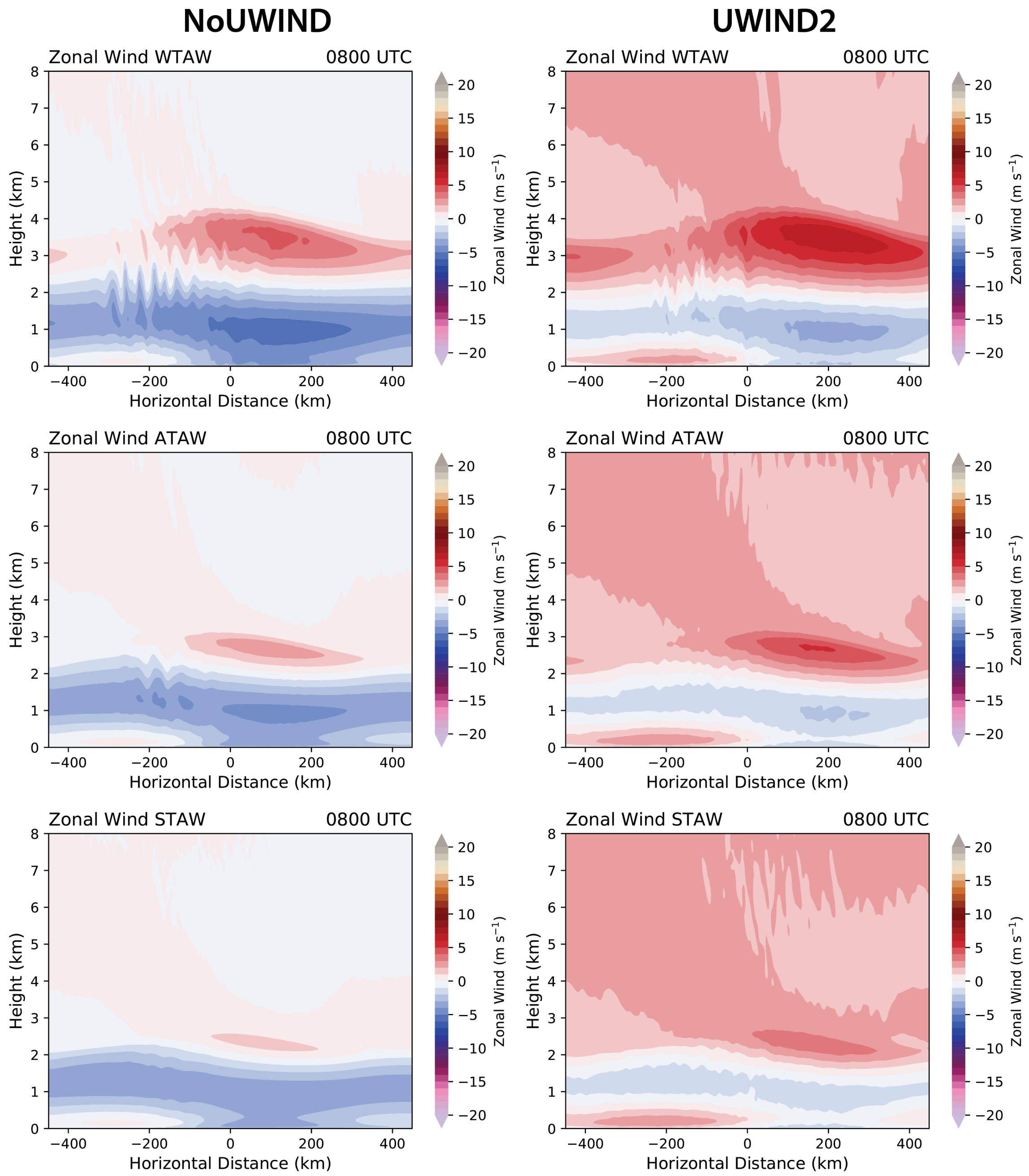

Figure 5.24: The zonal wind component at 0800 UTC for the AW simulations for (a),(b),(c), NoUWIND simulations and (d),(e),(f), UWIND2 simulations. Static stability increases from top to bottom. Height is on the y-axis and horizontal distance is on the x-axis.

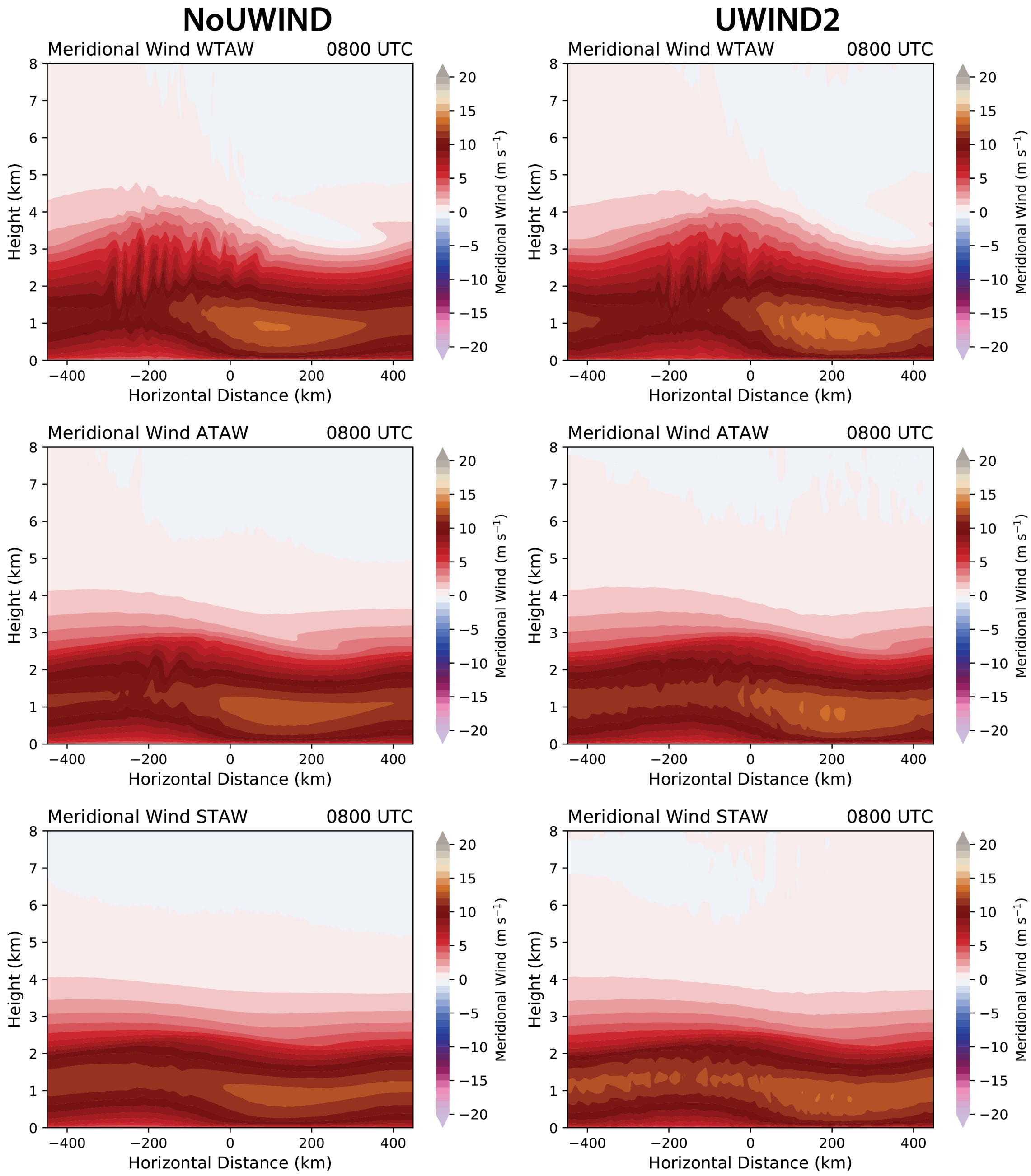

Figure 5.25: The meridional wind component at 0800 UTC for the AW simulations for (a),(b),(c), NoUWIND simulations and (d),(e),(f), UWIND2 simulations. Static stability increases from top to bottom. Height is on the y-axis and horizontal distance is on the x-axis.

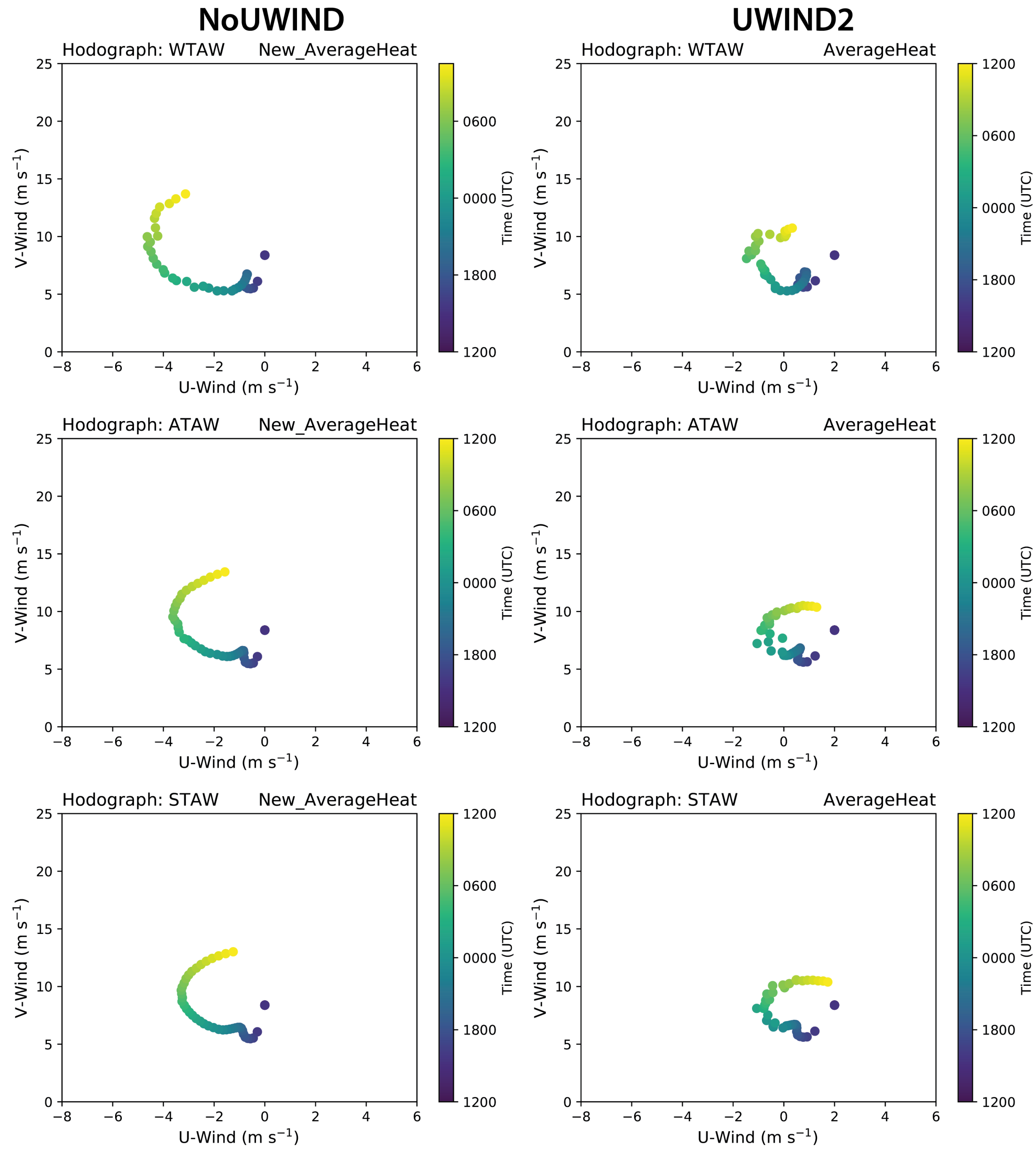

Figure 5.26: Hodographs for the AW simulations for (a),(b),(c), NoUWIND simulations and (d),(e),(f), UWIND2 simulations. Static stability increases from top to bottom. Height is on the y-axis and horizontal distance is on the x-axis. The zonal wind is on the x-axis and the meridional wind is on the y-axis. The color of the dot gets lighter as time increase.

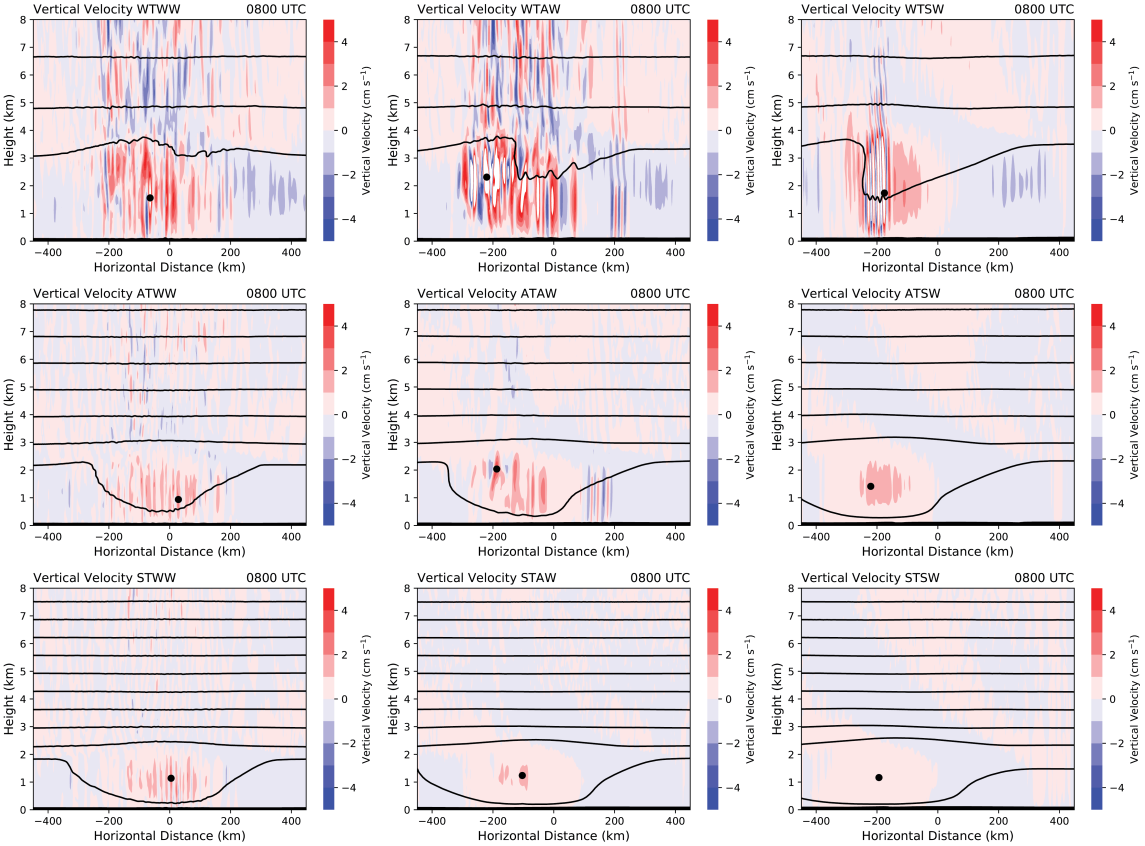

Figure 5.27: Vertical velocity (color-filled; cm s^{-1}) and potential temperature (contoured every 2 K) for the (a) WTWW, (b) WTAW, (c) WTSW, (d) ATWW, (e) ATAW, (f) ATSW, (g) STWW, (h) STAW, and (i) STSW simulations under the average heating.

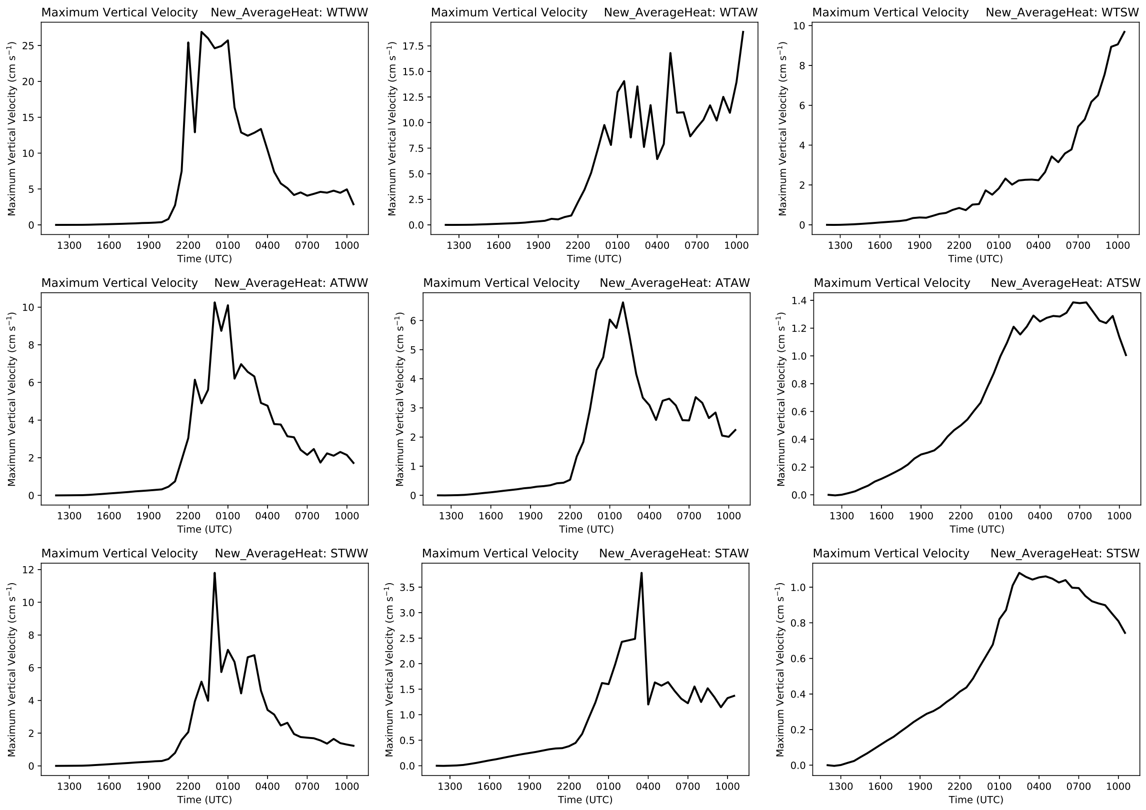

Figure 5.28: Maximum vertical velocity (cm s^{-1}) for the (a) WTWW, (b) WTAW, (c) WTSW, (d) ATWW, (e) ATAW, (f) ATSW, (g) STWW, (h) STAW, and (i) STSW simulations under the average heating.

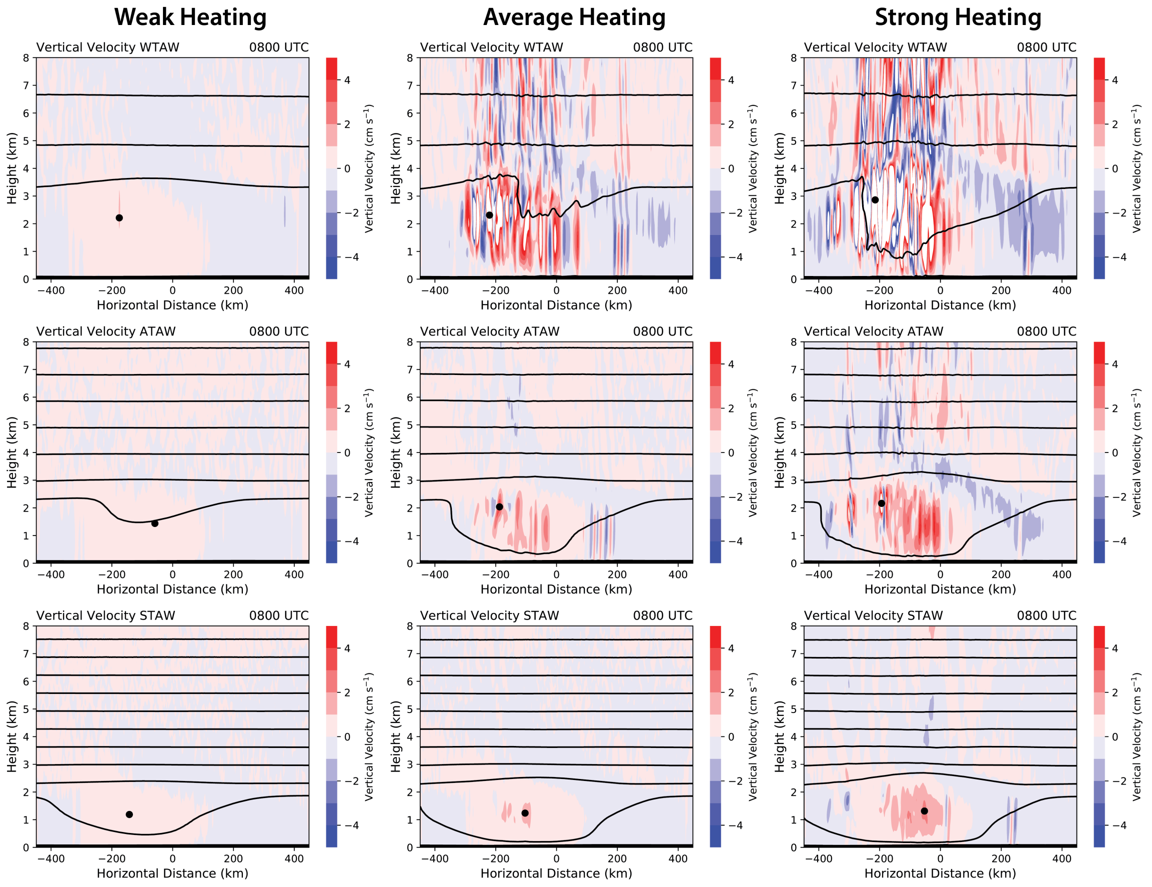

Figure 5.29: Vertical velocity (color-filled; cm s^{-1}) and potential temperature (contoured every 2 K) for (a),(b),(c) weak heating (10 K hr^{-1} max), (d),(e),(f), average heating (20 K hr^{-1} max), and (g),(h),(i), strong heating (30 K hr^{-1} max). The mid-level stability in these simulations increases from top to bottom.

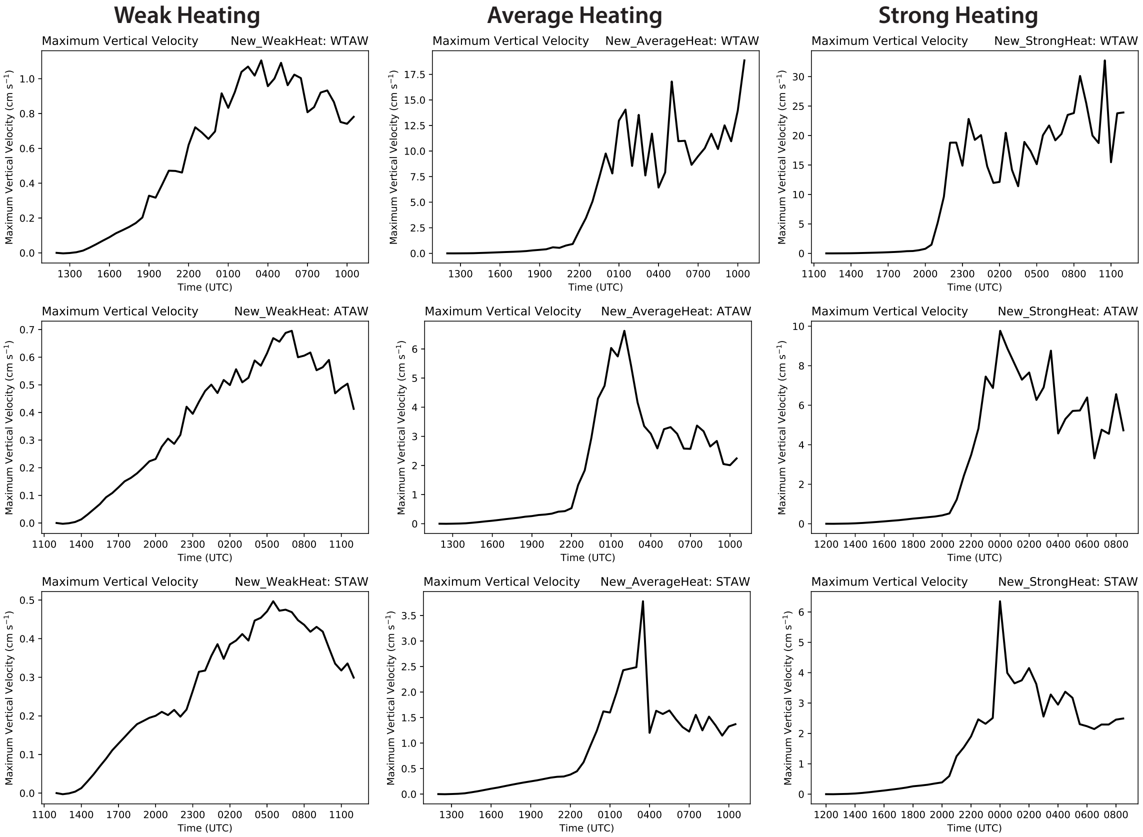

Figure 5.30: Maximum vertical velocity (cm s^{-1}) for (a),(b),(c) weak heating (10 K hr^{-1} max), (d),(e),(f), average heating (20 K hr^{-1} max), and (g),(h),(i), strong heating (30 K hr^{-1} max). The mid-level stability in these simulations increases from top to bottom.

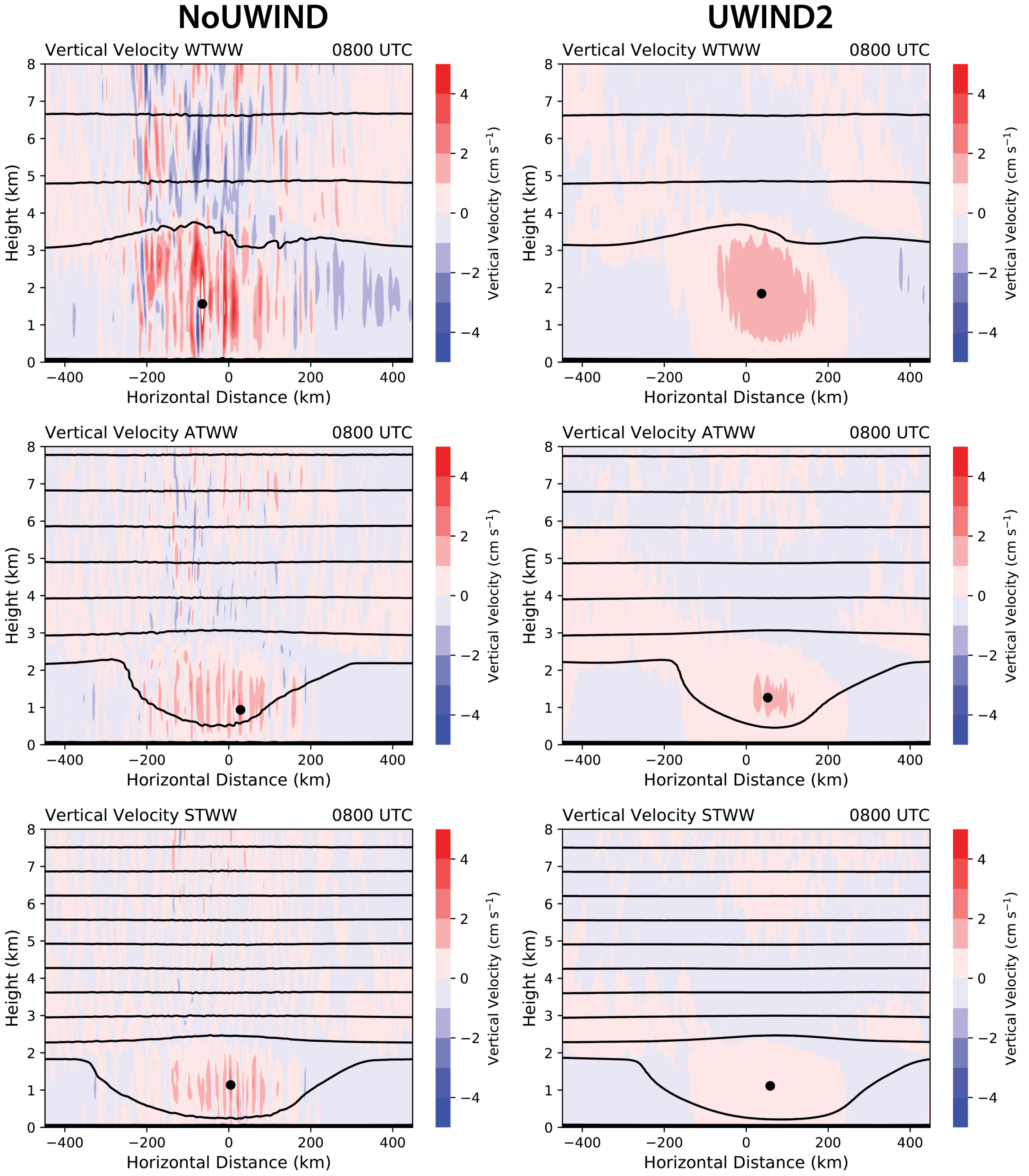

Figure 5.31: Vertical velocity (color-filled; cm s^{-1}) and potential temperature (contoured every 2 K) for the (a),(b),(c) NoUWIND, and (d),(e),(f) UWIND2 WW simulations. The mid-level stability in these simulations increases from top to bottom.

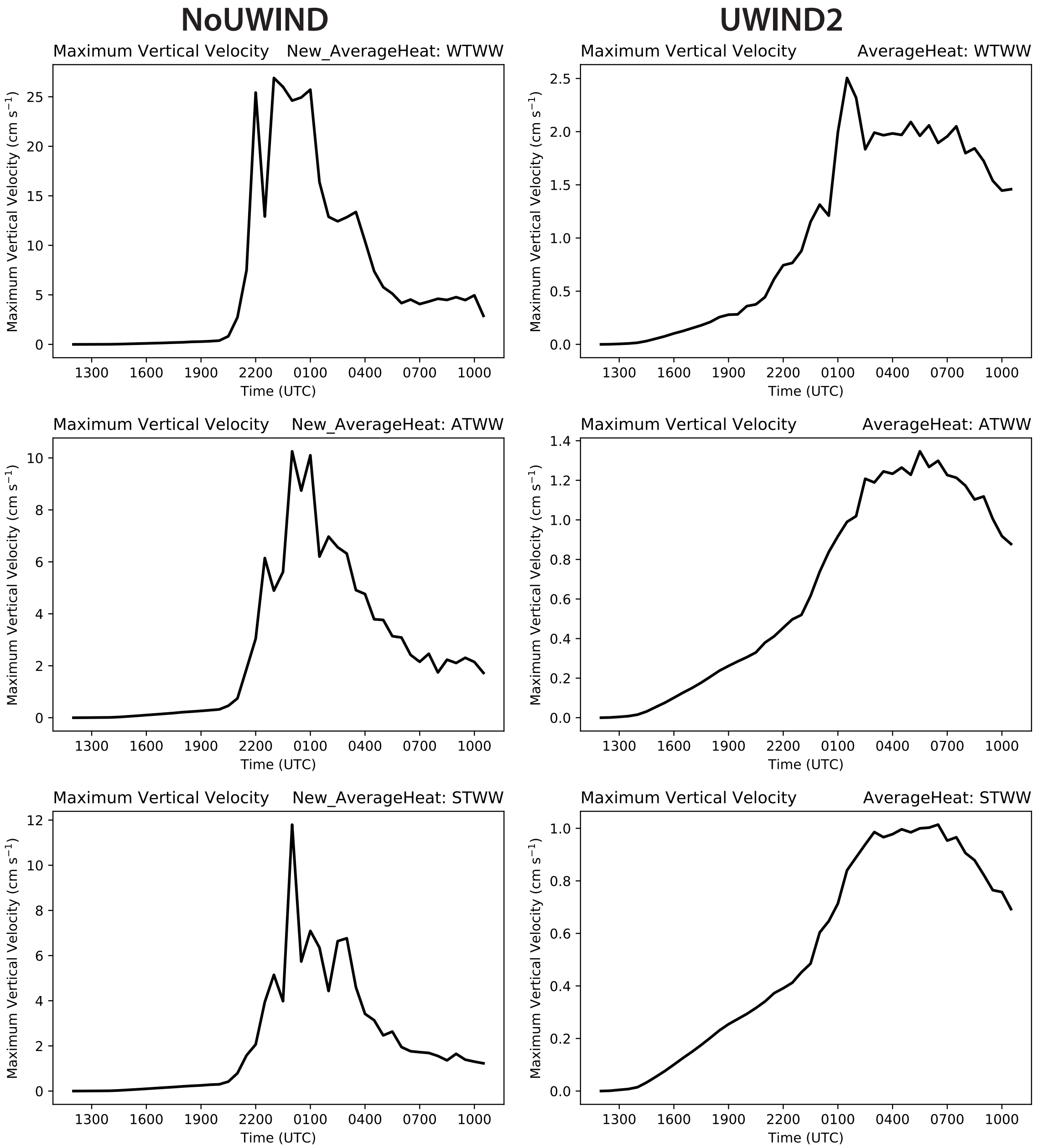

Figure 5.32: Maximum vertical velocity (cm s^{-1}) for the (a),(b),(c) NoUWIND, and (d),(e),(f) UWIND2 WW simulations. The mid-level stability in these simulations increases from top to bottom.

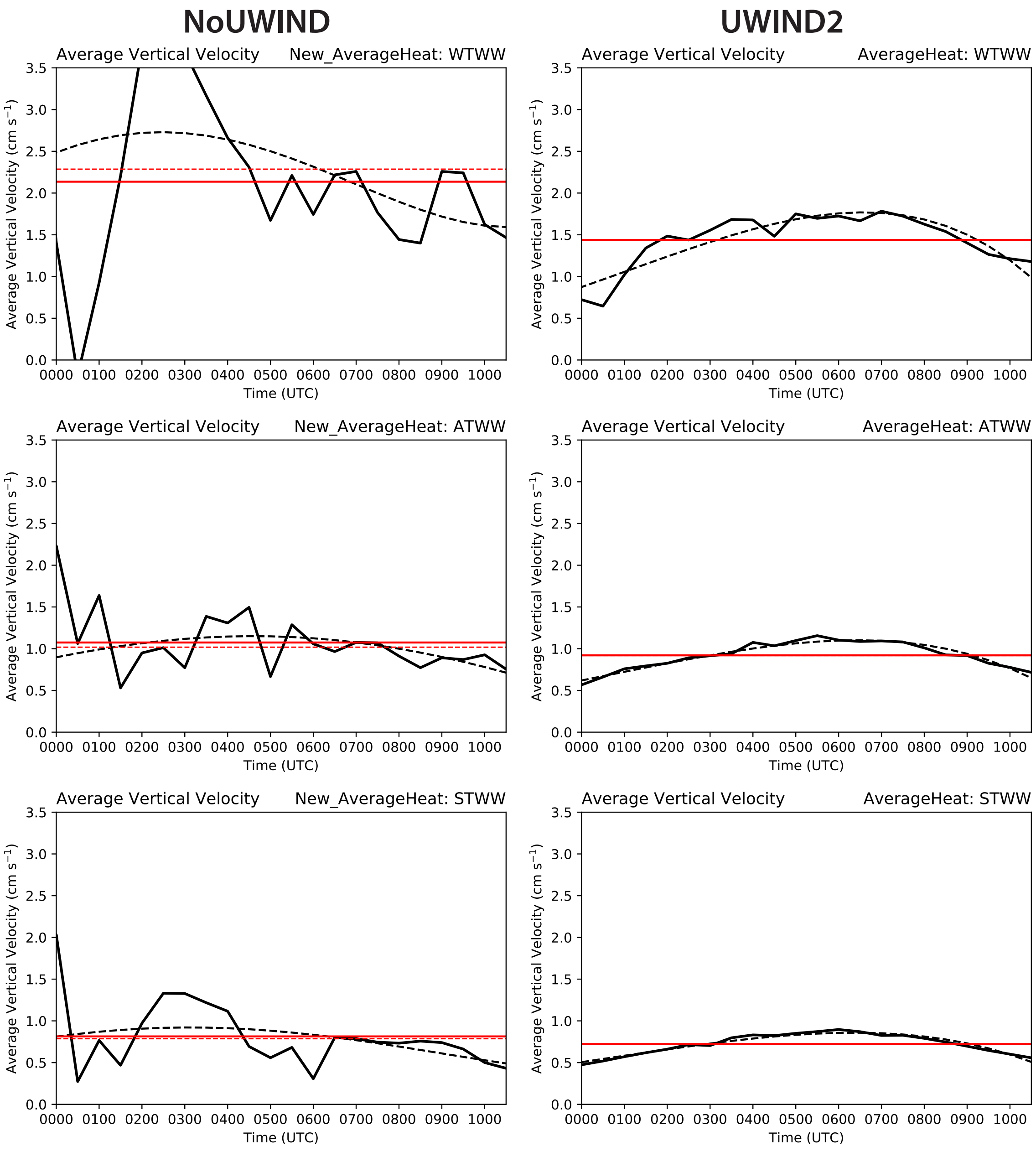

Figure 5.33: Average vertical velocity (cm s^{-1}) for the (a),(b),(c) NoUWIND, and (d),(e),(f) UWIND2 WW simulations. The mid-level stability in these simulations increases from top to bottom. The dashed black curve is a fourth-order polynomial fit. The solid red line is the average vertical velocity over the time period and the dashed red line is the average vertical velocity over the same time computed from the fitted curve.

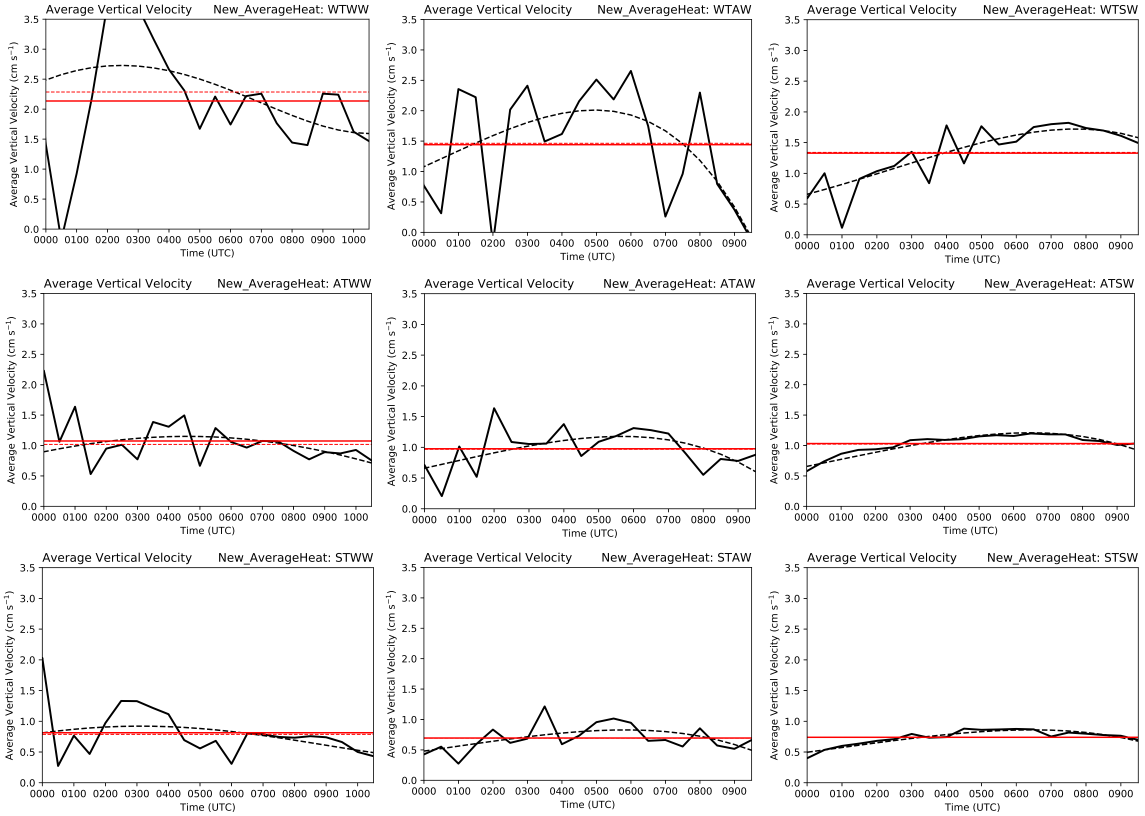

Figure 5.34: As in Fig. 5.33, but for the (a) WTWW, (b) WTAW, (c) WTSW, (d) ATWW, (e) ATAW, (f) ATSW, (g) STWW, (h) STAW, and (i) STSW average-heating simulations.

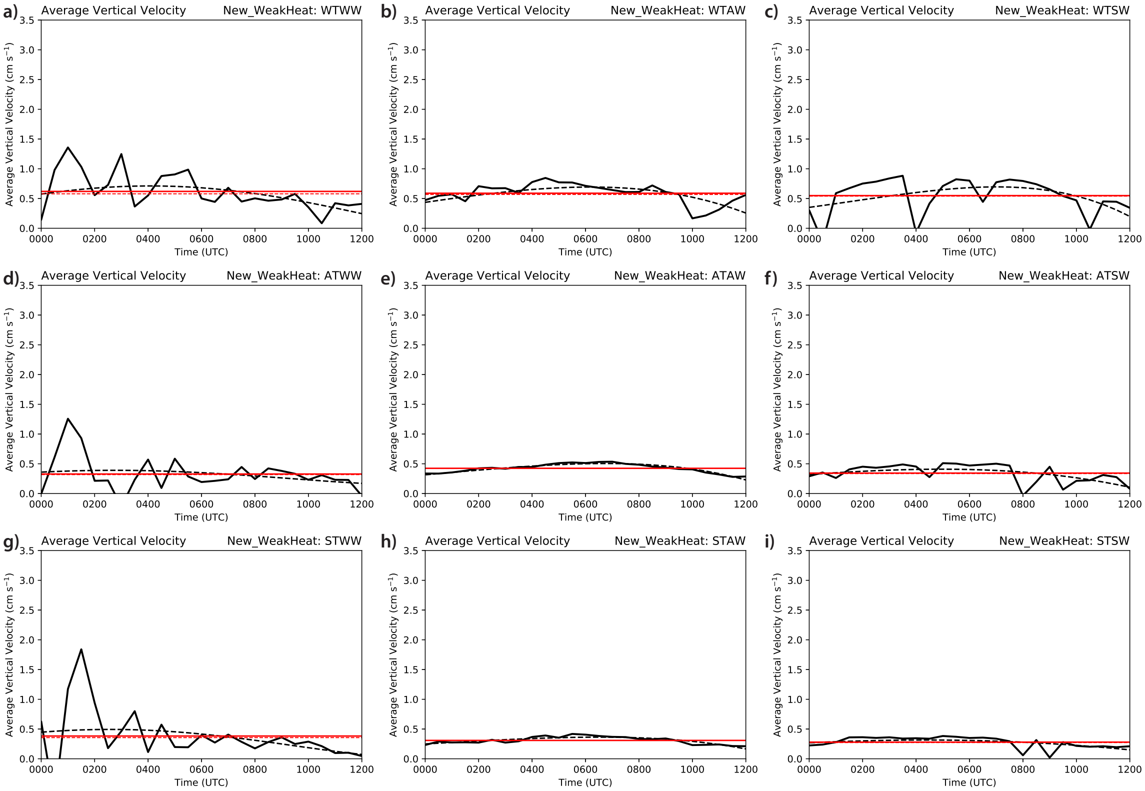

Figure 5.35: As in Fig. 5.34, but for the weak-heating simulations.

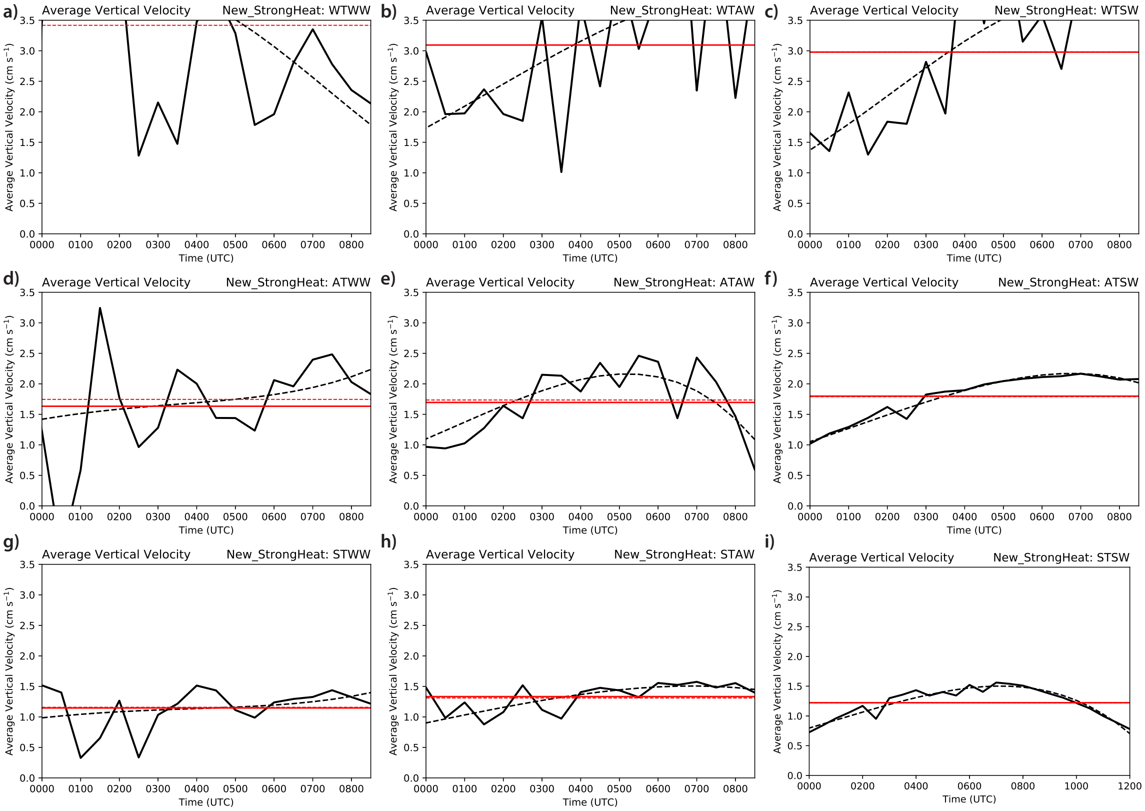

Figure 5.36: As in Fig. 5.34, but for the strong-heating simulations.

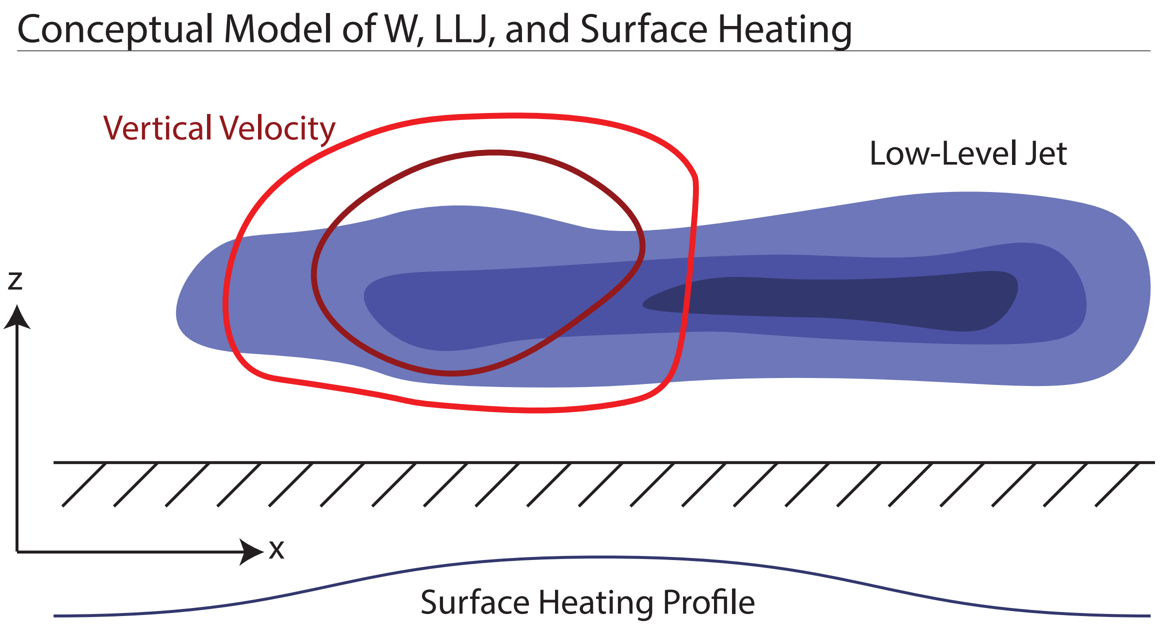

Figure 5.37: Illustration of an X-Z cross section of the vertical velocity location relative to the jet maximum and the surface heating. The red contours represent vertical velocity (deeper reds indicate stronger vertical velocities), and the blue shading represents the southerly component of the wind associated with the LLJ (darker blues indicate stronger wind speeds). The westward offset of w compared to the LLJ maximum is due to the advection of it by the inertial oscillation.

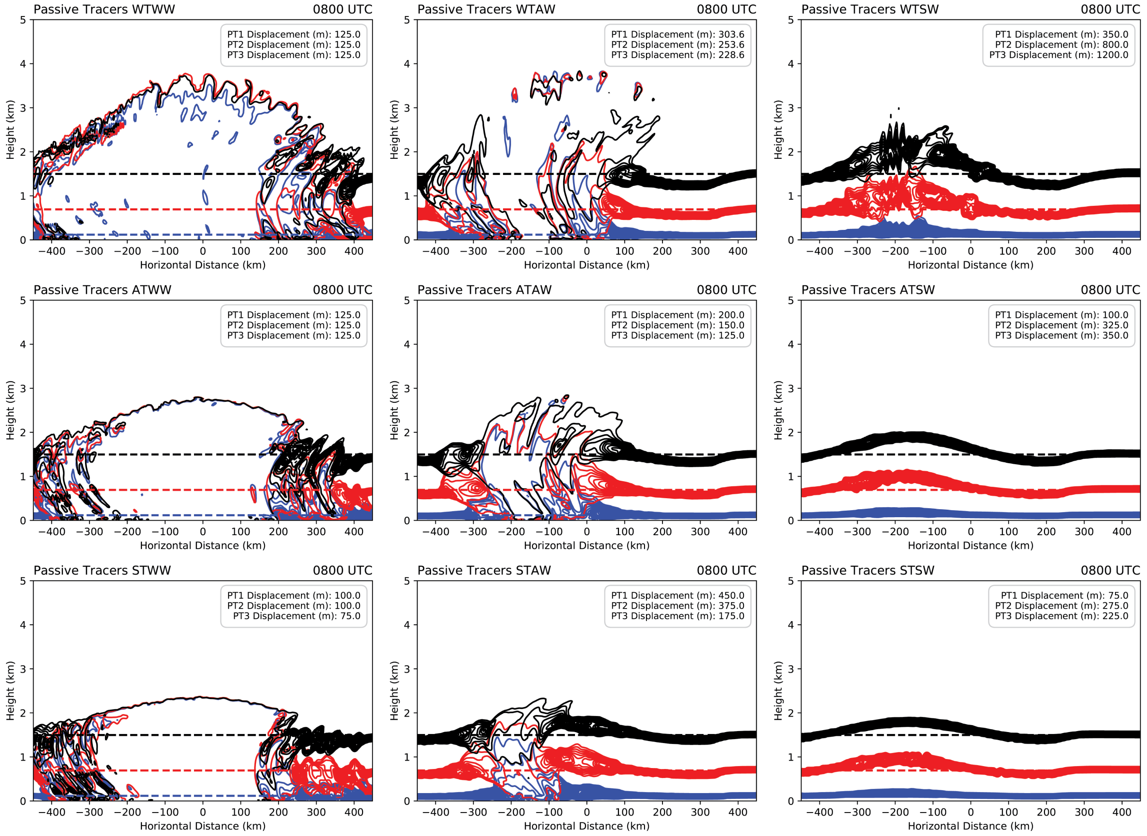

Figure 5.38: Passive tracers initialized at three levels for the (a) WTWW, (b) WTAW, (c) WTSW, (d) ATWW, (e) ATAW, (f) ATSW, (g) STWW, (h) STAW, and (i) STSW average-heating simulationsat 0800 UTC. The blue curve (pt1) represents tracers initialized at 125 m AGL, the red curve (pt2) represents tracers initialized at 700 m AGL, and the black curve (pt3) represents tracers initialized at 1500 m AGL. The displacements in the upper right are the difference in the 0800 UTC maximum position and the 0000 UTC maximum position.

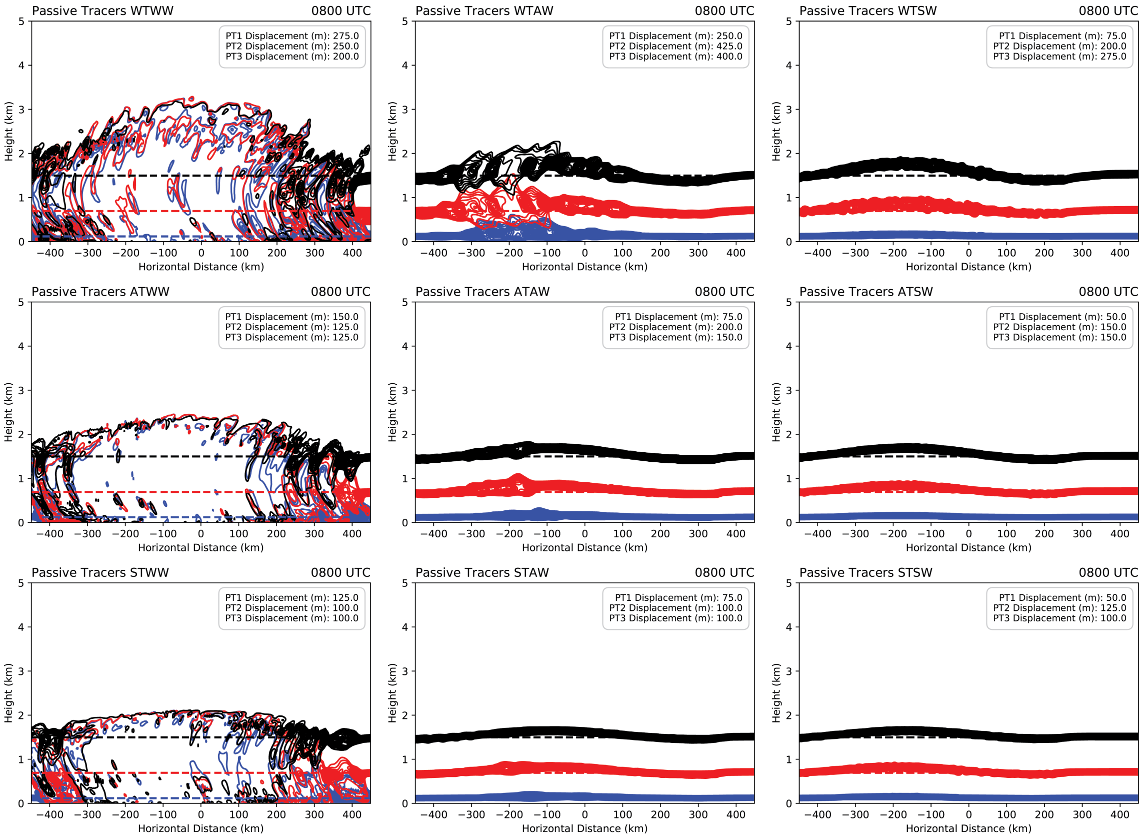

Figure 5.39: As in Fig. 5.38, but for the weak-heating simulations.

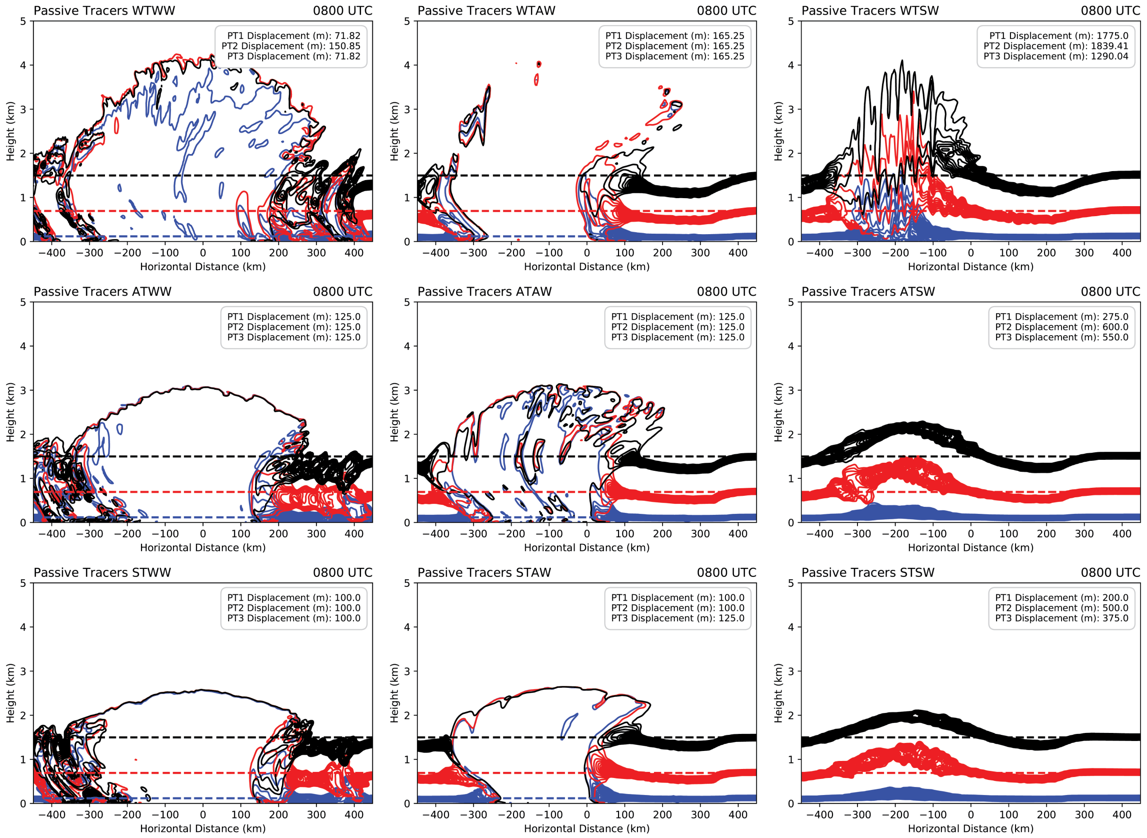

Figure 5.40: As in Fig. 5.38, but for the strong-heating simulations.

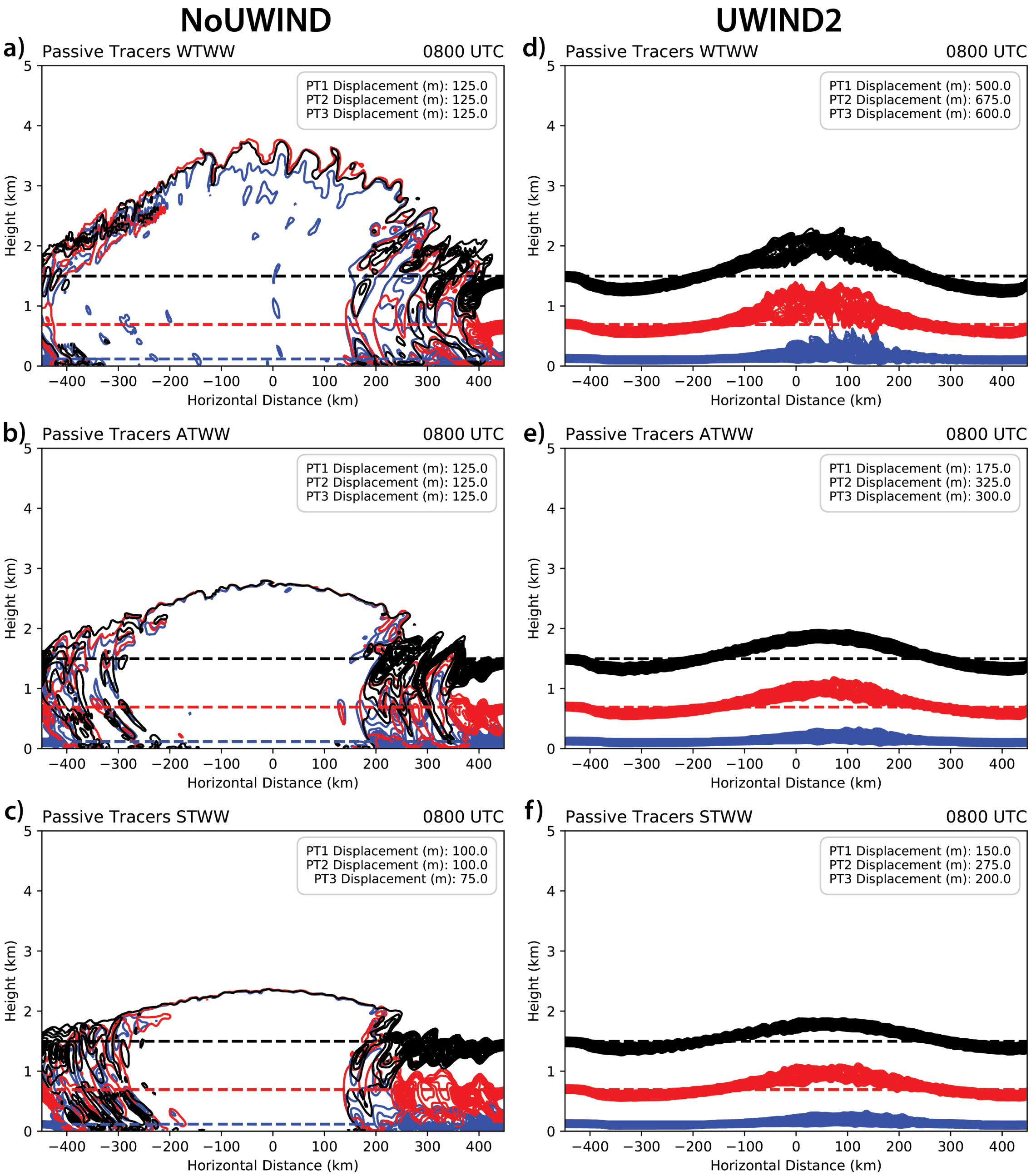

Figure 5.41: As in Fig. 5.38 but for the (a),(b),(c) NoUWIND and (d),(e),(f) UWIND2 WW simulations at 0800 UTC. Static stability increases from top to bottom.

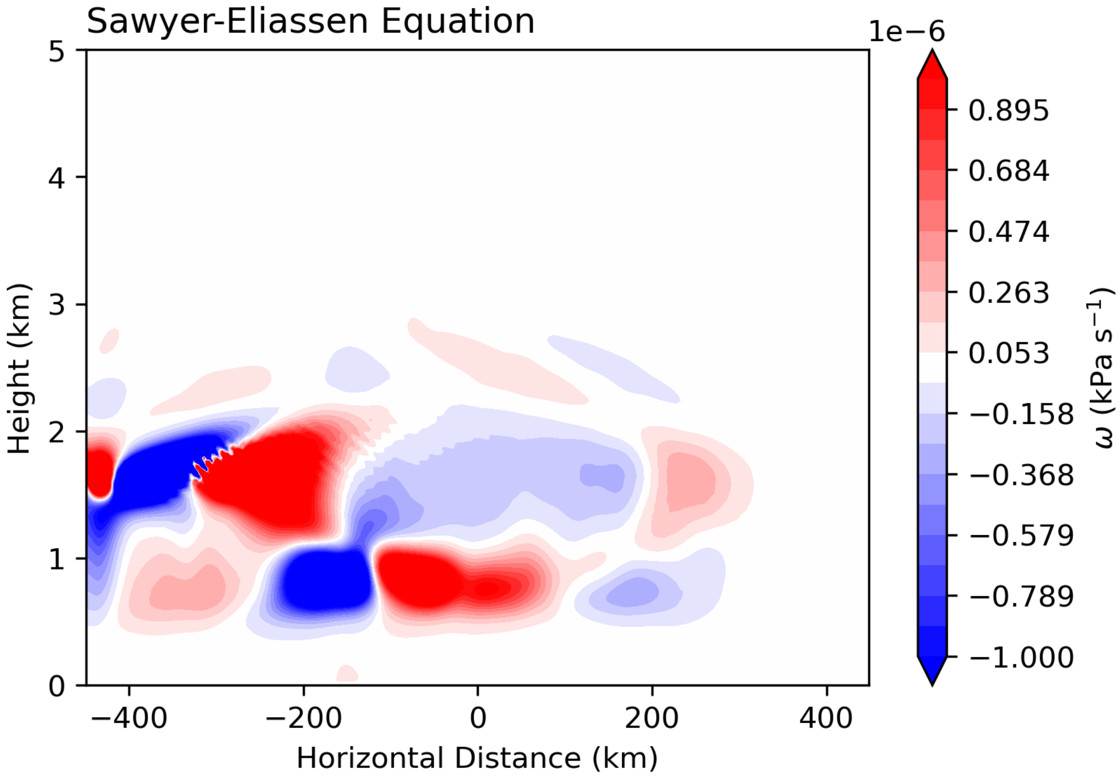

Figure 5.42: ω (kPa s^{-1}) computed from the Sawyer-Eliassen equation. This result uses the total wind rather than the geostrophic wind, and the model data were smoothed to prevent numerical instability.

Chapter 6

PV Anomalies

6.1 Introduction

The timing and eastward propagation speed of PV anomalies over the Great Plains are similar to those of the eastward propagation of the precipitation signal. This connection has led to the speculation that these propagating PV anomalies are important for the precipitation maximum over the Plains (e.g., Carbone et al. 2002). Previous studies have shown that the ascent associated with PV anomalies is around 1 cm s^{-1} (Raymond and Jiang 1990; Li and Smith 2010), which is similar to the magnitude of the broad mesoscale ascent associated with the LLJ. However, parcels remain in the zone of ascent associated with the LLJ for longer periods of time since their motion is usually parallel to the orientation of the jet axis. In the absence of vertical wind shear, parcels will rotate around the PV anomaly in its reference frame, resulting in no net vertical displacements of air parcels and no vertical motion. In the presence of vertical wind shear, there is a baroclinic zone. The presence of this vertical wind shear and baroclinic zone means that there is quasi-geostrophic ascent and this ascent occurs downshear of the PV anomaly (e.g., Raymond and Jiang 1990, Fig. 1.18). While QG theory can explain the rising motion due to PV anomalies in the presence of vertical wind shear, potential links between ascent associated with cyclonic PV anomalies and CI remain unclear.

To study potential links between PV anomalies and potential CI, five idealized PV anomalies are created. These are weak anomalies (1 PVU), average anomalies (2 PVU), and strong anomalies (3 PVU). The naming convention for these anomalies will be XX# where XX represents the lapse rate and # represents the anomaly strength (1, 2, or 3 PVU). The acronyms for XX are WL for a weak potential temperature lapse rate (least stable), AL for average potential lapse rate, and SL for strong potential temperature lapse rate (most stable). For example, the 2 PVU anomaly in the average-lapse rate environment will be referred to as the AL2 anomaly. The PV inversion technique will be utilized to obtain the potential temperature and wind field associated with these anomalies. Once obtained, the vertical velocity and net displacement of air parcels associated with these anomalies can be explored.

6.2 Base-State Environment/Anomaly Creation

The three vertical potential temperature gradients are 1.5 K km^{-1} (WL), 3.5 K km^{-1} (AL), and 6.5 K km^{-1} (SL) (Figs. 6.1a-c) and contribute to the background PV. These gradients correspond to an average potential vorticity in the troposphere (computed using planetary vorticity because the relative vorticity is zero) of 0.24 PVU, 0.57 PVU, and 1.13 PVU, respectively (Figs. 6.1d-f). Analyzing these five anomalies will allow us to understand how typical nocturnal environments are affected by the presence of PV anomalies. When inverting the flow, attempting to put a strong anomaly in the WL environment caused extremely sharp gradients, and the computation was unstable. The 1.5 K km^{-1} lapse rate is used instead of the 0.5 K km^{-1} lapse rate for the WL1 anomaly because the former is numerically unstable for these PV anomalies. Environments in which there is a 3 PVU anomaly in a base-state vertical potential temperature gradient of 0.5 K km^{-1} are unrealistic, so those types of unrealistic environments are not studied here.

These vertical gradients (in potential temperature and PV) are horizontally homogeneous. There is no near-surface stable layer in these environments, unlike in the previous setups. The lack of a near-surface stable layer keeps the analysis simple. Because the PV anomaly is centered at 3 km AGL (the height where diabatic effects due to solar heating of the Rocky Mountains is most pronounced; e.g., Li and Smith (2010)), any ascent would occur above this near-surface stable layer. Because the ascent associated with these PV anomalies would occur above the near-surface stable and because the near-surface stable layer would reduce the vertical velocity and net displacement, near-surface stable layer is neglected in these analyses. The environment is also a resting base-state (i.e., there is no wind). The PV inversion techniques require a streamfunction, which depends on the horizontal gradients of the wind's u and v components. If the wind is horizontally homogeneous (which it has been for the previous two analyses), then the gradients are zero. The PV inversion can be performed with zero base-state wind, and the resulting wind speed after the inversion technique is the cyclonic wind perturbation from the PV anomaly. This PV-induced wind field can be added to different horizontally homogeneous wind fields to analyze the vertical velocity and net vertical displacement due to isentropic ascent in different environments.

The geopotential is computed from the potential temperature gradient (following the boundary condition in Equation 2.7). As in Davis and Emanuel (1991), a "pseudoheight" is computed. The Exner function (and pressure) are computed from this pseudoheight, and then the geopotential is computed from this pseudoheight, temperature gradient, and Exner function. This computed geopotential already satisfies the boundary condition, keeping the computation simple.

The anomalies were created to keep the inversion process as simple as possible while maintaining a reasonable approximation of the nocturnal environment for NB CI mode events. Is a 3 PVU anomaly over the Great Plains from diabatic effects over the Rockies alone reasonable? Probably not, but we can test the ascent associated with these extremes and assess the potential for CI in that environment. If extreme environments cannot produce enough ascent, one can conclude that weaker environments cannot produce CI.

6.3 Error Analysis Associated with PV Inversion

Before we begin analyzing the PV inverted fields, we will take this opportunity to discuss possible sources of error associated with the fields. The primary issue when inverting the field in a resting atmosphere is the definition of the streamfunction. Without any gradients in the horizontal wind speed, the streamfunction can be defined by any constant. The chosen streamfunction in this analysis is based on the upper and lower boundary conditions defined by Equation 2.7. When inverting the flow of a "real" atmosphere, the base-state streamfunction is defined, so this issue is mitigated in that scenario.

One challenge when inverting is the large number of derivatives (especially second derivatives) that need to be computed. Taking a derivative acts to "roughen" the field (as opposed to integration which acts to "smoothen" the field), so any sharp points, even small ones, can result in large second derivatives. With each iteration, these large gradients become larger, and the computation becomes unstable. For this reason, the initial PV field was smoothed to help reduce these possible sharp gradients in the field. However, smoothing the field is one possible, but albeit small, source or error when inverting the field. The difference between the unsmoothed and smoothed fields results in differences around the anomaly itself, but the errors away from the anomaly are small (around 0.01 PVU) (Fig. 6.2).

6.4 Characteristics of PV Anomalies

This 0.38 PVU anomaly is embedded in a background PV of 0.24 PVU. Note that this decrease in the anomaly strength (from 1 PVU) occurred during the smoothing process. After inversion, the structure of the isentropes is similar to the structure of known PV anomalies (Thorpe 1986), but the amount of pull on the isentropes is considerable, especially near 850 hPa (Fig. 6.3). Recall that PV is a product of three variables: the inverse of the density, the vertical potential temperature gradient, and the absolute vorticity. Density appears in the denominator, so as the density gets smaller, the product of the vertical potential temperature gradient and the absolute vorticity has to get smaller, explaining the reduction of the anomaly's effects with height. The resulting difference is related to the product of the potential temperature gradient and the absolute vorticity.

The PV can be explained by the following: the environmental stratification, the cyclonic perturbation wind field, or a combination of the two. For example, strong cyclonic PV anomalies can be explained by strong environmental stratification and weak winds, weak environmental stratification and strong winds, or something in between those two. The stratification in the WL1 anomaly is 1.5 K km^{-1}, visualized by the vertically spaced-out isentropes. Given the same PV anomaly, as the stratification increases, the isentropes get "pulled" towards the anomaly less (compare the response in the SL1 anomaly). It takes less of a change of the isentropes' vertical pull to create the same factor of increase in the gradient.

A PV anomaly by itself does not mean too much without knowledge of the background PV. A 3 PVU anomaly embedded in a 10 PVU field will produce a much weaker response than a 3 PVU anomaly embedded in a 1 PVU background field. The strength of the anomaly should be noted relative to the background PV. Thus, while the strength of the PV anomalies and the environmental stratifications are representative of the nocturnal environment, one cannot safely say that the strongest anomaly will produce the strongest response. In this case, the anomaly is over 1.5 times as strong as the background PV.

The maximum wind speed associated with the WL1 anomaly is 4.35 m s^{-1}. The radius of maximum winds is 158 km from the center of the anomaly, and the cyclonic perturbation extends over 500 km away from the anomaly. The Rossby penetration depth is 4 km (assuming an average Brunt-Väisälä frequency of 0.007 s^{-1} and an assumed Rossby radius of deformation of around 300 km).

The PV anomaly associated with the AL1 anomaly is 0.38 PVU, and the average background PV is 0.57 PVU, so the anomaly is 66% stronger than the background PV (less than half of the relative strength than that of the WL1 anomaly). As expected, the isentropes are pulled less notably than in the WL1 anomaly, and the maximum wind speed is weaker (2.7 m s^{-1} compared to the 4.35 m s^{-1} associated with the WL1 anomaly) (Fig. 6.4). These reductions are because this is a relatively weaker anomaly than the WL1 anomaly, so the response is weaker, even though the magnitude of the anomaly is the same as that of the WL1 anomaly. The Rossby penetration depth is 2.7 km.

Finally, the 0.38 PV anomaly in the high lapse-rate environment (SL1 anomaly) is only 33% stronger than the background PV. Relative to the background PV, this is the weakest of all of these 1PVU anomalies. As expected, the potential temperature's response is weak, and the maximum wind speed is only 1.7 m s^{-1} (Fig. 6.5). The Rossby penetration depth is 2 km.

The decrease in the Rossby penetration depth is due to the increase in the Brunt-Väisälä frequency. This depth (and similar Rossby radius of deformation) does not take the strength of the anomaly itself into consideration, only the environmental Brunt Väisälä frequency. The relative weaker anomaly in the same environment will by associated with a smaller Rossby radius of deformation and a shallower Rossby penetration depth.

In the James and Johnson (2010) climatology of MCVs over the Great Plains, the background PV was 0.5 PVU and the maximum PV associated with the PV anomaly was greater than 1 PVU. In this study, Based on the typical potential temperature gradient of 3.5 K km^{-1} and an anomaly strength of 0.77 PVU, the AL2 anomaly likely best represents the anomalies found over the Great Plains. This anomaly's strength, while weaker than the composite anomaly in James and Johnson (2010) is likely representative of typical diabatically-generated PV anomalies over the Great Plains. This anomaly is 1.35 times the strength of the background PV, so it is (so far) the second strongest anomaly relative to the background PV in this study. The isentrope pattern is more similar to that of the WL1 anomaly, and the maximum wind speed is 4.9 m s^{-1} (Fig. 6.6). A quick calculation of the wind speed associated with the composite PV anomaly in James and Johnson (2010) results in a wind speed of approximately 6-7 m s^{-1} using a horizontal distance of 250 km and a vorticity of 6×10^{-5} s^{-1}. The horizontal response to the anomaly is larger than that of the WL1 anomaly. These anomalies are relatively similar, but the Brunt-Väisälä frequency of the environment is larger in the AL2 anomaly, which results in a larger (smaller)

Rossby radius of deformation (Rossby penetration depth). Overall, the environment's response to this anomaly appears similar to that of the WL1 environment, indicating that the PV anomaly's relative strength is likely more important than its magnitude.

The last anomaly in this study is the SL3 anomaly (Fig. 6.7). This 1.15 PVU anomaly is just over 100% stronger than the background PV, making it the third-strongest anomaly relative to the background PV. The response in the isentrope pattern is similar to that of the AL2, but slightly "weaker". The maximum wind speed is 4.7 m s^{-1}, weaker than that of the AL2 anomaly, but similar to the WL1 anomaly. The horizontal extent of this anomaly is similar to the AL2 and WL1 anomalies, even though this is the weakest anomaly of the three relative to the background PV. From strongest to weakest, the strength of the anomalies relative to their background PV is WL1, AL2, SL3, AL1, and SL1.

6.5 Ascent associated with PV anomalies

Analyzing the ascent associated with these anomalies will be done in a diagnostic sense because the field is inverted at a specific time. We will examine the maximum displacement associated with the anomalies, even if this displacement is unrealistic. If this maximum displacement is insufficient to produce CI, then anything less will not produce CI either. We assume that there are no diabatic processes associated with this anomaly; otherwise, the PV anomaly's strength and possible its structure would change. In the absence of diabatic processes, the air parcels' net displacement will be similar, if not identical to the isentropes' displacement.

The maximum possible net displacement must be for a parcel moving right through the center of the anomaly since that is where the isentropes are displaced the most. Assume that the parcel is stationary and embedded in non-zero background flow. In this case, the parcel could catch up to the PV anomaly and go right through its center. This assumption is unrealistic, however, because it assumes that a parcel can "catch up" to the PV anomaly. The background flow would advect the PV anomaly (ignoring diabatic and friction effects), and the parcel would not catch up in the real atmosphere. Even if it could, the circulation associated with the anomaly would cause the parcel to rotate around the anomaly, preventing most parcels from going through the center (Fig. 6.8). To analyze the maximum possible net displacement, we will assume the parcel can move through the anomaly's center, however unrealistic this assumption might be. The actual net displacement achieved in more realistic assumptions is lower than this unrealistic net displacement.

6.5.1 Presence of Vertical Wind Shear

Ascent occurs on the downshear side of the PV anomaly (Raymond and Jiang 1990). This vertical wind shear is associated with a baroclinic zone. In the case of westerly wind shear, this temperature gradient points to the south. Because the parcels remain on their isentropes in the absence of diabatic effects, this upward motion along the tilted isentropes will result in ascent downshear or the anomaly and subsidence upshear of it. This upward motion on the tilted isentrope is analogous to temperature advection in constant pressure surfaces.

The magnitude of this wind shear depends on the magnitude of the baroclinic zone. The relationship between these two is expressed in the thermal wind equation

$$\frac{\partial v_g}{\partial z} = \frac{g}{f}\hat{k} \times \nabla_H(\ln T) \tag{6.1}$$

where $\frac{\partial v_g}{\partial z}$ is the vertical wind shear and $\nabla_H(\ln T)$ is the horizontal temperature gradient. The NB CI mode events occur in environments without significant baroclinicity. This weak baroclinicity also implies that the vertical wind shear (aside from the shear associated with the LLJ) is weak. If there were westerly wind shear and southerly winds throughout the Plains (which is fairly common), CI would likely occur far more often than it does. Because NB CI is not this common, other mechanisms are responsible for CI to occur. Is one of these mechanisms the ascent associated with the PV anomaly embedded in this westerly shear?

The maximum vertical wind shear occurs near 1 km AGL and rapidly decreases to near 0 m s^{-1} km^{-1} by 1.2 km (Fig. 6.9a). The v-component of the wind shear has similar behavior (Fig. 6.9b). This layer below 1.2 km AGL is where the effects of the LLJ are felt, and since we are not considering the effects of the LLJ on this PV anomaly, only the shear above the jet will be considered. The average westerly wind shear between 1.2 km (where the effects of the jet are no longer seen) and 5 km AGL is -0.12 m s^{-1} km^{-1}. These two layers are chosen because the PV anomaly is centered at 3 km AGL. The maximum and minimum wind shear are computed from a 10-point running mean to minimize the noise due to the high vertical resolution of the composite sounding. The maximum shear is 1 m s^{-1} km^{-1}, and the minimum is -1.46 m s^{-1} km^{-1}. A 1 m s^{-1} km^{-1} vertical wind shear in an environment with a lapse rate of 3.5 K km^{-1} corresponds to a meridional temperature gradient of approximately -2 K $(1000\ km)^{-1}$.

As expected, the vertical shear is relatively weak (and the average above the jet is near 0 m s^{-1} km^{-1}). This weak vertical shear implies a weak baroclinic zone, thereby reducing the slope of the isentropes and the magnitude of the ascent suggested by Raymond and Jiang (1990) in these NB CI mode environments.

Before we start with the analysis of the PV-modified fields, we first need to compute the slope of the isentropes associated with different wind vertical shear. We will use 0.25 m s^{-1} km^{-1}, 0.5 m s^{-1} km^{-1}, and 1 m s^{-1} km^{-1}. These shear magnitudes are larger than the average shear, but testing larger values will provide an opportunity to examine the maximum possible net displacement. The slope of the 290 K isentrope associated with the AL1 anomaly in environments of 0.25 m s^{-1} km^{-1} shear is 0.00018 (180 m $[1000\ km]^{-1}$), the slope associated with the 0.5 m s^{-1} km^{-1} shear is 0.00039 (390 m $[1000\ km]^{-1}$), and the slope associated with the 1 m s^{-1} km^{-1} is 0.0008 (800 m $[1000\ km]^{-1}$).

This slope is the base-state slope; it is independent of the presence of the PV anomaly. The average and maximum slopes associated with the base-state fields (mean) and the anomaly-modified slopes (maximum) are listed in Table 6.2. Consider a meridional wind component of 10 m s^{-1}. A parcel can move horizontally 432 km in 12 hours. Given this reasonable assumption of the meridional wind speed, a parcel will only be displaced vertically by 77 m, 169 m, and 345 m, respectively.

These displacements have a caveat, however. A 345 m displacement is enough to initiate convection in some of the more optimal NB CI mode environments, so is the CI related to this background slope? It is unlikely that this is the case. The slope of the isentropes was computed using the maximum possible typical vertical wind shear. The average vertical wind shear based on the composite sounding is close to zero, so the net displacement associated with this isentropic ascent would be close to zero as well. How does the PV anomaly impact the structure of these isotherms in the presence of westerly wind shear? The background slope will be increased in some places around the anomaly and decreased in others. While the overall net displacement through the anomaly remains similar, there is an enhancement on the anomaly's southern side due to this westerly wind shear (Fig. 6.10). The mean slopes and the maximum slope along that isentrope are listed in Table 6.2.

We can apply the maximum wind associated with the PV anomaly itself to the background isentrope slope to give use the average ascent. The isentropic ascent via the PV-induced wind field and the baroclinic zone is the ascent outlined in Raymond and Jiang (1990). This ascent (for the 1 m s^{-1} km^{-1} shear) is 0.6 cm s^{-1} in the WL1 anomaly, 0.2 cm $^{-1}$ in the AL1 anomaly, 0.07 cm s^{-1} in the SL1 anomaly, 0.4 cm $^{-1}$ in the AL2 anomaly, and 0.2 cm s^{-1} in the SL3 anomaly (Table 6.1). This ascent is less than that of previous studies that showed the ascent to be between 2 and 5 cm s^{-1}, but the PV anomalies in those studies were associated with squall lines, so the atmosphere may be more unstable than in these environments. The average meridional wind at the radius of the maximum winds (on one side of the PV anomaly) is less than the magnitude of the wind speed at the radius of maximum winds. Because the average meridional wind speed is lower than this maximum wind speed, the average ascent obtained from this average wind speed is lower than that obtained from the maximum wind speed. Suppose we want this average ascent associated with the average meridional wind associated with the PV anomaly. As the parcel starts moving towards the north from the southern end of the PV anomaly, the meridional wind speed is zero, reaching a maximum east of the PV anomaly. Once this maximum wind

Table 6.1: Vertical velocity and net displacement of parcels associated with PV anomalies in environments with westerly wind shear of 1 m s^{-1} km $^{-1}$

1 m s^{-1} km $^{-1}$ Vertical Wind Shear	WL1	AL1	SL1	AL2	SL3
Vertical Velocity (cm s^{-1})					
Anomaly Winds (Environmental Slope)	0.61	0.21	0.07	0.36	0.19
Anomaly and Environmental Winds (Environmental Slope)	1.80	0.86	0.44	1.00	0.54
Anomaly and Environmental Winds (PV-Modified Slope)	5.07	2.01	0.80	3.57	1.94
Net Displacement (m)					
Anomaly Winds (Environmental Slope; 12 hours)	209	90	31	169	90
Environmental Winds (Environmental Slope; 12 hours)	517	284	157	274	151

speed is reached, the parcel turns towards the west, decreasing the meridional wind speed before reaching zero again at the norther-most point. This pattern in the meridional wind component is a sine wave. To obtain the average meridional wind speed, we need to scale the maximum wind speed by $\frac{2}{\pi}$, or the average of sine over 180°. This scaling reduces the ascent by a factor of about 0.63.

In the NB CI mode events, the meridional wind is usually not 0 m s^{-1}. In the composite sounding, the average meridional wind between 1.2 km and 5 km is 1.5 m s^{-1}, the maximum wind speed is 8.6 m s^{-1} and the minimum wind speed is -1.36 m s^{-1}. The meridional wind will either add to (if southerly) or subtract from (if northerly) the wind associated with the PV anomaly. Taking the maximum wind speed of 8.6 m s^{-1} and adding it to the radius of maximum winds (as this is the maximum ascent associated with the base temperature gradient) results in an ascent of.8 cm s^{-1} for the WL1 anomaly, 0.9 cm s^{-1} for the AL1 anomaly, 0.4 cm s^{-1} for the SL1 anomaly, 1.0 cm s^{-1} for the AL2 anomaly, and 0.5 cm s^{-1} for the SL3 anomaly. This ascent somewhat agrees with that of previous studies, but the potential for CI still cannot be assessed. The slope used for this ascent is the average slope associated with the westerly wind shear, not the slope of the isentropes modified by the PV anomaly.

Table 6.2: Isentrope slopes ($\times 10^{-3}$) for the environment modified by westerly wind shear (the mean slope) and the environment modified by the PV anomaly and the westerly wind shear (the maximum slope).

	WL1	AL1	SL1	AL2	SL3
0.25 m s^{-1} km^{-1} Mean slope	0.4	0.2	0.1	0.2	1.1
0.25 m s^{-1} km^{-1} max slope	2.3	1.2	0.5	2.0	0.9
0.5 m s^{-1} km^{-1} Mean slope	0.8	0.4	0.2	0.4	0.2
0.5 m s^{-1} km^{-1} max slope	2.8	1.3	0.6	2.2	1.2
1.0 m s^{-1} km^{-1} Mean slope	1.3	0.8	0.4	0.7	0.4
1.0 m s^{-1} km^{-1} max slope	4.0	1.8	0.8	2.6	1.5

The modification to the isentropes' slope via the PV anomaly is shown in Table 6.2. The slope modification ranges from very small (in the SL anomalies) to large (in the WL and AL anomalies). This modification of the slope is almost an order of magnitude in the AL anomalies. The ascent that is a combination of the wind speed associated with the anomaly and the environmental wind speed is 5.1 cm s^{-1} for the WL1 anomaly, 2.0 cm $^{-1}$ for the AL1 anomaly, 0.8 cm s^{-1} for the SL1 anomaly, 3.6 cm s^{-1} for the AL2 anomaly, and 1.9 cm s $^{-1}$ for the SL3 anomaly.

A problem with these vertical velocities is that they result from a combination of the anomaly winds and the environmental meridional wind. In reality, the meridional wind should not affect the ascent up the isentropes modified by the PV anomaly because the anomalies will move at the same speed as the meridional wind. In the reference frame of the PV anomaly, there is no environmental wind.

6.5.2 Analysis using quasi-geostrophic theory

Vertical motion can be diagnosed using quasi-geostrophic (QG) theory. These three forms are the traditional form, the Sutcliffe-Trenberth form, and the Q-Vector form. The traditional form involved diagnosing vertical motion temperature advection and differential vorticity advection, the Sutcliffe-Trenberth form involves knowledge of the thermal wind and vorticity, and the Q-vector form involves knowledge of the horizontal temperature and wind gradients (Bluestein 1992). Because all three forms give similar answers and we know the thermal wind and vorticity, the Sutcliffe-Trenberth form will be used.

The Sutcliffe-Trenberth form of the QG omega equation neglecting the friction and deformation terms is

$$\left(\nabla_H^2 + \frac{f_0^2}{\sigma}\frac{\partial^2}{\partial p^2}\right)\omega = \frac{f_0}{\sigma}2\left[-\left(-\frac{\partial v_g}{\partial p}\cdot\nabla_p\zeta_g\right)\right], \tag{6.2}$$

where f_0 is the Coriolis parameter and σ is the static stability parameter. Given the imposed westerly wind shear and vorticity associated with the PV anomaly, the operator on the left-hand side can be inverted to obtain ω. The process to invert the operator is explained in Appendix A.

Based on the forcing function of Equation 6.2, we expect ascent where there is cyclonic vorticity advection by the thermal wind. In our examples of westerly wind shear, rising motion should occur downshear of the anomaly. This location corresponds well with the location shown in the previous analysis.

Recall that we estimated a combination of the ascent associated with the WL1 anomaly in 1 m s^{-1} km^{-1} of westerly wind shear to be on the order of 1-10 cm s^{-1}. While this shear is small, sustained over several hours, the ascent could result in a net displacement of at least a few hundred meters (however, it is unlikely that this parcel remains in that area for that long). Results of a scale analysis of the Sutcliffe-Trenberth form of the QG omega equation are given in Table 6.3. Assuming a horizontal distance of 300 km (typical scale of this PV anomaly), the typical vertical velocity under these conditions results in ascent

Table 6.3: Typical Scales used in the Scale Analysis

Parameter	Value
f_0	10^{-4} s^{-1}
$\frac{\partial v_g}{\partial p}$	$\frac{10 \text{ m s}^{-1}}{100000 \text{ Pa}}$
$\nabla_H \zeta g$	$\frac{4 \text{ m s}^{-1}}{300^2 \text{ km}^2}$
T	200 K
θ	300 K
$\frac{\partial \theta}{\partial p}$	$\frac{100 \text{ K}}{100000 \text{ Pa}}$

on the order of 0.1 cm s^{-1}. This scale corresponds well with the isentropic ascent from the previous section, giving credence to the analyses.

The computed vertical velocity using the Sutcliffe-Trenberth form of the QG omega equation ranges from 0.1 cm s^{-1} (SL1) to almost 1 cm s^{-1} (WL1) (Fig. 6.11). These predicted values correspond well with the scale analysis, and the order from the strongest ascent to the weakest ascent is the same as the order using the isentropes and wind speed associated with the PV anomaly. The location of the maximum vertical velocity is on the radius of maximum winds. This location corresponds to where the vorticity gradient is largest and is also explained physically by where the isentropic ascent is maximized. The depth of the rising motion is the same as the depth of the PV anomaly, and the height of the maximum vertical velocity is the height where the anomaly is the strongest (700 hPa). This height is where the highest wind speeds are, resulting in faster motion of parcels up the isentropes, and is where the vorticity advection by the thermal wind is strongest.

This agreement in the vertical velocity among the QG omega equation, the analysis using the isentropes, and the similar vertical velocities is noted in previous studies. These vertical velocities are also similar to those seen in the LLJ analysis in the previous section. However, the potential for CI cannot be determined via the vertical velocity alone. The net vertical displacement of parcels needs to be analyzed to determine this potential.

6.5.3 Net Displacement

Consider a parcel moving from the south towards the anomaly. Next, assume that the parcel can move straight through the center of the anomaly without being deflected around. While this scenario does not happen in the atmosphere, it does provide the maximum net displacement of the isentropes associated with the PV anomaly without vertical shear. This displacement is 494 m for the WL1 anomaly, 227 m for the AL1 anomaly, 77 m for the SL1 anomaly, 447 m for the AL2 anomaly, and 247 m for the SL3 anomaly. However, a parcel will not achieve this net displacement because the anomaly would have to remain in a fixed position relative to the background flow.

Now consider the anomaly in the environment with westerly wind shear. The time it takes a parcel to rotate around the PV anomaly is essential in determining how far around the anomaly it will travel during the night. To do this, we will take the circumference of the anomaly and divide it by the wind speed at the radius of maximum winds. The residence time varies anywhere from 60 hours to 160 hours, depending on the wind speeds. However, how much of this distance do we care about? We only want the rising motion, so we can ignore at least half of the residence time.

Let us consider two distances. The first is how far a parcel rotating around the anomaly will move in 12 hours. The maximum distance is the maximum wind speed divided by 12 hours. That distance is the arc length, but the maximum meridional distance is the chord between the starting point and the ending point centered along the x-axis (Fig. 6.12). This distance ranges from 74 km to 200 km. The maximum displacement that a parcel achieves during this meridional distance is 210 m for the WL1 anomaly, 90 m for the AL1 anomaly, 31 m for the SL1 anomaly, 170 m for the AL2 anomaly, and 91 m for the SL3 anomaly (Table 6.1). These net displacements occur in environments with 1 m s^{-1} km^{-1} westerly wind shear. More typical wind shear values are less than this, so the net displacement will be less.

The second distance is the distance that a parcel moving with the environmental wind travels in 12 hours. A parcel moving at 8.6 m s^{-1} will travel 371 km. The net displacement associated with this wind speed in an environment with westerly wind shear of 1 m s^{-1} km^{-1} is 517 m for WL environments, 283 m for AL environments, and 150 m for SL environments. This displacement is independent of the anomaly's presence, and the total displacement via this mechanism and the PV-modified environment is not the sum of the two displacements (Fig. 6.13). It is also unlikely that a parcel will achieve this maximum net displacement. To compute this displacement, the maximum possible westerly wind shear (1 m s^{-1} km^{-1}, the maximum tilt of the isentropes for NB-CI-mode events) and the strongest meridional winds (8.6 m s^{-1}) were used. In more average environments, the net displacement associated with this mechanism is likely far less than the analysis shown here and could be as small as 0 m.

6.6 Summary

The average maximum vertical velocity associated with PV anomalies in NB CI mode environments is typically between 0.1 and 1 cm s^{-1}. This ascent changes depending on the relative strength of the anomaly and the magnitude of the vertical wind shear. Stronger anomalies in environments with stronger wind shear will be associated with more substantial vertical velocities.

The potential for CI cannot be determined by analyzing the magnitude of the vertical velocity alone. The net vertical displacement of parcels by the PV anomaly needs to be analyzed to quantify the potential for CI. The maximum possible net displacement associated with PV anomalies in environments with westerly wind shear is between 100 and 400 m. These displacements assumed the maximum possible values in the composite sounding and the maximum possible displacement associated with the modification by the PV anomaly (which is straight through the center) over 12 hours. The average meridional wind speed associated with the average nocturnal environment is near zero, and the average westerly wind shear is near zero.

This analysis assumed favorable conditions to produce the maximum possible net displacement, which is less than 400 m. These net displacements are larger than typical net displacement because the background westerly wind shear used in this analysis is stronger than the average westerly wind shear (1 m s^{-1} km^{-1} compared to 0.1 m s^{-1} km^{-1}; Fig. 6.9). These small displacements will be even smaller if the average shear is used because the isentropes will be tilted less. Furthermore, parcels are transient around the anomaly, and very few will ever reach this maximum possible ascent because they would need to move northward straight through the anomaly's center. Most parcels will experience a much lower net displacement than this.

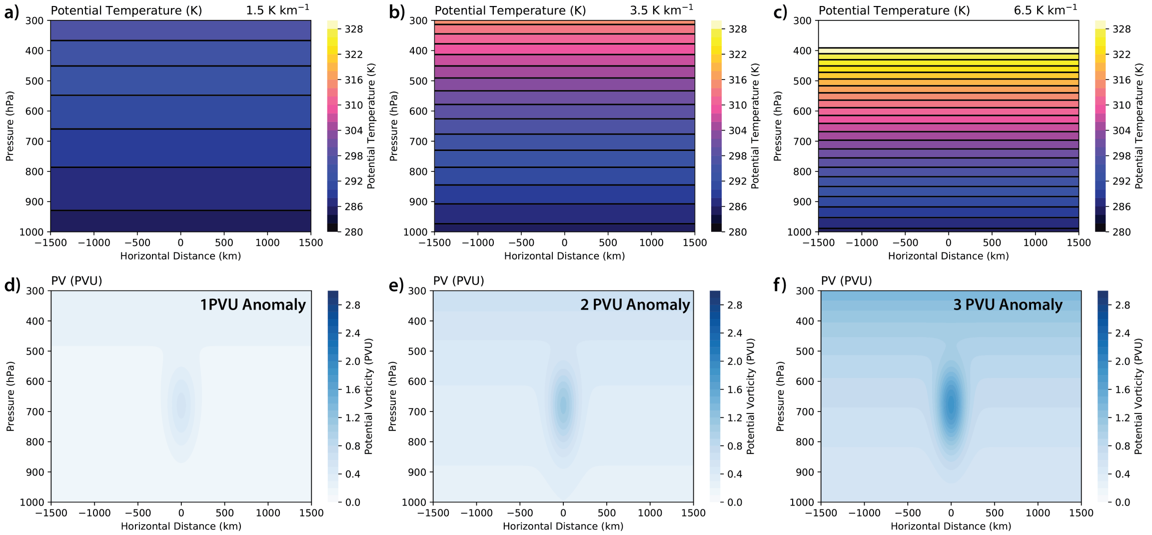

Figure 6.1: Base-state potential temperature for a) WL environments (1.5 K km^{-1}), b) SL environments (3.5 K km^{-1}), and c) SL environments (6.5 K km^{-1}). d) 1 PVU anomaly, e) 2 PVU anomaly, and f) 3 PVU anomaly (prior to smoothing) embedded in the environment in a), b), and c), respectively.

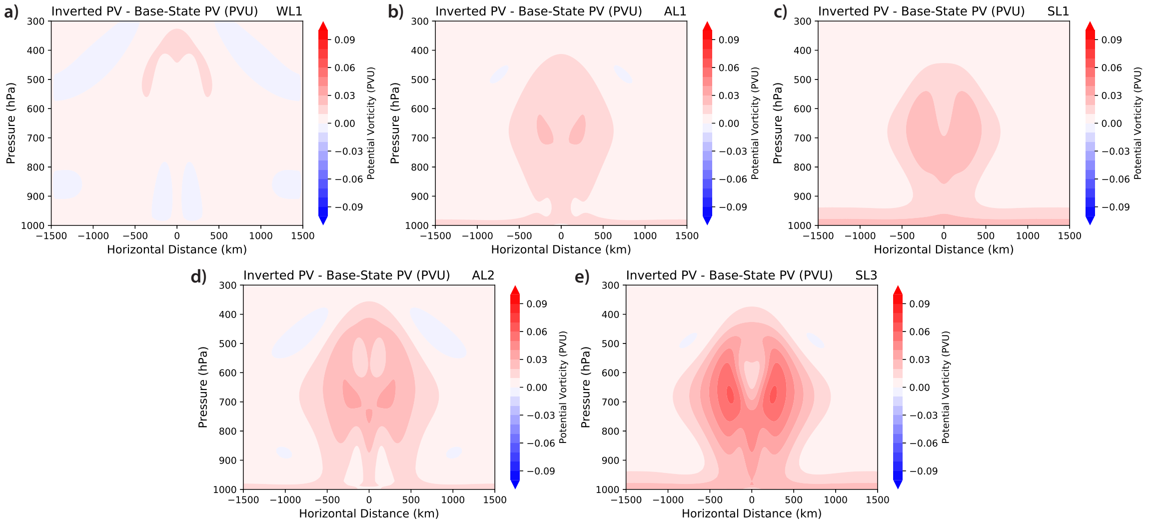

Figure 6.2: PV difference between iteration and initial PV field for a) WL1, b) AL1, c), SL1, d), AL2, and e) SL3 anomalies. Positive differences indicates the inverted field is stronger.

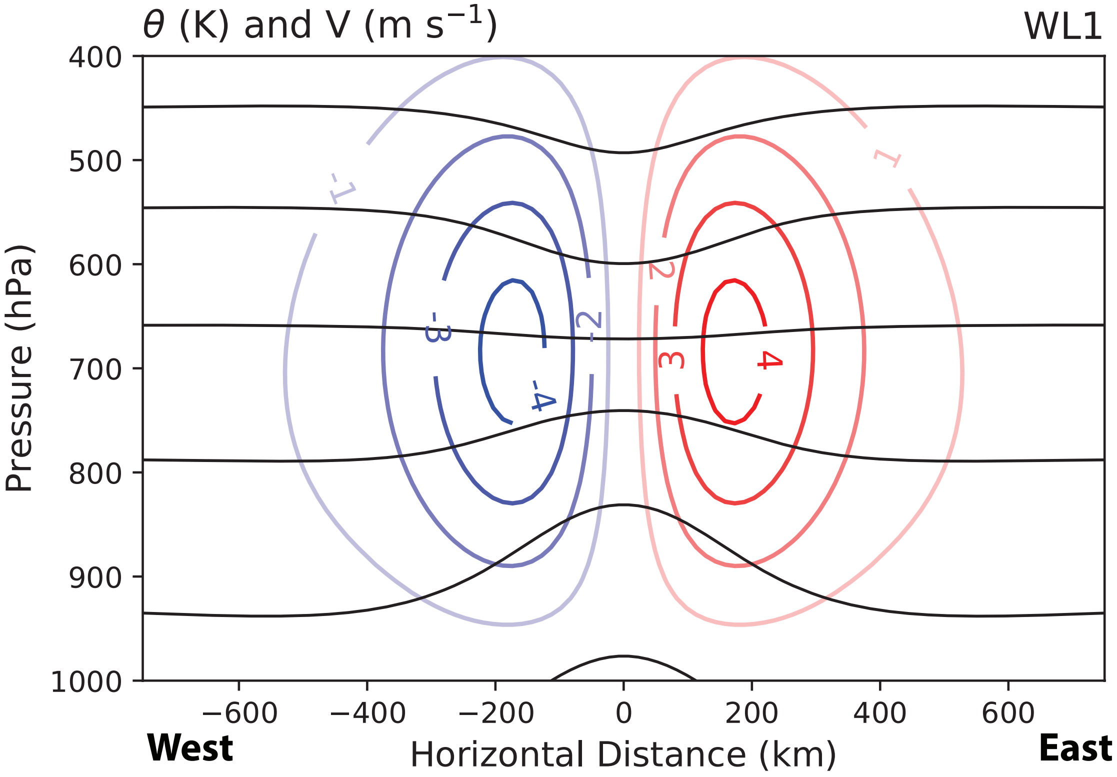

Figure 6.3: Potential temperature (black lines; contoured every 2 K) and meridional wind speed (contoured every 1 m s^{-1}; the red curve is positive, blue curve is negative) for the WL1 anomaly.

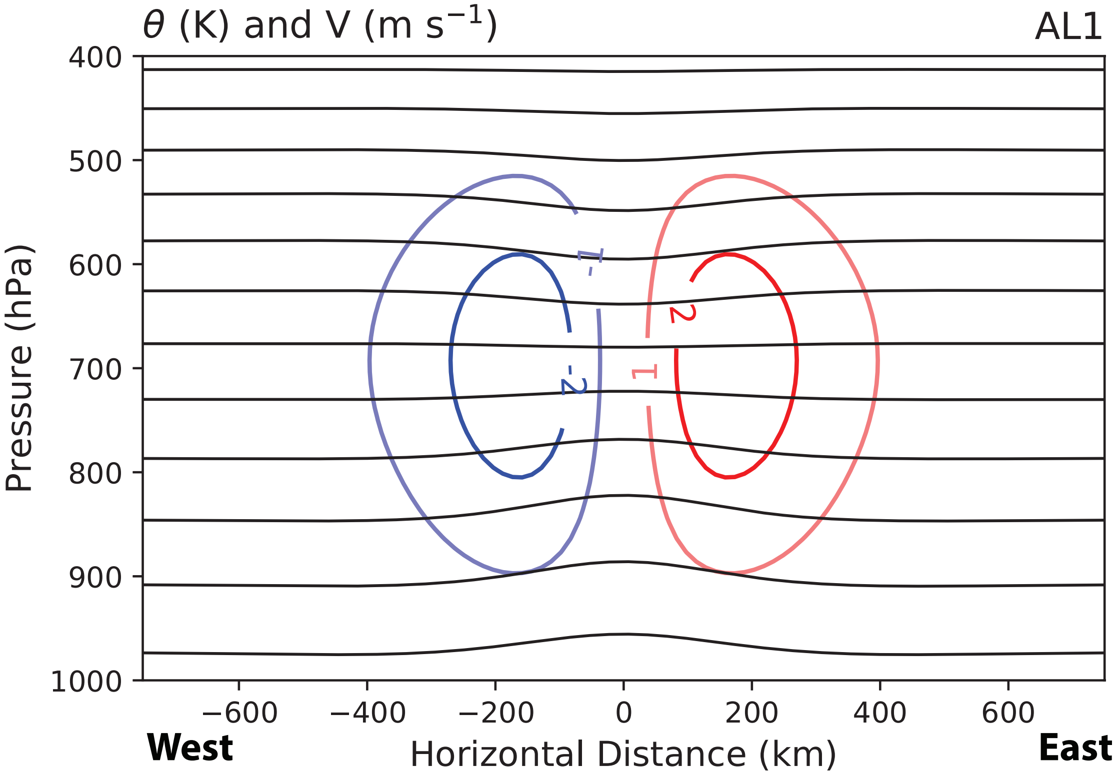

Figure 6.4: As in Fig. 6.3, but for the AL1 anomaly

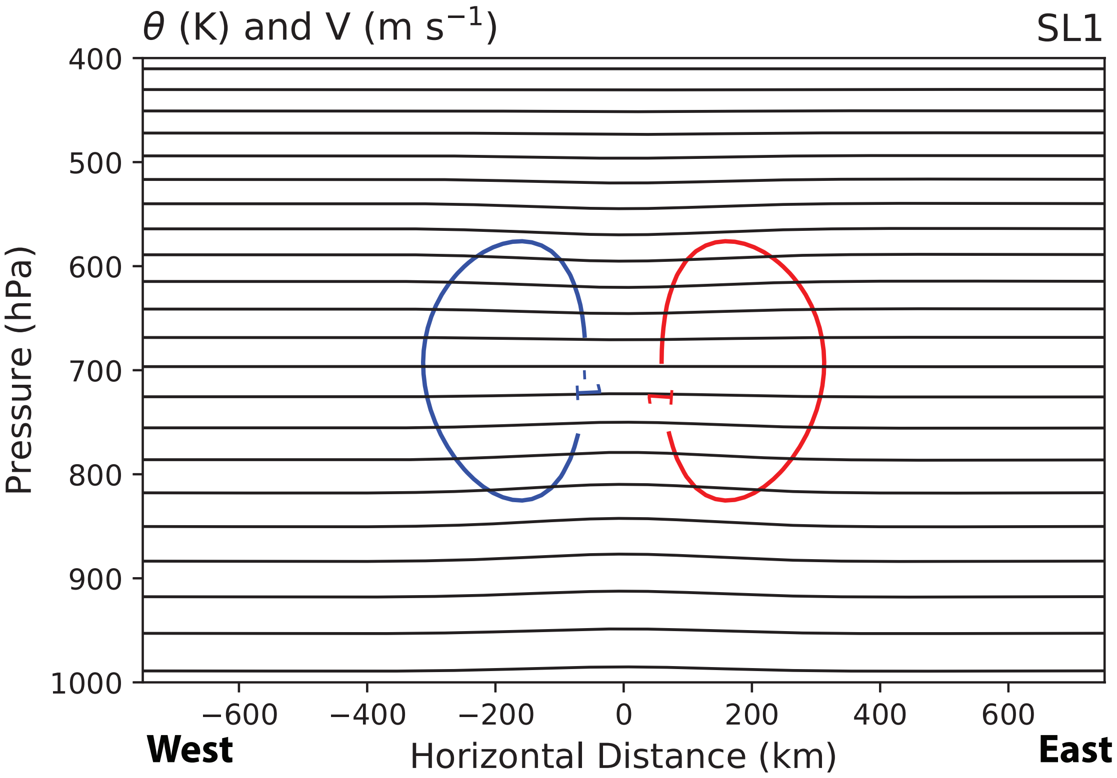

Figure 6.5: As in Fig. 6.3, but for the SL1 anomaly

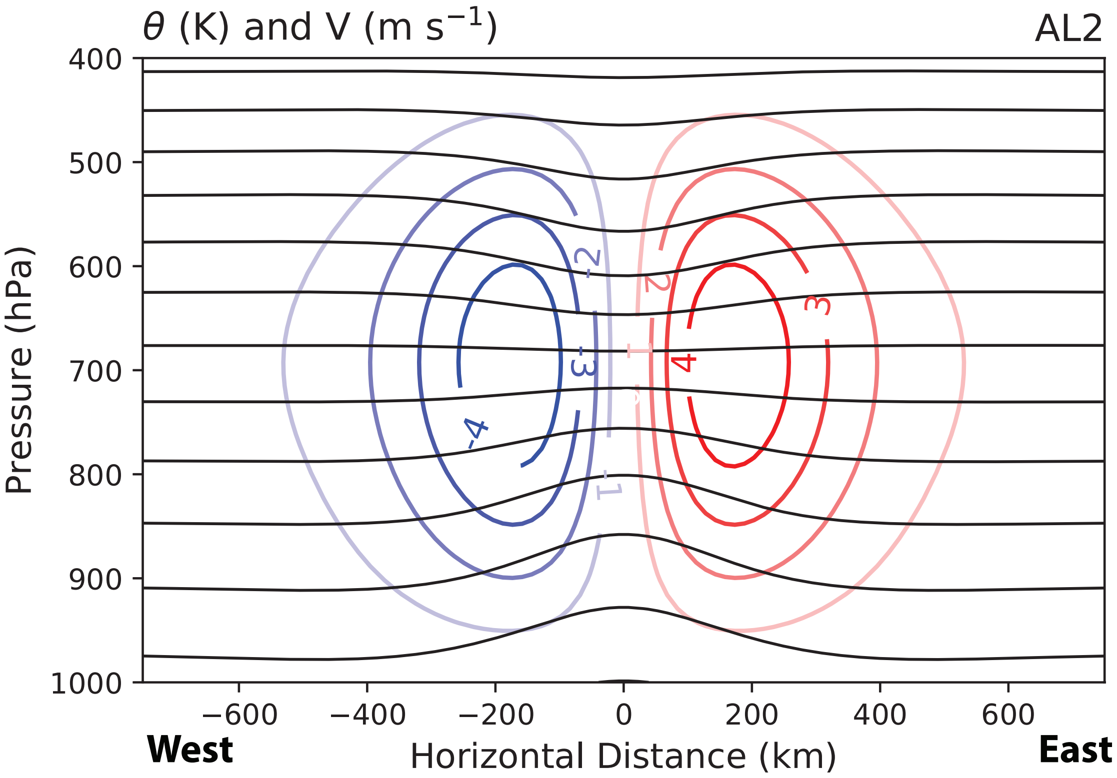

Figure 6.6: As in Fig. 6.3, but for the AL2 anomaly

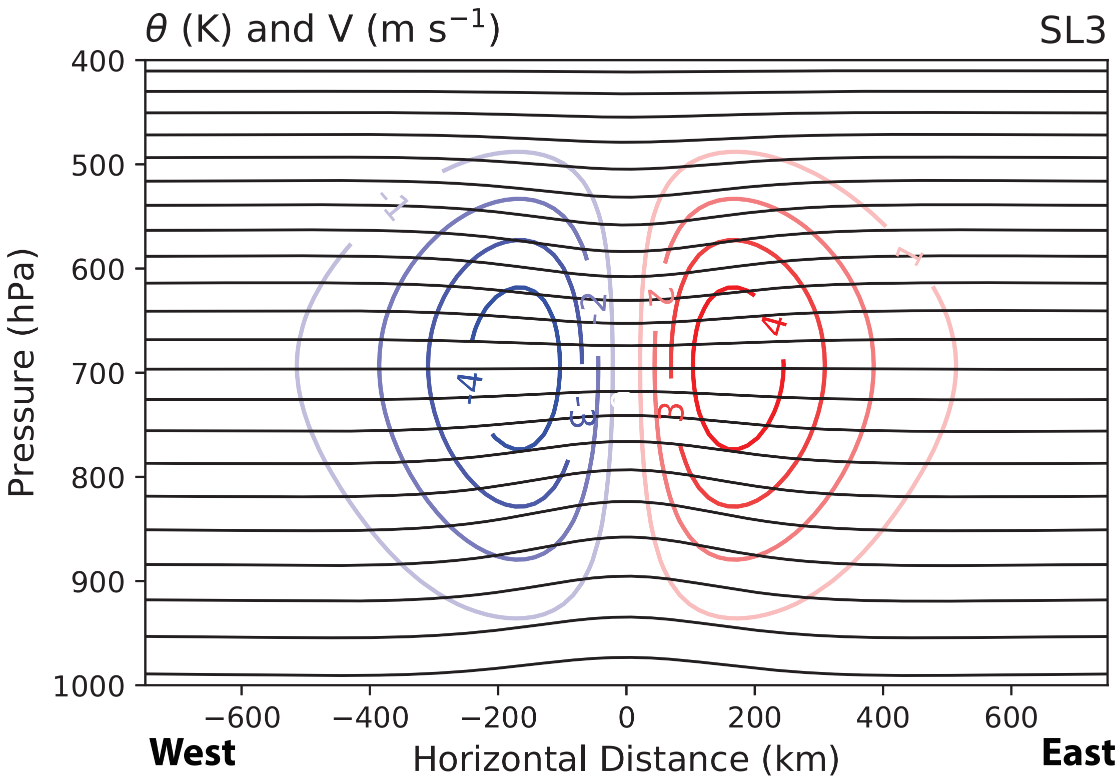

Figure 6.7: As in Fig. 6.3, but for the SL3 anomaly

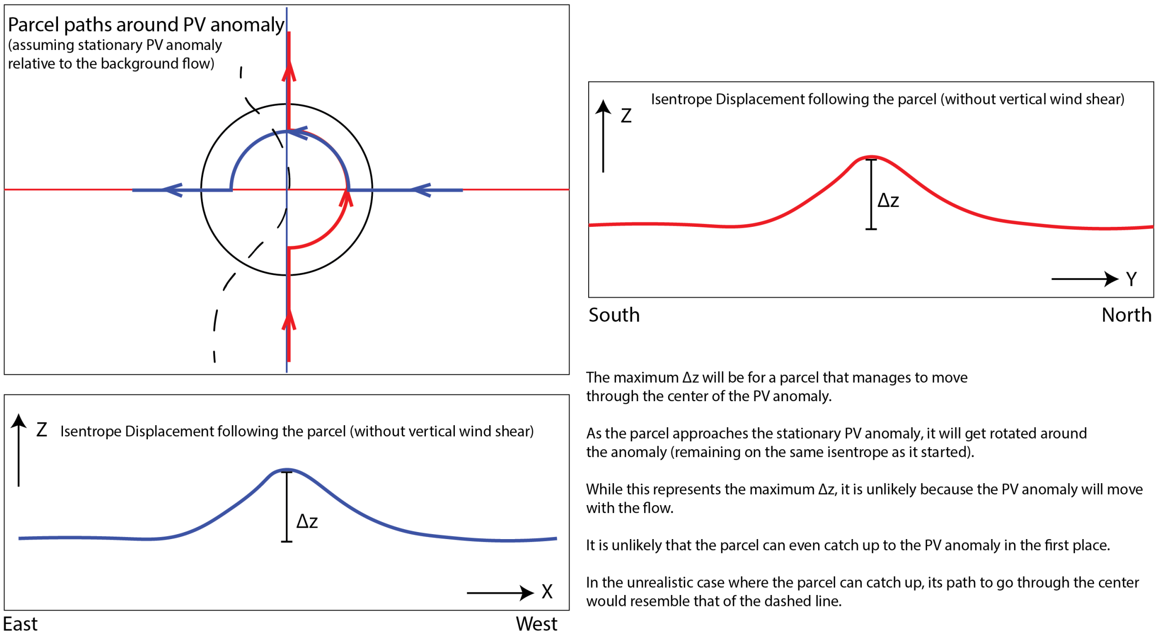

The maximum Δz will be for a parcel that manages to move through the center of the PV anomaly.

As the parcel approaches the stationary PV anomaly, it will get rotated around the anomaly (remaining on the same isentrope as it started).

While this represents the maximum Δz, it is unlikely because the PV anomaly will move with the flow.

It is unlikely that the parcel can even catch up to the PV anomaly in the first place.

In the unrealistic case where the parcel can catch up, its path to go through the center would resemble that of the dashed line.

Figure 6.8: Schematic of possible trajectories around a stationary PV anomaly embedded in background flow. The red line in the right panel represents the displacement of a parcel moving from south to north. The blue line in the bottom panel represents the displacement of a parcel moving from east to west.

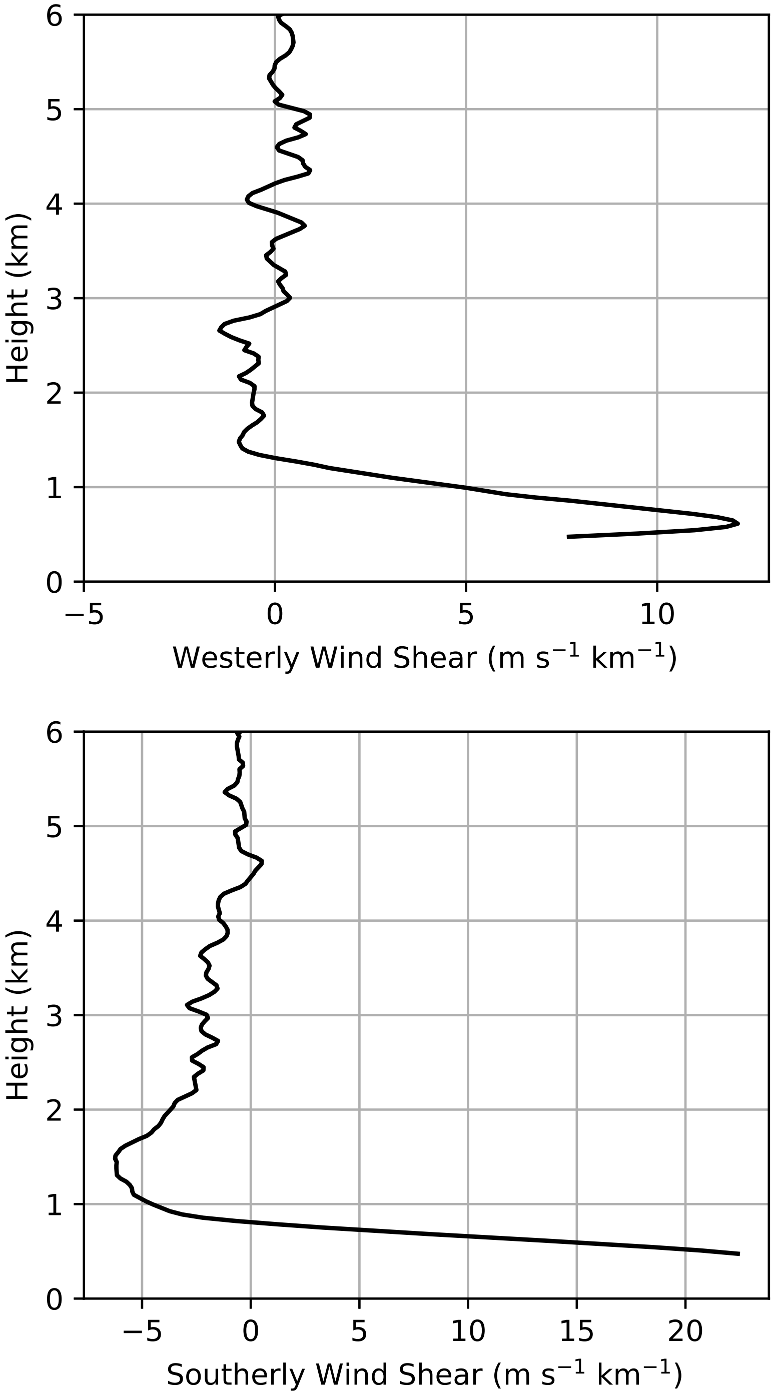

Figure 6.9: a) Westerly wind shear (m s^{-1} km^{-1}) and b) southerly wind shear (m s^{-1} km^{-1}) from the composite sounding.

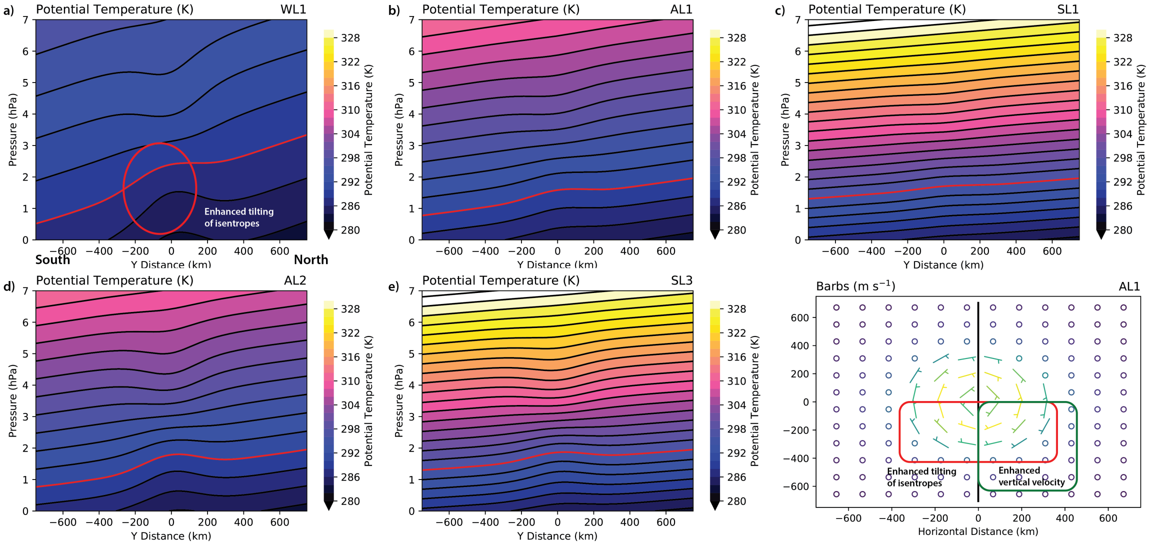

Figure 6.10: North-south cross section of the potential temperature field modified by the PV anomaly and the 1 m s^{-1} km^{-1} westerly vertical wind shear for the a) Wl1, b) AL1, c) SL1, d) AL2, and e) SL3 anomalies. f) Schematic of the cyclonic circulation. The red box indicates the location of the more stronger potential temperature modification and the green box represents where the vertical velocity would be strongest (based on the slope of the isentropes).

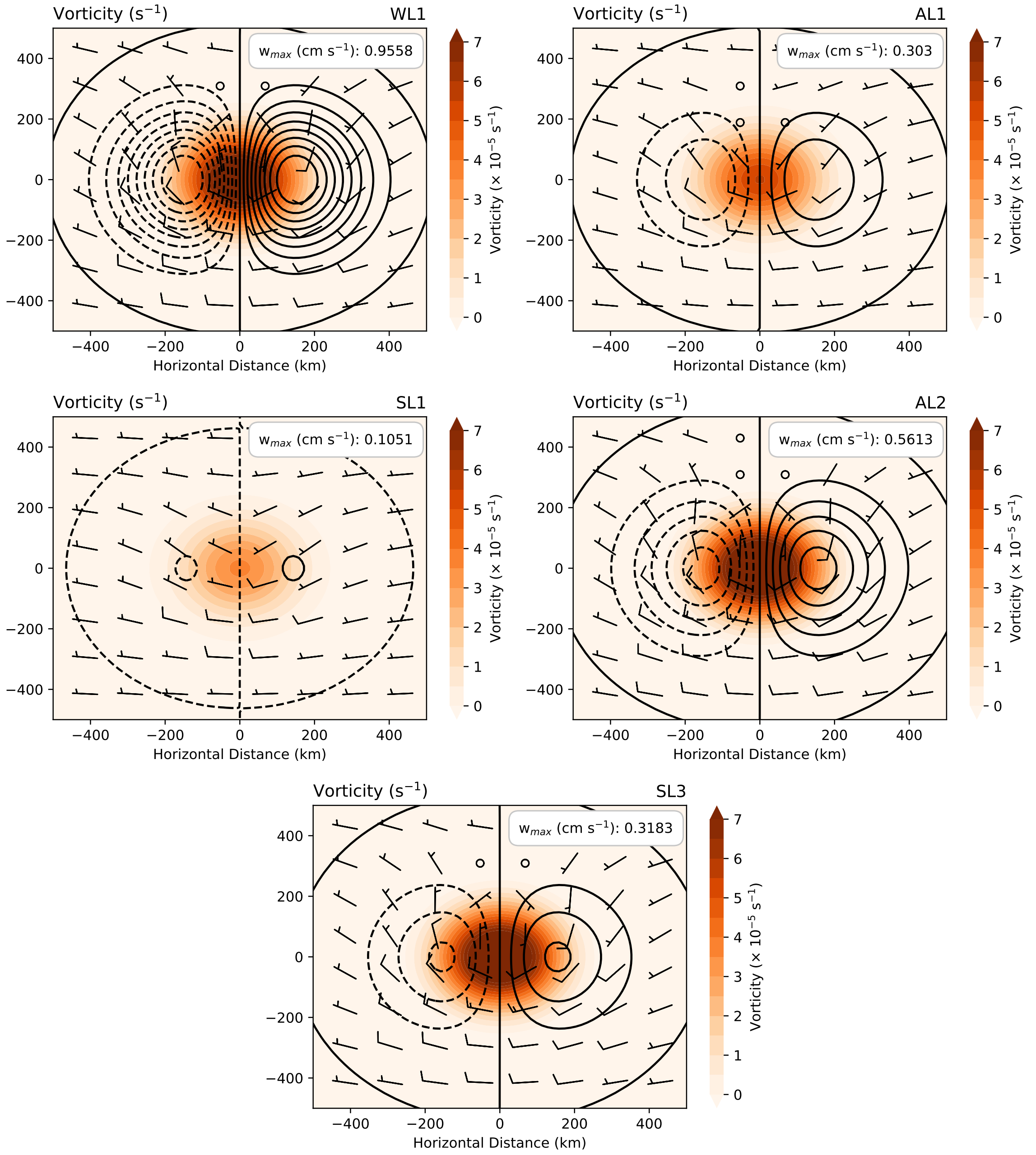

Figure 6.11: Vertical vorticity ($\times 10^{-5}$ s^{-1}) and vertical velocity computed from the Sutcliffe-Trenberth form of the QG omega equation (contoured every 0.1 cm s^{-1}) for the a) WL1, b) AL1, c) SL1, d) AL2, and e) SL3 PV anomalies.

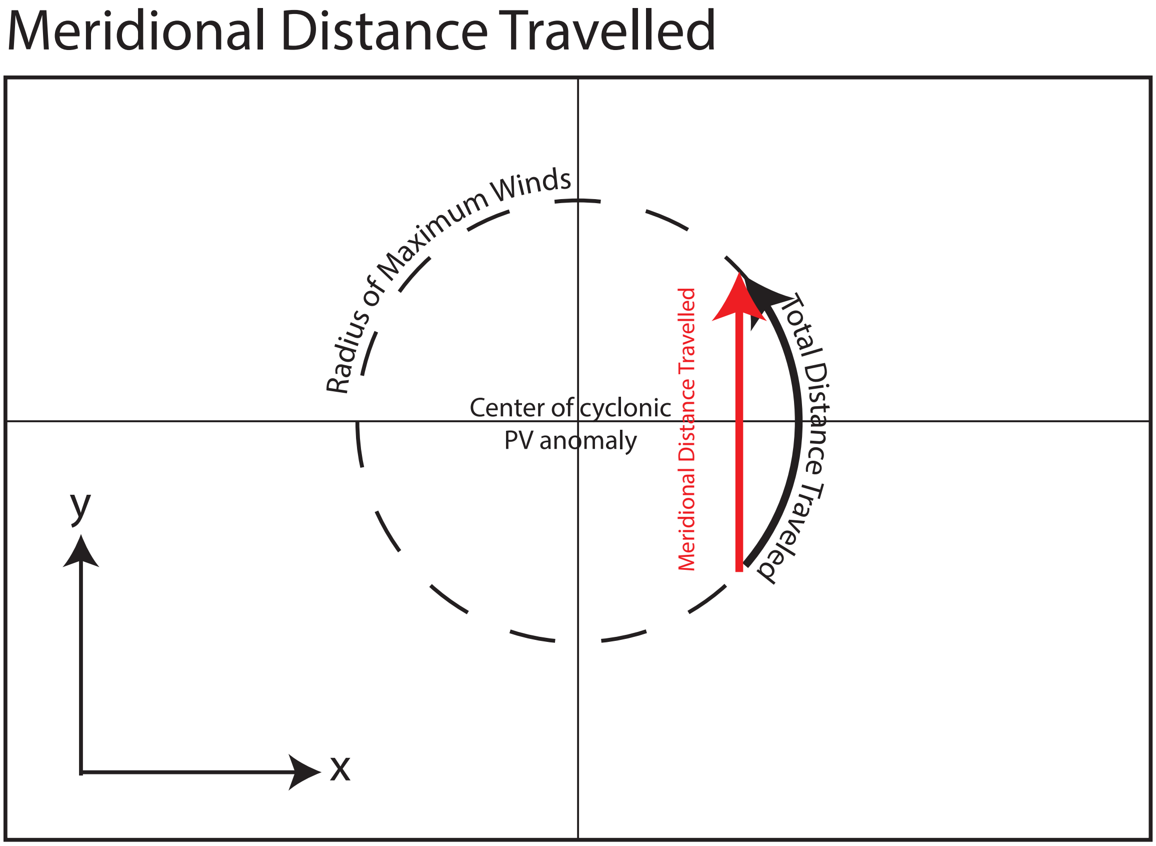

Figure 6.12: The total distance traveled during the night for an air parcel (black curved arrow) at the radius of maximum winds (dashed circle) and the meridional distance traveled (the red arrow) for the same air parcel. The net displacement that air parcels experience depends on the meridional distance traveled (the red arrow), not the total distance traveled (the black arrow).

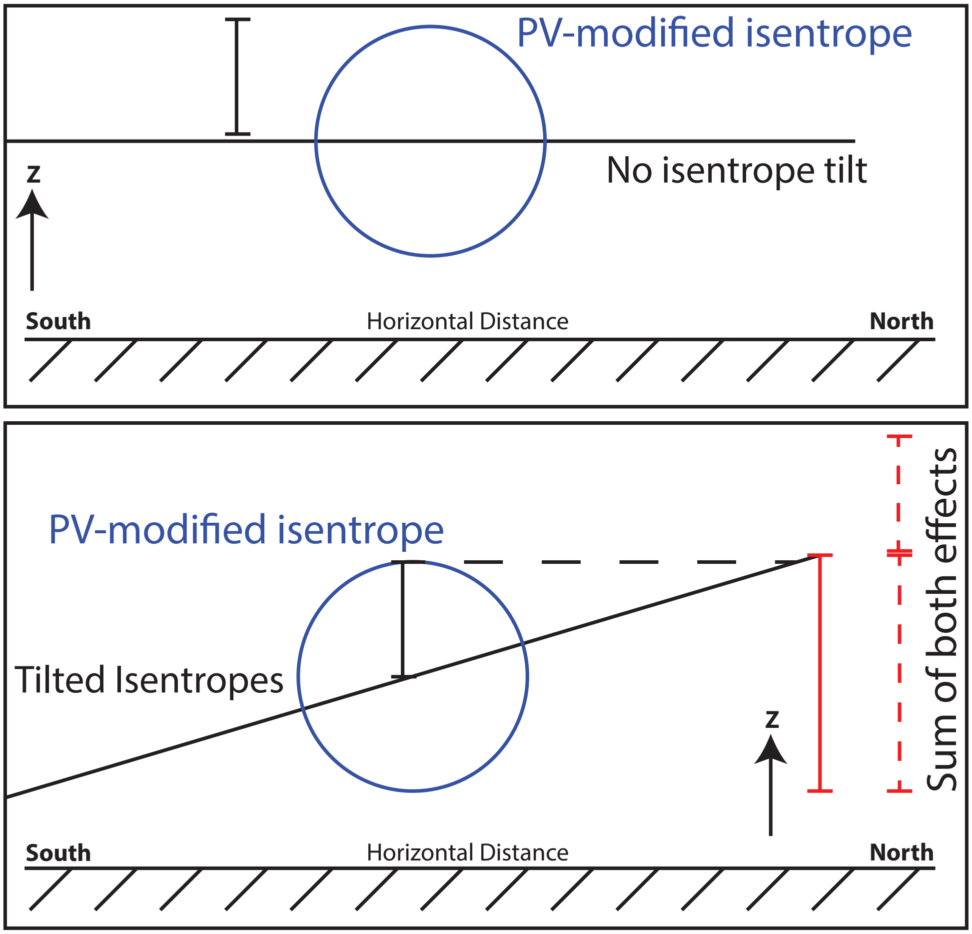

Figure 6.13: An X-Z cross section of the net displacement associated with the PV anomaly in an environment without vertical shear (top panel) and one with vertical shear (bottom panel). The isentropes associated with the environment are black and those associated with the PV anomaly are blue. The parcel in an environment with vertical shear realized a higher net displacement in a shorter horizontal distance than a parcel in an environment without vertical wind shear. However, the parcel's total displacement through the anomaly in an environment with vertical shear (red line) is not the sum of the displacement of the environmental isentrope and the PV-modified isentrope (dashed red line).

Chapter 7

Summary

Three initiation mechanisms were examined to identity the vertical velocity and net vertical displacement associated with each mechanism. The gravity wave (GW) and low-level jet (LLJ) mechanisms were studied using idealized numerical simulations, and the potential vorticity (PV) mechanism was studied using the PV inversion technique. While the ascent associated with atmospheric bores has been studied in previous studies, this study uses three-dimensional idealized numerical simulations to test the potential for CI in a variety of typical nighttime environments over the Great Plains. Previous studies using numerical simulations have relied on the use of two-dimensional idealized simulations (e.g., Crook 1988) or simulations of real cases (e.g., Blake et al. 2017). Additionally, these LLJ simulations are the first three-dimensional idealized simulations of the broad mesoscale ascent due to the release of the friction constraint outlined in Shapiro et al. (2018). Creating a PV anomaly via diabatic processes alone (through a heating bubble) produced unwanted gravity waves throughout the simulation, complicating the vertical motion analysis. Because of this difficulty, a numerical simulation was not used to analyze ascent associated with PV. A PV inversion technique is used to study the ascent associated with idealized PV anomalies that represent typical anomalies generated by diabatic effects over the Rocky Mountains. While the PV inversion technique is not new, its application here to determine the vertical velocity and net displacement of air parcels in typical nocturnal environments is new.

To study the effects of these features on typical nocturnal environments, a composite sounding was created from 108 proximity soundings from the Reif and Bluestein (2017) 20-year climatology. This sounding represents the typical environment for NB CI mode events, and the ±1 standard deviation of the stability and wind profiles create nine typical environments. These include the low lapse rate (WT), average lapse rate (WT), and high lapse rate (ST) environments and the weak wind (WW), average wind (WW), and strong wind (SW) environments. These nine environments are studied to see how each mechanism affects the typical range of NB CI mode environments.

Modifying this typical environment's dewpoint temperature indicated that small adjustments to the low-level (900 – 700 hPa) moisture increases the CAPE and lowers the LCL and the LFC. A reduction of the dewpoint depression of 50% had a larger impact at lower heights and resulted in CAPE of nearly 1000 J kg^{-1}. In these 50% modified environments, a parcel only needed to be lifted between 500 and 900 m to reach its LFC. The simple modification to the dewpoint was not entirely accurate, however. The temperature would need to be modified as well. In the case of persistent mesoscale ascent, the formation of a MAUL can drastically reduce this necessary displacement to a few hundred meters at most.

In the gravity wave simulations, the environments of the WT simulations were nearly neutrally stratified, and no bores formed in any of them. However, for the bores that did form in the AT and ST simulations, increasing the stratification reduced the vertical velocity and net displacement associated with the bore. Increasing the incoming wind speed increased the vertical velocity and net displacement of air parcels (likely due to more favorable wave trapping). These net displacements were approximately 200-300 m for the bores in the AT simulations and 100-150 m for those in the ST simulations. The vertical velocity was 0.4 m s^{-1} for the bores in the AT simulations and 0.2 for those in the ST simulations. These velocities and displacements are lower than those of observed bores in which the vertical velocity and net displacement can be upwards of 2 m s^{-1} and 1 km, respectively.

While the density current in those simulations was weaker than many observed density currents (due to the extreme near-surface stratification), when a stronger density current was simulated, the net displacement and vertical velocities increased, especially in the ST simulations. Increasing the density current's strength increased the net displacement from 200-300 m to nearly 500 m and increased the vertical velocity from 0.5 m s^{-1} to 1 m s^{-1}, which more closely resembles those for observed bores.

In those simulations without vertical wind shear, there were no significant differences between the 0° bores and the 45° bores. This similarity is likely because the conditions for wave trapping and bore generation are highly favorable throughout the domain. The small reduction of the system-relative wind speed is unlikely to have had any significant impact.

When vertical wind shear was added, there were notable changes in the bore's characteristics. The 0° bores mainly remained the same with and without vertical wind shear. However, the 45° bore had a more variable wavelength. At times, the leading wave was larger, and at other times, the second wave was larger. There was also a difference between the 45° and the -45° bores. At times the 45° bore was stronger than the -45°, and at other times it was weaker.

In general, atmospheric bores in typical nocturnal environments have a net displacement of 200-500 m, and this effect extends through the lowest few km of the atmosphere. The vertical velocities in these simulations ranged from < 0.5 m s^{-1} to over 1 m s^{-1}. Nocturnal CI by atmospheric bores is certainly a plausible mechanism if the waves can propagate far ahead of the MCS that triggered the bore.

The LLJ is associated with ascent that results from convergence at its terminus, ascent as air is lifted over a surface boundary and elevated convergence due to the inhomogeneous veering with time. In this study, we explored ascent resulting from a preexisting surface baroclinic zone and the LLJ. During the daytime, the PBL was well-mixed and extended up to 2-3 km AGL, and during the nighttime, an LLJ developed in this residual layer. These peak winds of the LLJ were east of the maximum surface heating, and there was an inertial oscillation throughout the night. The simulated LLJ shared many characteristics of observed LLJs and was a reasonable approximation in these idealized numerical simulations.

During the night, a persistent zone of ascent started near the maximum surface daytime heating and was west of the LLJ during the night. This nearly 400-km-wide area lasted the entire night, and the vertical velocity reached its peak intensity between 0500 and 0800

UTC. The magnitude of this ascent ranged from 0.3 cm s^{-1} to just over 1 cm s^{-1}, but this sustained ascent over 12 hours can result in net displacements from 200 m to over 1 km.

Not only is the net displacement associated with the LLJ-related ascent large, but the modification to the atmosphere by the LLJ is likely equally important. The jet is responsible for advecting warmer and moister air from the south. This advection can make the atmosphere more conducive to CI (see analysis in Chapter 3), and smaller net displacements will be necessary for CI by these more-favorable environments. LLJ-related ascent due to the surface buoyancy gradient is a likely nocturnal CI mechanism. Another possible mechanism is the tilting of planetary vorticity onto the horizontal by the LLJ. Rising motion would exist above the jet on the eastern side of the jet maximum. While this mechanism is not explored in this study, it is worth further exploration.

The final CI mechanism explored was ascent related to cyclonic PV anomalies in westerly wind shear. These cyclonic PV anomalies are generated over the lee of the Rockies and propagate eastward throughout the Plains. In this study, the PV anomaly generation was not explored, only the response to a preexisting PV anomaly in typical nocturnal environments. In the most extreme conditions typical for NB CI mode events, the vertical velocity associated with the PV anomaly is < 1 cm s^{-1}, and the net displacements are less than 200 m. The ascent and net displacements associated with PV anomalies in more typical environments are < 0.1 cm s^{-1}, and the net displacements are less than 50 m. The ascent related to PV anomalies in NB CI mode environments (i.e., those with weak vertical wind shear) is unlikely to result in CI.

That being said, the PV anomaly could modify the environment to make it more conducive to CI and make it easier for another mechanism (such as the LLJ or gravity waves) to cause CI. The more-tilted isentropes would allot parcels to achieve higher net displacements in shorter periods. If the PV anomaly is located west of the LLJ, then the added wind speed from the anomaly to the jet may increase the ascent of parcels up the isentropes. Furthermore, the more tilted isentropes could allow for stronger net displacements associated with atmospheric bores. However, the interaction of the PV anomaly and these other initiation mechanisms is unclear.

While providing a good approximation of the mechanisms in terms of their magnitude and time evolution, these simulations have problems. For example, the three-dimensional gravity wave simulations could be improved by creating a more-realistic density current. However, it is difficult to create a deep ($>$ 750 m) density current when the stratification is greater than 3-5 K km^{-1} (see Reif et al. (2020) for density currents in different stratifications). A deeper initial cold block ($>$3 km) with a potential perturbation of $<$ -20 K might do it, but this could also create unrealistic effects such as unwanted gravity waves due to model shock because of the extremely strong and deep dam-break problem.

The runaway surface cooling in the LLJ simulations at night occurs because the surface heating caused by the heating pad is heating in addition to that from the radiation scheme. This additional heating could cause the model to overcorrect this excess heat by cooling rapidly during the night, decoupling the surface from the atmosphere just above. Furthermore, the lack of PBL schemes in CM1 does not allow for testing to see if a local scheme would handle this excess heat in CM1 better than the non-local YSU scheme. Future work on these simulations would be to mitigate this runaway cooling while maintaining the horizontal baroclinic zone. Additional PBL schemes might help, but a different method to generate the baroclinicity other than an artificial heating pad might also help.

Improving the PV inversion technique would be to specify a horizontally heterogeneous initial wind field representing the typical nocturnal environment. However, to understand the ascent related to the PV anomaly, including this wind field is unlikely to have a notable impact, but it would make representing the lateral boundary conditions for Ψ more realistic.

In all simulations, moisture is neglected, meaning that CI cannot actually occur. Furthermore, in the GW simulations, the time evolution of the LLJ and mesoscale variations of features such as temperature, pressure, and wind are neglected. The LLJ simulations are assumed to be horizontally homogeneous, except for the heating pad. More realistic simulations could likely be achieved by including spatiotemporal variations in moisture and in the variables mentioned above (i.e., allow features such as the LLJ and surface temperature to evolve with time rather than hold them fixed). However, the analysis of the net displacement due to a specific mechanism would be more complicated. Because this study aimed to identify the potential for CI due to the mechanism itself, the simulations were kept as simple as possible. Numerical simulations from real data (e.g., a WRF simulation of a real case) will include these effects and produce realistic simulations of these features, but isolating the cause of the ascent due to a specific mechanism in a real WRF simulation is virtually impossible.

The maximum net displacement for these mechanisms is approximately 100 m for PV anomalies, 300-500 m for atmospheric bores in these simulations (though the net displacement has been observed to be 1000 m), and over 1000 m for the LLJ in these simulations. However, the potential for CI is dependent on how conducive the environment is for CI in these environments. Due to the weak forcing associated with these events, analyses of typical soundings associated with NB CI mode events suggest that low-level warm advection and a low-level moisture maximum is critical to make the environment more conducive to CI. The moisture likely originates from decaying convection over the Rockies, and the southerly wind across the east-west oriented baroclinic zone causes warm advection (the baroclinic zone is related to the westerly vertical wind shear). If there are warm advection and positive moisture advection in the environment, then it is more likely that these mechanisms can cause CI because the environment is more conducive for CI.

Results from this study confirm the magnitude of ascent and the typical net displacements associated with atmospheric bores. They also confirm the ascent mechanism noted in Shapiro et al. (2018) regarding ascent generated by a baroclinic zone and the release of the friction constraint at night. The magnitude of that ascent and net displacement of parcels associated with that ascent is confirmed here. While this study confirms these results from previous studies, *this study is the first to perform three-dimensional idealized numerical simulations of these mechanisms in a wide range of nocturnal environments*. These Idealized numerical simulations let us isolate a specific type of ascent associated with these mechanisms and assess how important that specific mechanism is important to CI.

The results from the PV inversion would suggest that PV anomalies are unlikely to initiate CI by themselves in the NB CI mode environments. This is contrary to a popular belief that because the phase of the precipitation signal and the phase of the drifting PV anomalies are similar, that PV is important to this precipitation. It is undeniable that the PV signal and the precipitation signal are related, but it is likely that the PV generated by latent heating associated with the precipitation is a contributor to the similar phases.

Observations of each mechanism will improve our understanding of the ascent associated with each mechanism, but observing the ascent associated with the LLJ and PV anomalies is challenging due to their weak magnitudes. To observe this persistent ascent associated with the LLJ, observations that span multiple nights would be necessary to generate a large enough sample size. There would also need to be a horizontal baroclinic zone of roughly 1 K (100 km)$^{-1}$ to ensure that the ascent that is observed is the same ascent studied here and in Shapiro et al. (2018). Averaging the ascent for the LLJ over multiple nights would help average out the higher magnitude, but more transient updrafts that result from other features, including possible KH billows, thunderstorms, and gravity waves. Applying a band-pass filter to filter out these higher-frequency signals could help further isolate this persistent ascent.

Observing ascent related to diabatically-generated cyclonic PV anomalies would require observing ascent rooted between 800 and 600 hPa (where the decaying convection over the Rockies that generate these drifting anomalies is). These eastward drifting PV anomalies are smaller than the LLJ, so targeted observations would require planning and instruments sensitive enough to observe weak vertical velocities at 3 km AGL. Establishing a climatology of these diabatically-generated PV anomalies from the Rockies would help determine their frequency and size, further improving our understanding of these features. Using reanalysis data from sources such as the ERA5 to identify these drifting PV anomalies to create a climatology would improve our understanding.

In summary, the gravity wave and the LLJ CI mechanisms are likely CI mechanisms for pristine NB CI mode events. Previous studies have documented CI associated with each of these mechanisms. However, this study is the first to simulate these features in three-dimensional idealized numerical simulations and quantify the vertical velocities and net displacements over a wide range of typical NB CI mode environments. Furthermore, this study quantified the net displacements and vertical velocities associated with PV anomalies and corrected the misconception that ascent associated with PV anomalies alone in these NB CI mode events can cause CI.

Bibliography

Adams-Selin, R. D., 2020: Impact of convectively generated low-frequency gravity waves on evolution of mesoscale convective systems. *J. Atmos. Sci.*, **77 (10)**, 3441–3460, doi:10.1175/JAS-D-19-0250.1.

Adams-Selin, R. D., and R. H. Johnson, 2013: Examination of gravity waves associated with the 13 march 2003 bow echo. *Mon. Wea. Rev.*, **141 (11)**, 3735–3756, doi:10.1175/MWR-D-12-00343.1.

Arritt, R. W., T. D. Rink, M. Segal, D. P. Todey, C. A. Clark, M. J. Mitchell, and K. M. Labas, 1997: The great plains low-level jet during the warm season of 1993. *Mon. Wea. Rev.*, **125 (9)**, 2176–2192, doi:10.1175/1520-0493(1997)125⟨2176:TGPLLJ⟩2.0.CO;2.

Augustine, J. A., and F. Caracena, 1994: Lower-tropospheric precursors to nocturnal mcs development over the central united states. *Wea. Forecasting*, **9 (1)**, 116–135, doi:10.1175/1520-0434(1994)009⟨0116:LTPTNM⟩2.0.CO;2.

Baines, P., and P. Davies, 1980: Laboratory studies of topographic effects in rotating and/or stratified fluids. *Orographic Effects in Planetary Flows*, **23**, 233–299.

Blackadar, A. K., 1957: Boundary layer wind maxima and their significance for the growth of nocturnal inversions. *Bull. Amer. Meteor. Soc.*, **38 (5)**, 283–290, doi:10.1175/1520-0477-38.5.283.

Blake, B. T., D. B. Parsons, K. R. Haghi, and S. G. Castleberry, 2017: The structure, evolution, and dynamics of a nocturnal convective system simulated using the wrf-arw model. *Mon. Wea. Rev.*, **145 (8)**, 3179–3201, doi:10.1175/MWR-D-16-0360.1.

Bluestein, H. B., 1992: *Synoptic-dynamic meteorology in midlatitudes: Volume 1, principles of kinematics and dynamics*. New York, NY (United States); Oxford Univ. Press.

Bluestein, H. B., 1993: *Synoptic-dynamic meteorology in midlatitudes. Volume II. Observations and theory of weather systems*. New York, NY (United States); Oxford University Press.

Bluestein, H. B., G. S. Romine, R. Rotunno, D. W. Reif, and C. C. Weiss, 2018: On the anomalous counterclockwise turning of the surface wind with time in the plains of the united states. *Mon. Wea. Rev.*, **146 (2)**, 467–484, doi:10.1175/MWR-D-17-0297.1.

Bluestein, H. B., and J. C. Snyder, 2015: An observational study of the effects of dry air produced in dissipating convective storms on the predictability of severe weather. *Wea. Forecasting*, **30 (1)**, 79–114, doi:10.1175/WAF-D-14-00065.1.

Bonner, W. D., 1966: Case study of thunderstorm activity in relation to the low-level jet. *Mon. Wea. Rev*, **94 (3)**, 167–178, doi:10.1175/1520-0493(1966)094⟨0167:CSOTAI⟩2.3.CO;2.

Bonner, W. D., 1968: Climatology of the low level jet. *Mon. Wea. Rev*, **96 (12)**, 833–850, doi:10.1175/1520-0493(1968)096⟨0833:COTLLJ⟩2.0.CO;2.

Bonner, W. D., and J. Paegle, 1970: Diurnal variations in boundary layer winds over the south-central united states in summer. *Mon. Wea. Rev.*, **98 (10)**, 735–744, doi:10.1175/1520-0493(1970)098⟨0735:DVIBLW⟩2.3.CO;2.

Brennan, M. J., G. M. Lackmann, and K. M. Mahoney, 2008: Potential vorticity (pv) thinking in operations: The utility of nonconservation. *Wea. Forecasting*, **23 (1)**, 168–182, doi:10.1175/2007WAF2006044.1.

Browning, K., A. Thorpe, A. Montani, D. Parsons, M. Griffiths, P. Panagi, and E. Dicks, 2000: Interactions of tropopause depressions with an ex–tropical cyclone and sensitivity of forecasts to analysis errors. *Mon. Wea. Rev.*, **128 (8)**, 2734–2755, doi:10.1175/1520-0493(2000)128⟨2734:IOTDWA⟩2.0.CO;2.

Bryan, G. H., 2016: The governing equations for cm1. *Technical Note. UCAR: Boulder, CO. http://www2. mmm. ucar. edu/people/bryan/cm1/cm1 equations. pdf (accessed 23 October 2016).*

Bryan, G. H., and J. M. Fritsch, 2000: Moist absolute instability: The sixth static stability state. *Bull. Amer. Meteor. Soc.*, **81 (6)**, 1207–1230, doi:10.1175/1520-0477(2000)081⟨1287:MAITSS⟩2.3.CO;2.

Bryan, G. H., J. C. Wyngaard, and J. M. Fritsch, 2003: Resolution requirements for the simulation of deep moist convection. *Mon. Wea. Rev.*, **131 (10)**, 2394–2416, doi:10.1175/1520-0493(2003)131⟨2394:RRFTSO⟩2.0.CO;2.

Carbone, R., J. Conway, N. Crook, and M. Moncrieff, 1990: The generation and propagation of a nocturnal squall line. part i: Observations and implications for mesoscale predictability. *Mon. Wea. Rev.*, **118 (1)**, 26–49, doi:10.1175/1520-0493(1990)118⟨0026:TGAPOA⟩2.0.CO;2.

Carbone, R., and J. Tuttle, 2008: Rainfall occurrence in the us warm season: The diurnal cycle. *Journal of Climate*, **21 (16)**, 4132–4146, doi:10.1175/2008JCLI2275.1.

Carbone, R., J. Tuttle, D. Ahijevych, and S. Trier, 2002: Inferences of predictability associated with warm season precipitation episodes. *J. Atmos. Sci.*, **59 (13)**, 2033–2056, doi:10.1175/1520-0469(2002)059⟨2033:IOPAWW⟩2.0.CO;2.

Cavallo, S. M., and G. J. Hakim, 2010: Composite structure of tropopause polar cyclones. *Mon. Wea. Rev.*, **138 (10)**, 3840–3857, doi:10.1175/2010MWR3371.1.

Charney, J., 1955: The use of the primitive equations of motion in numerical prediction. *Tellus*, **7 (1)**, 22–26, doi:10.1111/j.2153-3490.1955.tb01138.x.

Cheeks, S. M., S. Fueglistaler, and S. T. Garner, 2020: A satellite-based climatology of central and southeastern us mesoscale convective systems. *Mon. Wea. Rev.*, **148 (6)**, 2607–2621, doi:MWR-D-20-0027.1.

Chipilski, H. G., X. Wang, and D. B. Parsons, 2018: Object-based algorithm for the identification and tracking of convective outflow boundaries in numerical models. *Mon. Wea. Rev.*, **146 (12)**, 4179–4200, doi:10.1175/MWR-D-18-0116.1.

Clarke, R. H., 1972: The morning glory: An atmospheric hydraulic jump. *Journal of Applied Meteorology*, **11 (2)**, 304–311, doi:10.1175/1520-0450(1972)011⟨0304:TMGAAH⟩2.0.CO;2.

Cohen, A. E., S. M. Cavallo, M. C. Coniglio, and H. E. Brooks, 2015: A review of planetary boundary layer parameterization schemes and their sensitivity in simulating southeastern us cold season severe weather environments. *Wea. Forecasting*, **30 (3)**, 591–612, doi:10.1175/WAF-D-14-00105.1.

Coleman, T. A., K. R. Knupp, and D. E. Herzmann, 2010: An undular bore and gravity waves illustrated by dramatic time-lapse photography. *J. Atmos. Oceanic Technol.*, **27 (8)**, 1355–1361, doi:10.1175/2010JTECHA1472.1.

Colman, B. R., 1990: Thunderstorms above frontal surfaces in environments without positive cape. part i: A climatology. *Mon. Wea. Rev.*, **118 (5)**, 1103–1122, doi:10.1175/1520-0493(1990)118⟨1103:TAFSIE⟩2.0.CO;2.

Coniglio, M. C., J. Y. Hwang, and D. J. Stensrud, 2010: Environmental factors in the upscale growth and longevity of mcss derived from rapid update cycle analyses. *Mon. Wea. Rev.*, **138 (9)**, 3514–3539, doi:10.1175/2010MWR3233.1.

Conzemius, R. J., R. W. Moore, M. T. Montgomery, and C. A. Davis, 2007: Mesoscale convective vortex formation in a weakly sheared moist neutral environment. *J. Atmos. Sci.*, **64 (5)**, 1443–1466, doi:10.1175/JAS3898.1.

Corfidi, S. F., S. J. Corfidi, and D. M. Schultz, 2008: Elevated convection and castellanus: Ambiguities, significance, and questions. *Wea. Forecasting*, **23 (6)**, 1280–1303, doi:10.1175/2008WAF2222118.1.

Crook, N. A., 1986: The effect of ambient stratification and moisture on the motion of atmospheric undular bores. *J. Atmos. Sci.*, **43 (2)**, 171–181, doi:10.1175/1520-0469(1986)043⟨0171:TEOASA⟩2.0.CO;2.

Crook, N. A., 1988: Trapping of low-level internal gravity waves. *J. Atmos. Sci.*, **45 (10)**, 1533–1541, doi:10.1175/1520-0469(1988)045⟨1533:TOLLIG⟩2.0.CO;2.

Danielsen, E. F., 1968: Stratospheric-tropospheric exchange based on radioactivity, ozone and potential vorticity. *J. Atmos. Sci.*, **25 (3)**, 502–518, doi:10.1175/1520-0469(1968)025⟨0502:STEBOR⟩2.0.CO;2.

Davies, H. C., and M. Didone, 2013: Diagnosis and dynamics of forecast error growth. *Mon. Wea. Rev.*, **141 (7)**, 2483–2501, doi:10.1175/MWR-D-12-00242.1.

Davis, C. A., and K. A. Emanuel, 1991: Potential vorticity diagnostics of cyclogenesis. *Mon. Wea. Rev.*, **119 (8)**, 1929–1953, doi:10.1175/1520-0493(1991)119⟨1929:PVDOC⟩2.0.CO;2.

Davis, C. A., K. W. Manning, R. E. Carbone, S. B. Trier, and J. D. Tuttle, 2003: Coherence of warm-season continental rainfall in numerical weather prediction models. *Mon. Wea. Rev.*, **131 (11)**, 2667–2679, doi:10.1175/1520-0493(2003)131⟨2667:COWCRI⟩2.0.CO;2.

Davis, C. A., and S. B. Trier, 2002: Cloud-resolving simulations of mesoscale vortex intensification and its effect on a serial mesoscale convective system. *Mon. Wea. Rev.*, **130 (12)**, 2839–2858, doi:10.1175/1520-0493(2002)130⟨2839:CRSOMV⟩2.0.CO;2.

Degelia, S. K., X. Wang, D. J. Stensrud, and A. Johnson, 2018: Understanding the impact of radar and in situ observations on the prediction of a nocturnal convection initiation event on 25 june 2013 using an ensemble-based multiscale data assimilation system. *Mon. Wea. Rev.*, **146 (6)**, 1837–1859, doi:10.1175/MWR-D-17-0128.1.

Dirren, S., M. Didone, and H. Davies, 2003: Diagnosis of "forecast-analysis" differences of a weather prediction system. *Geophysical research letters*, **30 (20)**, doi:10.1029/2003GL017986.

Durran, D. R., 1986a: Another look at downslope windstorms. part i: The development of analogs to supercritical flow in an infinitely deep, continuously stratified fluid. *J. Atmos. Sci*, **43 (21)**, 2527–2543, doi:10.1175/1520-0469(1986)043⟨2527:ALADWP⟩2.0.CO;2.

Durran, D. R., 1986b: *Mountain Waves*, 472–492. American Meteorological Society, Boston, MA, doi:10.1007/978-1-935704-20-1_20, URL https://doi.org/10.1007/978-1-935704-20-1_20.

Durran, D. R., 1990: Mountain waves and downslope winds. *Atmospheric processes over complex terrain*, Springer, 59–81.

Durran, D. R., M. O. Hills, and P. N. Blossey, 2015: The dissipation of trapped lee waves. part i: Leakage of inviscid waves into the stratosphere. *J. Atmos. Sci.*, **72 (4)**, 1569–1584, doi:10.1175/JAS-D-14-0238.1.

Easterling, D. R., and P. J. Robinson, 1985: The diurnal variation of thunderstorm activity in the united states. *Journal of Climate and Applied Meteorology*, **24 (10)**, 1048–1058, doi:10.1175/1520-0450(1985)024⟨1048:TDVOTA⟩2.0.CO;2.

Ertel, H., 1942: Ein neuer hydrodynarnischer wirbelsatz. *Meteor. Z*, **59**, 271–281.

Fedorovich, E., J. A. Gibbs, and A. Shapiro, 2017: Numerical study of nocturnal low-level jets over gently sloping terrain. *J. Atmos. Sci*, **74 (9)**, 2813–2834, doi:10.1175/JAS-D-17-0013.1.

Fovell, R. G., G. L. Mullendore, and S.-H. Kim, 2006: Discrete propagation in numerically simulated nocturnal squall lines. *Mon. Wea. Rev.*, **134 (12)**, 3735–3752, doi:10.1175/MWR3268.1.

French, A. J., and M. D. Parker, 2010: The response of simulated nocturnal convective systems to a developing low-level jet. *Journal of the atmospheric sciences*, **67 (10)**, 3384–3408, doi:10.1175/2010JAS3329.1.

Fritsch, J., R. Kane, and C. Chelius, 1986: The contribution of mesoscale convective weather systems to the warm-season precipitation in the united states. *Journal of climate and applied meteorology*, **25 (10)**, 1333–1345, doi:10.1175/1520-0450(1986)025⟨1333:TCOMCW⟩2.0.CO;2.

Gal-Chen, T., and R. C. Somerville, 1975: On the use of a coordinate transformation for the solution of the navier-stokes equations. *Journal of Computational Physics*, **17 (2)**, 209–228, doi:10.1016/0021-9991(75)90037-6.

Gebauer, J. G., E. Fedorovich, and A. Shapiro, 2017: A 1d theoretical analysis of northerly low-level jets over the great plains. *J. Atmos. Sci.*, **74 (10)**, 3419–3431, doi:10.1175/JAS-D-16-0333.1.

Gebauer, J. G., and A. Shapiro, 2019: Clarifying the baroclinic contribution to the great plains low-level jet frequency maximum. *Mon. Wea. Rev.*, **147 (9)**, 3481–3493, doi:10.1175/MWR-D-19-0024.1.

Gebauer, J. G., A. Shapiro, E. Fedorovich, and P. Klein, 2018: Convection initiation caused by heterogeneous low-level jets over the great plains. *Mon. Wea. Rev.*, **146 (8)**, 2615–2637, doi:10.1175/MWR-D-18-0002.1.

Geerts, B., and Coauthors, 2017: The 2015 plains elevated convection at night field project. *Bull. Amer. Meteor. Soc.*, **98 (4)**, 767–786, doi:BAMS-D-15-00257.1.

Grasmick, C., B. Geerts, D. D. Turner, Z. Wang, and T. Weckwerth, 2018: The relation between nocturnal mcs evolution and its outflow boundaries in the stable boundary layer: An observational study of the 15 july 2015 mcs in pecan. *Mon. Wea. Rev.*, **146 (10)**, 3203–3226, doi:10.1175/MWR-D-18-0169.1.

Haghi, K. R., and D. R. Durran, 2020: On the dynamics of atmospheric bores. *J. Atmos. Sci.*, **1 (aop)**, 1–46, doi:10.1175/JAS-D-20-0181.1.

Haghi, K. R., D. B. Parsons, and A. Shapiro, 2017: Bores observed during ihop_2002: The relationship of bores to the nocturnal environment. *Mon. Wea. Rev.*, **145 (10)**, 3929–3946, doi:10.1175/MWR-D-16-0415.1.

Haghi, K. R., and Coauthors, 2019: Bore-ing into nocturnal convection. *Bull. Amer. Meteor. Soc.*, **100 (6)**, 1103–1121, doi:10.1175/BAMS-D-17-0250.1.

Hakim, G. J., D. Keyser, and L. F. Bosart, 1996: The ohio valley wave-merger cyclogenesis event of 25–26 january 1978. part ii: Diagnosis using quasigeostrophic potential vorticity inversion. *Mon. Wea. Rev.*, **124 (10)**, 2176–2205, doi:10.1175/1520-0493(1996)124⟨2176:TOVWMC⟩2.0.CO;2.

Hardy, S., D. M. Schultz, and G. Vaughan, 2017: The 23–26 september 2012 uk floods: Using pv surgery to quantify sensitivity to upper-level forcing. *Mon. Wea. Rev.*, **145 (10)**, 4055–4079, doi:10.1175/MWR-D-16-0434.1.

Hersbach, H., 2016: The era5 atmospheric reanalysis. *AGUFM*, **2016**, NG33D–01.

Hitchcock, S. M., and R. S. Schumacher, 2020: Analysis of back-building convection in simulations with a strong low-level stable layer. *Mon. Wea. Rev.*, **148 (9)**, 3773–3797, doi:10.1175/MWR-D-19-0246.1.

Holton, J. R., 1967: The diurnal boundary layer wind oscillation above sloping terrain. *Tellus*, **19 (2)**, 200–205, doi:10.1111/j.2153-3490.1967.tb01473.x.

Hong, S.-Y., Y. Noh, and J. Dudhia, 2006: A new vertical diffusion package with an explicit treatment of entrainment processes. *Mon. Wea. Rev.*, **134 (9)**, 2318–2341, doi:10.1175/MWR3199.1.

Horgan, K. L., D. M. Schultz, J. E. Hales Jr, S. F. Corfidi, and R. H. Johns, 2007: A five-year climatology of elevated severe convective storms in the united states east of the rocky mountains. *Wea. Forecasting*, **22 (5)**, 1031–1044, doi:10.1175/WAF1032.1.

Hoskins, B. J., M. E. McIntyre, and A. W. Robertson, 1985: On the use and significance of isentropic potential vorticity maps. *Quart. J. Roy. Meteor. Soc.*, **111 (470)**, 877–946, doi:10.1002/qj.49711147002.

Hutson, A., C. Weiss, and G. Bryan, 2019: Using the translation speed and vertical structure of gust fronts to infer buoyancy deficits within thunderstorm outflow. *Mon. Wea. Rev.*, **147 (10)**, 3575–3594, doi:10.1175/MWR-D-18-0439.1.

James, E. P., and R. H. Johnson, 2010: A climatology of midlatitude mesoscale convective vortices in the rapid update cycle. *Mon. Wea. Rev.*, **138 (5)**, 1940–1956, doi:10.1175/2009MWR3208.1.

Jiang, H., and D. J. Raymond, 1995: Simulation of a mature mesoscale convective system using a nonlinear balance model. *J. Atmos. Sci.*, **52 (2)**, 161–175, doi:10.1175/1520-0469(1995)052⟨0161:SOAMMC⟩2.0.CO;2.

Jiménez, P. A., J. Dudhia, J. F. González-Rouco, J. Navarro, J. P. Montávez, and E. García-Bustamante, 2012: A revised scheme for the wrf surface layer formulation. *Mon. Wea. Rev.*, **140 (3)**, 898–918, doi:10.1175/MWR-D-11-00056.1.

Jirak, I. L., and W. R. Cotton, 2007: Observational analysis of the predictability of mesoscale convective systems. *Wea. Forecasting*, **22 (4)**, 813–838, doi:10.1175/WAF1012.1.

Jones, P. A., and P. R. Bannon, 2002: A mixed-layer model of the diurnal dryline. *J. Atmos. Sci.*, **59 (17)**, 2582–2593, doi:10.1175/1520-0469(2002)059⟨2582:AMLMOT⟩2.0.CO;2.

Karyampudi, V. M., S. E. Koch, C. Chen, J. W. Rottman, and M. L. Kaplan, 1995: The influence of the rocky mountains on the 13–14 april 1986 severe weather outbreak. part ii: Evolution of a prefrontal bore and its role in triggering a squall line. *Mon. Wea. Rev.*, **123 (5)**, 1423–1446, doi:10.1175/1520-0493(1995)123⟨1423:TIOTRM⟩2.0.CO;2.

Keene, K. M., and R. S. Schumacher, 2013: The bow and arrow mesoscale convective structure. *Mon. Wea. Rev.*, **141 (5)**, 1648–1672, doi:10.1175/MWR-D-12-00172.1.

Kincer, J. B., 1916: Daytime and nighttime precipitation and their economic significance. *Mon. Wea. Rev.*, **44 (11)**, 628–633, doi:10.1175/1520-0493(1916)44⟨628:DANPAT⟩2.0.CO;2.

Klemp, J., J. Dudhia, and A. Hassiotis, 2008: An upper gravity-wave absorbing layer for nwp applications. *Mon. Wea. Rev.*, **136 (10)**, 3987–4004, doi:10.1175/2008MWR2596.1.

Knight, C. A., L. Jay Miller, and W. D. Hall, 2004: Deep convection and "first echoes" within anvil precipitation. *Mon. Wea. Rev.*, **132 (7)**, 1877–1890, doi:10.1175/1520-0493(2004)132⟨1877:DCAFEW⟩2.0.CO;2.

Knupp, K., 2006: Observational analysis of a gust front to bore to solitary wave transition within an evolving nocturnal boundary layer. *J. Atmos. Sci.*, **63 (8)**, 2016–2035, doi:10.1175/JAS3731.1.

Koch, S. E., P. B. Dorian, R. Ferrare, S. Melfi, W. C. Skillman, and D. Whiteman, 1991: Structure of an internal bore and dissipating gravity current as revealed by raman lidar. *Mon. Wea. Rev.*, **119 (4)**, 857–887, doi:10.1175/1520-0493(1991)119⟨0857:SOAIBA⟩2.0.CO;2.

Koch, S. E., W. Feltz, F. Fabry, M. Pagowski, B. Geerts, K. M. Bedka, D. O. Miller, and J. W. Wilson, 2008a: Turbulent mixing processes in atmospheric bores and solitary waves deduced from profiling systems and numerical simulation. *Mon. Wea. Rev.*, **136 (4)**, 1373–1400, doi:10.1175/2007MWR2252.1.

Koch, S. E., C. Flamant, J. W. Wilson, B. M. Gentry, and B. D. Jamison, 2008b: An atmospheric soliton observed with doppler radar, differential absorption lidar, and a molecular doppler lidar. *J. Atmos. Oceanic Technol.*, **25 (8)**, 1267–1287, doi:10.1175/2007JTECHA951.1.

Koch, S. E., and Coauthors, 2005: Turbulence and gravity waves within an upper-level front. *J. Atmos. Sci.*, **62 (11)**, 3885–3908, doi:10.1175/JAS3574.1.

Lackmann, G. M., 2002: Cold-frontal potential vorticity maxima, the low-level jet, and moisture transport in extratropical cyclones. *Mon. Wea. Rev.*, **130 (1)**, 59–74, doi:10.1175/1520-0493(2002)130⟨0059:CFPVMT⟩2.0.CO;2.

Lane, T. P., and M. J. Reeder, 2001: Convectively generated gravity waves and their effect on the cloud environment. *J. Atmos. Sci.*, **58 (16)**, 2427–2440, doi:10.1175/1520-0469(2001)058⟨2427:CGGWAT⟩2.0.CO;2.

Li, Y., and R. B. Smith, 2010: The detection and significance of diurnal pressure and potential vorticity anomalies east of the rockies. *J. Atmos. Sci.*, **67 (9)**, 2734–2751, doi:10.1175/2010JAS3423.1.

Lindzen, R., and K. Tung, 1976: Banded convective activity and ducted gravity waves. *Mon. Wea. Rev.*, **104 (12)**, 1602–1617, doi:10.1175/1520-0493(1976)104⟨1602:BCAADG⟩2.0.CO;2.

Louis, J.-F., 1979: A parametric model of vertical eddy fluxes in the atmosphere. *Boundary-Layer Meteorology*, **17 (2)**, 187–202, doi:10.1007/BF00117978.

Loveless, D. M., T. J. Wagner, D. D. Turner, S. A. Ackerman, and W. F. Feltz, 2019: A composite perspective on bore passages during the pecan campaign. *Mon. Wea. Rev.*, **147 (4)**, 1395–1413, doi:10.1175/MWR-D-18-0291.1.

Maddox, R. A., 1983: Large-scale meteorological conditions associated with midlatitude, mesoscale convective complexes. *Mon. Wea. Rev.*, **111 (7)**, 1475–1493, doi:10.1175/1520-0493(1983)111⟨1475:LSMCAW⟩2.0.CO;2.

Markowski, P., and Y. Richardson, 2011: *Mesoscale meteorology in midlatitudes*, Vol. 2. John Wiley & Sons.

Marsham, J. H., S. B. Trier, T. M. Weckwerth, and J. W. Wilson, 2011: Observations of elevated convection initiation leading to a surface-based squall line during 13 june ihop_2002. *Mon. Wea. Rev.*, **139 (1)**, 247–271, doi:10.1175/2010MWR3422.1.

Martin, E. R., and R. H. Johnson, 2008: An observational and modeling study of an atmospheric internal bore during name 2004. *Monthly weather review*, **136 (11)**, 4150–4167, doi:10.1175/2008MWR2486.1.

Martin, J. E., 2013: *Mid-latitude atmospheric dynamics: a first course*. John Wiley & Sons.

Mesinger, F., and Coauthors, 2006: North american regional reanalysis. *Bull. Amer. Meteor. Soc.*, **87 (3)**, 343–360, doi:10.1175/BAMS-87-3-343.

Mitchell, M. J., R. W. Arritt, and K. Labas, 1995: A climatology of the warm season great plains low-level jet using wind profiler observations. *Wea. Forecasting*, **10 (3)**, 576–591, doi:10.1175/1520-0434(1995)010⟨0576:ACOTWS⟩2.0.CO;2.

Moore, J. T., F. H. Glass, C. E. Graves, S. M. Rochette, and M. J. Singer, 2003: The environment of warm-season elevated thunderstorms associated with heavy rainfall over the central united states. *Wea. Forecasting*, **18 (5)**, 861–878, doi:10.1175/1520-0434(2003)018⟨0861:TEOWET⟩2.0.CO;2.

Moore, R. W., and M. T. Montgomery, 2005: Analysis of an idealized, three-dimensional diabatic rossby vortex: A coherent structure of the moist baroclinic atmosphere. *J. Atmos. Sci.*, **62 (8)**, 2703–2725, doi:10.1175/JAS3472.1.

Morgan, M. C., and J. W. Nielsen-Gammon, 1998: Using tropopause maps to diagnose midlatitude weather systems. *Mon. Wea. Rev.*, **126 (10)**, 2555–2579, doi:10.1175/1520-0493(1998)126⟨2555:UTMTDM⟩2.0.CO;2.

Mueller, D., B. Geerts, Z. Wang, M. Deng, and C. Grasmick, 2017: Evolution and vertical structure of an undular bore observed on 20 june 2015 during pecan. *Mon. Wea. Rev.*, **145 (9)**, 3775–3794, doi:10.1175/MWR-D-16-0305.1.

Nielsen-Gammon, J. W., and D. A. Gold, 2008a: Potential vorticity diagnosis in the quasigeostrophic and nonlinear balance systems. *J. Atmos. Sci.*, **65 (1)**, 172–188, doi:10.1175/2007JAS2270.1.

Nielsen-Gammon, J. W., and D. A. Gold, 2008b: Potential vorticity diagnosis of the severe convective regime. part ii: The impact of idealized pv anomalies. *Mon. Wea. Rev.*, **136 (5)**, 1582–1592, doi:10.1175/2007MWR2091.1.

Parish, T. R., 2016: A comparative study of the 3 june 2015 great plains low-level jet. *Mon. Wea. Rev.*, **144 (8)**, 2963–2979, doi:10.1175/MWR-D-16-0071.1.

Parish, T. R., R. D. Clark, and T. D. Sikora, 2020: Nocturnal destabilization associated with the summertime great plains low-level jet. *Mon. Wea. Rev.*, **148 (11)**, 4641–4656, doi:10.1175/MWR-D-19-0394.1.

Parker, M. D., 2008: Response of simulated squall lines to low-level cooling. *J. Atmos. Sci.*, **65 (4)**, 1323–1341, doi:10.1175/2007JAS2507.1.

Parker, M. D., 2014: Composite vortex2 supercell environments from near-storm soundings. *Mon. Wea. Rev.*, **142 (2)**, 508–529, doi:10.1175/MWR-D-13-00167.1.

Parker, M. D., and D. A. Ahijevych, 2007: Convective episodes in the east-central united states. *Mon. Wea. Rev.*, **135 (11)**, 3707–3727, doi:10.1175/2007MWR2098.1.

Parsons, D. B., 1992: An explanation for intense frontal updrafts and narrow cold-frontal rainbands. *J. Atmos. Sci*, **49 (19)**, 1810–1825, doi:10.1175/1520-0469(1992)049⟨1810:AEFIFU⟩2.0.CO;2.

Parsons, D. B., K. R. Haghi, K. T. Halbert, B. Elmer, and J. Wang, 2019: The potential role of atmospheric bores and gravity waves in the initiation and maintenance of nocturnal convection over the southern great plains. *J. Atmos. Sci.*, **76 (1)**, 43–68, doi:10.1175/JAS-D-17-0172.1.

Peters, J. M., and R. S. Schumacher, 2015: Mechanisms for organization and echo training in a flash-flood-producing mesoscale convective system. *Mon. Wea. Rev.*, **143 (4)**, 1058–1085, doi:10.1175/MWR-D-14-00070.1.

Pitchford, K. L., and J. London, 1962: The low-level jet as related to nocturnal thunderstorms over midwest united states. *Journal of Applied Meteorology*, **1 (1)**, 43–47, doi:10.1175/1520-0450(1962)001⟨0043:TLLJAR⟩2.0.CO;2.

Pu, B., and R. E. Dickinson, 2014: Diurnal spatial variability of great plains summer precipitation related to the dynamics of the low-level jet. *J. Atmos. Sci.*, **71 (5)**, 1807–1817, doi:10.1175/JAS-D-13-0243.1.

Raymond, D., and H. Jiang, 1990: A theory for long-lived mesoscale convective systems. *J. Atmos. Sci.*, **47 (24)**, 3067–3077, doi:10.1175/1520-0469(1990)047⟨3067:ATFLLM⟩2.0.CO;2.

Reed, R. J., 1955: A study of a characteristic tpye of upper-level frontogenesis. *Journal of Meteorology*, **12 (3)**, 226–237, doi:10.1175/1520-0469(1955)012⟨0226:ASOACT⟩2.0.CO;2.

Reif, D. W., and H. B. Bluestein, 2017: A 20-year climatology of nocturnal convection initiation over the central and southern great plains during the warm season. *Mon. Wea. Rev.*, **145 (5)**, 1615–1639, doi:10.1175/MWR-D-16-0340.1.

Reif, D. W., and H. B. Bluestein, 2018: Initiation mechanisms of nocturnal convection without nearby surface boundaries over the central and southern great plains during the warm season. *Mon. Wea. Rev.*, **146 (9)**, 3053–3078, doi:10.1175/MWR-D-18-0040.1.

Reif, D. W., H. B. Bluestein, T. M. Weckwerth, Z. B. Wienhoff, and M. B. Chasteen, 2020: Estimating the maximum vertical velocity at the leading edge of a density current. *J. Atmos. Sci*, **77 (11)**, 3683–3700, doi:10.1175/JAS-D-20-0028.1.

Rickenbach, T. M., 2004: Nocturnal cloud systems and the diurnal variation of clouds and rainfall in southwestern amazonia. *Mon. Wea. Rev.*, **132 (5)**, 1201–1219, doi:10.1175/1520-0493(2004)132⟨1201:NCSATD⟩2.0.CO;2.

Riley, G. T., M. G. Landin, and L. F. Bosart, 1987: The diurnal variability of precipitation across the central rockies and adjacent great plains. *Mon. Wea. Rev.*, **115 (6)**, 1161–1172, doi:10.1175/1520-0493(1987)115⟨1161:TDVOPA⟩2.0.CO;2.

Roebber, P. J., D. M. Schultz, and R. Romero, 2002: Synoptic regulation of the 3 may 1999 tornado outbreak. *Wea. Forecasting*, **17 (3)**, 399–429, doi:10.1175/1520-0434(2002)017⟨0399:SROTMT⟩2.0.CO;2.

Rossby, C., 1939: Planetary flow patterns in the atmosphere. *Quart. J. Roy. Met. Soc*, **66**, 68–87.

Rottman, J. W., and J. E. Simpson, 1989: The formation of internal bores in the atmosphere: A laboratory model. *Quart. J. Roy. Meteor. Soc.*, **115 (488)**, 941–963, doi:10.1002/qj.49711548809.

Rotunno, R., J. B. Klemp, and M. L. Weisman, 1988: A theory for strong, long-lived squall lines. *J. Atmos. Sci*, **45 (3)**, 463–485, doi:10.1175/1520-0469(1988)045⟨0463:ATFSLL⟩2.0.CO;2.

Rotunno, R., G. S. Romine, and H. B. Bluestein, 2018: A simple model for the anomalous counterclockwise turning of the surface wind with time over the great plains of the united states. *J. Atmos. Sci*, **75 (9)**, 2971–2981, doi:10.1175/JAS-D-18-0074.1.

Scorer, R. S., 1949: Theory of waves in the lee of mountains. *Quart. J. Roy. Meteor. Soc.*, **75 (323)**, 41–56, doi:10.1002/qj.49707532308.

Seigel, R. B., and S. C. van den Heever, 2012: Simulated density currents beneath embedded stratified layers. *J. Atmos. Sci*, **69 (7)**, 2192–2200, doi:10.1175/JAS-D-11-0255.1.

Shapiro, A., and E. Fedorovich, 2009: Nocturnal low-level jet over a shallow slope. *Acta Geophysica*, **57 (4)**, 950–980, doi:10.2478/s11600-009-0026-5.

Shapiro, A., and E. Fedorovich, 2010: Analytical description of a nocturnal low-level jet. *Quart. J. Roy. Meteor. Soc.*, **136 (650)**, 1255–1262, doi:10.1002/qj.628.

Shapiro, A., E. Fedorovich, and J. G. Gebauer, 2018: Mesoscale ascent in nocturnal low-level jets. *J. Atmos. Sci.*, **75 (5)**, 1403–1427, doi:10.1175/JAS-D-17-0279.1.

Shapiro, A., E. Fedorovich, and S. Rahimi, 2016: A unified theory for the great plains nocturnal low-level jet. *J. Atmos. Sci.*, **73 (8)**, 3037–3057, doi:10.1175/JAS-D-15-0307.1.

Shapiro, M., 1980: Turbulent mixing within tropopause folds as a mechanism for the exchange of chemical constituents between the stratosphere and troposphere. *J. Atmos. Sci.*, **37 (5)**, 994–1004, doi:10.1175/1520-0469(1980)037⟨0994:TMWTFA⟩2.0.CO;2.

Shapiro, M., T. Hampel, and A. Krueger, 1987: The arctic tropopause fold. *Mon. Wea. Rev.*, **115 (2)**, 444–454, doi:10.1175/1520-0493(1987)115⟨0444:TATF⟩2.0.CO;2.

Skamarock, W. C., and Coauthors, 2008: G.: A description of the advanced research wrf version 3. *NCAR Tech. Note NCAR/TN-475+ STR*, Citeseer, doi:10.5065/D68S4MVH.

Smith, E. N., J. G. Gebauer, P. M. Klein, E. Fedorovich, and J. A. Gibbs, 2019: The great plains low-level jet during pecan: Observed and simulated characteristics. *Mon. Wea. Rev.*, **147 (6)**, 1845–1869, doi:10.1175/MWR-D-18-0293.1.

Smith, E. N., J. A. Gibbs, E. Fedorovich, and P. M. Klein, 2018: Wrf model study of the great plains low-level jet: Effects of grid spacing and boundary layer parameterization. *J. Appl. Meteor. Climatol.*, **57 (10)**, 2375–2397, doi:10.1175/JAMC-D-17-0361.1.

Smith, R. K., 1988: Travelling waves and bores in the lower atmosphere: the 'morning glory'and related phenomena. *Earth-Science Reviews*, **25 (4)**, 267–290, doi:10.1016/0012-8252(88)90069-4.

Song, J., K. Liao, R. L. Coulter, and B. M. Lesht, 2005: Climatology of the low-level jet at the southern great plains atmospheric boundary layer experiments site. *Journal of Applied Meteorology*, **44 (10)**, 1593–1606, doi:10.1175/JAM2294.1.

Squitieri, B. J., and W. A. Gallus Jr, 2016: Wrf forecasts of great plains nocturnal low-level jet-driven mcss. part i: Correlation between low-level jet forecast accuracy and mcs precipitation forecast skill. *Wea. Forecasting*, **31 (4)**, 1301–1323, doi:10.1175/WAF-D-15-0151.1.

Stelten, S., and W. A. Gallus Jr, 2017: Pristine nocturnal convective initiation: A climatology and preliminary examination of predictability. *Wea. Forecasting*, **32 (4)**, 1613–1635, doi:10.1175/WAF-D-16-0222.1.

Stull, R. B., 2012: *An introduction to boundary layer meteorology*, Vol. 13. Springer Science & Business Media.

Sukoriansky, S., B. Galperin, and V. Perov, 2005: Application of a new spectral theory of stably stratified turbulence to the atmospheric boundary layer over sea ice. *Boundary-layer meteorology*, **117 (2)**, 231–257, doi:10.1007/s10546-004-6848-4.

Sun, W.-Y., and C.-C. Wu, 1992: Formation and diurnal variation of the dryline. *J. Atmos. Sci.*, **49 (17)**, 1606–1619, doi:10.1175/1520-0469(1992)049⟨1606:FADVOT⟩2.0.CO;2.

Surcel, M., M. Berenguer, and I. Zawadzki, 2010: The diurnal cycle of precipitation from continental radar mosaics and numerical weather prediction models. part i: Methodology and seasonal comparison. *Mon. Wea. Rev.*, **138 (8)**, 3084–3106, doi:10.1175/2010MWR3125.1.

Tepper, M., 1950: A proposed mechanism of squall lines: The pressure jump line. *Journal of Meteorology*, **7 (1)**, 21–29, doi:10.1175/1520-0469(1950)007⟨0021:APMOSL⟩2.0.CO;2.

Thorpe, A. J., 1986: Synoptic scale disturbances with circular symmetry. *Mon. Wea. Rev.*, **114 (7)**, 1384–1389, doi:10.1175/1520-0493(1986)114⟨1384:SSDWCS⟩2.0.CO;2.

Tollerud, E. I., and Coauthors, 2008: Mesoscale moisture transport by the low-level jet during the ihop field experiment. *Mon. Wea. Rev.*, **136 (10)**, 3781–3795, doi:10.1175/2008MWR2421.1.

Toms, B. A., J. M. Tomaszewski, D. D. Turner, and S. E. Koch, 2017: Analysis of a lower-tropospheric gravity wave train using direct and remote sensing measurement systems. *Mon. Wea. Rev.*, **145 (7)**, 2791–2812, doi:10.1175/MWR-D-16-0216.1.

Torn, R. D., and G. S. Romine, 2015: Sensitivity of central oklahoma convection forecasts to upstream potential vorticity anomalies during two strongly forced cases during mpex. *Mon. Wea. Rev.*, **143 (10)**, 4064–4087, doi:10.1175/MWR-D-15-0085.1.

Trier, S., C. Davis, and W. Skamarock, 2000: Long-lived mesoconvective vortices and their environment. part ii: Induced thermodynamic destabilization in idealized simulations. *Mon. Wea. Rev.*, **128 (10)**, 3396–3412, doi:10.1175/1520-0493(2000)128⟨3396:LLMVAT⟩2.0.CO;2.

Trier, S. B., S. D. Kehler, and J. Hanesiak, 2020: Observations and simulation of elevated nocturnal convection initiation on 24 june 2015 during pecan. *Mon. Wea. Rev.*, **148 (2)**, 613–635, doi:10.1175/MWR-D-19-0218.1.

Trier, S. B., and D. B. Parsons, 1993: Evolution of environmental conditions preceding the development of a nocturnal mesoscale convective complex. *Mon. Wea. Rev.*, **121 (4)**, 1078–1098, doi:10.1175/1520-0493(1993)121⟨1078:EOECPT⟩2.0.CO;2.

Trier, S. B., J. W. Wilson, D. A. Ahijevych, and R. A. Sobash, 2017: Mesoscale vertical motions near nocturnal convection initiation in pecan. *Mon. Wea. Rev.*, **145 (8)**, 2919–2941, doi:10.1175/MWR-D-17-0005.1.

Tripoli, G. J., and W. R. Cotton, 1989a: Numerical study of an observed orogenic mesoscale convective system. part 1: Simulated genesis and comparison with observations. *Mon. Wea. Rev.*, **117 (2)**, 273–304, doi:10.1175/1520-0493(1989)117⟨0273:NSOAOO⟩2.0.CO;2.

Tripoli, G. J., and W. R. Cotton, 1989b: Numerical study of an observed orogenic mesoscale convective system. part 2: Analysis of governing dynamics. *Mon. Wea. Rev.*, **117 (2)**, 305–328, doi:10.1175/1520-0493(1989)117⟨0305:NSOAOO⟩2.0.CO;2.

Wallace, J. M., 1975: Diurnal variations in precipitation and thunderstorm frequency over the conterminous united states. *Mon. Wea. Rev.*, **103 (5)**, 406–419, doi:10.1175/1520-0493(1975)103⟨0406:DVIPAT⟩2.0.CO;2.

Wallace, J. M., and P. V. Hobbs, 2006: *Atmospheric science: an introductory survey*, Vol. 92. Elsevier.

Walters, C. K., and J. A. Winkler, 2001: Airflow configurations of warm season southerly low-level wind maxima in the great plains. part i: Spatial and temporal characteristics and relationship to convection. *Wea. Forecasting*, **16 (5)**, 513–530, doi:10.1175/1520-0434(2001)016⟨0513:ACOWSS⟩2.0.CO;2.

Weckwerth, T. M., J. Hanesiak, J. W. Wilson, S. B. Trier, S. K. Degelia, W. A. Gallus Jr, R. D. Roberts, and X. Wang, 2019: Nocturnal convection initiation during pecan 2015. *Bull. Amer. Meteor. Soc.*, **100 (11)**, 2223–2239, doi:10.1175/BAMS-D-18-0299.1.

Weckwerth, T. M., and U. Romatschke, 2019: Where, when, and why did it rain during pecan? *Mon. Wea. Rev.*, **147 (10)**, 3557–3573, doi:MWR-D-18-0458.1.

Weckwerth, T. M., and Coauthors, 2004: An overview of the international h2o project (ihop_2002) and some preliminary highlights. *Bull. Amer. Meteor. Soc.*, **85 (2)**, 253–278, doi:10.1175/BAMS-85-2-253.

Weijenborg, C., J. Chagnon, P. Friederichs, S. Gray, and A. Hense, 2017: Coherent evolution of potential vorticity anomalies associated with deep moist convection. *Quart. J. Roy. Meteor. Soc.*, **143 (704)**, 1254–1267, doi:10.1002/qj.3000.

Whiteman, C. D., X. Bian, and S. Zhong, 1997: Low-level jet climatology from enhanced rawinsonde observations at a site in the southern great plains. *Journal of Applied Meteorology*, **36 (10)**, 1363–1376, doi:10.1175/1520-0450(1997)036⟨1363:LLJCFE⟩2.0.CO;2.

Wilson, J., S. Trier, D. Reif, R. Roberts, and T. Weckwerth, 2018: Nocturnal elevated convection initiation of the pecan 4 july hailstorm. *Mon. Wea. Rev.*, **146 (1)**, 243–262, doi:10.1175/MWR-D-17-0176.1.

Wilson, J. W., and R. D. Roberts, 2006: Summary of convective storm initiation and evolution during ihop: Observational and modeling perspective. *Mon. Wea. Rev.*, **134 (1)**, 23–47, doi:10.1175/MWR3069.1.

Winters, A. C., and J. E. Martin, 2017: Diagnosis of a north american polar–subtropical jet superposition employing piecewise potential vorticity inversion. *Mon. Wea. Rev.*, **145 (5)**, 1853–1873, doi:10.1175/MWR-D-16-0262.1.

Wu, C.-C., and K. A. Emanuel, 1995: Potential vorticity diagnostics of hurricane movement. part 1: A case study of hurricane bob (1991). *Mon. Wea. Rev.*, **123 (1)**, 69–92, doi:10.1175/1520-0493(1995)123⟨0069:PVDOHM⟩2.0.CO;2.

Yang, X., J. Fei, X. Huang, X. Cheng, L. M. Carvalho, and H. He, 2015: Characteristics of mesoscale convective systems over china and its vicinity using geostationary satellite fy2. *Journal of Climate*, **28 (12)**, 4890–4907, doi:10.1175/JCLI-D-14-00491.1.

Yuan, W., R. Yu, M. Zhang, W. Lin, H. Chen, and J. Li, 2012: Regimes of diurnal variation of summer rainfall over subtropical east asia. *Journal of Climate*, **25 (9)**, 3307–3320, doi:10.1175/JCLI-D-11-00288.1.

Appendix A

Finite Differencing Scheme for 3-D Poisson Operators

The basic Poisson operator is given by

$$\left(a\frac{\partial^2}{\partial x^2}+b\frac{\partial^2}{\partial y^2}+c\frac{\partial^2}{\partial z^2}\right)D=F \tag{A.1}$$

where a, b, and c are constants, F is the forcing function, and D is the variable to solve for. The finite differencing schemes for the second derivatives are given by

$$a\frac{\partial^2 D}{\partial x^2}=a\left(\frac{D_{i+1,j,k}-2D_{i,j,k}+D_{i-1,j,k}}{\Delta x^2}\right) \tag{A.2}$$

$$b\frac{\partial^2 D}{\partial y^2}=b\left(\frac{D_{i,j+1,k}-2D_{i,j,k}+D_{i,j-1,k}}{\Delta y^2}\right) \tag{A.3}$$

$$c\frac{\partial^2 D}{\partial z^2}=c\left(\frac{D_{i,j,k+1}-2D_{i,j,k}+D_{i,j,k-1}}{\Delta z^2}\right) \tag{A.4}$$

Substituting these into A.1 yields

$$a\left(\frac{D_{i+1,j,k}-2D_{i,j,k}+D_{i-1,j,k}}{\Delta x^2}\right)+b\left(\frac{D_{i,j+1,k}-2D_{i,j,k}+D_{i,j-1,k}}{\Delta y^2}\right)+ c\left(\frac{D_{i,j,k+1}-2D_{i,j,k}+D_{i,j,k-1}}{\Delta z^2}\right)=F_{i,j,k} \tag{A.5}$$

Next we need to solve for $D_{i,j,k}$.

$$-a\frac{-2D_{i,j,k}}{\Delta x^2}-b\frac{-2D_{i,j,k}}{\Delta y^2}-c\frac{-2D_{i,j,k}}{\Delta z^2}+a\left(\frac{D_{i+1,j,k}+D_{i-1,j,k}}{\Delta x^2}\right)+ b\left(\frac{D_{i,j+1,k}+D_{i,j-1,k}}{\Delta y^2}\right)+c\left(\frac{D_{i,j,k+1}+D_{i,j,k-1}}{\Delta z^2}\right)=F_{i,j,k} \tag{A.6}$$

$$2D_{i,j,k}\left(\frac{a}{\Delta x^2}+\frac{b}{\Delta y^2}+\frac{c}{\Delta z^2}\right)=a\left(\frac{D_{i+1,j,k}+D_{i-1,j,k}}{\Delta x^2}\right)+ b\left(\frac{D_{i,j+1,k}+D_{i,j-1,k}}{\Delta y^2}\right)+c\left(\frac{D_{i,j,k+1}+D_{i,j,k-1}}{\Delta z^2}\right)-F_{i,j,k} \tag{A.7}$$

$$D_{i,j,k} = \frac{1}{2\left(\frac{a}{\Delta x^2} + \frac{b}{\Delta y^2} + \frac{c}{\Delta z^2}\right)} \left[a\left(\frac{D_{i+1,j,k} + D_{i-1,j,k}}{\Delta x^2}\right) + \right.$$

$$\left. b\left(\frac{D_{i,j+1,k} + D_{i,j-1,k}}{\Delta y^2}\right) + c\left(\frac{D_{i,j,k+1} + D_{i,j,k-1}}{\Delta z^2}\right) - F_{i,j,k} \right] \quad \text{(A.8)}$$

Equation A.8 is solved via iteration. $F_{i,j,k}$ is independent of the iteration (constant forcing function) and the non i, j, k terms for D are the previous iteration (or the initial guess in the case of the first iteration).